Durham University

Durham E-Theses

On the structure of accretion flows in compact accreting objects: a variability study across scales

VERESVARSKA, MARTINA

How to cite:

VERESVARSKA, MARTINA (2025) *On the structure of accretion flows in compact accreting objects: a variability study across scales*, Durham theses, Durham University. Available at Durham E-Theses Online: http://etheses.dur.ac.uk/16357/

Use policy

This work is licensed under a Creative Commons Attribution 3.0 (CC BY)

Academic Support Office, The Palatine Centre, Durham University, Stockton Road, Durham, DH1 3LE
e-mail: e-theses.admin@durham.ac.uk Tel: +44 0191 334 6107
http://etheses.dur.ac.uk

On the Structure of Accretion Flows in Compact Accreting Objects: A Variability Study Across Scales

Martina Veresvarska

A thesis presented for the degree of
Doctor of Philosophy

Centre For Extragalactic Astronomy
Department of Physics
Durham University
United Kingdom

November 2025

On the Structure of Accretion Flows in Compact Accreting Objects: A Variability Study Across Scales

Martina Veresvarska

Abstract:

Accretion is the most efficient process in the Universe that we know of generating energy from matter. It is behind some of the most luminous phenomena ever observed and is present across all scale sizes, from supermassive black holes at the centres of galaxies through stellar mass black holes to degenerate dead cores of stars, such as white dwarfs and neutron stars. Accretion is fundamental for understanding how elements are redistributed across the Universe and what happens to stars after they run out of nuclear fuel.

This thesis focuses mostly on white dwarfs accreting material via Roche-Lobe overflow from a donor in a binary system and low-mass X-ray binaries, where the accretor is a neutron star. The goal of this thesis is to demonstrate the similarities in geometrical structure of accretion flow around these systems, especially in the context of broad-band aperiodic and non-coherent quasi-periodic variability.

Firstly, this thesis presents the first detection of an outer edge of the thin accretion disc in an ultra-compact accreting double white dwarf system SDSS J190+3940. I use this discovery to showcase the similarity to a disc dominated broad-band variability of X-ray binaries by adapting an X-ray binary model to model the accretion flows in SDSS J190+3940, showing consistent results with the detected disc edge region.

This thesis also reports on the discovery of a new type of quasi-periodic oscillation in accreting white dwarf systems, which are analogous to well known quasi-periodic oscillations in X-ray binaries. Here I propose to explain this behaviour as due to precession of an inner accretion flow lifted from the accretion disc plane by magnetic warping torque. This model originally proposed to explain similar phenomena in neutron star binaries also represents another link between accretion across scales. I further apply this model to a rare class of accreting neutron stars, so called pulsating ultra-luminous X-ray sources. Currently only three systems show

these oscillations whilst being confirmed neutron stars. Therefore, measuring their intrinsic magnetic is still an open question. In this instance the model applied in this thesis also allows to constrain the lower limit of the magnetic field of the neutron stars to $\gtrsim 10^{12}$ G.

Furthermore some transient phenomenology of accreting white dwarfs, referred to as micronovae are discussed. Micronova bursts serve as a link to thermonuclear bursts in neutron star X-ray binaries. Here two new systems displaying these bursts are shown. One of them, an intermediate polar DW Cancri, is also found to be undergoing transient behaviour of pole-flipping, which begins shortly prior to the burst.

In summary, this thesis pertains to varied observational phenomena in accreting systems. The overarching theme focuses on the links between different accreting systems, showcasing the scale-invariant nature of accretion physics as a tool in studying accretion flow geometry.

Supervisor: Dr Simone Scaringi

Contents

List of Figures

List of Tables

Declaration

The work in this thesis is based on research carried out at the Centre for Extragalctic Astronomy, Department of Physics, University of Durham, England. No part of this thesis has been submitted elsewhere for any other degree or qualification, and it is the sole work of the author unless referenced to the contrary in the text.

Some of the work presented in this thesis has been published in journals - the relevant publications are listed below.

Publications

Chapter 3: Veresvarska, M., & Scaringi, S. (2023), MNRAS, 518, 5576.

Chapter 4: Veresvarska, M., Scaringi, S., Knigge, C., Paice, J., Buckley, D. A. H., Segura, N. C., de Martino, D., Groot, P. J., Ingram, A., Irving, Z. A., & Szkody, P. (2024b), MNRAS, 534, 3087.

Chapter 5: Veresvarska, M., Imbrogno M., Amato R., Israel G. L., Scaringi S., Casella P., Martino D. de, Fürst F., A. Gúrpide Lasheras, C. Knigge, Middleton M. J. (2025b), MNRAS, 541, 3627. arXiv e-prints, arXiv:2505.05557.

Chapter 6: Veresvarska, M., Scaringi, S., Hagen, S., De Martino, D., Done, C., Ilkiewicz, K., Knigge, C., & Littlefield, C. (2024a), MNRAS, 529, 664.

Chapter 7: Veresvarska, M., Scaringi S., Littlefield C., de Martino D., Knigge C.,Paice J., Altamirano D., Castro A., Michel R., Castro Segura N., Echevarría J., Groot P. J., Hernández Santisteban J. V., Irving Z.A., Altamirano-Dévora L., Sahu A., Buckley D.A.H., F. Vincentelli (2025a), MNRAS, 539, 2424.

Copyright © 2025 by

"*The copyright of this thesis rests with the author. No quotation from it should be published without the author's prior written consent and information derived from it should be acknowledged*".

Copyright © November 2025 by Martina Veresvarska.

"The copyright of this thesis rests with the author. No quotations from it should be published without the author's prior written consent and information derived from it should be acknowledged."

Acknowledgements

There are many people which I would like to acknowledge and without which this thesis would not have been completed. First and foremost I would like to thank my PhD supervisor, Dr Simone Scaringi, for his support and guidance through the past four years. I am very grateful for all your help in helping me find my feet as a (slightly) independent scientist and as a person. I would like to recognise all the opportunities that you have provided me during this PhD, including a very short notice observing run in Chile, which have made this time a truly unique experience. I realise that I may not be the easiest student to supervise at times, but I am grateful for all you have taught me, especially the enthusiasm for science, even though I am not as adept at expressing it. And I promise not to give up on white dwarfs.

Throughout my PhD, I have been lucky enough to meet many great researchers, without whose help this thesis would be a much thinner volume. I would like to especially thank Prof Christian Knigge for all his help with all of my papers and especially for his excellent abstract writing skills, which I unfortunately fail to replicate. I would also like to thank Dr Domitilla De Martino for her extensive help during my PhD and her excellent feedback on all my papers and proposals. Reading through your comments always makes me motivated to keep improving my drafts.

I would like to also acknowledge the support and help of the broader Durham community. In particular, Prof Chris Done, who has always been keen to help, even in cases that did not involve Xspec or swimming in the North Sea. I would especially like to thank Prof Dave Alexander and Prof Alastair Edge for their support of Cakes for Good, without whom this initiative wouldn't exist. Naturally, Cakes for Good would not be here without Dr Annagrazia Puglisi, whose mentorship has helped us through the shaky beginnings.

Apart from the Durham community, I have been incredibly lucky to be a part of a broader community, whose help and weekly discussions have always been of great help. I would also like to thank Dr John Paice, for always making my figures look better and for drawing great sketches, proving that one figure can speak a thousand words.

When moving to Durham at the tail end of Covid, I could not have imagined meeting so many great people. Many thanks to Carolina, Hannah and Filip for taking a scared first year PhD student under their wing. In particular, thank you Carolina for all the long conversations and for listening to all my complaints, without you the PhD experience would not be the same! And thank you for Cakes for Good, I will always feel it has been our brainchild and I am very proud of us for what it has accomplished! Thank you Filip for all the hikes and for surviving for 2 years in one of the most unpleasant student houses I have ever lived in. Thank you Hannah, for all the stories, which I will always think of. Many thanks also to Scott for getting through the PhD together, especially through the last year. We may have struggled to get through the application season, but I wouldn't have chosen to suffer through it with anyone else. Also, thanks for not breaking the INT, when I was supposed to be in charge. Many thanks also go to Tom, for being a great office mate and alway being ready to contribute to a conversation, irrespective of the workload. Thank you all for the great time during these past 4 years, and for all the wine and cheese nights I will miss dearly. Many thanks to Ciera, for taking over Cakes for Good, I couldn't pick anyone better for this. Also many thanks to the Durham PhD community for all the Friday pubs and (many) coffee breaks.

Veľmi by som sa chcela poďakovať svojej rodine, a úplne najviac mojim rodičom, ktorí pri mne vždy stáli a vždy ma podporovali vo všetkých výmysloch. Bez vás by nič z toho, čo som dokázala, nebolo možné. Som veľmi vďačná za všetko, čo ste pre mňa urobili, aj keď to so mnou nebolo vždy jednoduché. Mami, ďakujem za všetky kávy, čo sme spolu vypili, a hodiny, čo sme prečítali v kaviarňach. A tati, ďakujem za podporu, vždy som chcela dosiahnuť, aby si bol na mňa hrdý. Vždy som mala pocit, že vesmír je niečo, čo nás spája, a aj preto celá táto práca je aj pre teba. Veľmi by som chcela poďakovať aj svojim súrodencom, Danovi a Teri, aj keď už nie sme taká vlčia svorka ako kedysi. A špeciálne Teri, za všetko to, že si prerobila všetky moje výmysly na naozaj krásne nákresy.

Finally, I would like to thank the person who has been my greatest support through this PhD, my partner Stephen. Thank you, for always being there for me, through the nice and hard times equally. Without you, life would not be the same and this PhD would have never happened. Thank you for sharing your life and this journey with me and please forgive me for not finding the right words to express just how much you mean to me.

Chapter 1

Introduction

For most of the history of astronomy, Newton's theory of gravity has provided the main and obvious source of energy considered for the stars and other celestial bodies. The discovery of nucleosynthesis in stellar cores has shone some new light on the processes that power stars and explain their lifespans. But it is accretion, the process by which matter can be converted into energy, or rather by which the potential energy bound in matter can be released as luminosity, which is at the core of many research branches of astronomy today.

1.1 Accretion as an Energy Source

Accretion is the most efficient process to release energy in the form of luminosity from matter (Frank et al., 2002a). Even more so, it impacts the entirety of the electromagnetic spectrum, from radio (Fender & Gallo, 2014) to gamma rays (Narayan et al., 2001). Furthermore, many accreting objects, with compact accreting binary systems as a leading example, are predicted to be important sources for new generation of gravitational wave detectors, such as the Laser Interferometer Space Antenna (*LISA*) (Amaro-Seoane et al., 2017; Kupfer et al., 2018; Burdge et al., 2020; Kupfer et al., 2024). There have been many discoveries over the past decades which have led to accretion becoming such a prominent field of study in astronomy today. One of them is the discovery of black holes (BHs) and the magnitude of their gravity's effect on their immediate surroundings (Webster & Murdin, 1972). Another great example is the association of strong X-ray emission to accreting stellar mass black holes and neutron stars (Remillard & McClintock, 2006). And one of the fundamental results of the past few years, the first image of a BH showing the hot gas surround the super massive black hole (SMBH) at the centre of a face on galaxy M87 (Event Horizon Telescope Collaboration et al., 2019)

and at the centre of the Milky Way Sagittarius A* (Event Horizon Telescope Collaboration et al., 2022). All of these advances showcase the power and universal nature of accretion, highlighting the need for better understanding of this process.

There are many types of systems with active accretion across all scale sizes in the Universe. On the most massive scale, there are SMBH in the centres of galaxies. These systems, when actively accreting are known as Active Galactic Nuclei (AGN) (Netzer, 2015) and are the most luminous persistent objects in the Universe. They play a fundamental role in the galaxy evolution and feedback, being substantially responsible for the Universe we observe today (Harrison & Ramos Almeida, 2024). On a smaller scale, there are X-ray binary systems (XRBs) which host a stellar mass black hole or a neutron star as the accretor (Done et al., 2007). These stellar remnants provide insight into stellar evolution as they vary on much shorter timescales, making it easier to probe the high energy processes that regulate their behaviour. Larger, but less dense are accreting white dwarfs (AWDs), which in binary systems accrete predominantly via Roche lobe overflow (Warner, 2003, 1995). Depending on their donor type and evolution they are divided into cataclysmic variables (CVs) (Warner, 2003) or AM CVns (Warner, 1995) (see Section 1.3 for more detail). Other types of AWDs are also symbiotic stars (Munari, 2019), which have extremely long orbital periods ($\sim$ years), where accretion occurs mostly through stellar wind. Most stars end their life as white dwarfs, making them closest and most numerous population of all the accreting systems (Althaus et al., 2010). Their relatively fast variability ($\sim$minutes to $\sim$years) coupled with most emission being in the optical part of the spectrum makes them the ideal laboratories for studying accretion as a process. AWDs are also crucial for understanding the origins of Supernovae, high energy transient phenomena, which are fundamental to the evolution of the Universe at large scales. Studying the dynamics of AWDs can also improve our understanding of the origins of gravitational waves as these systems form some of the most local sources of gravitational waves in our galaxy (Kupfer et al., 2018; Burdge et al., 2020; Scaringi et al., 2023; Kupfer et al., 2024).

As mentioned previously, accretion is the process by which luminosity is released from the potential energy of the accreted matter (Frank et al., 2002a). The energy released by the accretion of mass δm onto a compact object with mass M_* and radius R_* can be approximately estimated as:

$$\Delta E_{acc} = \frac{GM_*\delta m}{R_*} \tag{1.1.1}$$

where G is the gravitational constant. Given the released energy ΔE_{acc} the corresponding luminosity over time δt would be:

$$L = \frac{GM_*}{R_*}\frac{\delta m}{\delta t} \tag{1.1.2}$$

by defining the rate at which the matter is accreted, the accretion rate, as:

$$\dot{M} = \frac{\delta m}{\delta t} \tag{1.1.3}$$

the accretion luminosity from Equation 1.1.2 becomes:

$$L = \frac{GM_*\dot{M}}{R_*} \tag{1.1.4}$$

Equation 1.1.4 only holds up under the assumption that all the mass δm is accreted efficiently. To account for varying accretion efficiency in the process a dimensionless prescription η is adopted, so that $0 < \eta \leq 1$ (Frank et al., 2002a). Therefore the resulting accretion luminosity is scaled by this factor $L_{acc} = \eta L$. For accreting BHs the efficiency is thought to be between $0.06 < \eta < 0.3$, increasing with BH spin (Laor & Netzer, 1989; Bian & Zhao, 2003). However, the lack of consensus on measuring spin of BHs for individual systems means it is impossible to constrain accretion for any particular systems in a meaningful way. As opposed to BHs, accreting neutron stars (NSs) are thought to have $\eta \sim 0.15$ (Chashkina et al., 2017).

The above defined accretion rate $\dot{M}$ represents some matter δm accreted steadily onto the accretor over time δt. Assuming that accretion is spherically symmetric, steady and the matter being accreted is fully ionised Hydrogen exerting radiation pressure from Thomson scattering with a characteristic cross section σ_T, there should be a theoretical limit as to how big $\dot{M}$ can get. Working within the framework of these assumptions this limit can be obtained by considering the forces affecting the electron and proton pairs in the ionised gas. The gravitational force exerted on these particles by the accretor is:

$$F_g = \frac{GM_*m_p}{r^2} \tag{1.1.5}$$

where m_p is the mass of a proton and r is the radial distance of the electron proton pair away from the centre of the accretor. The other force at play is the outward push of the radiation pressure, which can be expressed as:

$$F_r = -\frac{L\sigma_T}{4\pi c r^2} \tag{1.1.6}$$

where L corresponds to the luminosity from Equation 1.1.4 and c represents the speed of light in a vacuum. Considering the two forces in Equations 1.1.5 and 1.1.6 the maximum accretion rate can be obtained for when $F_g = F_r$. This limit is referred to as the Eddington limit, and the corresponding limiting luminosity can be expressed through the equated forces as:

$$L_{Edd} = \frac{4\pi G M_* m_p c}{\sigma_T} \tag{1.1.7}$$

Therefore, given the assumptions, for $L > L_{Edd}$ radiation pressure exceeds the gravitational pull of the accretor and accretion halts. However, due to the assumptions leading to this limit, L_{Edd} is only an order of magnitude estimate of the accretion limit. Indeed there are many astrophysical sources that are known to have exceeded this limit (see Kaaret et al., 2017; Fabrika et al., 2021; King et al., 2023; Pinto & Walton, 2023, for recent reviews). Some such Supernovae exceed the Eddington limit due to their asymmetry, violating the spherically symmetric requirement. Others, such as the pulsating ultraluminous X-ray sources (PULXs) are also in violation of these assumptions and are discussed in greater detail in Chapter 5.

1.1.1 Accretion Disc and its Timescales

In Section 1.1, the accretion of matter onto a compact object has been assumed to be spherically symmetrical. This type of accretion is usually referred to as Bondi accretion (Bondi, 1952). However, for the purpose of this thesis it is necessary to examine accretion that doesn't adhere to this assumption. In the example of binary systems, the matter can accrete through the Lagrangian L1 point (details of such accretion are discussed in greater detail in Section 1.2) with some angular momentum. Assuming therefore that there is a flow of gas through the L1 point with a given angular momentum it will assume the least energetically taxing orbit around the accretor, which is circular. By assuming that the gas will continue to flow steadily, the outward transport of the angular momentum of the matter will eventually cause a disc to form around the accreting central compact object (Frank et al., 2002a).

The most commonly used accretion disc (AD) model is the Shakura-Sunyaev model (Shakura & Sunyaev, 1973), which has formed the basis of accretion theory for the past 50 years. It relies on the assumption that the accretion disc can be assumed to be geometrically thin

and optically thick. Furthermore, it is necessary to assume for this model that it can be approximated as a 2D flow. Overall, it is often referred to as the thin disc approximation.

In order to understand how an accretion disc is formed and how to estimate its observational signatures it is important to understand how matter and energy is propagated through it. Within the disc itself there are 3 different characteristic timescales which govern the transport of matter and energy within the disc. The details of the plasma physics related to these timescales from which they can be derived is discussed in great detail in Chapter 3 of Frank et al. (2002a). The shortest of these timescales is the dynamical timescale associated with the movement of matter around the disc in a Keplerian orbit:

$$\tau_{dyn} = \nu_{dyn}^{-1} = \Omega_K^{-1} = \sqrt{\frac{R^3}{GM_*}} \tag{1.1.8}$$

where R is the radial distance in the disc away from the accretor centre, ν_{dyn} represents the dynamical frequency and Ω_K the Keplerian angular frequency. As the AD is a turbulent flow, which can be subject to instabilities and irradiation, the timescale on which it re-adjusts to its thermal equilibrium is referred to as thermal timescale:

$$\tau_{th} = \nu_{th}^{-1} = \alpha^{-1}\tau_{dyn} = \alpha^{-1}\sqrt{\frac{R^3}{GM_*}} \tag{1.1.9}$$

where ν_{th} is the thermal timescale and α is a dimensionless viscosity prescription of the gas, such that $0 < \alpha < 1$, as defined in (Shakura & Sunyaev, 1973) and is often simplistically assumed to be constant through the AD. This prescription governs the behaviour of matter in the AD and is subject of study, with many attempts to constrain it through models and observations. Magneto-hydrodynamic (MHD) simulations have shown to be the most reliable way of inferring α, as its value strongly depends on the input magnetic field strength. The current estimates place it between $\sim 0.05 - 0.1$ for geometrically thin discs (Yuan & Narayan, 2014; Hawley & Balbus, 2002; Penna et al., 2013). However some observational constraints suggest that for extremely low mass transfer rates through the disc it can be as low as $\alpha \sim 0.006$ or even $\alpha \sim 0.003$ (Howell et al., 1995).

The longest timescale relates to the rate at which matter diffuses inwards through the AD:

$$\tau_{visc} = \nu_{visc}^{-1} = \left(\alpha\left(\frac{H}{R}\right)^2\right)^{-1}\tau_{dyn} = \left(\alpha\left(\frac{H}{R}\right)^2\right)^{-1}\sqrt{\frac{R^3}{GM_*}} \tag{1.1.10}$$

where H is the height of the disc at radius R in the vertical z direction. The viscosity

prescription α, combined with the scale height of the disc H/R, is an important parameter as it decouples the viscous timescale from the dynamical one.

Here I adopt the definition of dynamical timescale from Equation 1.1.8 (as used in e.g. Lyubarskii, 1997; Ingram & Done, 2011a) but note that the definition of τ_{dyn} can differ by a factor of 2π if considering the Keplerian orbital frequency (as adopted in Arévalo & Uttley, 2006a; Scaringi, 2014). The dynamical timescale can also be defined through the orbital period in Kepler's law (Arévalo & Uttley, 2006a; Scaringi, 2014), leading to a factor of 2π deviation from Equation 1.1.8.

To characterise the AD, a spectral energy distribution (SED) is needed. Therefore, considering these timescales, the AD can be built up by N number of "rings" of material so that each ring will have a characteristic temperature, dissipation and luminosity distribution. A simplified picture of this is shown in Figure 1.1. Hence, gas orbiting at ν_{dyn} timescales at radius R from the accretor centre would experience viscous dissipation per unit area from Frank et al. (2002a):

$$D\left(R\right)=\frac{3GM_{*}\dot{M}}{8\pi R^{3}}\left[1-\left(\frac{R_{*}}{R}\right)^{-1/2}\right] \tag{1.1.11}$$

Therefore, the entire luminosity of the disc can be obtained by integrating over all of these rings with area $2\pi RdR$, where dR is their width:

$$L_{disc}=2\int_{R_{*}}^{\infty}D\left(R\right)2\pi RdR=\frac{3GM_{*}\dot{M}}{2}\int_{R_{*}}^{\infty}\left[1-\left(\frac{R_{*}}{R}\right)^{2}\right]\frac{dR}{R}=\frac{GM_{*}\dot{M}}{2R_{*}} \tag{1.1.12}$$

Coincidentally, this estimate of disc luminosity also corresponds to half of the accretion luminosity estimated by Equation 1.1.4. The other half of the accretion luminosity is hence expected to be radiated closer to the accretor, i.e. in the form of boundary layer/inner flow that cannot be easily described by the standard Shakura-Sunyaev AD model.

Assuming that the AD is now optically thick in the z-direction (vertically in the disc plane), the emission of each of the disc rings can be modelled as a black body (BB). Using the Stefan-Boltzmann law for peak temperature of a BB $\sigma_{SB}T=D(R)$ the temperature of each disc ring can be estimated as:

$$T\left(R\right)=\left[\frac{3GM_{*}\dot{M}}{8\pi R^{3}\sigma_{SB}}\left(1-\left(\frac{R_{*}}{R}\right)^{1/2}\right)\right]^{1/4} \tag{1.1.13}$$

Equation 1.1.13 then describes a radial temperature distribution in the AD, where faster timescales closer to the accretor correspond to hotter temperatures of the gas and longer

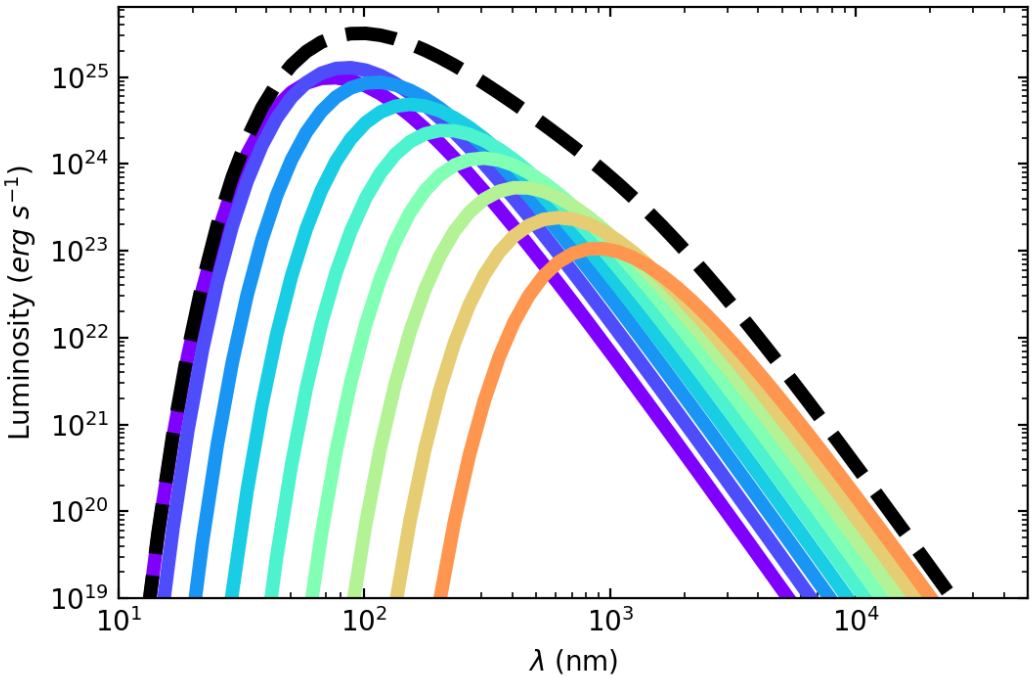

Figure 1.1: Schematic depiction of an AD model based on Shakura & Sunyaev (1973). The AD is divided into 10 rings each being represented by a black body spectrum. The black body spectra are colour coded based on their temperature (bluer colours representing hotter and redder colder temperatures). The Overall SED is shown by the dashed line.

timescales further out in the AD represent colder material. This translates into the peak wavelength at which each ring emits, with inner disc regions emitting primarily in shorter (more energetic) wavelengths and outer regions in longer (less energetic) ones. BB of each ring in Figure 1.1 can then be represented by Planck's distribution:

$$B_\lambda \left[T\left(R\right)\right] = \frac{2hc^2}{\lambda^5} \frac{1}{e^{\frac{hc}{\lambda k_B T(R)}} - 1} \tag{1.1.14}$$

where h is Planck's constant, λ represents wavelength and $T(R)$ the temperature of a given disc ring at radius R. Therefore, the overall flux of the SED of the AD can be obtained by integrating over all disc rings and their corresponding areas:

$$F_\lambda = \frac{2\pi cos(i)}{D^2} \int_{R_*}^{R_{out}} B_\lambda \left[T(R)\right] Rd = \frac{4\pi hc^2 cos(i)}{D^2 \lambda^5} \int_{R_*}^{R_{out}} \frac{RdR}{e^{\frac{hc}{\lambda k_B T(R)}} - 1} \tag{1.1.15}$$

where i represents the inclination of the system and D its distance from the observer. It is of note that the resulting expression for the SED in Equation 1.1.15 is independent of the viscosity prescription α due to the BB and steady disc assumptions. There are other nuances that may not be obvious within the assumptions and approximations of the Shakura & Sunyaev (1973) disc model. One such assumption is that of steady accretion. Accretion is not a monotonous process and as a result there are several different distinction between different "accretion rates". The instantaneous *accretion* rate of a system represents the mass being transferred onto the accretor whereas the mass *transfer* rate described the long-term transport of mass through the AD.

In many instances it has been shown that this simplistic picture of the AD described in this Section often fails (Gierliński & Done, 2004; Scaringi, 2014; Nixon & Pringle, 2019; Krawczynski et al., 2022). This is particularly true close to the accretor, where we observe significant X-ray emission that cannot be accounted for by the simple AD model shown in Figure 1.1. In many types of accreting sources an inner disc is thought to be optically thin and geometrically thick. It is often referred to as a corona, or boundary layer in some cases for accretors with a surface (Done et al., 2007).

1.2 Anatomy of Binary Systems

Most stars in the Universe are in a binary or multi-stellar system (Duchêne & Kraus, 2013). The resulting high stellar multiplicity highlights the importance of understanding the scenario

of mass transfer between the stars in a system. Overall, there are two main ways matter can be transferred between 2 stars:

1. Roche lobe overflow (see Section 1.2.1) - This scenario occurs when either one of the stars increases in its radius and files its Roche lobe or the orbit of the system itself shrinks through angular momentum loss until the Roche lobe is completely filled by one of the stars

2. Stellar wind - one of the stars in the systems ejects substantial part of its mass through stellar wind part of which is then accreted by the other star

For the purpose of this thesis, Roche lobe overflow is the main mass transfer mechanism of interest. Therefore, the following Sections 1.2.1 and 1.2.2 delve into the details of mass transfer via Roche lobe overflow and the resulting geometry (see Chapter 5 of Frank et al. (2002a) for detailed review).

1.2.1 Roche Lobe Overflow

For 2 massive bodies in a binary orbit which can be assumed to be spherical and Keplerian in a given plane (see Figure 1.2). In Figure 1.2 the 2 stars are represented by two black dots, corresponding to the two stars with masses M_1 and M_2, and radii R_1 and R_2 respectively. The binary separation between between the centres of the two stars (dots) is a, which is related to the orbital period of the system through Kepler's third law:

$$a = \left(\frac{GMP^2}{4\pi}\right)^{1/3} \tag{1.2.1}$$

where $M = M_1 + M_2 = mM_\odot$ is the combined mass of the binary and P is the binary orbit. An important quantity defining the shape of the gravitational potential of the system is hence the binary mass ratio:

$$q = \frac{M_2}{M_1} \tag{1.2.2}$$

The overall shape of the Roche potential in the binary system is hence the combination of the gravitational potentials of the two massive bodies and the Coriolis centripetal force experienced by a test mass in the system:

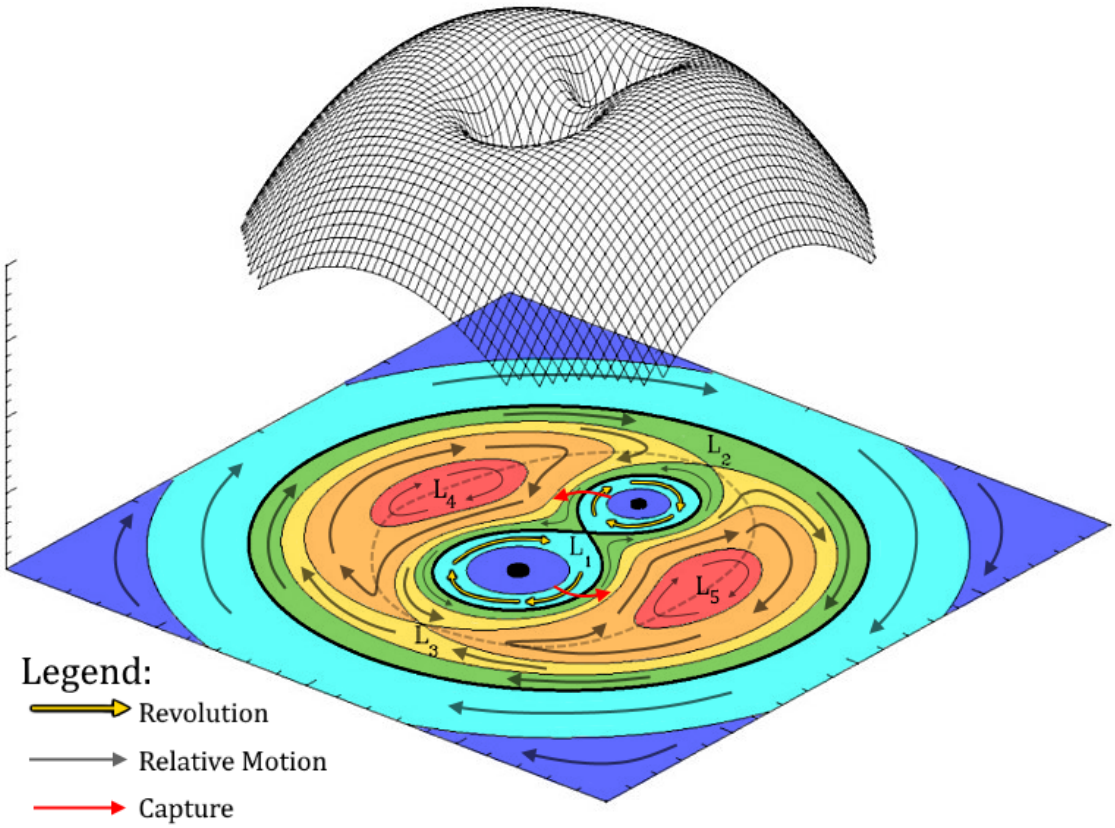

Figure 1.2: *Top:* 3D schematic depiction of the Roche potential depicting the potential wells of the 2 massive bodies in the binary system. *Bottom:* 2D representation of the above Roche potential with lines of equipotential marked. The 5 Lagrangian points are denoted as L_{1-5} with the shape of the Roche lobe highlighted by the bold 8-like shape at the intersection of the 2 potential wells at the L_1. Schematic Credit:`https://en.wikipedia.org/wiki/File:RochePotential_color.PNG`

$$\Phi_R(\underline{\mathbf{r}}) = -\frac{GM_1}{|\underline{\mathbf{r}} - \underline{r_1}|} - \frac{GM_2}{|\underline{\mathbf{r}} - \underline{r_2}|} - \frac{1}{2}\left(\underline{\omega} \wedge \underline{\mathbf{r}}\right)^2 \tag{1.2.3}$$

where $\underline{\mathbf{r}}$ represents the vector position of the test magnetic b $\underline{r_1}$ and $\underline{r_2}$ the vector positions of the two stars and $\underline{\omega}$ is the vector angular momentum of the binary system such that:

$$\underline{\omega} = \sqrt{\frac{GM}{a^3}}\underline{\mathbf{e}} \tag{1.2.4}$$

where $\underline{\mathbf{e}}$ is the unit vector normal to the orbital plane. Figure 1.2 displays the shape of the equipotential surfaces, with the 3D shape of the potential displayed above it. From the shape of the potential it is clear that q and a play vital roles in the shape the Roche potential takes and in the positions of its maxima. The potential maxima and minima, or the Lagrangian points (1 to 5) are also shown in Figure 1.2 and are denoted by L_{1-5}. Furthermore the gravitational potential and the resulting gravitational wells of each star are shown in Figure 1.2 in the 3D diagram and are represented by the concentric circles of equipotential lines below in the 2D panel. The equipotential line representing the intersection of the 2 wells (inner 8-like shape in Figure 1.2) is known as the Roche lobe of the system. The point of intersection occurs at the Lagrangian L_1 point, representing a saddle point in the Roche potential from Equation 1.2.3. Therefore, all matter in the proximity of the L_1 point is prone to passing through it from one potential well into another.

Within this geometry there are several scenarios based on the size relationship between individual objects and their respective Roche lobes. In the case where neither star is filling its Roche lobe, there is no mass transfer through the L_1 point. In such a case the system is a *detached* binary and mass transfer is only possible through stellar wind.

On the other hand, if one of the stars in the system is filling its Roche lobe then mass transfer can occur. In such a case the star filling its Roche lobe is known as the donor, or a secondary star and is transferring material onto the other star, referred to as the primary or the accretor. In such a scenario $q << 1$ and the donor filling its Roche lobe is deformed, assuming a peardrop-like shape affected by the primary's gravity. At that moment, any perturbation of the secondary star's material near the L_1 point will easily cause the matter to be "pushed" over into the potential well of the accretor. In this *semi-detached* state, mass transfers from the donor to the primary as long as the donor surface remains in contact with the Roche lobe. *Contact* binaries are the special case where both of the stars fill their respective Roche lobes and mass transfer becomes non-trivial (Fabry et al., 2023). However, such scenario is not of interest to this thesis.

1.2.2 Geometry of Binaries

The mass ratio q and the binary separation a (and hence binary orbit P by extension) that govern the geometry of a binary system and hence the behaviour of matter through the system. However, it is also useful to consider the sizes of the stars' respective Roche lobes. Given the shape of the Roche potential in Equation 1.2.3, this is best done analytically (Eggleton, 1983; Paczynski & Abramowicz, 1982), giving the size of the donor's Roche lobe as:

$$\frac{R_2}{a} = \frac{0.49q^{2/3}}{0.69q^{2/3} + ln(1+q^{1/3})} \tag{1.2.5}$$

which for a more restricted range $0.1 \lesssim q \lesssim 0.8$ can be simplified to $\frac{R_2}{a} = 0.462\left(\frac{M_2}{M_1+M2}\right)^{1/3}$. Substituting q^{-1} for q into Equation 1.2.5 gives the size of the accretor's Roche lobe as:

$$\frac{R_1}{a} = \frac{0.49q^{-2/3}}{0.69q^{-2/3} + ln(1+q^{-1/3})} \tag{1.2.6}$$

As mass transfers into R_1, an AD forms as has been discussed in Section 3.5.1. R_1 hence represents an absolute limit on the theoretical size of the AD. However, usually when material free falls from the L_1 point with some angular momentum it will enter into a circular orbit around the accretor at a specific radius, referred to as the circularisation radius. It's semi-analytical form can be expressed from (King & Wynn, 1999) as:

$$\frac{R_{circ}}{a} = (1+q)\left(0.500 - 0.227log\left(q\right)\right)^4 \tag{1.2.7}$$

This follows from a semi-analytical expression linking a distance b_1 from the primary's centre to the L_1 point (Plavec & Kratochvil, 1964):

$$\frac{b_1}{a} = 0.500 - 0.227log\left(q\right) \tag{1.2.8}$$

It is possible to transfer enough material to the Roche lobe of the accretor that the formed AD outgrows the circularisation radius. At such a point, another radius of note is the tidal radius, a radius where the disc starts to be distorted by the tidal interactions with the secondary. An analytical expression for this radius is given in (Warner, 2003):

$$\frac{R_{tidal}}{a} = \frac{0.6}{1+q} \tag{1.2.9}$$

This expression holds for mass ratios such that $0.03 < q < 1$.

As long as accretion is maintained, the binary parameters such as q and P (and consequently a) are altered. This is due to the angular momentum loss of the system from magnetic braking and gravitational wave radiation, which then becomes fundamental to the overall binary evolution (see Section 1.3 for more detail). Therefore to sustain accretion, other properties of the secondary, such as the radius of the secondary, must be altered. The details of binary evolution and its consequences are discussed in detail in Section 1.3.1 specifically in the context of AWDs which are the main focus of this thesis.

1.3 Accreting White Dwarfs

Accreting white dwarfs (AWDs) are binary systems in which a white dwarf (WD) accretes material from a donor star. The dominant population of AWDs is referred to as cataclysmic variables where mass transfer occurs through Roche lobe overflow from the hydrogen envelope of a low mass star (Warner, 2003; Knigge et al., 2011). In cases where the donor is a degenerate or semi-degenerate star they are referred to as AM CVn systems (Solheim, 2010).

1.3.1 Cataclysmic Variables

The general geometry of these systems is depicted in Figure 1.3. CVs in general have a long history of observations, with novae and Supernovae detections dating back thousands of years (Warner, 2003). The more common use of wide-field photography in the late 19^{th} century made the discovery of new systems easier. The term "dwarf nova", representing one of the main classes of CVs, was first coined in 1938 (Payne-Gaposchkin & Gaposchkin, 1938), however, the first recorded dwarf novae (DN) observed in 1850s (see Warner (1986) for summary of early observations of archetypal DN U Gem). The nature of the central accretor was then confirmed as a white dwarf in 1965 (Luyten & Hughes, 1965a,b). For an in-depth review of CVs and their history see Warner (2003).

In the "standard" model of CV evolution they evolve from detached binary systems with long orbital periods by losing angular momentum through gravitational waves (Paczyński, 1967; Webbink, 1976), but mostly through magnetic braking (Rappaport et al., 1982, 1983; Spruit & Ritter, 1983). When they reach about $P_{orb} \sim 6$ hours the donor star fills its Roche lobe and mass transfer through the L1 point begins. From this point on, the evolution to lower orbital periods is driven predominantly not by angular momentum loss through gravitational waves,

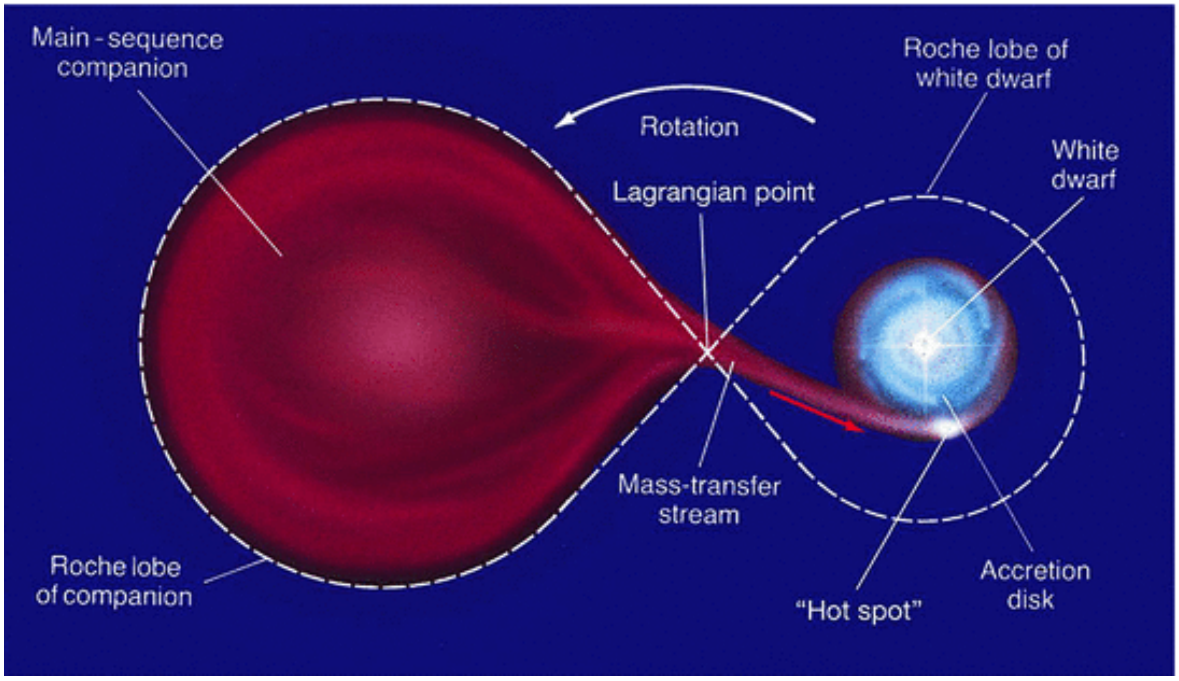

Figure 1.3: Schematic depiction of a CV system showing the WD accreting through the Lagrangian L1 point from a low mass donor star. An accretion disc with a bright spot, where the matter falls onto the accretion disc from the L1 point are shown as well. Schematic Credit: López Coto (2017)

but through magnetic braking. Magnetic braking is generally thought to be associated with the magnetic stellar wind originating from the donor star in the CV case. Therefore in CVs, a highly ionised and weak stellar wind co-rotating at the Alfvén radius exerts spin-down torque on the donor star. Due to the synchronisation of the Roche lobe overflow with the binary orbit, the wind extracts the momentum from the binary system itself, evolving it towards lower orbital periods at much faster rate than gravitational wave angular momentum loss. As such, the donor star is kept out of thermal equilibrium whilst mass transfer is occurring. There are many models for magnetic braking in CVs, with the main candidates (Verbunt & Zwaan, 1981; Rappaport et al., 1983; Kawaler, 1988; Mestel & Spruit, 1987; Andronov et al., 2003; Ivanova & Taam, 2003) discussed in detail in Knigge et al. (2011).

When the system orbital period reaches $\sim$ 3 hours it is generally agreed that the donor star becomes fully convective, causing an abrupt end to the magnetic braking in the system (MacGregor & Charbonneau, 1997; Charbonneau & MacGregor, 1997). In the absence of this mechanism that shrinks the orbit and hence the size of the Roche lobe, the donor keeps shrinking in order to reach its thermal equilibrium. As the donor is shrinking it detaches from the Roche lobe, which is shrinking at a much slower rate, only due to angular momentum loss from gravitational waves. This causes the overall mass transfer through the L1 point to stop

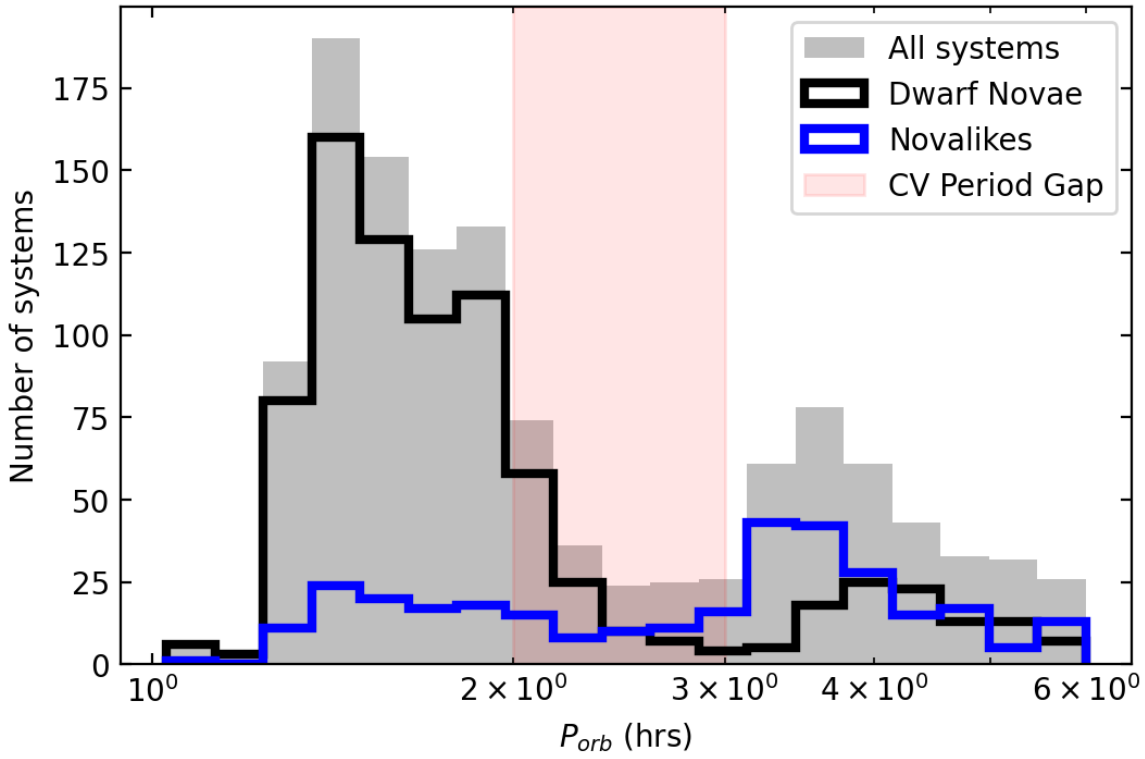

Figure 1.4: Orbital period distribution of CVs as using Ritter & Kolb (2003) catalogue v.7.21. Systems below the period gap are predominantly populated by dwarf novae (black lined distribution) as opposed to above the period gap populated by novalike systems (blue lined distribution). The period gap between 2 to 3 hrs is highlighted by a pink shaded region, populated by mostly magnetic systems.

as well, making the CV undistinguishable from other detached binary systems containing a near MS star and a WD. The slow evolution through this stage lasts until the orbital period reaches $\sim$ 2 hours. At this stage the Roche lobe has shrunk down so that the secondary star fills it again and mass transfer is restarted.

As such the orbital period range between $\sim$3 and $\sim$2 hours, where the system doesn't experience a phase of active mass transfer, is referred to as the period gap. This arises from the lack of observational evidence in this evolutionary stage that points to the potential past of a CV. These systems therefore go uncategorised as CVs and hence the overall period distribution of CVs shows a dearth of systems in this period range. A distribution of the orbital periods across the non-magnetic CV population is shown in Figure 1.4 . It is clear that the systems above the period gap are dominated by high accretion rate novalike systems whereas the orbital period is below the period gap are mostly populated by outbursting dwarf novae. This distinction is thought to be related to a progression of systems through different evolutionary stages, with younger, high mass transfer systems above the period gap evolving

into the outbursting, low mass transfer rate in quiescence systems below it. It is not yet well understood why the systems change their behaviour in this fashion after emerging from the period gap.

Based on the majority of population synthesis studies of CVs (Kolb, 1993; Kolb & Baraffe, 1999a; Barker & Kolb, 2003), there is an expected pileup of systems at a theoretically predicted minimum value of orbital periods that CVs should reach. This minimum is predicted at ∼65 minutes, and is expected to be a sharp cut off of the period distribution at low periods with majority of the galactic systems present near it. This is however at odds with observations due to the nature and shape of the orbital period distribution, which has systems <65 minutes. Furthermore, the observed period minimum has been determined to be 82.4 ± 0.7 minutes from the Sloan Digital Sky Survey (SDSS) CV sample (Gänsicke et al., 2009). There have been several suggestions that could explain this discrepancy, such as the potential effect of excess of spots on the donor star (Littlefair et al., 2008) and the possibility of continuing angular momentum loss above the rate from gravitational waves during the period minimum Patterson (1998). A revised version of the standard model produced by Knigge et al. (2011) based on the evolution of the donor radius reproduces the observed period minimum as well as the upper boundary for the period gap. Furthermore, these models predict that about 40% of all CVs should have evolved beyond this period minimum. After reaching the period minimum, the donor star stops shrinking since the mass loss occurs at much slower rates than the star's thermal timescale. As a consequence the orbital period of the system starts to increase again and the system "evolves back" towards longer orbital periods. As such, the models predict that there should be an abundance of these "period bouncers" forming up to 38-75% of the galactic CV population (Kolb, 1993; Goliasch & Nelson, 2015; Belloni et al., 2018). However, up to date only a handful of the systems have been found. A favoured explanation for this is the neglect of intrinsic WD magnetic field and its effect to the evolution of the system and angular momentum loss which could reduce the expected number of period bouncers down to 8-30%(Schreiber et al., 2023). However, this issue should be resolved by upcoming space-based gravitational waves detectors, such as *LISA* , which should be able to detect any "missing" period bouncers (Scaringi et al., 2023).

Classification of CVs

CVs have a long history of phenomenology with different classes of systems based on their displayed observational properties (Warner, 2003). Many of these categories are rooted in

purely observational phenomenology, and may not reflect underlying differences in physics driving the systems' behaviour. In this Section I will discuss the different CV categories and classes. A fundamental division of CVs lies in the intrinsic strength of their magnetic field. Whereas all accretors in CVs posses a magnetic field, CVs are generally divided into magnetic and non-magnetic based on whether the strength of the magnetic field is large enough to disrupt the accretion disc or to synchronise the binary orbit with the WD spin to some extent.

1. **Non-magnetic CVs**

   Non magnetic CVs, with the WD field $\lesssim 10^6$ G, are more common, representing $\sim 64\%$ of the volume limited sample of CVs (Pala et al., 2020). The main 2 dividing categories of non-magnetic CVs are dwarf novae and novalikes. As mentioned previously in Section 1.3.1 these are very likely related to different evolutionary stages of individual systems.

   (a) **Dwarf Novae**

   Dwarf novae (DN) are a type of non-magnetic CVs showing semi-periodic bursts during which the magnitude of a system increases by $\sim 4-5$ magnitudes. These bursts can last several days up to weeks and recur on weeks to years timescales. They have been named after the first discovered dwarf nova U Gem and the resemblance of its bursts to the much more energetic novae known previously (Warner, 1986). Generally speaking a dwarf novae outburst is understood to be caused by a temporary increase in mass transfer rate through the AD (Smak, 1971; Osaki, 1974). As a consequence the accretion disc grows in size and the extra material is deposited on the white dwarf. The disc starts to deplete and cool down, slowly returning to quiescence. The main theoretical explanation for these bursts is the Disc Instability Model (DIM), which has been extensively applied to explain outbursts in many accreting systems, from CVs to XRBs (Osaki, 1996; Lasota, 2001; Dubus et al., 2018; Dubus & Babusiaux, 2024). In the DIM the increase in accretion rate is driven by changes in local viscosity in the disc. In quiescence the low viscosity implies long timescales for matter propagating through the disc and leads to accumulation of material. In outburst the viscosity increases to ~ 0.1 and timescales become faster driving the increase in accretion rate. Since change in viscosity translates to a change in surface density, a DN burst in the DIM framework can be illustrated by an effective temperature-surface diagram as shown in Figure 1.5. Recent detailed studies of DIM applied to explain DN outbursts were

conducted by Dubus et al. (2018); Dubus & Babusiaux (2024) extended the treatment to include the effect of magnetic field on the system *Gaia* colour evolution. Following DIM treatment of DN outbursts the recurrence between DN outbursts becomes an indirect tracer of quiescent value of viscosity α (Howell et al., 1995; Hilton et al., 2007).

Some DN systems also experience so called superoutbursts, which last marginally longer than regular DN outburst. The rise of the superoutburst is similar as in a normal outburst, but accompanied by superhumps (see below) and achieving larger peak luminosity. Majority of systems that undergo superoutbursts are below the period gap with $P_{orb} \lesssim 2$ hrs, and are often referred to as SU UMa systems (Warner, 2003).

A very rare subtype of SU UMa systems are so called WZ Sge systems which only experience a superoutburst every couple of years (every ∼33 years in the case of WZ Sge). These systems show superoutburst of $\sim 8-9$ mag in amplitude that last ∼30 days. They also show positive superhumps as they are evolved systems with $P_{orb} \lesssim 2$ hours. Superhumps are observationally coherent signals appearing close to the orbital period of the system in the power spectrum. If the frequency of the superhump signal (ν_{SH}) is higher than that of the orbit (ν_{orb}), it is referred to as a negative superhump, so that $\nu^{-}_{SH} > \nu_{orb}$ (see next Section on novalikes for more details). If on the other hand the superhump frequency is lower than the orbital period it is known as a positive superhump, so that $\nu^{+}_{SH} > \nu_{orb}$ (Patterson et al., 2005). The signal is associated with the tidal stresses exerted by the secondary on the disc. These cause the disc to become eccentric and undergo apsidal precession in the prograde direction (Lubow, 1991), resulting in a 3:1 resonance. So the growing disc in a DN superoutburst easily reaches the tidal radius triggering the prograde precession of the accretion disc just after the superoutburst reaches its luminosity peak (Smak, 1993; Patterson et al., 2005; Smak, 2009; Kato, 2015; Hameury, 2020). As opposed to SU UMa type systems however, WZ Sge superoutbursts experience several rebrightenings or "echoes" during the decay phase, which cannot be explained by the standard DIM implementation. There are many potential explanation for these "echos", such as a potential propeller state (Campana et al., 2018), inner disc evaporation (Kimura et al., 2020; Castro Segura et al., 2021) or magnetic field effects (Kato, 2015).

Another rare class of DN are Z Cam stars. These systems exhibit regular DN

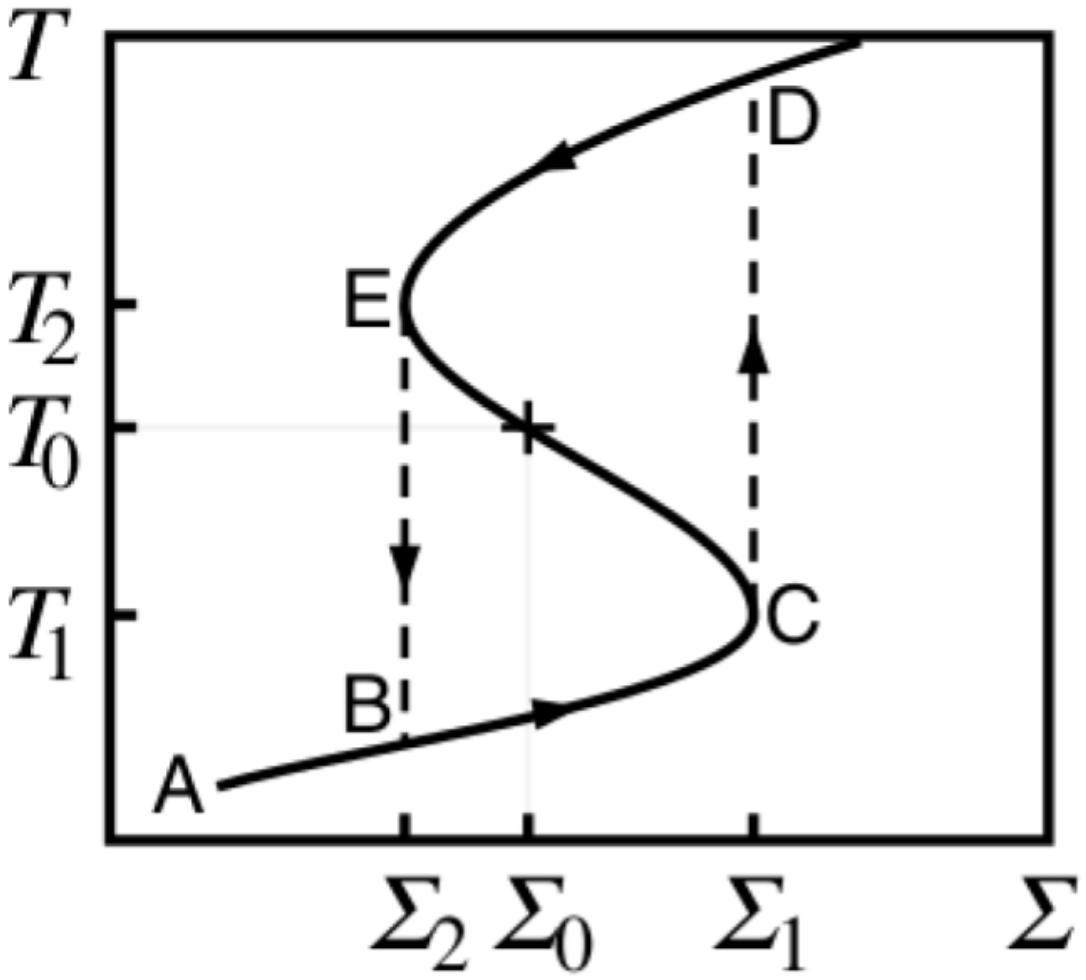

Figure 1.5: Effective temperature-surface density diagram showing the surface density and temperature evolution of a DN outburst Schematic Credit: Frank et al. (2002a)

outbursts and periods of "standstill" where the system luminosity doesn't quite return to the regular quiescent levels. Instead it stays at about third of the outburst luminosity exhibiting a novalike behaviour. The transition between these states is not yet well understood, but it has been suggested that novalikes are Z Cam like systems with extremely prolonged standstills (Szkody & Wade, 1981).

(b) **Novalikes**

Novalikes (NLs) are a type of non-magnetic CV often referred to as the VY Scl type systems. They are characterised by their high accretion rate, as opposed to the quiescent levels of DNs (Warner, 2003). Their orbital periods are usually $P_{orb} \gtrsim 3$ hrs, as can be seen in Figure 1.4, where they are shown as blue-lined distribution. Another characteristic behaviour of NLs is changes of state. These tend to be highly non-periodic, occurring every $\sim$ hundreds of days and they consist of sudden changes in brightness by more than 1 mag (Rosino et al., 1993; Hameury & Lasota, 2002; Hoard et al., 2004; Honeycutt & Kafka, 2004). In the general high state, it is thought that NLs live in the upper branch (between points D and E) of the curve in Figure 1.5.

The high states of these systems are marked by high variability in the optical ($\sim$30% root mean square (rms), as seen in Scaringi et al. (2012a)). They also display characteristic negative superhumps (Bruch, 2023), though these are not exclusive to NLs. As opposed to the positive superhumps, negative ones are thought to be caused by the retrograde nodal precession of a tilted accretion disc (Wood et al., 2009). The orbital excess of negative superhumps ($\epsilon = \frac{P_{nSH} - P_{orb}}{P_{orb}}$) shows an inverse correlation with the orbit of the system (Bruch, 2023) suggesting that the precession of the outer disc is in some sense related to the disc size.

The low states of NLs are much shorter in duration than the high states, lasting a couple of weeks to months as opposed to years. The reason why NLs enter low state is not yet well established (Rosino et al., 1993; Hameury & Lasota, 2002; Honeycutt & Kafka, 2004), but it is thought to be related to the changes in the long-term mass transfer rate through the AD. In comparison, in the high state the average accretion rate is $\gtrsim 10^{-8} M_{\odot} \mathrm{yr}^{-1}$, whereas in the low state it drops down to $\lesssim 10^{-11} M_{\odot} \mathrm{yr}^{-1}$. In the low state quasi-periodic $\sim$30 minute long bursts have been detected in the optical, recurring roughly every $\approx$2 hours. These magnetically gated bursts (see Section 1.3.1), are thought to be the result of a magnetically truncated disc at the magnetospheric radius r_M, due to the sudden

drop of accretion rate. Hence, as material builds up the r_M, blobs of matter get quasi-periodically accreted via the magnetic field lines, similarly as observed in NS. In this state it is possible to probe the magnetic field of these classically "non-magnetic" systems, by measuring the properties of the bursts (Scaringi et al., 2017a).

2. **Magnetic systems**

On the other hand, systems with magnetic field strength above $\sim 10^6$ G are referred to as magnetic (Warner, 2003). Depending on the WD magnetic field strength only an outer accretion disc may form. The inner parts will be inhibited by the Alfvén radius:

$$r_A = \left(\frac{2\pi^2}{\mu_0^2} \frac{\mu^4}{GM\dot{M}^2} \right)^{\frac{1}{7}}, \tag{1.3.1}$$

where μ is the stellar magnetic dipole moment such that $\mu = BR^3$, M is the accretor mass, R is the accretor radius, $\dot{M}$ its accretion rate, G is the gravitational constant and μ_0 is the vacuum permeability. Hence the inner disc will be truncated at the magnetospheric radius:

$$r_M = \eta \, r_A = \eta \left(\frac{2\pi^2}{\mu_0^2} \frac{\mu^4}{GM\dot{M}^2} \right)^{\frac{1}{7}}, \tag{1.3.2}$$

where η is a dimensionless parameter describing the geometry of the accretion flow and the relation between the Alfvén and magnetospheric radius. It is usually set to 0.5 for magnetic systems (Ghosh & Lamb, 1979a; Mönkkönen et al., 2022).

At r_M the matter attaches to magnetic field lines and is accreted onto the magnetic poles of the WD via accretion columns. In these systems, the spin period of the WD is not synchronized with the orbital period; they generally display a periodic modulation on the WD spin frequency associated with emission from the accretion column. Such systems are known as Intermediate Polars (IPs), where the matter is accreted via an arc-shaped curtain (Rosen et al., 1988). For larger magnetic fields the magnetospheric radius can lie outside of the disc co-rotation radius r_{CO}, such that $r_M > r_{CO}$, which inhibits entirely the formation of an accretion disc. In majority of these systems, the WD spin and binary orbit are synchronised and are commonly known as Polars, with the exception of rare discless IPs such as V2400 Oph (Buckley et al., 1995).

Bursts in CVs

CVs and AWDs in general display various types of transient-like brightness increases. Some of these bursts, micronovae in particular, are discussed in detail in Chapters 6 and 7.

1. **Dwarf Novae**

   The most common and well-established bursts in CVs are dwarf nova outbursts, in which a sudden increase in accretion rate, thought to be driven by thermal-viscous disc instabilities (Osaki, 1996; Lasota, 2001; Dubus et al., 2018), causes the temperature, disc size and hence luminosity of the disc to increase. These outbursts usually last several days to months. With longer orbital period systems tend to have longer outbursts due to their larger discs. Once a cooling wave due to a lower ionisation level passes through and stops the outburst, the temperature of the disc will return to its quiescent level (Lasota, 2001). The outbursts occur semi-periodically with some special cases where they increase in luminosity amplitude, leading up to a superoutburst. Whereas dwarf nova outbursts are very common in non-magnetic AWDs, they are extremely rare in magnetic systems (Hameury & Lasota, 2017), due to their smaller, truncated discs inhibiting formation of sufficient instabilities.

2. **Novae**

   Classical Novae (CN) and Recurrent Novae (RN) are luminous bursts in AWDs, where a WD accreted from a non-degenerate companion (Gallagher & Starrfield, 1978) reaching ∼6 to 19 mag increase in luminosity lasting weeks to years. These bursts occur when an accreted layer of material on the WD's surface undergoes unstable nuclear burning and reaches critical mass (Starrfield et al., 1972; Townsley & Bildsten, 2004). This thermonuclear runaway (TNR) effect results in an envelope of the accreted material being ejected at high speeds creating a nova shell moving through the interstellar medium as it cools. This process transports heavy elements from outer layers of the WD into the surrounding environment and can be detected thousands of years after the nova explosion itself. For a more detailed review see Chomiuk et al. (2021). The novae are more common in high mass WD, due to the WD being close to the Chandrasekhar mass, with some heavy ($M_{WD} > 1.2M_{\odot}$) and extremely high accretion rate systems showing recurring novae bursts (Yaron et al., 2005; Shara et al., 2018). Overall after the type I X-ray bursts (see Section 1.4 for more details) novae are the 2^{nd} most frequent TNR eruptions with ∼20 to 70 occurring per year in the Milky Way (Darnley

et al., 2006; Shafter, 2017). Novae are also sometimes thought to be the transition link between dwarf novae and novalikes evolutionary stages of CVs. This is referred to as the hibernation scenario (Prialnik & Shara, 1986; Shara et al., 1986; Kovetz et al., 1988; Hillman et al., 2020), where a DN will undergo a novae explosion once enough material has built up on the WD. After the nova the system will enter a high accretion rate state where no DN outbursts occur - the system "hibernates". Over time the system may cool down and so the accretion rate slows enough for the system to morph into a DN again.

3. **Magnetic Gating**

A different type of burst exhibited by AWDs is the so-called magnetic gated bursts, which appear only in systems with low magnetic field WDs (Scaringi et al., 2017a). In these systems, the material is accumulated at the edge of a truncated inner disc close to the WD surface, confined by the spinning magnetosphere. When the disc pressure exceeds the pressure of the spinning magnetosphere matter can then accrete onto the WD. Several systems have now shown magnetically gated bursts (MV Lyrae: Scaringi et al. 2017a, TW Pic: Scaringi et al. 2022a, V1233 Sgr: Hameury et al. 2022, V1025 Cen: Littlefield et al. 2022).

4. **Micronovae**

A very different kind of burst is displayed by a growing number of systems. They are fast ($\gtrsim$ 1 day), bright, and somewhat isolated bursts which cannot be fully reconciled with magnetic gating. One example is TV Col, which has been shown to display fast outflows during burst maximum (Szkody & Mateo, 1984). These bursts, which appear phenomenologically different from all of the aforementioned types of bursts are usually referred to as micrononvae (Scaringi et al., 2022d). One hypothesis for the origin of these bursts is that they are the result of a localised thermonuclear runaway occurring on the WD magnetic poles(Scaringi et al., 2022c), however their true physical origin is yet to be unambiguously determined. These bursts can last from $\sim$ 10 hours up to a few days. To date, there have been very few targets reported to show these bursts (Scaringi et al., 2022d; Veresvarska et al., 2024a; Iłkiewicz et al., 2024; Irving et al., 2024), however with the advent of new synoptic sky surveys (e.g., *BlackGEM*; Groot et al. 2024 and *LSST*; Ivezić et al. 2019), the number of detections is expected to rise allowing for a better population characterisation of these systems.

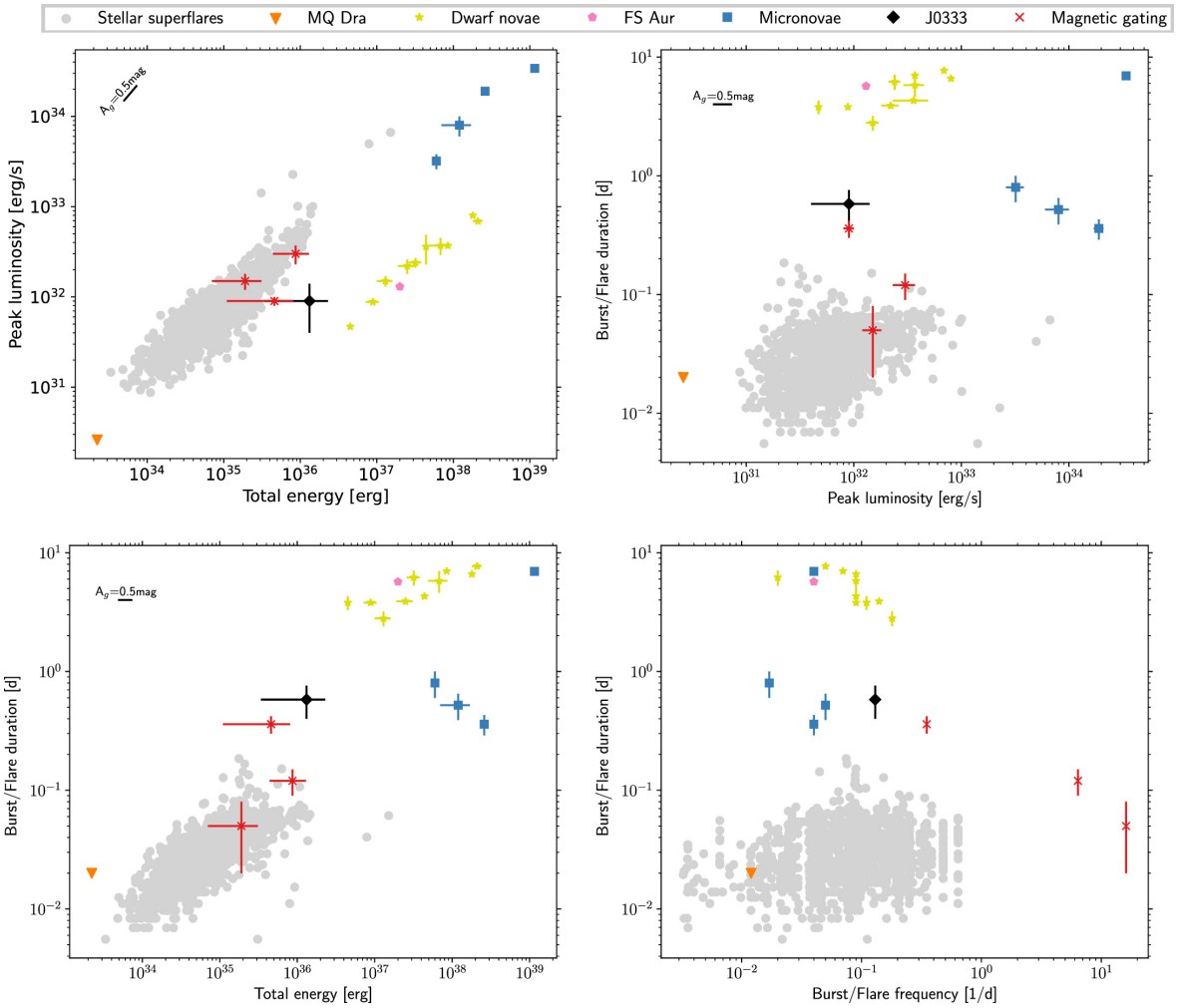

Figure 1.6: Diagnostic diagram from Iłkiewicz et al. (2024) showing parameter space of burst properties, namely their energy, luminosity, duration and recurrence. Figure Credit: Iłkiewicz et al. (2024)

A convenient way to potentially distinguish between the observational characteristics of the various types of bursts observed in AWDs via diagnostic diagrams has been introduced in Iłkiewicz et al. (2024). The diagnostic diagrams show that the burst-related energies, peak luminosities, durations, and recurrence times of dwarf novae, micronovae, and magnetically-gated bursts occupy distinct regions of parameter space, which suggests that these phenomena all arise from distinct physical mechanisms. The diagrams are shown in Figure 1.6, as published in Iłkiewicz et al. (2024).

1.3.2 AM CVns

AM CVn systems are compact interacting binaries in which both stars possess degenerate equations of state, and have orbital periods in the range of $\sim$ 5 min to about $\sim$ 65 min for the known objects. Such short orbital periods places them well below the CV theoretical period

minimum of 65 minutes (Kolb & Baraffe, 1999b; Howell et al., 2001) and observational one of 82.4 ± 0.7 minutes from the Sloan Digital Sky Survey (SDSS) CV sample (Gänsicke et al., 2009). Additionally to their relatively short periods they differ in their formation channel when compared to CVs. Ramsay et al. (2018) discusses three widely accepted evolutionary paths AM CVn systems can take, with Solheim (2010) providing a general overview. In some scenarios, AM CVn systems can also be considered as progenitors of type Ia Supernovae. Broadly speaking however, there are 3 main evolutionary channels that can lead to an AM CVn system. The first 2 channels both rely on the decreasing orbital period driven by angular momentum loss, similarly to CVs. As opposed to CVs however, pre-AM CVn systems undergo 2 separate common envelope (CE) evolutionary stages (Solheim, 2010). In a CE stage one of the stars expands its surface sufficiently to include the secondary star in it as well. This is particularly complex stage and is the subject of many studies (Passy et al., 2012; Ricker & Taam, 2012; Kramer et al., 2020; Sand et al., 2020; Röpke & De Marco, 2023). The first of these evolutionary channels consists of 2 WDs with Roche lobe overflow, with the donor being the the smaller and more He rich one (Paczyński, 1967; Faulkner et al., 1972). The other stage also relies on accretion, but from a low mass non-degenerate He donor (Savonije et al., 1986; Iben & Tutukov, 1987). The last evolutionary channel and unconfirmed until very recently (Burdge et al., 2022) is known as the CV channel. In the CV channel the AM CVn is a CV in which the donor has been stripped off all of its H envelope, triggering He accretion (Tutukov et al., 1985; Podsiadlowski et al., 2003).

AM CVns are quite rare systems, with $\lesssim$100 known up to date. However, they show many striking similarities to CVs. For example, some AM CVns also show bursts, which are thought to be driven by viscosity changes, similarly to DN outbursts and can be explained by the DIM (Tsugawa & Osaki, 1997; Cannizzo & Nelemans, 2015). Furthermore, their accretion rates correlate with the orbital period, such that $\dot{M} \propto P_{orb}^{-5/2}$ (Warner, 1995; Tsugawa & Osaki, 1997). Similarly to CVs, AM CVns can be broadly divided into 2 groups, based on their state and orbital period (Green et al., 2024). The "high" state systems, resembling novalikes, which have orbital periods in the range of $\sim 5 \lesssim P_{orb} \lesssim 25$ minutes. The "quiescent" systems have orbital periods so that $\sim 25 \lesssim P_{orb} \lesssim 60$ minutes and resemble DN in CVs. Similarly to CVs, AM CVn systems are known to show superhumps (Patterson et al., 1993), which is to be expected for extremely compact object. Some AM CVn also show coherent pulsations thought to be potentially associated with the WD stellar pulsations (Kupfer et al., 2015).

AM CVn systems also currently comprise 11 out of 16 *LISA* verification sources (Stroeer & Vecchio, 2006; **?**; Marsh, 2011; Kupfer et al., 2018) for gravitational wave detection. Given

their relatively small size, these systems are also well suited for MHD simulations of the entire accretion disc (Kotko & Lasota, 2012; Coleman et al., 2018).

1.4 X-ray Binary Systems

Binary systems where a stellar mass BH or a NS accrete from a non-degenerate companion star emit most of their energy in X-rays and are called X-ray binaries (Tauris & van den Heuvel, 2006). These systems are thought to originate from a binary system where one of the stars collapses and forms a BH or a NS. For this to occur a moderately massive progenitor is required (Fryer & Kalogera, 2001). Generally speaking, these systems can be divided into 2 groups based on their accretion mode into high mass XRBs (HMXBs) and low mass XRBs (LMXBs) (Podsiadlowski et al., 2003; Tauris & van den Heuvel, 2006):

1. HMXBs are mostly young systems where the BH/NS orbits the donor star and accretes predominantly through stellar wind
2. LMXBs are systems where the donor orbits the compact object and accretion occurs via Roche lobe overflow

Considering that LMXBs (see Bahramian & Degenaar (2023) for a review) share the most similarities with AWDs, they are of more interest for this thesis. Similarly to AWDs, XRBs have a similar structure as binary systems, with an accretion disc forming as a consequence of mass transfer (Done et al., 2007). Similarly to AWDs, XRBs also display a variety of bursting behaviour (Lewin et al., 1993; Strohmayer & Bildsten, 2003). However, in XRBs these bursts are usually classified into two shorter transient types, type I and type II and longer bursts, akin to DN in AWDs. Type II bursts are usually accretion flares in a magnetically truncated discs, similarly to magnetic gating bursts in AWDs (Kouveliotou et al., 1996). All of these types of bursts are briefly reviewed in the following Sections, with long mass transfer driven outbursts discussed in Section 1.4.1 and type I and II in Sections 1.4.2 and 1.4.3 respectively.

1.4.1 XRB Outbursts

The general geometry of an XRB is influenced by these long outbursts and changes of states which occur in cycles on timescales of ∼years and bear strong similarities to the DN bursts. One such cycle is shown in Figure 1.7 as adopted from the review Fender & Gallo (2014).

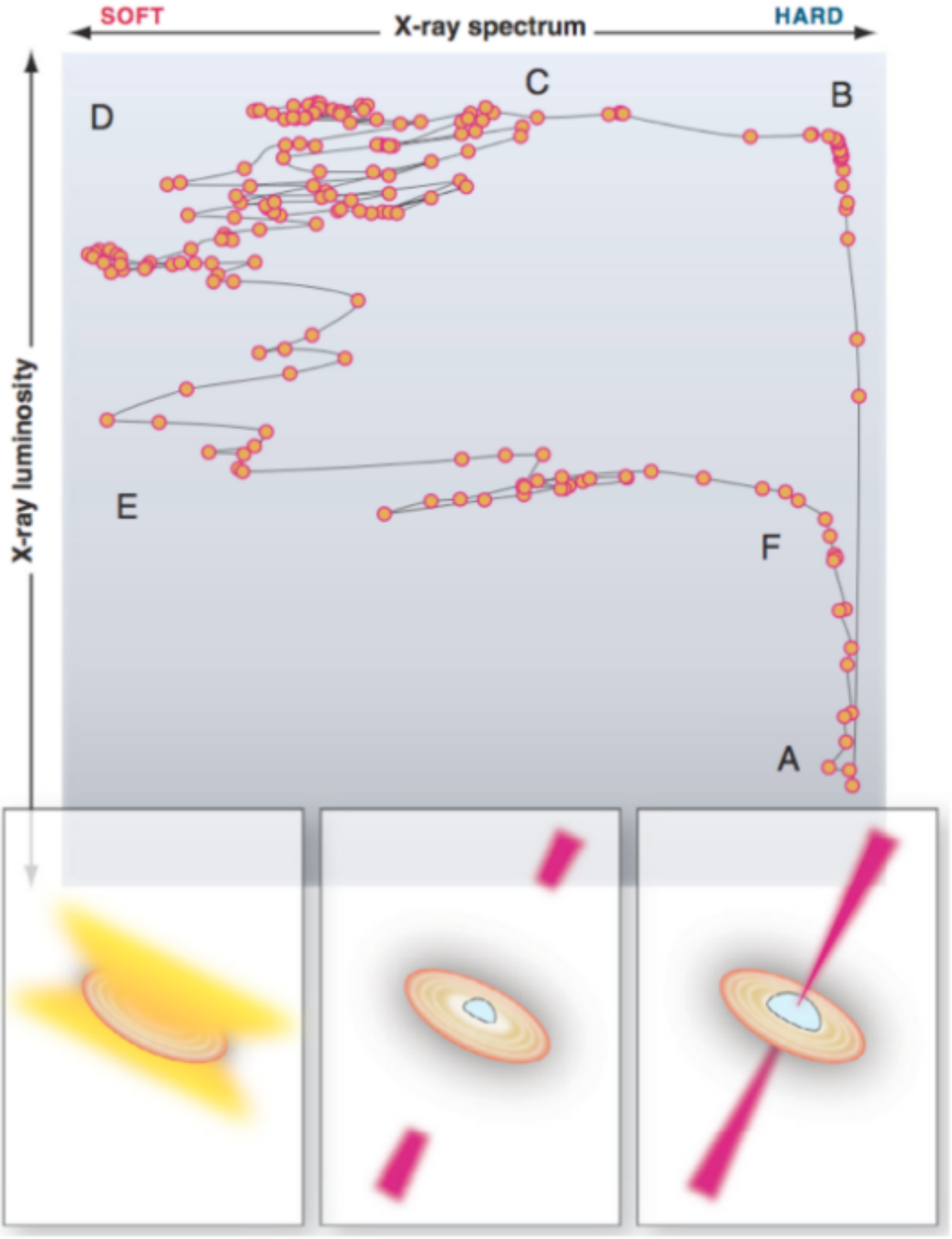

Figure 1.7: XRB hardness evolution "q" diagram during an outburst showing the changes in X-ray hardness, luminosity and system geometry. Schematic Credit: Fender & Gallo (2014)

Similarly to DNs, these bursts in XRBs are thought to be driven by viscosity changes in the AD and can be explained by DIM. In quiescence (Fender & Gallo, 2014) the systems are X-ray "hard" and with low X-ray luminosities ($\sim 10^{30-32}\,\mathrm{erg\,s^{-1}}$). X-ray "hardness" represents the difference in energy emitted in the more and less energetic X-ray bandpass scaled to the total energy emitted over both of the bandpasses. Therefore the "hard" state corresponds to more high energy photons being detected and in the "soft" state more low energy photons are detected. However, considering the low luminosity of sources in quiescence, there is significant observational bias influencing their population, especially at the lower luminosity end. This low, quiescent state is marked as "A" in Figure 1.7.

The viscosity change driven burst shown in Figure 1.7 consists of several state changes associated with changes of X-ray hardness, i.e. the change in relative strength of spectral components and geometry. As the system emerges from quiescence the main change is in drastically increasing luminosity, but the hard spectral state is maintained (Motta et al., 2009). From the DIM point of view, a sudden increase in viscosity is accompanied by increase in accretion rate and luminosity ($\gtrsim 10^{38}\,\mathrm{erg\,s^{-1}}$) on timescales of days (Coriat et al., 2012). In this state it is expected that the emission comes from the thermal Comptonisation in the hot plasma (corona) close to the accretor and is accompanied by high X-ray variability ($\sim$40 % root mean square (r.m.s.). Whereas in this state, a significant proportion of energy is expected in the UV, which unfortunately cannot be observed due to the substantial dust extinction in the galactic plane. Consequently, XRBs in this state are observed as "harder when brighter" (Plotkin et al., 2014). This transition corresponds to section of A to B in Figure 1.7.

At peak luminosity ($L_x \sim 10^{37}\,\mathrm{erg\,s^{-1}}$), the system then transitions from hard to soft state (from B, through C to D in Figure 1.7) (Dunn et al., 2010) on the timescale of several days to weeks. It is at this stage where the appearance of quasi-periodic oscillations (QPOs) is very common (Casella et al., 2005a). QPOs are variations in the light curves of accreting systems which exhibit a Lorentzian-like shape in the broad-band power spectrum (see Ingram & Motta (2019) for a detailed review). They are more closely discussed in Section 1.5.2. They are broadly divided into 3 types, A, B and C, based on their coherence and most common time and duration of occurrence (Casella et al., 2005a), with type B being the most common during this state transition. Furthermore it is thought that this state transition may be associated with the jet launch (Soleri et al., 2008; Fender et al., 2009; Miller-Jones et al., 2012) and is accompanied by radio flares.

In general, in the soft state (D to E) the spectrum of the system is dominated by a thermal component represented best by a multi-temperature black body spectrum peaking at ~ 1 keV. This is associated most usually to an optically thick AD and is accompanied by a drastic drop in X-ray variability ($\sim$5%) and radio emission from the synchrotron emission associated with the radio jet. Overall the difference between hard and soft states can be summarised by strong, quasi-steady jets with weak disc wind in the hard state Castro Segura et al. (2022). This is opposed to very weak jets and strong disc winds in the soft state (Miller et al., 2006; Neilsen & Lee, 2009).

1.4.2 Type I X-ray bursts

The other type of bursts in XRBs, type I, are generally short $\sim$1 minute long X-ray flashes resulting from unstable thermonuclear burning on the NS surface in LMXBs. The thermonuclear runaway process is triggered by ignition of an accreted layer of material. The unstable burning of the bottom of this layer then spreads across the whole surface of the NS in under 10 seconds. As a result the accreted Hydrogen and Helium are converted to heavy-element ashes. The bursts themselves have a distinct shape following a fast rise, a variable, sometime multi-peaked maximum and a slow exponential decay. At peak of the bursts, the system can reach close to Eddington luminosity (Lewin et al., 1993).

Type I bursts can in general be classified into 3 separate classes, based on the burst luminosity, duration and recurrence. The "classic" type I bursts last $\sim$1 minute and repeat frequently (every hour or so) (Grindlay et al., 1976; Lewin et al., 1993). The "intermediate" bursts have extended duration of $\sim$30 minutes and substantial radiation pressure effects (in't Zand et al., 2011). As opposed to the mixed H and He burning in the classic bursts these are thought to be the result of pure He layer being ignited after being accreted at low accretion rates over longer period of time. The mass that is burnt in these intermediate bursts is thought to be 10 to 100 times larger than that of classical bursts (in't Zand et al., 2005; Cumming et al., 2006). The last class is the "superoutburst" class. These bursts last $\sim$10 hours and are thought to be the result of C ignition at large column depths (Cornelisse et al., 2000; Cumming & Bildsten, 2001; Strohmayer & Brown, 2002). Some systems experiencing type I bursts re-ignite before a new layer is reformed completely due to leftover fuel from a previous burst. This results in repeated bursts with lower peak luminosity and shorter decay times in shorter succession (Boirin et al., 2007).

1.4.3 Type II X-ray bursts

Type II bursts are particularly short in duration, from ∼100 ms to ∼10 minutes and with recurrence times of couple of seconds up to an hour (Bagnoli et al., 2015). These bursts are semi-periodic with peak luminosities reaching up to L_{Edd} and showing correlation between the burst energy and their recurrence time (Lewin et al., 1993). A common explanation for the bursts, similarly to magnetically gated bursts in AWDs (see Section 1.3.1), is accumulation of material at the magnetically truncated inner disc radius, which is accreted episodically in an burst of accretion instability (Lewin et al., 1993; Spruit & Taam, 1993; Lewin et al., 1995; Bagnoli et al., 2015).

1.4.4 Ultraluminous X-ray Sources

Ultraluminous X-ray sources (ULXs) are a class of X-ray binaries with luminosities $L_X \gtrsim 10^{39}\,\mathrm{erg\,s^{-1}}$, exceeding the Eddington limit ($L_{EDD} \simeq 1.3 \times 10^{38} M/M_\odot\,\mathrm{erg\,s^{-1}}$, with M being the mass of the accretor) of a $\sim 10\,\mathrm{M}_\odot$ black hole (BH; see Kaaret et al., 2017; Fabrika et al., 2021; King et al., 2023; Pinto & Walton, 2023, for recent reviews). First detected by the *Einstein Observatory* in the off-nuclear regions of nearby galaxies (Fabbiano, 1989), they were considered as possible intermediate-mass black hole (IMBH) candidates with $M_{\mathrm{BH}} \simeq 10^2 - 10^6 M_\odot$, accreting at sub-Eddington rates (see e.g. Colbert & Mushotzky, 1999). The presence of mHz QPOs in some ULXs (see e.g. Strohmayer et al., 2007; Strohmayer & Mushotzky, 2009; Pasham et al., 2015; Atapin et al., 2019), interpreted as the low-frequency counterparts of QPOs in Galactic BH binaries (van der Klis, 1989), was proposed to support this hypothesis. Furthermore the inferred masses from the QPO frequencies based on the mass-frequency scaling derived from Galactic BH binaries (e.g. Aschenbach, 2004; Remillard & McClintock, 2006; Smith et al., 2018) with suggested masses in the IMBH range (see e.g. Casella et al., 2008 and Figure 4 of Smith et al., 2018). However, the lack of concordance with other expected behaviours, e.g. the relative location of characteristic timescales, cast doubt on such simple analogies (Middleton et al., 2011).

With the advent of *Chandra* (Weisskopf et al., 2000), *XMM-Newton* (Jansen et al., 2001), and later *NuSTAR* (Harrison et al., 2013), high-quality spectra of ULXs showed the presence of peculiar spectral states (Gladstone et al., 2009; Sutton et al., 2013), consistent with them harbouring either a stellar-mass BH or NS accreting at super Eddington rates (King et al., 2001; Poutanen et al., 2007; Zampieri & Roberts, 2009). A definitive confirmation of this scenario came when Bachetti et al. (2014) detected spin pulsations at a period $P \simeq 1.37\,\mathrm{s}$ in M82 X-2,

the first pulsating ULX (PULX) powered by an accreting NS. Since then, other ∼3 persistent PULXs mostly emitting at super-Eddington luminosities (as high as $\sim 1000 L_{\rm Edd}$) have been discovered (Fürst et al., 2016; Israel et al., 2017a,b; Carpano et al., 2018; Sathyaprakash et al., 2019; Rodríguez Castillo et al., 2020).

1.5 Variability in Accreting Systems

Being able to resolve the individual components of an accreting system through imaging is impossible at the current state of technology. Therefore, there is a need for alternative methods for indirect inference of the geometry and study of behaviour of accreting systems. Variability in general refers to changes in the emission of the system over time and can give invaluable insights into the workings of the accretion process itself. Variability can in general be best studied through frequency domain as opposed to the time domain, making Fast Fourier transforms (Oppenheim & Schafer, 1975) and similar algorithms such as Lomb-Scargle (Lomb, 1976) very useful tools.

In the frequency domain it is easier to constrain and quantify what frequencies (and hence timescales) govern the variability of a system and at which times most energy is emitted. As such, the Discrete Fourier Transform (DFT) for a given time series a_k with associated times kdt, where k is an integer number of data points within the time series from 1 to N, the expression for for the DFT is:

$$A_j = \frac{1}{N} \sum_{k=1}^{N} a_k e^{i2\pi jk/N} \tag{1.5.1}$$

The inverse of this DFT, i.e. the conversion of A_j back to a_k, where A_j contains N data points in frequency space sampled by $\nu_j = jd\nu = j/(Ndt)$ and with integer j sampled from $-N/2+1$ to $N/2$ is:

$$a_k = \sum_{-N/2+1}^{N/2} A_j e^{-2\pi jk/N} \tag{1.5.2}$$

Therefore for a_k to be a physical signal it has to be real and complex conjugate symmetric so that $A_j = A_j^*$. The power spectra considered here are the amplitude of the DFT $|A_j|^2$. Using Parseval's theorem for a time series with mean μ and variance σ^2 and duration T so that $T = Ndt$, it can be shown that:

$$\sum_{j=1}^{N/2} |A_j|^2 d\nu - \frac{|A_{N/2}|^2 d\nu}{2} = \frac{\sigma^2}{2T} \tag{1.5.3}$$

It is hence possible to normalise the power spectrum so that the integral under all positive frequencies gives the variance of the time series. The limiting factor on the highest possible frequency (and the shortest timescale) that can be probed by a DFT, or an equivalent, is given by the Nyquist frequency:

$$\nu_{Nyq} = \frac{1}{2\Delta t} \tag{1.5.4}$$

where Δt is the sampling of the time series. The low frequencies (long timescales) are on the other hand limited by the total length of the time series T, hence the lowest possible frequency is $1/T$. For a more conservative estimate $3/T$ may be adopted, in order to insure that the longest timescales considered has several cycles present. This is useful in particular when considering long coherent signals comparable to the timescale of the data set.

DFT has a requirement for strictly regularly sampled data, as can be seen from Equation 1.5.1. For dealing with real astrophysical data this can be quite problematic, due to the data being prone to gaps. The many possible issues that may arise, causing considerable data gaps are observability constraints (i.e daytime, weather, target may be observable only during limited time of the year), but also instrumental effects intrinsic to many instruments (see Section 2.1.2 for the *K2* issue). Whereas it is possible to interpolate between the gaps or sacrifice some of the high frequency sensitivity, there are other alternative methods that can be used instead to handle unevenly sampled data.

Lomb-Scargle (Lomb, 1976) is a well known and used algorithm for detecting periodicities in unevenly sampled data. For a detailed description on the algorithm, its uses and shortcomings, see VanderPlas (2018). As opposed to a DFT in Equation 1.5.1, its periodogram can be expressed as:

$$P(\nu) = \frac{A^2}{2}\left(\sum_n g_n cos(2\pi\nu[t_n - \tau])\right)^2 + \frac{B^2}{2}\left(\sum_n g_n sin(2\pi\nu[t_n - \tau])\right)^2 \tag{1.5.5}$$

where A, B and τ are arbitrary functions of frequency ν and time series observations at times t_i. Assuming that A and B are such that the power spectrum is indistinguishable from a DFT if the observations are evenly sampled, the power spectrum can be analytically computed and is not sensitive to global time shifts in the data. Equation 1.5.5 can be expressed as:

$$P_{LS}(\nu) = \frac{1}{2}\left(\frac{(\sum_n g_n cos(2\pi\nu[t_n-\tau]))^2}{\sum_n cos^2(2\pi\nu[t_n-\tau])} + \frac{(\sum_n g_n sin(2\pi\nu[t_n-\tau]))^2}{\sum_n sin^2(2\pi\nu[t_n-\tau])}\right) \quad (1.5.6)$$

To ensure time invariance for each frequency:

$$\tau = \frac{1}{4\pi\nu} tan^{-1}\left(\frac{\sum_n sin(4\pi\nu t_n)}{\sum_n cos(4\pi\nu t_n)}\right) \quad (1.5.7)$$

Throughout this thesis, Lomb-Scargle (LS) is used in all AWD cases instead of the DFT due to the length of the observations with unpredictable sampling. DFT and LS algorithms are primarily used to detect periodic variability, i.e. signals not changing or changing negligibly over the course of the observation duration. These signals, often appearing as δ-like spikes in the power spectral distribution (PSD) correspond usually to orbital periods of the binaries P, the spin frequencies of the accretors and the beats between the respective signals and superhumps (for more details on superhumps see Section 1.3.1). However, non-periodic signals still contribute significantly to the PSD and this creates the broad-band component of the PSD. They can be very roughly, split into aperiodic variability, often called flickering and quasi-periodic variability. In the following Sections the broad-band and quasi-periodic variability in accreting systems are discussed in greater detail.

1.5.1 Flickering

Flickering (aperiodic broad-band variability) is present in all types of accreting systems (Scaringi et al., 2012a; Uttley & McHardy, 2001; Uttley et al., 2005; Van de Sande et al., 2015; Gandhi, 2009). Although there has been plenty of observational evidence for this (Belloni et al., 2002; McHardy et al., 2006; Scaringi et al., 2012b), the generally accepted explanation is that the variability is driven by local accretion rate fluctuations propagating inwards through the accretion flow on local viscous timescales (Lyubarskii, 1997; Arévalo & Uttley, 2006a, also referred to as the fluctuating accretion disc model). The inward transfer of material is triggered by the outward transfer of angular momentum. This in turn is caused by the viscous stresses of the separate disc rings as the material flows around the disc at different Keplerian velocities (Frank et al., 2002a). The standard Shakura-Sunyaev disc model (Shakura & Sunyaev, 1973) defines a dimensionless viscosity prescription parameter α, which in many circumstances is assumed constant through the disc. Flickering is however thought to be caused by local fluctuations in the viscosity of the disc (Lyubarskii, 1997). MHD simulations have shown to be the most reliable way of inferring α, as its value strongly depends

on the input magnetic field strength. The current estimates place it between $\sim 0.05 - 0.1$ for geometrically thin discs (Yuan & Narayan, 2014; Hawley & Balbus, 2002; Penna et al., 2013).

In many cases the fluctuating accretion disc model has been successfully applied at X-ray wavelengths to an optically thin, geometrically thick, inner flow (sometimes referred to as a corona) in X-ray binaries (van der Klis, 2006) and at optical wavelengths in CVs (Scaringi, 2014).

Rms-flux relation

A fundamental property of broad-band variability in all accreting systems is the rms-flux relation (Uttley & McHardy, 2001; Gleissner et al., 2004; Uttley et al., 2005; Heil & Vaughan, 2010; Scaringi et al., 2012a). It is the linear relation between the rms variability amplitude and the flux level of a source in a stationary state, signifying that accreting systems are more variable when they are brighter. In principle, because of the relation holds even when the source is stationary, it is showcasing that this variability is intrinsic to the accretion process itself and not related to a change of state. Further implications are that the variability at low frequencies (long timescales) are linked to that in high frequencies (short timescales) (Uttley et al., 2005). In essence, it can be explained by the propagating accretion rate fluctuations model, where the variability of each disc "ring" (Figure 3.7) is the product of all the previous ones. This means that the inward propagation of matter is a multiplicative process.

The rms-flux relation has been reported in all accreting systems, from AGN to XRBs (Uttley & McHardy, 2001; Uttley et al., 2005). In AWDs, it has been seen in NLs (Scaringi et al., 2012a) and DNs (Van de Sande et al., 2015) alike.

Propagating Accretion Rate Fluctuations Model

The most common explanation for flickering is related to propagating local fluctuations in the accretion rate through the accretion disc on viscous time scales (Lyubarskii, 1997; Ingram & Done, 2011a, 2012; Ingram & van der Klis, 2013). In this scenario the variability is caused by local perturbations to the viscosity parameter α and/or $\frac{H}{R}$ as defined within the standard accretion disc model (Shakura & Sunyaev, 1973). The viscosity perturbations are hence translated into local perturbations in the accretion rate. A change in accretion rate changes the variability of the light curve, such that the affected timescale is governed by where the

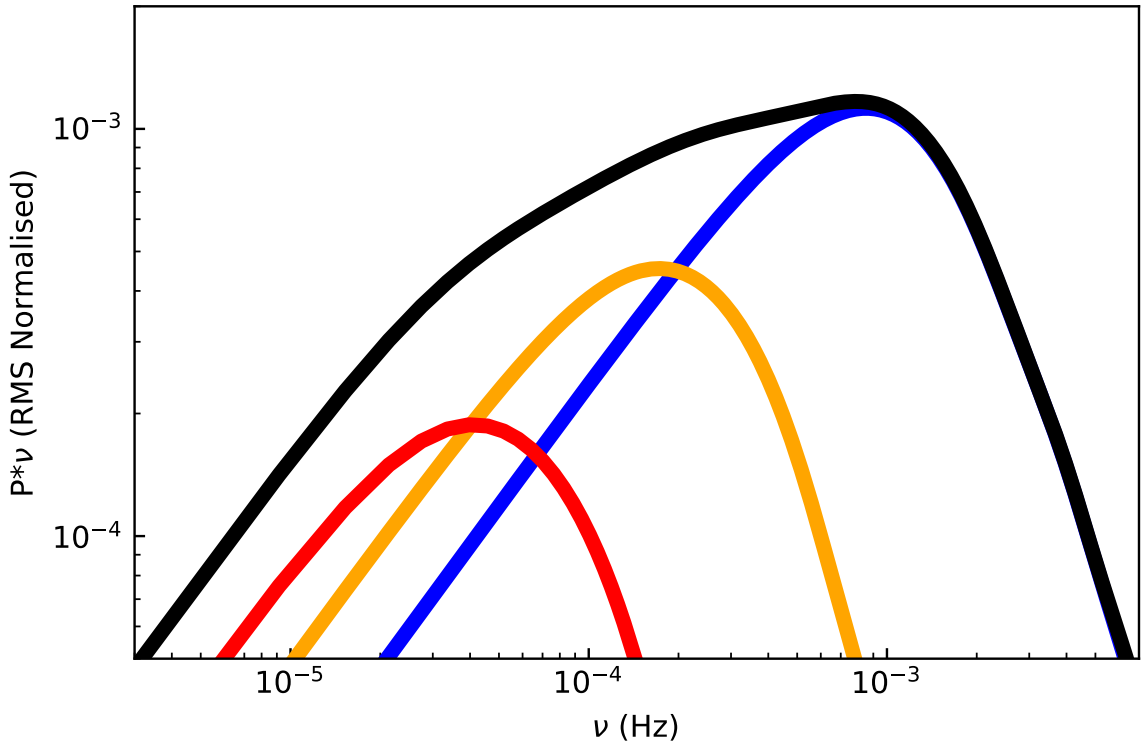

Figure 1.8: A schematic representation of how Lorentians representing inwardly propagating accretion fluctuations combine to construct the overall broad-band shape of the power spectrum of an accreting system. The accreting system here is assumed to be a $0.8M_{\odot}$ white dwarf.

driving change is occurring. This means that an initial perturbation of the viscosity at the outer disc edge initiates a slow mass transfer rate variability. As this propagates inwards, again on the local viscous timescale, the initial perturbation couples with other perturbations generated further in the disc.

I implement this model using the prescription of Ingram & van der Klis (2013). This divides the disc into N rings which are logarithmically spaced between the inner and outer disc edges, such that the $\frac{dr_n}{r_n}$ quantity remains constant, with r_n representing radius from the centre of the compact object to the middle of N^{th} annulus and dr_n its width. This assumption enforces the linear rms-flux relation (Uttley & McHardy, 2001; Uttley et al., 2005; Scaringi et al., 2015) and ensures the model adheres to observations of the linear rms-flux relation in accreting systems. Within Ingram & van der Klis (2013) and Scaringi (2014) the intrinsic variability of each annulus is modelled as a zero-centred Lorentzian peaking at the viscous frequency associated with a specific disc radius:

$$\left|A_n(\nu)\right|^2 = \frac{\sigma^2}{T\pi}\frac{\Delta\nu_n}{(\Delta\nu_n)^2+\nu^2} \tag{1.5.8}$$

where $\Delta\nu_n$ is the viscous frequency at r_n so that $\nu_{visc}(r_n) = \alpha\left(\frac{h}{r_n}\right)^2 \nu_{dyn}(r_n)$, σ^2 is the variance of the light curve of the annulus and T the corresponding duration of the light curve. This equation generates the intrinsic PSD of each annulus within the disc. The overall PSD is then a series of nested convolutions of these individual Lorentzians moving from the outside inwards.

Accretion rate fluctuations are converted to luminosity fluctuations via the emissivity $\epsilon(r_n)$. The emissivity profile is governed by the emissivity index γ and boundary condition $b(r_n)$, such that $\epsilon(r_n) \propto r_n^{-\gamma} b(r_n)$. For a flow extending all the way to the white dwarf surface a stressed $b = 1$ boundary condition as adopted in Scaringi (2014) is a reasonable assumption. In contrast, black hole and stress-free conditions are used in Ingram & van der Klis (2013) where $b(r_n) = 3\left(1 - \sqrt{\frac{r_n}{r}}\right)$.

In Ingram & Done (2011a) the model was applied to XRBs where the $\alpha\left(\frac{H}{R}\right)^2$ parameter is treated as a power-law. Scaringi (2014) adapted the model for white dwarfs by simplifying the treatment of $\alpha\left(\frac{H}{R}\right)^2$ as a constant through the disc, effectively assuming a single flow responsible for the variability. This was a reasonable assumption within the data considered as it was used to only fit to the highest frequency break corresponding to an inner geometrically thick and optically thin flow extending all the way to the white dwarf surface.

1.5.2 Quasi-periodic variability

Quasi-periodic variability in light curves of accreting systems is a very well known and studied phenomenon (Warner et al., 2003; Ingram & Motta, 2019). However, not all accreting systems use the same definition of such variability. For the purpose of this thesis, all quasi-periodic oscillations (QPOs) are taken to refer to the variability of the signal in frequency at which it is observed, not to the time-dependent nature of a coherent signal. Therefore, in the following sections, the main observational properties and theoretical explanations for these QPOs are outlined in the context of XRBs. The history of the use of the term QPO in AWDs is summarised in the introduction to Chapter 4.1.

QPOs in XRBs

Quasi-period oscillations (QPOs) are non-coherent brightness variations in the X-ray flux, widely recognised in X-ray binary systems (XRBs). In the context of XRBs the flux fluctuations manifest as characteristically broad features in the power spectra, due to the unstable

quasi-periodic nature of the signal. They are present both in neutron star (NS) and black hole (BH) XRBs with a variety of different types (see Ingram & Motta 2019 for a detailed review). BH XRBs exhibit low ($\lesssim$ 30 Hz) and high ($\gtrsim$ 60 Hz) frequency QPOs, with low frequency QPOs being somewhat more common. The low frequency QPOs show different broad types depending on their strength, width and frequency, one of which is known as Type-C. The broadness of a QPO is characterised by its quality factor $Q = \frac{\nu_0}{2\Delta}$, where ν_0 is the centroid frequency of the Lorentzian representing the QPO and Δ its half width at half maximum. Type-C QPOs in particular are strong and narrow, with $Q \gtrsim 8$, and are also known to display strong harmonics. Similarly, NS XRBs show kHz QPOs and low frequency QPOs, however as opposed to BH XRBs the kHz QPOs are more common. They also display colour evolution on the hardness-intensity diagram, similarly to BH XRBs (Homan, 2001; Belloni & Motta, 2016). Based on the QPO-colour evolution they are classified as FBO (flaring branch oscillations), NBO (normal branch oscillations) and HBO (horizontal branch oscillations). Type-C and HBO QPOs are known to follow a linear correlation with a broad-band aperiodic low-frequency break (Wijnands & van der Klis, 1999), with a characteristic decrease in power with increasing frequency.

QPOs in ULXs

Numerous ULXs are known to show QPOs, particularly in the mHz regime (see e.g. Strohmayer et al., 2007; Strohmayer & Mushotzky, 2009; Pasham et al., 2015; Atapin et al., 2019) with various models proposed to explain their presence. Middleton et al. (2019) proposed that mHz QPOs arise from a precessing inner flow of the disc. The general relativistic frame-dragging torque (inducing Lense-Thirring precession) is then communicated to the launched winds, whose precession is expected to cause the much longer super-orbital period seen in many (P)ULXs (see e.g. Kong et al., 2016; Walton et al., 2016; Fürst et al., 2018; Vasilopoulos et al., 2020; Brightman et al., 2020, 2022). Atapin et al. (2019), instead, proposed that the propagating fluctuations mechanism from Lyubarskii (1997) can explain both the QPO and the flat-topped noise observed in a sample of ULXs. Majumder et al. (2023) followed Das et al. (2021) to link the QPO frequency to the infall time towards the inner radius of the disc, and hence proposing to use the QPO frequency to infer the masses of the central object, assumed to be a BH. A similar mechanism for generating quasi-periodic variability but for NSs is also explored in Mushtukov et al. (2024).

Contrary to BHs, in the case of PULXs the presence of a magnetosphere is unavoidable and

it is expected to induce additional torques to the inner flow. This has been proposed for both magnetised NSs and T Tauri stars by Lai (1999) and more recently for weakly magnetised accreting white dwarfs (WDs) by Veresvarska et al. (2024a) (discussed in detail in Chater 4 and referred to as the magnetically-driven precession model (MDP) in Chapter 5).

1.6 This Thesis

In this thesis I will discuss the physics of accretion as applied mostly to AWDs and the links between the accretion in AWDs and other accreting systems. For this purpose, most of the relevant data discussed here comes from optical to near infrared missions such as *TESS* and *Kepler* . As data from these telescopes is used across most of the Chapters, in Chapter 2 I will introduce these missions and instruments in greater detail. I will also outline the type of observations they provide and their calibration to absolute luminosity using ground based missions such as *ASAS-SN* and *ATLAS* . For the remainder of the thesis, each Chapter corresponds to a separate publication, as outlined in the Declaration. In Chapter 3 I will showcase the broad-band properties of an AM CVn system SDSS J1908+3940. Furthermore I will highlight the first detection of the outer region of the thin disc as confirmed by empirical fit and an analytical implementation of the propagating accretion rate fluctuation model. In Chapter 4 I will present the first detection of a new type of QPO in AWDs, showing direct observational analogies to type-C QPOs in XRBs. I will also present a new application of the magnetically driven precession QPO model which allows the prediction of magnetic field strength of the accretor. In Chapter 5 I will show an application of this model to the mHz QPOs in PULXs. Chapter 7 centres around newly detected micronova bursts in a novalike CP Pup. Chapter 7 discusses another micronova, in a well known IP DW Cnc and the accompanying strange behaviour of pole-flipping prior to the burst. In Chapter 8 summarizes the overall conclusions of this thesis and comments on the future work.

Chapter 2

Observations

2.1 Space-based Observations

In the following Section I will discuss the configurations and data obtained by space-based telescopes such as *TESS* and *Kepler* whose data are exhaustively used in Chapters 3, 4, 5, 6 and 7. Since the same methods and instruments have been used throughout these chapters, the broader details are gathered here, with more specific details and techniques mentioned in the relevant chapters.

2.1.1 *TESS*

The Transiting Exoplanet Satellite Survey (*TESS*) is a NASA sponsored Astrophysics Explorer class mission operated by Massachusetts Institute of Technology (MIT) (Ricker et al., 2015). It is a near all-sky survey, covering over 95% of the sky at optical to near infrared wavelengths. *TESS*'s primary science goal is to discover new sub-Neptune exoplanets around smaller (redder) stars with the possibility of spectroscopic follow-up. The spectroscopic follow-up is intended with instruments such as the James Webb Space Telescope (*JWST*) in order to study the planets atmosphere's and constrain their masses.

The telescope itself is mounted on a NGIs LEOStar-21750 satellite and carries a single scientific instrument. The instrument, a photometer, is composed of 4 identical wide Field of View (FOV) optical cameras. Apart from the cameras themselves the telescope also contains the hoods shielding the cameras' aperture, the mount, Sun shield and the Data Handling Units (DHU). The cameras point such that the their respective FOVs lined up one above the other (see Figure 2.2) with combined FOV of $24° \times 96°$. The lens diameter is 10.5 cm, with

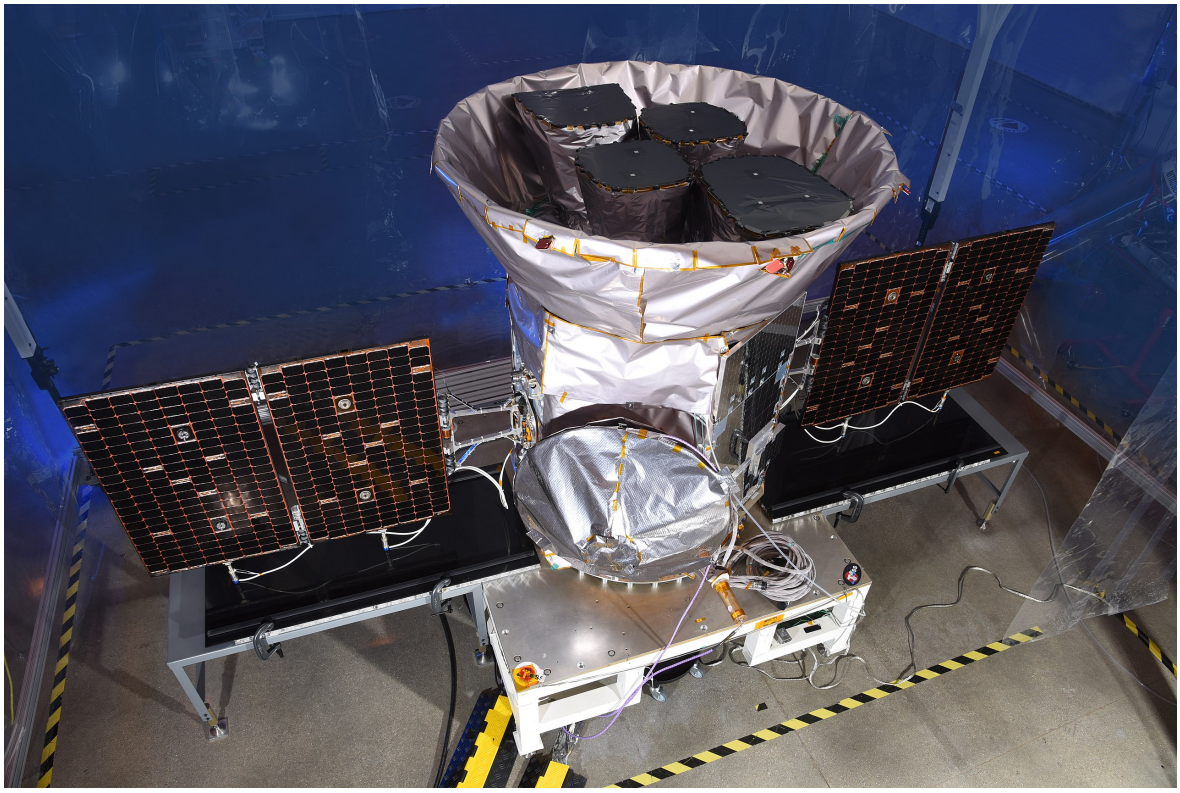

Figure 2.1: *TESS* spacecraft and instrument pre-launch. Schematic Credit: MIT

focal ratio of $f/1.4$. More detailed information on the instrument is summarised in Ricker et al. (2015).

The wavelength range, $\sim 600 - 1000$ nm, and response of the instrument is shown in Figure 2.3. The bandpass is centred on the Cousins I-band ($\lambda_{central} \sim 786.5$ nm). This bandpass was chosen to complement the primary science objective of the mission, since it has increased sensitivity to small transiting planets as compared to other similar missions with bluer bandpasses, like *Kepler* (Section 2.1.2). It was also chosen to reduce the photon counting noise, however the red end of the bandpass is limited by the quantum efficiency of the CCD. The blue end on the other hand is limited by the long-pass filter coating on the camera lenses. Since *TESS* is an all-sky survey with wide FOV, the resulting pixel size is also on the larger end at 21".

TESS launched in April 2018 and is situated in a unique elliptical HEO orbit, with an orbital period of 12 to 15 days at 2:1 resonance with the Moon. The observing strategy is composed of observing individual "Sectors", i.e. one FOV for 2 consecutive orbits ($\sim$ 27 days). At the time of launch, *TESS* was intended to have a 2 year long primary mission and has since had 2 extended missions, with a third being planned.

The primary mission was composed of 26 consecutive Sectors, with 13 in the northern and

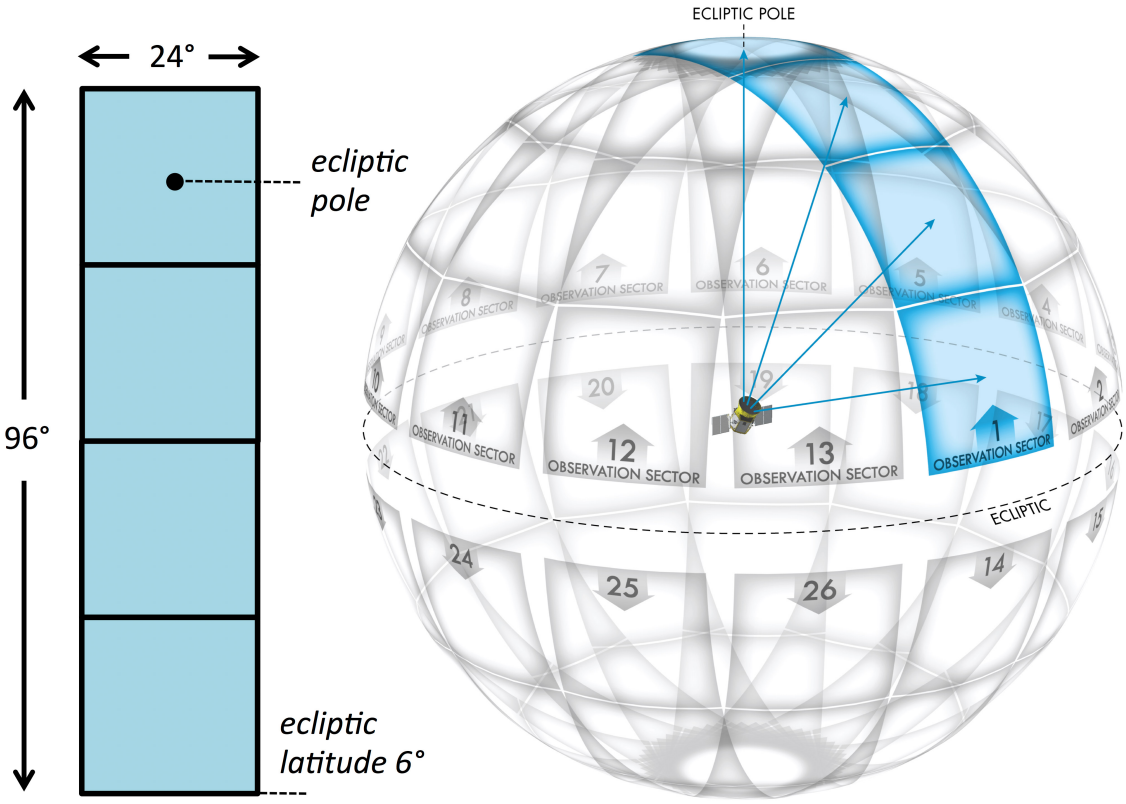

Figure 2.2: *TESS* FOV and camera line up projected on the sky with visualisation of the first 26 Sectors from the primary mission. Schematic Credit: `https://heasarc.gsfc.nasa.gov/docs/tess/telescope_information.html`

13 in the southern hemisphere, as shown in Figure 2.2. To observe each hemisphere took a year, with the southern one being observed first. The cadence of *TESS* observations in the primary mission was 2 minutes for all targets in the TIC catalogue, composed of the primary catalogue and ∼10 000 Guest Investigator (GI) targets. On top of this, *TESS* also takes a Full Frame Image (FFI) of the entire FOV every 30 minutes.

The 1st extended mission lasted 2 years, and again observed both hemispheres in a similar fashion to the primary mission. However, in contrast to the primary mission, 4 Sectors (42 to 46) were designated for ecliptic pointings, hence increasing *TESS* sky coverage. As opposed to the primary mission, around 80% of *TESS* targets were designated from the GI proposals. Another point of difference was the introduction of higher 20 s cadence option for a small number (∼600) of targets. This also allowed the FFI cadence to be altered to 10 minutes, instead of the original half hour.

The 2nd extended mission was planned for 3 years, covering a range of Sectors in both northern and southern hemisphere, as well as some ecliptic ones. Each Sector had a limit of ∼8000

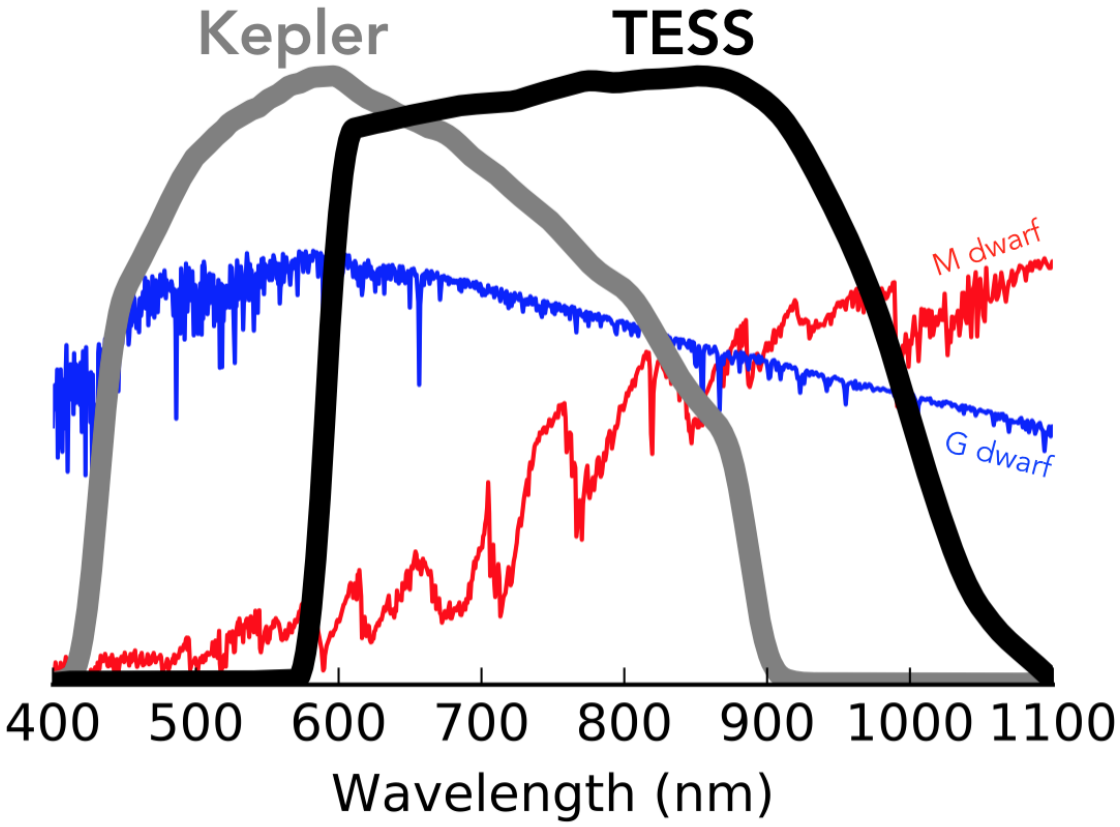

Figure 2.3: *TESS* and *Kepler* bandpass sensitivity curve compared to a spectrum of an M dwarf and a G dwarf. Schematic Credit: `https://heasarc.gsfc.nasa.gov/docs/tess/telescope_information.html`

2 minute and $\sim$ 2000 20 second cadence targets. Furthermore, the FFI cadence was lowered to 200 seconds.

TESS provides excellent relative photometry in the units of $e^{-}s^{-1}$. *TESS* data can be accessed on the Mikulski Archive for Space Telescopes (MAST[1]). A convenient way to access and download *TESS* data is through the LIGHTKURVE package[2]. All *TESS* data has an associated quality flag, with values ranging from 0 to 32768 based on the severity of the effect (Fausnaugh et al., 2018). For all data analysis in this thesis, only data with quality flag 0 (i.e. no effect) is considered. Cosmic rays are also filtered out on board of the space craft (Ricker et al., 2015). *TESS* provides two separate types of flux. The Simple Aperture Photometry (SAP) flux, corresponds to the raw, calibrated flux with no further alterations. Pre-search Data Conditioning (PDCSAP) flux is an alternative option with transit detection optimisation included in the flux, which can remove long-term intrinsic variability of the

[1] `https://mast.stsci.edu/portal/Mashup/Clients/Mast/Portal.html`
[2] `https://lightkurve.github.io/lightkurve/`

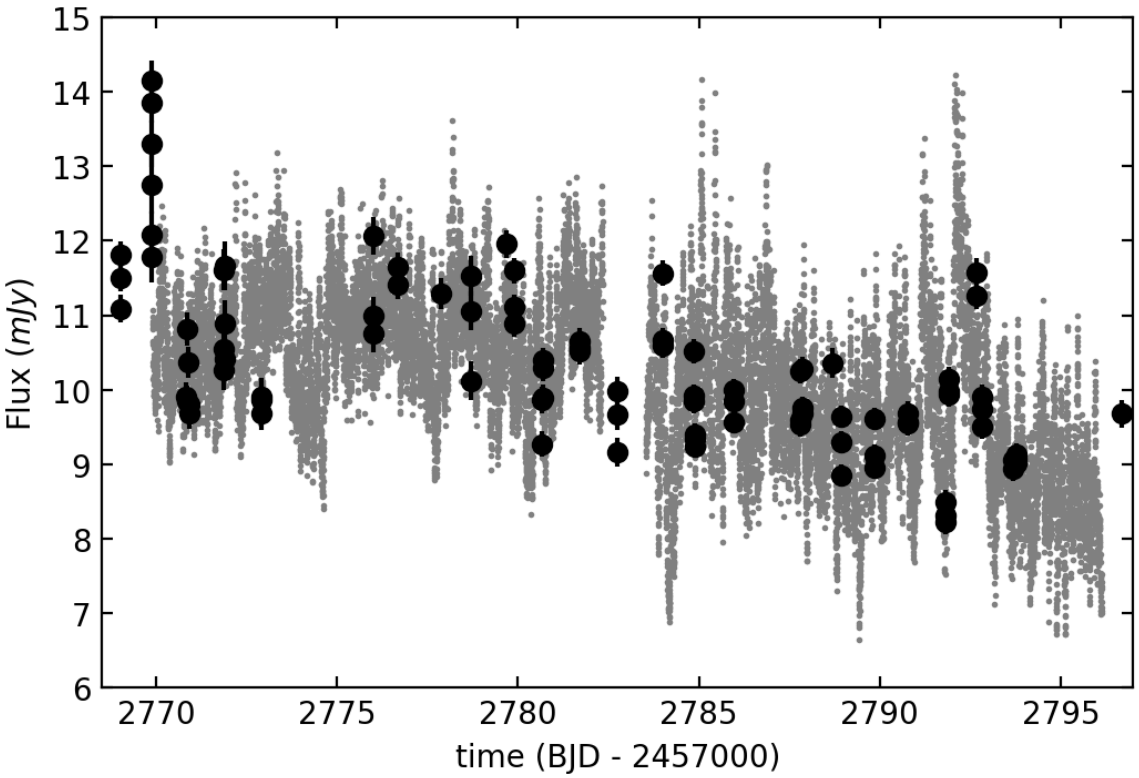

Figure 2.4: An example of *TESS* light curve of a novalike MV Lyr from Sector 54 (shown in grey). The *TESS* light curve has been calibrated to absolute flux (in mJy) through the quasi-simultaneous *ASAS-SN* light curve (black circles), details of which are discussed in Section 2.3.

source. It is for this reason that in this thesis, only SAP flux is used, to conserve all the intrinsic variability. An example of *TESS* light curve, with flagged data is shown in Figure 2.4.

TESS data were downloaded and cosmic rays were removed using the LIGHTKURVE package[3]. The Simple Aperture Photometry (SAP) flux is used to retain intrinsic variability of the systems while avoiding the transit detection optimisation of the Pre-search Data Conditioning (PDCSAP) flux. Data points are further excluded if their quality flag > 0.

An extensive, but not exhaustive list of Guest Investigator (GI) *TESS* programmes pertaining to compact and accreting binaries, from which the data used in this thesis comes from is shown in Table 2.1. The overall number of accreting white dwarfs and accreting white dwarf candidates in these programs is $\gtrsim$3100.

[3] `https://docs.lightkurve.org/index.html`

TESS Cycle	GI Program number	Primary Investigator
Cycle 1	G011268	Scaringi
Cycle 1	G011123	Schlegel
Cycle 1	G011235	Garnavich
Cycle 2	G022055	Coti Zelati
Cycle 2	G022071	Scaringi
Cycle 2	G022237	Rivera Sandoval
Cycle 2	G022254	Sion
Cycle 2	G022126	Schlegel
Cycle 2	G022230	Littlefield
Cycle 2	G022116	Wood
Cycle 2	G022078	Kemp
Cycle 3	G03284	Schwab
Cycle 3	G03071	Scaringi
Cycle 3	G03127	Maccarone
Cycle 3	G03180	Rivera Sandoval
Cycle 3	G03240	Wood
Cycle 3	G03245	Littlefield
Cycle 3	G03044	Scaringi
Cycle 4	G04208	Littlefield
Cycle 4	G04165	Rivera Sandoval
Cycle 4	G04009	Ramsay
Cycle 4	G04046	Scaringi
Cycle 4	G04152	Schlegel
Cycle 5	G05094	Scaringi
Cycle 5	G05135	Rivera Sandoval
Cycle 6	G06152	Rivera Sandoval
Cycle 6	G06143	Sokolovsky
Cycle 6	G06027	Scaringi
Cycle 6	G06156	Kashyap
Cycle 6	G06158	Pichardo
Cycle 6	G06101	Rucas
Cycle 7	G07007	Martin
Cycle 7	G07025	Scaringi
Cycle 7	G07074	Hinkle
Cycle 7	G07108	Unnati
Cycle 7	G07145	Rivera Sandoval
Cycle 7	G07154	Pichardo
Cycle 7	G07187	Walter

Table 2.1: List of *TESS* GI programmes, their numbers and primary investigators concerning programs focussed on compact and accreting binaries. All *TESS* data used in this thesis is drawn from this list.

2.1.2 *Kepler*

Another mission that is featured to a lesser extent in this thesis is *Kepler* , particularly in Chapter 3. *Kepler* is the 10^{th} low-cost and low-development time mission operated by NASA and it is part of the Discovery class science missions. *Kepler* , similarly to *TESS* was designed to discover low mass Earth-like exoplanets through their transits (Van Cleve et al., 2016). However, as opposed to *TESS* , *Kepler* focused on planets around orbiting sun-like stars. It was launched in March 2009 with a single instrument on board and was retired in 2018 after running out of fuel. The instrument was composed of 21 CCD modules, each of which had two 2200×1024 pixel CCDs, as shown in Figure 2.5. Each module had a FOV of $\sim 5\text{deg}^2$ with 116 deg^2 in total. The instrument itself contained a 0.95 m aperture Schmidt telescope with a single bandpass spanning from $\sim 420 - 900$ nm, as shown in Figure 2.3, with *TESS* redder bandpass as a reference.

The spacecraft itself is in an Earth-trailing heliocentric orbit, with the first *Kepler* mission focusing on observing a single field for ~ 3 years. The footprint of this field is shown in Figure 2.6. The default cadence of the targets observed in *Kepler* field was 60 seconds. However, in 2013 the 2^{nd} reaction wheel on the spacecraft stopped working, requiring a redesign of the mission operations and objectives. The new mission was named *K2* and it observed a series of fields around the ecliptic plane as a replacement for *Kepler* . The new method of orienting the spacecraft utilised a combination of the 2 remaining reaction wheels, the limiting torque on the spacecraft when pointed towards the ecliptic fields and the radiation pressure on the solar panels. Combined with the Sun angle constraints the length of time each field could be observed was limited to ∼80 days. As opposed to the primary mission, all *K2* targets were chosen from GI proposals.

For the purpose of this thesis, only downloading and handling *TESS* data is relevant. All *Kepler* data used in this thesis (see Chapter 3) was provided in its reduced form in Kupfer et al. (2015). However, LIGHTKURVE provides similar tools and procedures to handle *TESS* , *Kepler* and *K2* data, with all relevant information being detailed in (Lightkurve Collaboration et al., 2018).

2.2 Ground-based Observations

In this Section I will briefly describe the ground-based facilities whose data are discussed in Section 6 and 7. All ground-based data of interest here is from surveys, not targeted

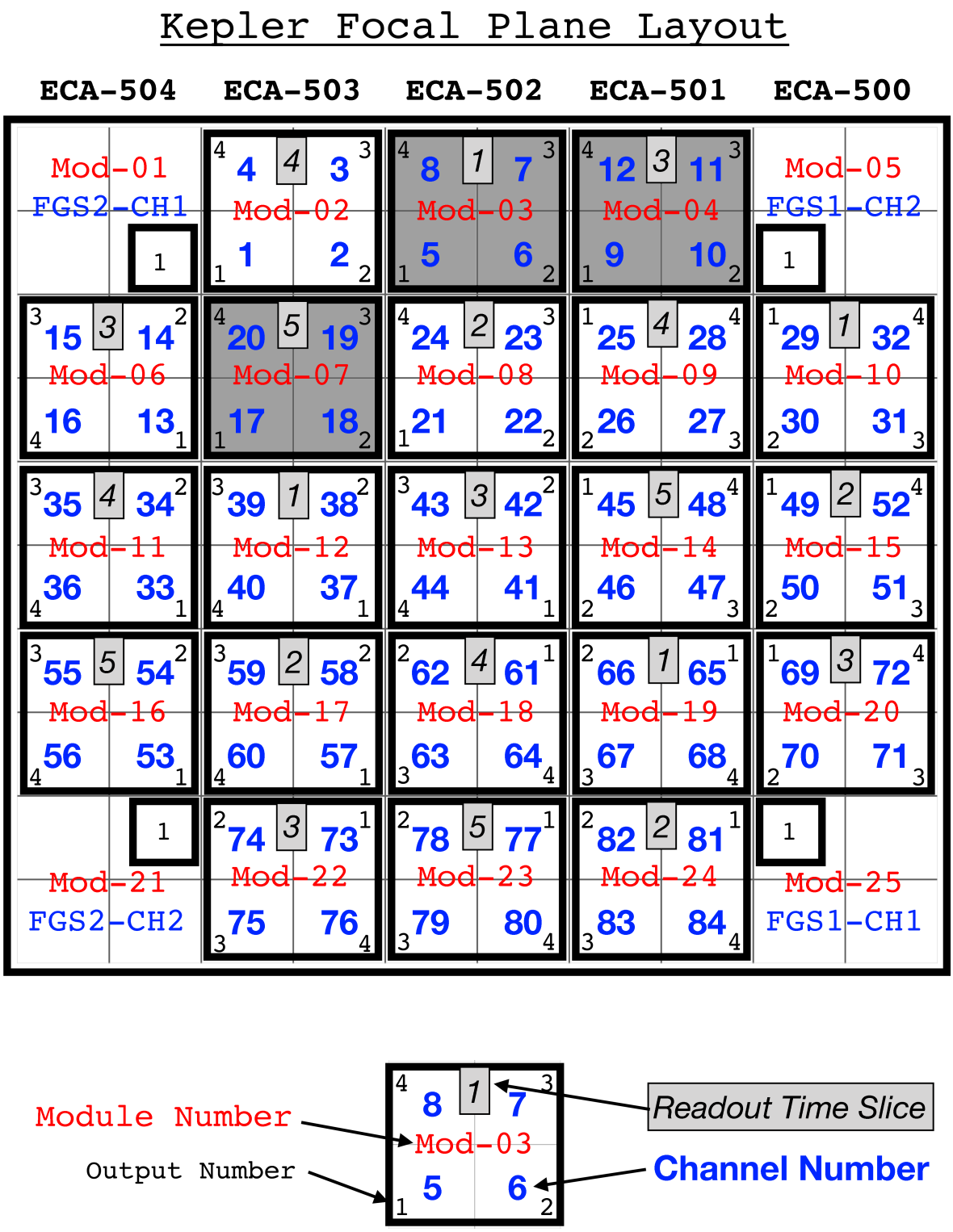

Figure 2.5: *Kepler* CCD modules layout with the corresponding channels. Schematic Credit: Van Cleve & Caldwell (2016)

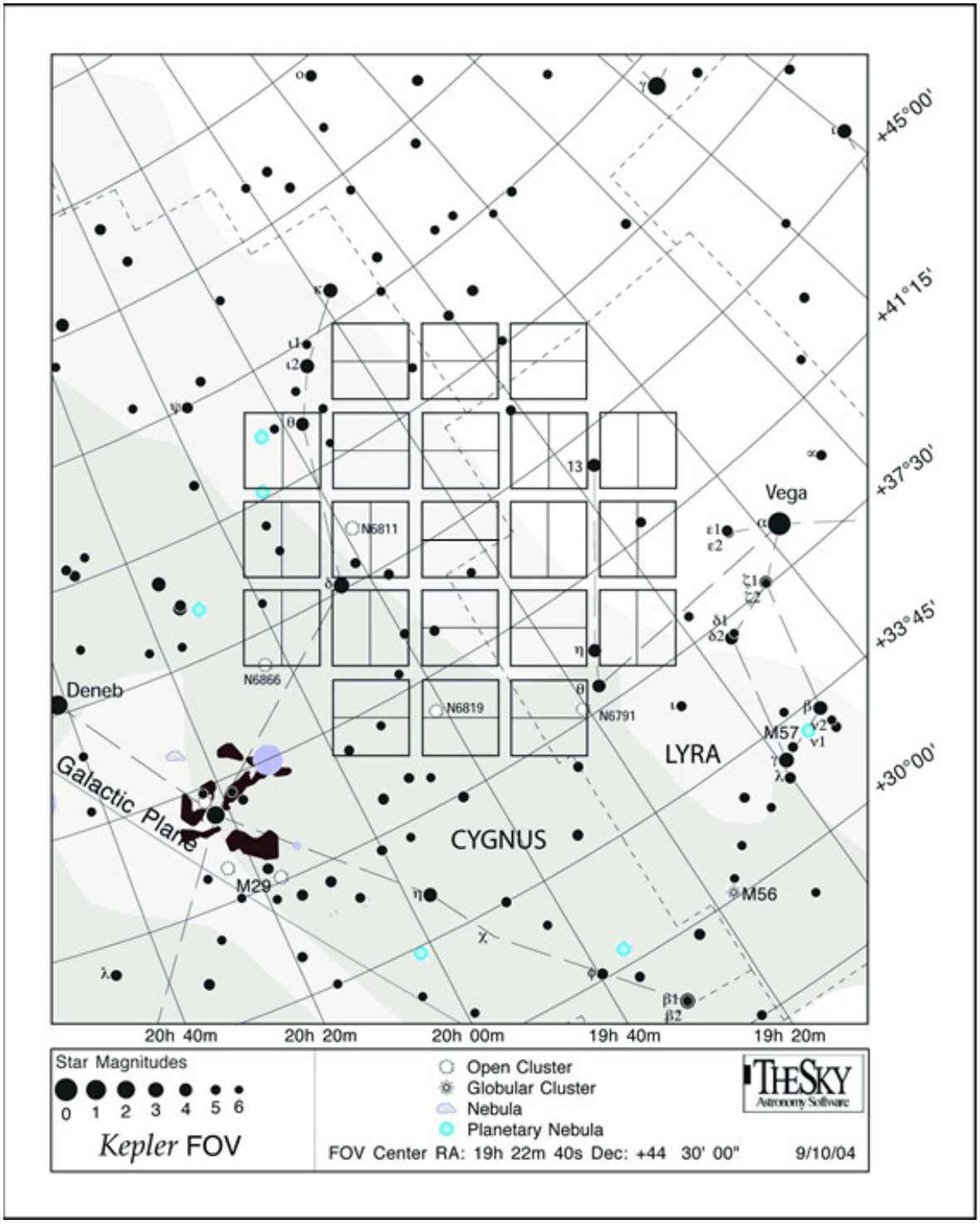

Figure 2.6: *Kepler* FOV with the footprint of the CCD modules overlayed on top. Constellations and clusters are marked in the field as well, with stars down to 6 mag. Schematic Credit: Van Cleve & Caldwell (2016)

observations and is often used to calibrate more high cadence photometry from space-based instruments mentioned in Section 2.1.

2.2.1 *ASAS-SN*

The All-Sky Automated Survey for Supernovae (*ASAS-SN*) is an optical survey scanning the entire sky every night down to $\sim$ 18 mag. It comprises of 24 fully robotic 14 cm telescopes across several locations in Hawaii, Chile, South Africa, Texas and China. It started operating in V-band (Hawaii and Chile), but now transitioned into g-band in all stations since 2018. *ASAS-SN* g-band (Shappee et al., 2014; Kochanek et al., 2017) is centred at 475 nm with 140 nm in width. All *ASAS-SN* observations are carried out in sets of 3 dithered 90 s exposures, with the data being accessible via an online portal[4].

2.2.2 *ATLAS*

ATLAS is an asteroid early warning system developed by University of Hawaii and is funded by NASA. It comprises of 4 telescopes, with 2 in Hawaii, one in Chile and 1 in South Africa. It scans the whole sky several times a night down to almost 20 mag. The telescopes observe in a series of 4 30 s exposures per night over 1 hour period (Tonry et al., 2018). As opposed to the *ASAS-SN* g-band, *ATLAS* uses its own 2-coloured bands. *ATLAS* o-band covering the redder part of the *ATLAS* visible spectrum from 560 to 820 nm and the c-band extends from 420 to 650 nm. The data reduction and forced photometry process is described in detail in Tonry et al. (2018); Smith et al. (2020).

2.3 *TESS* Calibration with Ground-based Photometry

TESS provides excellent precision relative photometry in units of $e^{-}s^{-1}$, which does not provide any information on the absolute flux of the target, only relative brightness. To obtain absolute photometry in mJy, we convert these measurements using quasi-simultaneous ground-based observations from *ASAS-SN* , without accounting for any bolometric correction. This conversion is based on assuming a linear relation between the *TESS* and *ASAS-SN* fluxes (an example shown in Figure reference). This method has been previously used (Scaringi et al., 2022d; Veresvarska et al., 2024a), but it requires quasi-simultaneous coverage of the

[4] `https://asas-sn.osu.edu/`

target by both *TESS* and *ASAS-SN* , which for this purpose is assumed to consist of all *ASAS-SN* observations within a *TESS* cadence. The *ASAS-SN* g-band is centred at 475 nm with 140 nm width, with a partial overlap with the *TESS* band-pass (600 - 1000 nm). Although the pass-bands do not exactly overlap, we assume here that any colour-term variation are minimal. The conversion is done separately for each half Sector, to avoid any instrumental effects and offsets. Assuming a linear relation between the 2 bands a direct conversion can be established in the form of:

$$F_{ASAS-SN}\,[mJy] = A \times F_{TESS}\left[e^{-}s^{-1}\right] + C \tag{2.3.1}$$

where $F_{ASAS-SN}$ is the *ASAS-SN* flux in mJy and F_{TESS} is *TESS* SAP flux in $e^{-}s^{-1}$. A and C are the conversion coefficients as defined by the linear relationship between the two fluxes. In the framework of the aforementioned assumptions, the *TESS* light curves in the *ASAS-SN* mJy units can be converted to luminosity using the *Gaia* DR3 parallax. Such calibration can provide lower limits on energies emitted in the *TESS* band, but should be treated with caution as the linear relationship tends to break for fainter sources, or for systems with poor *ASAS-SN* coverage. Lack of ground-based calibration often prohibits any measurements of the energetics being made. However, with the advent of more synoptic sky surveys (e.g. BlackGEM Groot et al. 2024) space-based calibrations will be more easily achieved due to wider sky coverage.

Despite the non-complete overlap of *TESS* and *ASAS-SN* passbands, no bolometric correction is applied in this calibration. This is to avoid any effects due to a potential change in the SED during the observations, which would affect any bolometric correction. In general, astrophysical systems tend to be bluer when brighter. As a result the obtained luminosities of the corrected *TESS* light curves should be treated as a lower limit, with more uncertainty in brighter targets. It is however possible to estimate the effect the bolometric correction could have on the luminosity. This can be done by comparing luminosities of the sources in different bandpasses, from X-ray to UV in accreting sources, to estimate a factor by which the actual luminosity is most likely underestimated. Future missions, such as *PLATO*, that will offer timing observations of similar cadence and length but in multiple bands will be able to help this issue (Rauer & Heras, 2018).

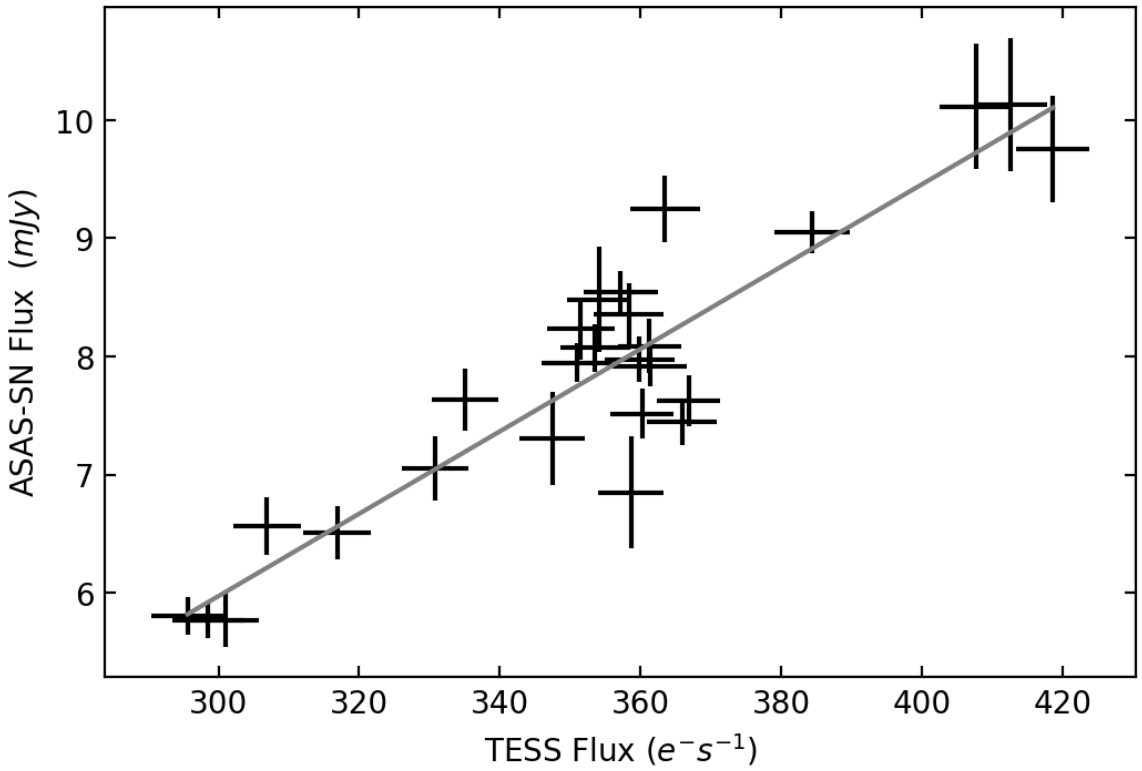

Figure 2.7: Example showing the linear relation between quasi-simultaneous *TESS* and *ASAS-SN* light curves. The example shows the relation for 1st half of *TESS* Sector 54, whose result is shown in Figure 2.4.

Chapter 3

Outer disc edge: properties of low frequency aperiodic variability in ultracompact interacting binaries

Abstract

Flickering, and more specifically aperiodic broad-band variability, is an important phenomenon used in understanding the geometry and dynamics of accretion flows. Although the inner regions of accretion flows are known to generate variability on relatively fast timescales, the broad-band variability generated in the outer regions have mostly remained elusive due to their long intrinsic variability timescales. Ultra-compact AM CVn systems are relatively small when compared to other accreting binaries and are well suited to search and characterise low frequency variability. Here I present the first low frequency power spectral analysis of the ultracompact accreting white dwarf system SDSS J1908+3940. The analysis reveals a low frequency break at $\sim 6.8 \times 10^{-7}$ *Hz in the time-averaged power spectrum as well as a second higher frequency component with characteristic frequency of* $\sim 1.3 \times 10^{-4}$ *Hz. I associate both components to the viscous timescales within the disc through empirical fits to the power spectrum as well as analytical fits using the fluctuating accretion disk model. My results show that the low frequency break can be associated with the disk outer regions of a geometrically thin accretion flow. The detection of the low frequency break in SDSS J1908+3940 provides a precedent for further detection of similar features in other ultracompact accreting systems. More importantly, it provides a new observable that can help constrain simulations of accretion flows.*

Co-author contribution

I have conducted the analysis as described in this Chapter and reported in Veresvarska & Scaringi (2023) under the supervision of Dr Simone Scaringi.

3.1 Introduction

AM CVn systems are compact interacting binaries with orbital periods well below the observed and theoretical minimum orbital period of CVs (Kolb & Baraffe, 1999b; Howell et al., 2001; McAllister et al., 2019). A review of their properties and evolutionary channels is given in Solheim (2010) and Ramsay et al. (2018), with an introduction to these systems and summarised overview being given in Section 1.3.2.

AM CVn systems currently comprise 11 out of 16 *LISA* verification sources (Kupfer et al., 2018; Marsh, 2011; Stroeer & Vecchio, 2006) for gravitational wave detection. Given their relatively small size, these systems are also well suited for magneto-hydrodynamic (MHD) simulations of entire accretion discs (Coleman et al., 2018; Kotko & Lasota, 2012). In this Chapter, I aim to leverage the compactness of these systems to study the low frequency broad-band variability.

The detection of SDSS J1908+3940 (hereafter J1908) was first reported by Stoughton et al. (2002) and Yanny et al. (2009) and identified as an AM CVn system by Fontaine et al. (2011) through the use of *Kepler* photometry. Its accretor has a reported white dwarf mass of $0.8 M_{\odot}$ (Fontaine et al., 2011; Kupfer et al., 2015) with a binary mass ratio of $q \sim 0.33$ (Fontaine et al., 2011; Kupfer et al., 2015). Kupfer et al. (2015) followed-up this system through phase-resolved spectroscopy to measure the orbital period of $\sim$ 18 min, making this system one of the very rare AM CVns with an orbital period below 20 minutes. Though inconclusive, Kupfer et al. (2015) identified a potential negative superhump of the system at 75 cd^{-1} and excluded a multitude of scenarios for the origin of the rest of the signals detected through photometry. The likely candidate explanation for these periodic photometric signals remains white dwarf g-mode pulsations (Hermes et al., 2014).

With the spectroscopic orbital period measured, J1908 joins AM CVn itself and HP Lib as one of 3 known high state AM CVn systems (Ramsay et al., 2018). High state AM CVn systems may be somewhat akin to CV nova-likes with similarly high accretion rates. In J1908 the inferred mass transfer from Ramsay et al. (2018) is $\sim 6.6 \times 10^{-7} M_{\odot} \mathrm{yr}^{-1}$ based on fitting the spectral energy distribution of the source, while Coleman et al. (2018) report a value of $3.5 - 8 \times 10^{-9} M_{\odot} \mathrm{yr}^{-1}$ based on non-local thermodynamic equilibrium (NLTE) accretion disc fits to optical high resolution spectra.

In this Chapter I will examine the broad-band properties of J1908 based on the propagating accretion rate fluctuations model discussed in detail in Section 1.5.1.

In many cases, as detailed in Section 1.5.1, the fluctuating accretion disc model has been successfully applied at X-ray wavelengths to an optically thin, geometrically thick inner flow (sometimes referred to as a corona) in X-ray binaries (van der Klis, 2006) and at optical wavelengths in CVs (Scaringi, 2014). Assuming the fluctuations propagate through the disc from the very outer edge, it should also be possible to observe variability originating from the geometrically thin, optically thick, outer-disc regions. However, this requires the assumption that the fluctuations originating in the outermost disc regions are not completely damped by the time they reach the emitting region generating the variability signal. In XRBs the variability generated from a geometrically thin disc component is generally assumed to have negligible influence and power on the observed high frequency variability (Kawamura et al., 2022).

The viscous timescale of interest at the outer-edge disc radius can be defined by Equation 1.1.10 (Shakura & Sunyaev, 1973) and is related to the dynamical timescale (Equation 1.1.8). The viscosity prescription α, combined with the scale height of the disc H/R, is an important parameter as it decouples the viscous timescale from the dynamical one. Under the strong constraint that the outer disc cannot exceed the 1^{st} Lagrangian point, the viscous timescale associated with CVs and X-ray binaries can be inferred to be a few tens to a few hundred days for $\alpha \left(\frac{H}{R}\right)^2 \sim 10^{-3} - 10^{-5}$. Because of their smaller size, the viscous timescale of the outer disk in AM CVn systems with orbital periods of ~ 20 minutes is substantially shorter. The corresponding viscous frequency associated with the outer-disk edge in this case is in the range of $\sim 10^{-7}$Hz - 10^{-5}Hz. In comparison CVs and XRBs with an orbital period in the $\sim$ 6 hours to $\sim$1 day range would yield viscous frequencies in the range $\sim 10^{-9}$Hz - 10^{-7}Hz.

A convenient way of visualising the amount of power output by a system at a given timescale is through Fourier analysis and PSDs described by a combination of Lorentzian-shaped components (see Section 1.5 for further detail).

The highest frequency Lorentzian component is generally detectable, unless the system is too faint, in which case the highest frequencies are dominated by Poisson-induced white noise. The lowest frequencies are generally only described with a red-noise power law, but this does not necessarily exclude the existence of lower frequency Lorentzians. The fluctuating accretion disc model associates the broad-band aperiodic noise components observed as Lorentzians to somewhat discrete regions in the accretion flow (Section 1.5.1). Alternatively,

transitions between different emission mechanisms and/or changes in disc viscosity or scale height can also alter the shape and positions of the Lorentzian components. Nonetheless, the lowest frequency Lorentzian would be associated with the outer-disc regions, while the highest frequency Lorentzian would be associated with the inner-disc ones. Naturally, the low frequency break could also be associated with a specific feature present in the outer disc region, such as the bright spot where the stream of material from the donor impacts the out accretion disc edge. Any variability resulting from such features would also mark the outer disc region. A different interpretation may instead be that the lowest frequency variability directly traces mass loss variations from the donor star at the L1 point. Changes in the mass transfer rate may then directly affect the outer disc. The observed variability could still contain signals generated in-situ at the outer disc and be driven by viscous interactions. Disentangling these two variability generating processes remains non-trivial.

In this Chapter I discuss the *Kepler* data of the AM CVn system J1908 in Section 3.2. Data analysis and empirical model fits to the PSD are presented in Section 3.3. I also describe the analytical propagating fluctuations model as adapted from Lyubarskii (1997), Ingram & van der Klis (2013) and Scaringi (2014) with the corresponding multi-component changes that I employ here in Section 3.3.4. In Section 3.4 I discuss the results of the empirical PSD fit and as well as the inferred physical system constraints. In Section 3.5 I explore the physical implications of the accretion disc structure before making my final conclusions of the findings in Section 3.6.

3.2 Observations

The data used here on J1908 was obtained by *Kepler* in short cadence mode (58.9 s) during quarters 6 to 17. This corresponds to the period between 24^{th} of June 2010 to 11^{th} of May 2013. The raw data can be obtained from the Mikulski Archive for Space Telescopes (MAST[2]). Fontaine et al. (2011) reports the detection of J1908 alongside a 2^{nd} G-type star within 5 arcseconds. Due to the close proximity of both objects it is likely that the simple aperture photometry of J1908 is contaminated by the bright neighbouring star. This is addressed in Kupfer et al. (2015), where the `PyKE` software (Still Martin, 2012) was used to perform point-spread-function (PSF) photometry. The J1908 light curve produced in Kupfer et al. (2015) is further corrected for the linear instrument trend on a quarterly basis. The

[2] `https://mast.stsci.edu/portal/Mashup/Clients/Mast/Portal.html`

final normalised light curve provided by Kupfer et al. (2015) is used in this work and further cleaned of cosmic rays through the use of Jenkins (2017) the `Lightkurve` package[3]. The final light curve is shown in Figure 3.1, alongside a 1-day mean. The mean shown Figure 3.1 demonstrates the low-amplitude, low-frequency, variability on longer timescales in J1908. This is particularly clear in the bottom panel of Figure 3.1, where the mean clearly shows variability generated from a non-Gaussian process.

3.3 Methods and Analysis

In this Section I first describe the method used in constructing the time-averaged PSD of J1908. I further describe the empirical model fit to the time-averaged PSD and discuss the statistical significance of the detected low frequency break. I also describe the analytical 2 flow damped fluctuating accretion disc model also used to fit the time-averaged PSD of J1908.

3.3.1 Time-averaged PSD

To study the broad-band variability of J1908 I calculated the time-averaged power spectrum. Using the time-averaged power spectrum reduces the scatter across frequencies in the PSD. I do this by dividing the light curve into independent segments of equal length and compute the Lomb-Scargle Periodogram (Lomb, 1976; Scargle, 1998) for all of them separately. I then take the average of all PSDs and bin this in logarithmically-spaced frequency bins. I normalise each individual PSD such that the integrated power is equal to the variance of the light curve (Miyamoto et al., 1991; Belloni et al., 2002), which follows directly from van der Klis (1988). This methodology is similar to that applied in Scaringi et al. (2012a).

In order to select an appropriate segment size it is necessary to consider where a low frequency break might be expected. The dynamical frequency at the L1 point for J1908, being the absolute limit of where the disc can extend to, is $\sim 1.2 \times 10^{-2}$ Hz. This is then linked to the viscous frequency via the $\alpha \left(\frac{H}{R}\right)^2$ parameter. For a geometrically thin, optically thick, disc as may be expected in the outermost regions one would expect a characteristic viscous frequency of $\sim 10^{-5}$ - 10^{-7} Hz, but this strongly depends on the value of the α and $\frac{H}{R}$.

Segmenting the light curve can cause the power at the lowest frequencies to be artificially reduced due to the frequency range being comparable to the segment size. I discuss this

[3] `https://docs.lightkurve.org/index.html`

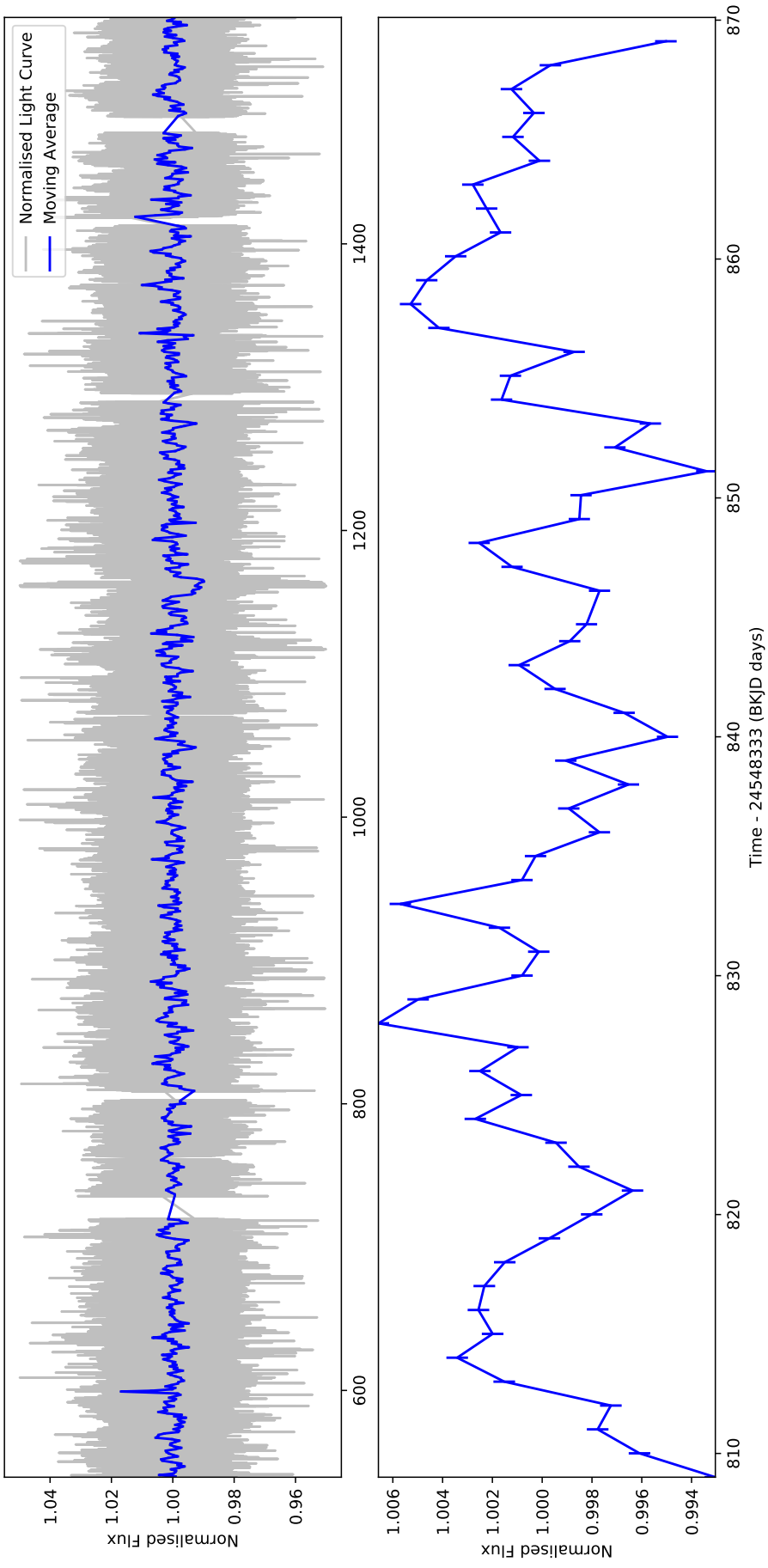

Figure 3.1: *Top:* Normalised *Kepler* light curve of J1908 (grey) with the 1 day average (blue). *Bottom:* Zoom in on a 60 day segment of the top panel.

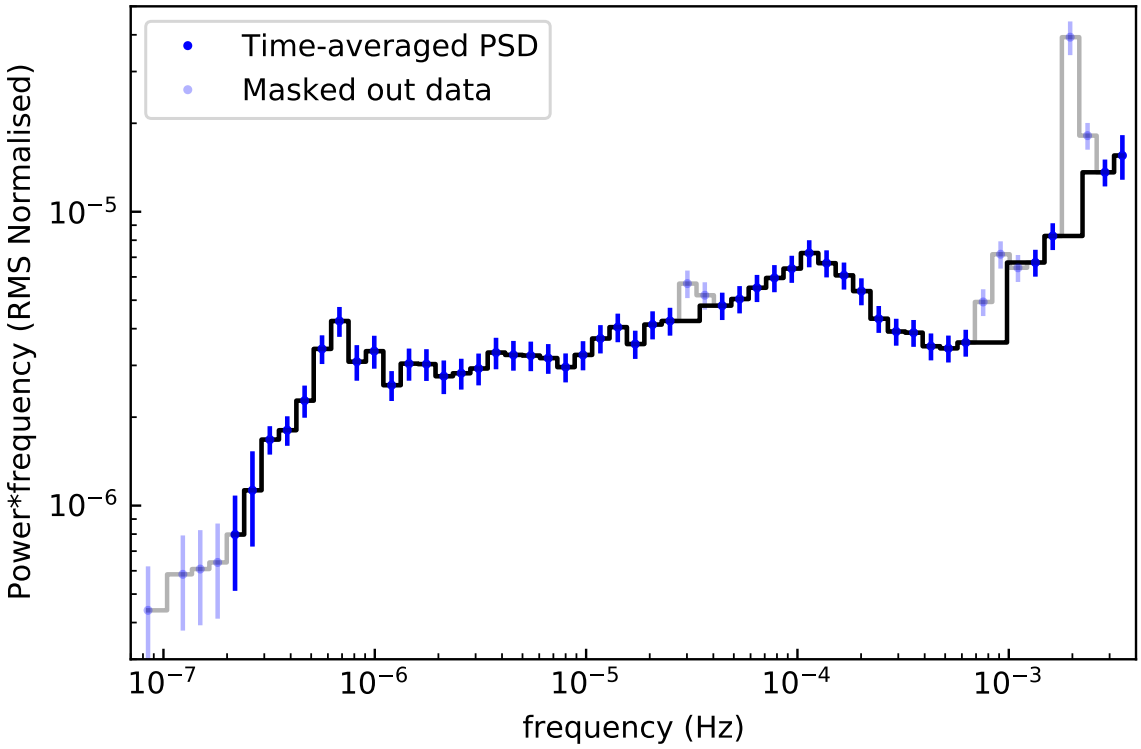

Figure 3.2: Time-averaged PSD of J1908 adopting a segment length of 60 days. Masked out periodic signals as well as frequencies lower than the segment window length are marked with the grey solid lines.

effect in further detail in Section 3.3.3. I have explored segment sizes between $\sim$ 15 days to $\sim$ 100 days to isolate the effect of the artificial drop in power to the real frequency break. In fixing the range of the segment length another variable that has been taken into account is the ability to divide the light curve into quasi-continuous segments. I define this by ensuring each segment has no gaps bigger than 1 day. My final selection to compute the time-averaged PSD is constructed from 11 $\times$ 60 day long segments, as shown in Figure 3.2. Further details on verification of whether the break can be caused by the chosen binning or segment size is discussed in section 3.3.3. I also test and confirm that the 11 individual PSDs are stationary and can be reliably averaged to produce a time-averaged PSD. Details of this can be found in Appendix A.2.

As discussed previously, J1908 shows many periodic signals, and most of these can be observed above the Poisson dominated white noise component at the highest frequencies. These signals have already been discussed and some have been identified (Kupfer et al., 2015). Here I mask these out as their variability cannot be associated with the broad-band aperiodic variability of interest. I further mask frequencies $< 2 \times 10^{-7}$ Hz as they appear to be an artefact of the chosen segment size (see Section 3.3.3 for more details).

The masked out frequency bins are shown in Figure 3.2. The choice of power × frequency on the y-axis better displays any broad-band features in the PSD. The PSD covers ~ 4 decades in frequency before the white noise begins to dominate the signal above $\sim 10^{-3}$ Hz. The PSD shows 2 clear broad-band components with highest power attained at $\sim 10^{-4}$ Hz and $\sim 7 \times 10^{-7}$ Hz. There is a clear declining slope between these towards the low frequencies. The decrease in power at $\sim 7 \times 10^{-7}$ Hz (referred as the low frequency break) covers almost an order of magnitude in fractional RMS power in just over half a decade in frequency.

The time-averaged PSD also shows a quasi-periodic structure at $\sim 3 \times 10^{-5}$ Hz. The feature is consistently present in the PSD irrespective of binning. To better understand the origin of this feature and its level of coherence I have visually inspected the individual power spectra in linear frequency space. I find that the origin of this feature may be related to quasi-periodic variability as no coherent periodicity could be identified above the noise level. It is interesting to consider whether this feature may be related to a super-orbital precession frequency of a tilted disc as observed in several accreting white dwarfs. In this context, Kupfer et al. (2015) identified a signal at 8.787856×10^{-4} Hz as a potential negative superhump. The resulting super-orbital modulation would appear at $\sim 8.8 \times 10^{-4}$ Hz for J1908, and this is inconsistent with the feature identified at $\sim 3 \times 10^{-5}$ Hz. I cannot at this stage discern whether this feature is the result of a dynamical or viscous process in the disk.

3.3.2 Empirical fit

In order to provide quantitative measurements of the frequencies associated with the 2 breaks in the time-averaged PSD of J1908, I fit the entire PSD with 2 separate Lorentzians to capture the low and high frequency breaks, a bending power law with a further 2 breaks to capture plateau between the breaks, and a further power law to capture the high frequency Poisson noise component. The Lorentzians take the form of:

$$P(\nu) = \frac{r^2 \Delta}{\pi} \frac{1}{\Delta^2 + (\nu - \nu_0)^2} \tag{3.3.1}$$

where r^2 represents the integrated fractional RMS power, Δ is the HWHM of the Lorentzian and ν_0 the centred frequency so the the maximum power of the Lorentzian is at $\nu_{peak} = \sqrt{\Delta^2 + \nu_0^2}$. The bending power-law is adapted from (McHardy et al., 2004) which and is defined as:

$$P(\nu) = A\nu^{-\alpha_1}\Pi_{i=1}^{N}\left(1 + \left(\frac{\nu}{\nu_{b_i}}\right)^{\alpha_{i+1}-\alpha_i}\right)^{-1}. \quad (3.3.2)$$

Contrary to the use in McHardy et al. (2004) where the A parameter is defined as the power at 1 Hz, I here leave it as a free parameter. The ν_{b_i} terms correspond to the break frequencies of the power laws and α_i are the power law indices, with $N = 2$ being the number of breaks. I further include a power-law component at the highest frequencies to capture the Poisson white noise variability using:

$$P(\nu) = P_0\nu^{\beta} \quad (3.3.3)$$

where P_0 is the normalisation constant and β is the power law index, expected to be close to 0 for a purely Poisson noise contribution.

This empirical model can be used to fit the overall time-averaged PSD as well as the individual segments. This is particularly useful to determine the level of stationary of the various components throughout the entire lightcurve duration. The results of the overall time-averaged empirical fit compared to the fit of its separate segments are discussed in the Appendix A.2. I find negligible differences between the characteristic frequencies between the individual PSD segments, which in turn supports the assumption that the PSD is stationary during the interval over which the segments are averaged.

3.3.3 Low frequency break significance

As mentioned above in Section 3.3.1 the choice of binning and segment size may induce an artificial drop in power in the PSD at the lowest frequencies. Furthermore, the errors at the lowest frequencies are affected by fewer measurements due to the logarithmically spaced bins, which in turn increase the errors. In any case it is necessary to test for robustness and ensure that the low frequency break at $\sim 7 \times 10^{-7}$ Hz is intrinsic to the data and not an artefact of the segment size and/or binning.

I test for this using a method based on Timmer & König (1995). The method consists of generating simulated light curves with an assumed underlying model for the PSD. In practice this is done by randomising the phase and amplitude of the model PSD at each frequency, and taking the inverse Fourier transform to generate a light curve. In my case I will simulate light curves with an underlying PSD that does not have a low frequency break. After sampling the simulated light curves using the same *Kepler* sampling of the true data, and after binning and averaging the simulated data as described in Section 3.3.1, I can test if the low frequency

break is an artefact of the methodology or not. I thus reproduce the empirical fit from Section 3.3.2 but without the low frequency Lorentzian component. I further set the central bending power-law Eq. (3.3.2) to only have the higher frequency cut-off. This then allows the central power-law to extend to low frequencies without having a frequency break.

The new PSD is then used as an input to the Timmer & König (1995) method, and I simulate 10^3 artificial light curves. The artificial light curves are sampled on the timestamps of the *Kepler* light curve, and these are then used to produce a time-averaged PSD in the same way as in the data as described in Section 3.3.1.

I have inspected the distribution of powers in each frequency bin in the simulated time-averaged PSD and found these to follow a χ^2 distribution. The 93.32% and 99.977% levels, corresponding to 3σ and 5σ detection significance, are taken and shown as the confidence contours on the time-averaged simulated PSD Figure 3.3. These represent the significance levels in the RMS in each independent frequency bin. It is clear from Figure 3.3 how the time-averaged simulated PSD departs from the input PSD at the lowest frequencies. This is due to the segment size selection, and demonstrates that frequencies below 1.9×10^{-7} Hz are severely affected by the methodology. At higher frequencies however it is also clear that the simulated PSD closely follows the underlying input PSD.

Figure 3.4 shows the results of the Timmer & König (1995) simulation overlayed onto the real time-averaged PSD. I have now limited the lowest frequency to not include the artificial drop in power caused by the segment size selection. It is evident from inspecting Figure 3.4 how the broad-band component and associated low frequency break at 7×10^{-7} Hz is not reproduced by the simulation as one may expect. I further note that the Timmer & König (1995) method used here to determine significance levels considers frequency bins to be independent of each other, and is thus robust for testing coherent signals. The quoted significance levels must thus be considered as lower limits when considering aperiodic broad-band components in the PSD. This is because the clear drop in power associated with the low frequency break constitutes several consecutive and independent frequency bins. I thus associate the low frequency break as intrinsic to the data and not an artefact of the methodology.

Additionally to testing the significance of the low frequency break, the Timmer & König (1995) simulation also allows us to better quantify the significance of other features in the PSD. Specifically I find that the feature at $\sim 3 \times 10^{-5}$ Hz is $> 99.977\%$ significant.

Finally, I further verify that the observed low frequency break is not related to any instrumental artefact. I have selected 3 neighbouring short cadence *Kepler* targets to J1908. Having

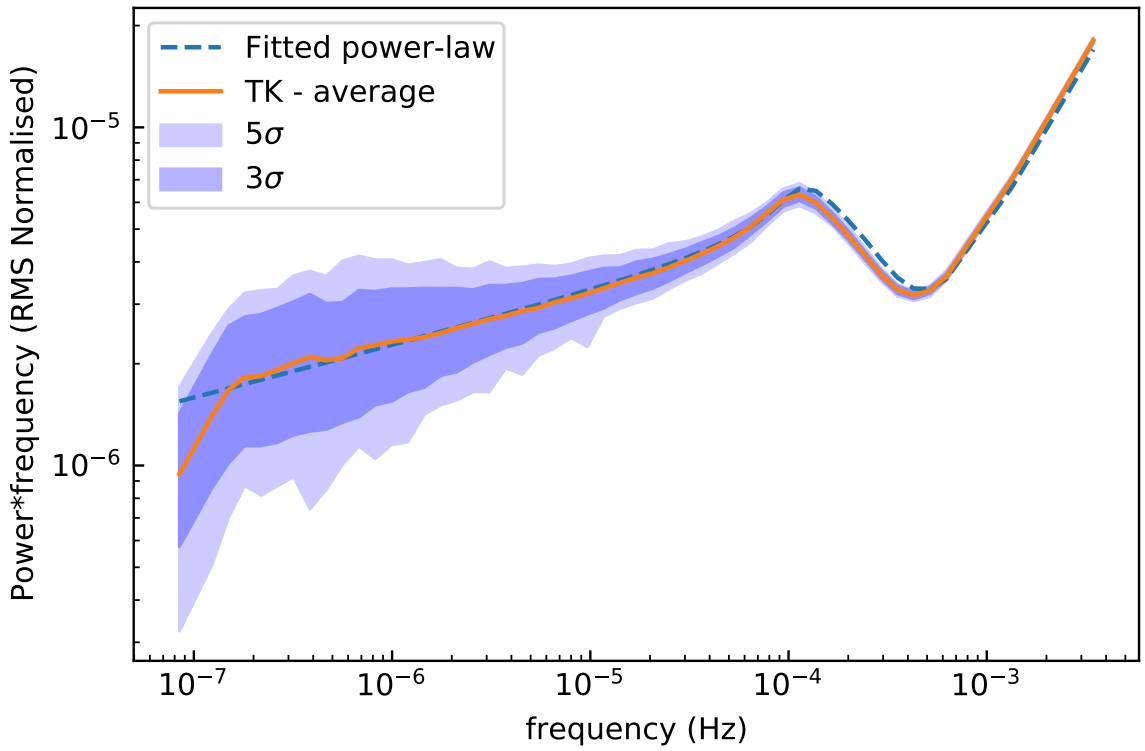

Figure 3.3: Fitted power law of the time-averaged PSD of J1908 without the low frequency break (dashed blue line). The Timmer & König (1995) simulation and significance contours for 93.32% and 99.977% (shaded blue regions). The mean of the simulations (solid orange line) clearly shows an induced break at 1.9×10^{-7} Hz corresponding to the segment length.

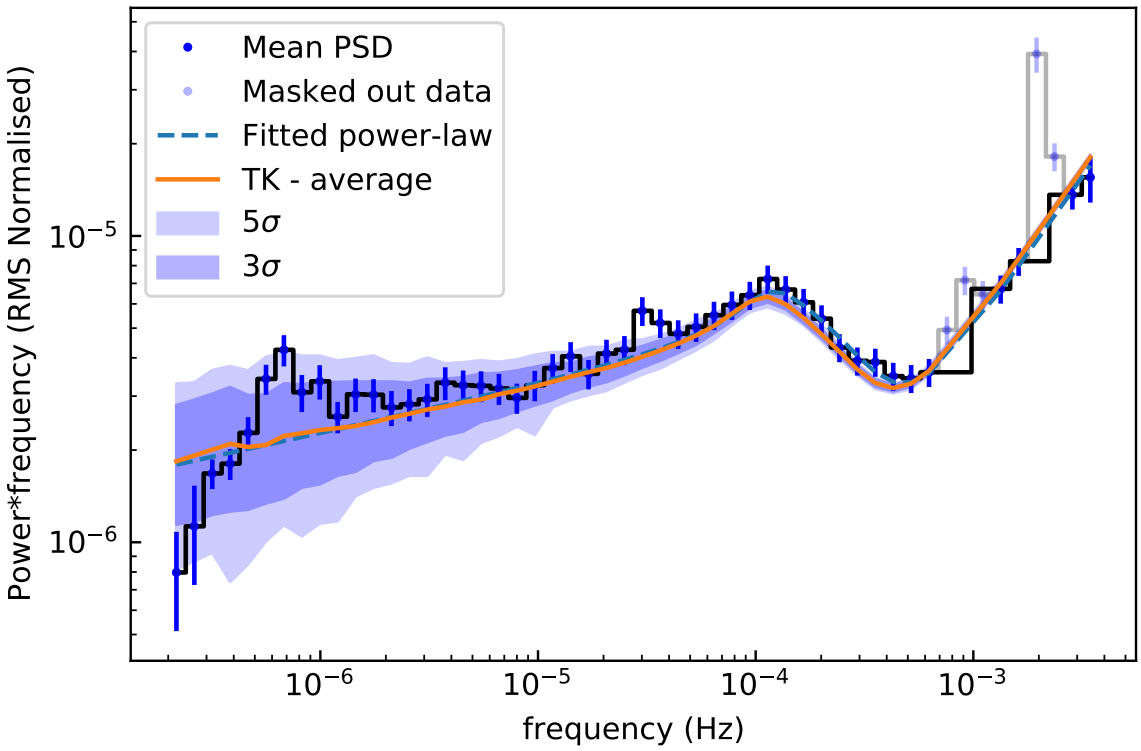

Figure 3.4: Time-averaged PSD of J1908 with the fitted power law without a low frequency break at $\sim 7{\times}10^{-7}$ Hz. The 93.32% and 99.977% significance levels of the PSD are determined from the Timmer & König (1995) simulation of light curve from an underlying power law. This is showing the significance of the lower frequency break and that the average simulated time-averaged PSD (orange) does not show any break from the binning of the data.

performed an identical analysis to what has been done for J19080 (see Appendix A.1) I am left to conclude that the low-frequency break described in Section 3.4 is intrinsic to the target.

3.3.4 Analytical model

The most common explanation for flickering is related to propagating local fluctuations in the accretion rate through the accretion disc on viscous time scales (Lyubarskii, 1997; Ingram & Done, 2011a, 2012; Ingram & van der Klis, 2013). In this scenario the variability is caused by local perturbations to the viscosity parameter α and/or $\frac{H}{R}$ as defined within the standard accretion disc model (Shakura & Sunyaev, 1973). The viscosity perturbations are hence translated into local perturbations in the accretion rate. A change in accretion rate changes the variability of the light curve, such that the affected timescale is governed by where the driving change is occurring. This means that an initial perturbation of the viscosity at the outer disc edge initiates a slow mass transfer rate variability. As this propagates inwards, again on the local viscous timescale, the initial perturbation couples with other perturbations generated further in the disc.

I implement this model using the prescription of Ingram & van der Klis (2013). This divides the disc into N rings which are logarithmically spaced between the inner and outer disc edges, such that the $\frac{dr_n}{r_n}$ quantity remains constant, with r_n representing radius from the centre of the compact object to the middle of N^{th} annulus and dr_n its width. This assumption enforces the linear rms-flux relation (Uttley & McHardy, 2001; Uttley et al., 2005; Scaringi et al., 2015) and ensures the model adheres to observations of the linear rms-flux relation in accreting systems. Within Ingram & van der Klis (2013) and Scaringi (2014) the intrinsic variability of each annulus is modelled as a zero-centred Lorentzian peaking at the viscous frequency associated with a specific disc radius:

$$\left|A_n(\nu)\right|^2 = \frac{\sigma^2}{T\pi}\frac{\Delta\nu_n}{(\Delta\nu_n)^2+\nu^2} \tag{3.3.4}$$

where $\Delta\nu_n$ is the viscous frequency at r_n so that $\nu_{visc}(r_n) = \alpha\left(\frac{h}{r_n}\right)^2\nu_{dyn}(r_n)$, σ^2 is the variance of the light curve of the annulus and T the corresponding duration of the light curve. This equation generates the intrinsic PSD of each annulus within the disc. The overall PSD is then a series of nested convolutions of these individual Lorentzians moving from the outside inwards.

Accretion rate fluctuations are converted to luminosity fluctuations via the emissivity $\epsilon(r_n)$. The emissivity profile is governed by the emissivity index γ and boundary condition $b(r_n)$, such that $\epsilon(r_n) \propto r_n^{-\gamma} b(r_n)$. For a flow extending all the way to the white dwarf surface a stressed $b = 1$ boundary condition as adopted in Scaringi (2014) is a reasonable assumption. In contrast, black hole and stress-free conditions are used in Ingram & van der Klis (2013) where $b(r_n) = 3\left(1 - \sqrt{\frac{r_n}{r}}\right)$.

In Ingram & Done (2011a) the model was applied to XRBs where the $\alpha \left(\frac{H}{R}\right)^2$ parameter is treated as a power-law. Scaringi (2014) adapted the model for white dwarfs by simplifying the treatment of $\alpha \left(\frac{H}{R}\right)^2$ as a constant through the disc, effectively assuming a single flow responsible for the variability. This was a reasonable assumption within the data considered as it was used to only fit to the highest frequency break corresponding to an inner geometrically thick and optically thin flow extending all the way to the white dwarf surface.

Here I further adapt the fluctuating disc model to include multiple disc components in an attempt to reproduce the overall PSD shape observed in J1908. As opposed to Scaringi (2014) where $\alpha \left(\frac{H}{R}\right)^2$ was assumed constant throughout the entire accretion flow, I define two flows each with independent values of $\alpha \left(\frac{H}{R}\right)^2$. In reality $\alpha \left(\frac{H}{R}\right)^2$ may be smoothly varying throughout the disc, but I here only consider two discrete flows for simplicity and in order to search for the best-fit parameters in a reasonable computational time. In fitting the PSD I also include a high frequency white noise component as done in Section 3.3.2.

I point out that it is not clear which of the two boundary conditions (stressed or stress-free) may be more appropriate for modelling the observed J1908 PSD. If there are no higher frequency breaks beyond $\sim 10^{-4}$ Hz, then a stressed boundary condition may be more appropriate, as the highest frequency component traces the accretion flow all the way up to the white dwarf surface. If on the other hand there exists a higher frequency break beyond $\sim 10^{-4}$ Hz (as observed in several other accreting white dwarfs, e.g. Scaringi et al., 2013), then I should either include additional stressed inner flow, or place a different boundary condition on the model using two flows. The boundary condition in this case would have be defined as a "mildly" stressed boundary condition as it would have to encapsulate the Keplerian rotational velocity at the transition between the innermost flow and that generating the peak in power at $\sim 10^{-4}$ Hz. I adopt the simplistic approach of a stressed boundary condition, but are aware of the limitations of this approach.

Scaringi (2014) applied this model to infer a geometrically thick and optically thin disc, possibly related to an advection-dominated accretion flows (ADAF, Narayan & Yi, 1994,

Table 3.1: Free parameters of the analytical model of propagating accretion rate fluctuations with 2 distinct accretion flows defined by different constant values of $\alpha\left(\frac{H}{R}\right)^2$.

Free parameters	description
r_{in}	inner disc edge
r_{tr}	transition radius between the flows
r_{out}	outer disc edge
γ	emissivity index
$(\alpha\left(\frac{H}{R}\right)^2)_{in}$	inner flow viscosity and scale height
$(\alpha\left(\frac{H}{R}\right)^2)_{out}$	outer flow viscosity and scale height
$F_{var,in}$	fractional variability of the inner flow generated per decade
$F_{var,out}$	fractional variability of the outer flow generated per decade
D	Damping parameter of the optically thick flow

1995a,b). Here I additionally consider the effects of fluctuations being damped as they propagate through the flow (Churazov et al., 2001). This is particularly important as the PSD may originate from a geometrically thin and optically thick disc which would be more prone to damping than a geometrically thick disc.

Towards the outermost edges of the disc the effect of damping would be small as fluctuations have not travelled inwards enough to be substantially damped. However, this may not necessarily be the case further in the disc. I verify the potential effects of damping on the model by implementing the damping prescription described by Rapisarda et al. (2017). The effect of damping is described by the Green function which damps out fluctuations intrinsic to the disc as they propagate. The change in power is described by the Fourier transform of the Green function:

$$G\left(r_n, r_l, \nu\right) = e^{-D\Delta t_{ln}\nu} e^{-i2\pi\Delta t_{ln}\nu} \tag{3.3.5}$$

where Δt_{ln} describes the time to propagate a fluctuation between the disc radii r_l and r_n and D is the damping factor prescribing the amplitude of damping.

To illustrate the overall effects of damping I compare the damped and an non-damped model for a mock system of J1908 in Figure 3.5. The models evaluated in Figure 3.5 are computed assuming two accretion flows. The inner flow is assumed to have $\alpha\left(\frac{H}{R}\right)^2 = 1 \times 10^{-3}$ and radially extends between $0.01R_{\odot}$ and $0.03R_{\odot}$. The outer flow is assumed to have $\alpha\left(\frac{H}{R}\right)^2 = 4 \times 10^{-5}$ between $0.03R_{\odot}$ and $0.1R_{\odot}$. To show the effect of damping on both flows I vary the damping factor D in Equation 3.3.5 between 0 (no damping) and 50. The highest damping factor used here is for illustrative purposes only and is not related to a specific physical

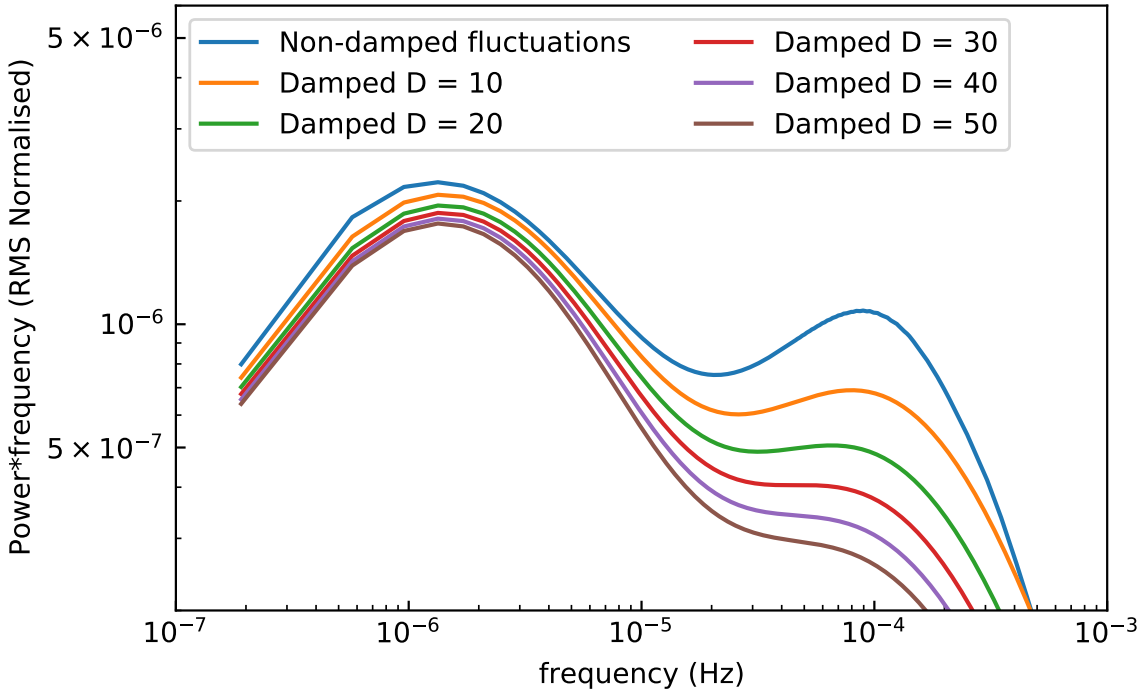

Figure 3.5: A comparison of damped and a non-damped analytical propagating fluctuations model for a 2 accretion flows between $0.01R_{\odot}$ and $0.1R_{\odot}$ with transition at $0.03R_{\odot}$. THe flows are characterised by $\alpha\left(\frac{H}{R}\right)^2 = 4 \times 10^{-5}$ in the outer flow and $\alpha\left(\frac{H}{R}\right)^2 = 1 \times 10^{-3}$ in the inner flow. A central white dwarf accretor of the same mass as J1908 $M_{WD} = 0.8M_{\odot}$ is assumed. The damping factor D varies between 0 and 50.

limitation. Figure 3.5 demonstrates how the effects of damping are close to negligible for the outer flow, but become substantial for the inner flow as expected. Specifically, damping causes the higher frequency break to appear shifted to lower frequencies as more high frequency modulations are damped. In this implementation of the model I only include damping for the inner flow, and leave the damping parameter as free during the fit. Conversely I fix the damping parameter to $D = 0$ for the outer flow.

Overall Table 3.1 shows a list of all free parameters in my implementation. The size of the inner flow associated with the high frequency component has been left as a free parameter. This allows us to investigate whether the model prefers this component to reach the white dwarf surface and thus support the stressed boundary condition assumption used, but note the limitations induced by the damping factor. In this implementation I fix the white dwarf mass and radius to $M_{WD} = 0.8 M_{\odot}$ as reported in Fontaine et al. (2011) and Kupfer et al. (2015). The corresponding white dwarf radius from the mass-radius relation (Nauenberg, 1972a) then yields $R_{WD} = 0.01 R_{\odot}$.

3.4 Results

In this section the results of the empirical fit are presented and discussed as well as those from the analytical two-flow propagating accretion rate fluctuations model.

3.4.1 Empirical fit

The best fit obtained with the model described in Section 3.3.2 is shown in Figure 3.6. I obtain a reduced $\chi^2_{\nu} = 0.6$. My obtained best fit values are shown in Table 3.2. The best fit is achieved through a Levenberg-Marquardt least-square method as implemented in `SciPy`. As the determined fit is acceptable no other fitting methods are pursued. The relatively low χ^2_{ν} of the fit may suggest an over-parameterization of the empirical model. Nonetheless, the frequency breaks of interest appear to be well constrained.

3.4.2 Analytical 2 flow model

The best fit of the model described in Section 3.3.4 is obtained using the same Levenberg-Marquardt least-square method as used in Section 3.4.1. For this I obtain a $\chi^2_{\nu} = 1.5$, with the resulting model shown in Figure 3.7. My best fit values are quoted in Table 3.3. I point

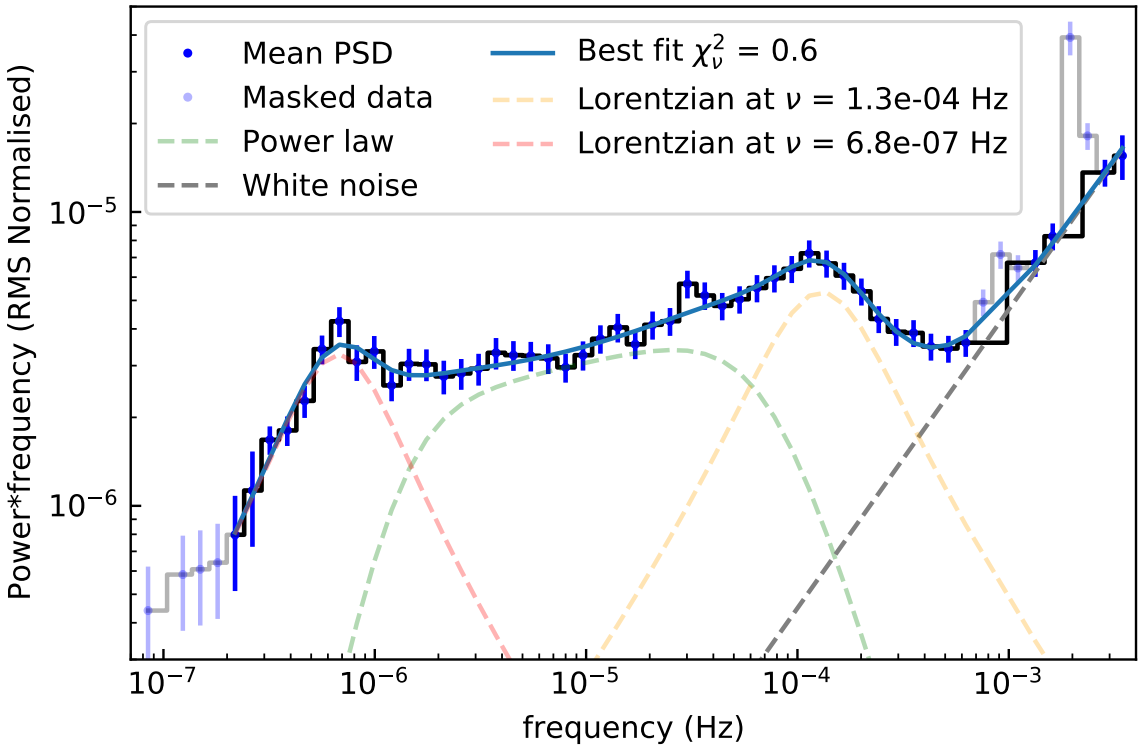

Figure 3.6: Empirical fit of the time-averaged PSD of J1908 showing the separate components with the 2 distinctive broad band breaks at $\nu_{break,1} = 1.3 \pm 0.4 \times 10^{-4}$ Hz and $\nu_{break,2} = 7 \pm 2 \times 10^{-7}$ Hz.

Table 3.2: Free parameters of the empirical fit of the time-averaged PSD of J1908 as described in section 3.3.2. The the best fit value of the parameters for the power law are A, power law amplitude, a_{1-3}, bending power law indexes when going from low to high frequency, and ν_{1-2}, bending power law frequencies at which the power law transitions between the different indexes. For the Lorentzian components: r_{1-2}, integrated fractional rms power of the Lorentzian components of the fit, $\Delta\nu_{1-2}$, HWHM of the Lorentzians and $\nu_{0,1-2}$, central frequency of the Lorentzians. For the white noise component: β, white noise power law index and P_0, white noise normalisation.

Component	Parameter	Best fit value
Power law	A	2 ± 5
	a_1	-0.2 ± 0.2
	a_2	-3 ± 3
	a_3	0 ± 5
	ν_1	$1.3 \pm 0.6 \times 10^{-6}$ Hz
	ν_2	$7 \pm 7 \times 10^{-5}$ Hz
High ν Lorentzian	r_1	4 ± 1
	$\Delta\nu_1$	$9 \pm 1 \times 10^{-5}$ Hz
	$\nu_{0,1}$	$9 \pm 3 \times 10^{-5}$ Hz
Low ν Lorentzian	r_2	$2.7 \pm 0.4 \times 10^{-3}$
	$\Delta\nu_2$	$4 \pm 1 \times 10^{-7}$ Hz
	$\nu_{0,2}$	$5.2 \pm 0.5 \times 10^{-7}$ Hz
White noise	β	0.0 ± 0.1
	P_0	$5 \pm 4 \times 10^{-3}$

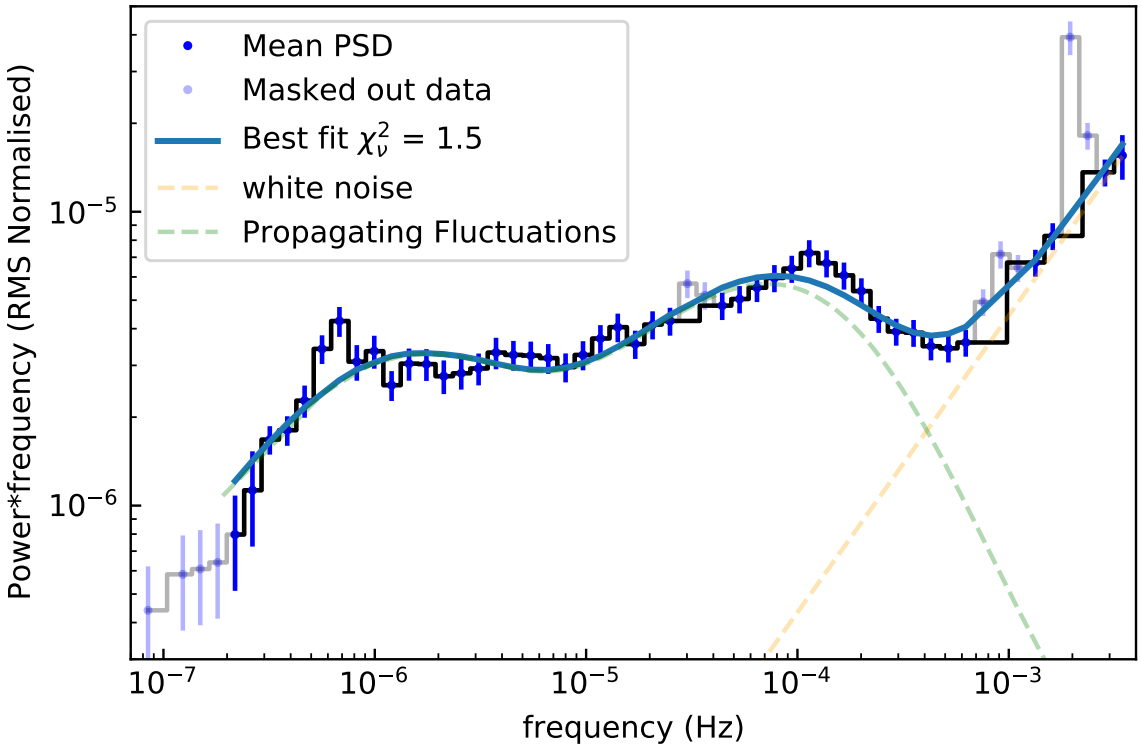

Figure 3.7: Propagating fluctuations analytical model fit to the time-averaged PSD of J1908 with 2 discrete accretion flows from $0.01R_\odot \sim R_{WD}$ to $0.03R_\odot$ and a characteristic $\alpha \left(\frac{H}{R}\right)^2 \sim 7 \times 10^{-3}$ and an outer flow from $0.03R_\odot$ to $0.1R_\odot$ and a characteristic $\alpha \left(\frac{H}{R}\right)^2 \sim 4 \times 10^{-4}$.

out that the white noise component was fixed to that determined in the empirical Lorentzian fit from Table 3.2 in order to reduce the number of free parameters.

The parameter uncertainties quoted in Table 3.3 are determined from a 2 dimensional grid search around the best fit value. Due to the large computational cost of the model implementation, and the large number of free parameters involved, it is not practically possible for us to preform a grid search across the full 9-dimensional parameter space. Using a Markov chain Monte Carlo method to obtain the errors also proved to be computationally expensive and unfeasible within a reasonable time constraint.

I thus assume that the best fit yielding a reduced $\chi^2_\nu = 1.5$ corresponds to the global minimum. Figure 3.8 shows a corner plot where each subplot displays the confidence contours of 2 parameters in the fit, while keeping all other parameters fixed at their best fit value. The errors quoted in Table 3.3 correspond to the 99% confidence level determined via the contours in Figure 3.8. I note that this methodology only provides lower limits on the true parameter errors.

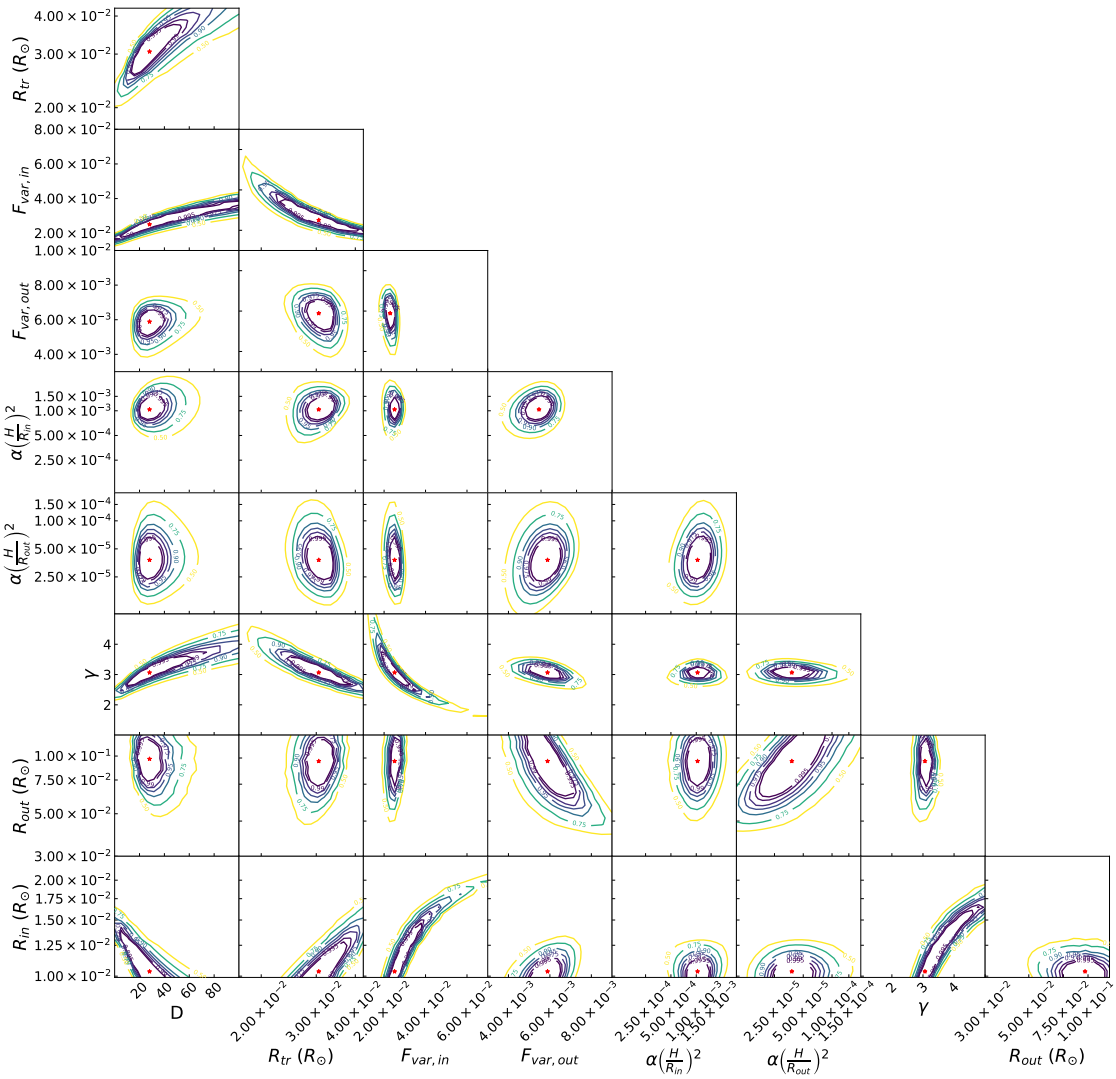

Figure 3.8: Corner plot showing the best fit values of the analytical model as recovered by least-square method in Table 3.3, denoted by the red stars. Each subplot shows the 99.5%, 99%, 97.5%, 95%, 90%, 75% and 50% confidence contours for the corresponding 2 varied parameters, with all other parameters being held fixed at the values from Table 3.3.

Table 3.3: Best fit values of the free parameters of the analytical model of propagating accretion rate fluctuations with 2 distinct accretion flows defined by different constant values of $\alpha\left(\frac{H}{R}\right)^2$ as described in Table 3.1.

Parameter	Best fit value
$log\,(R_{in})$	$-1.99^{+0.2}_{-0.02}\ log\,(R_{\odot})$
$log\,(R_{tr})$	$-1.5^{+0.1}_{-0.1}\ log\,(R_{\odot})$
$log\,(R_{out})$	$-1.0^{+0.1}_{-0.2}\ log\,(R_{\odot})$
γ	$3.1^{+1.7}_{-0.4}$
$log\left(\left(\alpha\left(\frac{H}{R}\right)^2\right)_{in}\right)$	$-3.0^{+0.2}_{-0.1}$
$log\left(\left(\alpha\left(\frac{H}{R}\right)^2\right)_{out}\right)$	$-4.4^{+0.4}_{-0.3}$
$log\,(F_{var,in})$	$-1.6^{+0.2}_{-0.2}$
$log\,(F_{var,out})$	$-2.23^{+0.09}_{-0.08}$
D	30^{+70}_{-30}

3.5 Discussion

The characteristic frequencies in the PSD are governed by the $\alpha\left(\frac{H}{R}\right)^2$ parameter within the propagating fluctuations model. Whereas the viscosity parameter α cannot be separated directly, the $\alpha\left(\frac{H}{R}\right)^2$ parameter provides an indication on the disc radial extent. If I assume that the empirical fit frequencies tabulated in Table 3.2 are associated with the viscous frequency at a specific disc radius I can then place constraints on $\alpha\left(\frac{H}{R}\right)^2$ through rearranging Equation 1.1.10 and setting the viscous frequency to be equal to the break frequency:

$$R = \left(\alpha\left(\frac{H}{R}\right)^2 \frac{GM}{\nu_{break}^2}\right)^{\frac{1}{3}} \tag{3.5.1}$$

Figure 3.9 shows the resulting constraints using the 2 frequency breaks measured in Section 3.4.1. The disc radius is further constrained in J1908 to be between the white dwarf radius (purple dashed line) and the absolute upper limit of the outer disc edge at the L1 point (red dashed line). A further constraint can be considered if I assume the disc to not extend beyond the tidal radius (Warner, 2003). This is the radius at which the disc starts to be distorted by the tidal interactions with the secondary and is given by $R_{tidal} = a\frac{0.6}{1+q}$ where a denotes the radius to the L1 point and q the ratio of the objects masses for $0.03 < q < 1$. Whereas the tidal radius does not represent a hard limit on the outer disc edge, the disc can extend beyond the R_{tidal} temporarily and hence acts as a soft limit. I show this in Figure 3.9 with the blue dashed line. I also include the disc circularisation radius for reference with the green

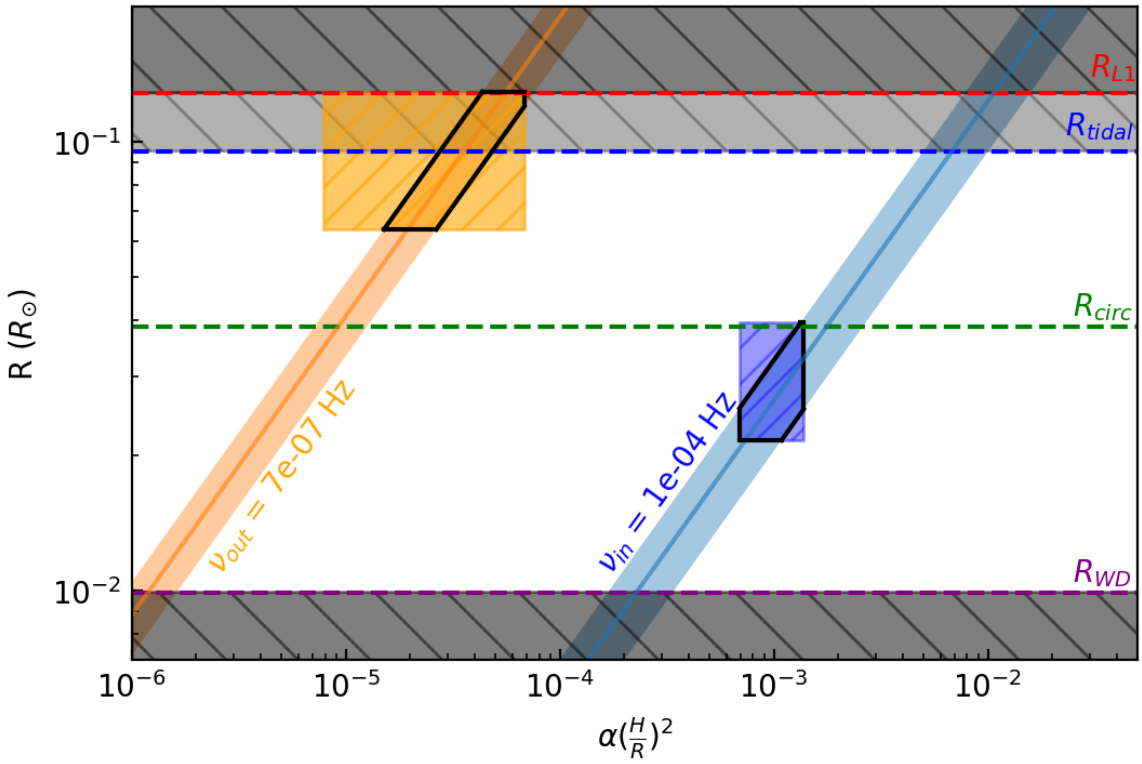

Figure 3.9: A comparison of disc radii as a function of $\alpha\left(\frac{H}{R}\right)^2$ for the PSD breaks listed in Table 3.2 which are assumed to be viscous in nature. Dashed lines represent the white dwarf radius, circularisation radius, tidal radius and the L1 point. The dark shaded region denotes a space, where it is physically impossible for the disc to extend to. The lighter grey shaded region signifies a region between the tidal radius and the L1 point where the disc can temporarily extend to. The hatched orange and blue areas denote the ranges of best fit values for the analytical model with 99% significance. The regions with black borders show a cross-section of possible values where the empirical fit and analytical model agree.

dashed line.

The low frequency break at $\nu \sim 6.8 \times 10^{-7}$ Hz (orange line and shaded region) shows how the outer disc edge may be constrained to have $\alpha \left(\frac{H}{R}\right)^2 < 3 \times 10^{-5}$ as it must reside within the tidal radius. Similarly, the higher frequency break at $\nu \sim 1.3 \times 10^{-4}$ Hz must be produced at radii larger than the white dwarf surface. This then constrains $\alpha \left(\frac{H}{R}\right)^2 \geq 2 \times 10^{-4}$. I point out that a dynamical interpretation of both breaks is ruled out, as these would place the equivalent disc radii at > 600 times the distance to the L1 point for the low frequency break and at ~ 20 times the distance to the L1 point for the higher frequency break.

The resulting ranges of $\alpha \left(\frac{H}{R}\right)^2$ for both frequency breaks may suggest that a geometrically thin flow is responsible for the observed variability in J1908. The upper limit placed on the higher frequency break of $\alpha \left(\frac{H}{R}\right)^2 \sim 5 \times 10^{-3}$ is 2 orders of magnitude smaller than that inferred for the geometrically thick, optically thin, flow responsible for the high frequency break observed in the nova-like MV Lyrae Scaringi (2014).

The inferred values of $\alpha \left(\frac{H}{R}\right)^2$ obtained from the analytical fit presented in Section 3.4.2 are consistent with the constraints of the empirical fit. For the outer flow the obtained constraints on $\alpha \left(\frac{H}{R}\right)^2$ and R_{out} are shown in Figure 3.9 by the hatched orange region. The overlap between the constraints obtained from both the empirical and analytical fits are marked by the solid black border. Similarly, the constraints for the inner flow obtained from the analytical fit are also consistent with the corresponding values from the empirical fit. The blue hatched region in Figure 3.9 denotes the area constrained by the analytical model values of $\alpha \left(\frac{H}{R}\right)^2$ and the transition radius. Similarly to the outer flow and low frequency break there is a range of $\alpha \left(\frac{H}{R}\right)^2$ and radii that are consistent with both methods shown by the black solid borders.

3.5.1 Disc geometry

I can attempt to interpret the geometry of the disc by considering the fitted parameters of the fluctuating accretion disk model presented in Section 3.4.2 at face value. The outer flow associated with the break at $\nu \sim 6.8 \times 10^{-7}$ Hz would then correspond to the edge of geometrically thin disc. The model parameters then place the radial extent of this disc component to be from R_{tr} up to R_{out}. Similarly the characteristic feature at 1.3×10^{-4} Hz is related to a flow extending from the white dwarf surface R_{in} to the inner edge of the outer flow R_{tr}.

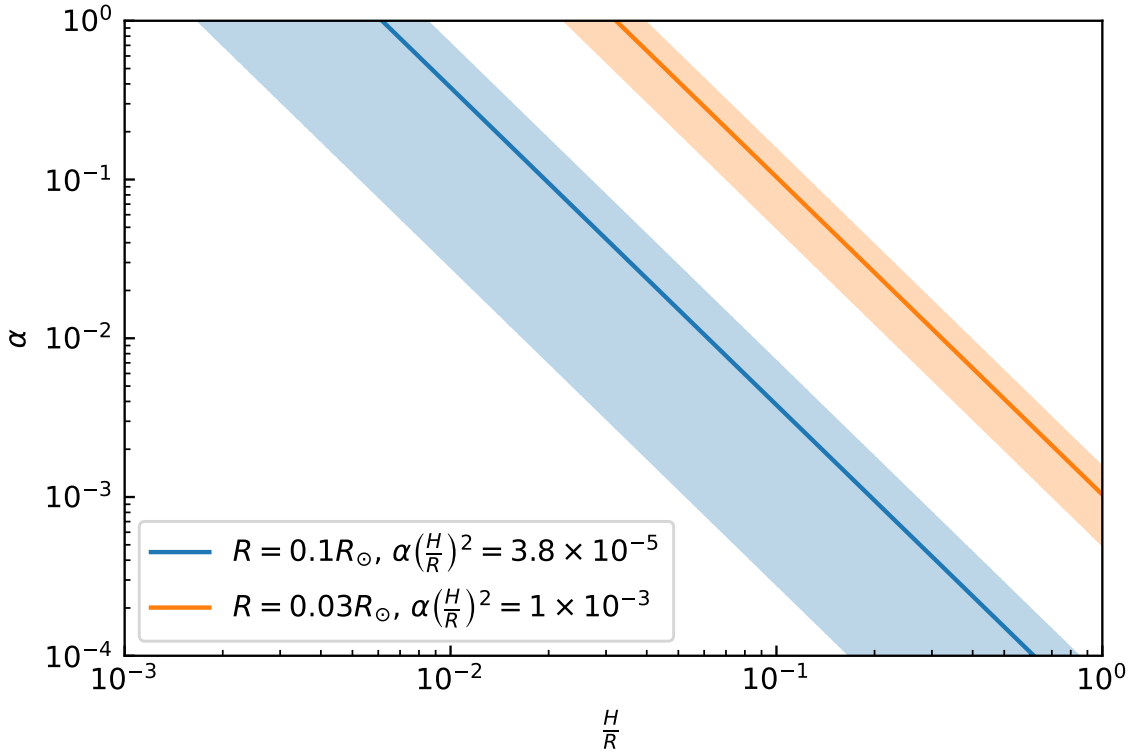

Figure 3.10: Parameter space of the $\alpha\left(\frac{H}{R}\right)^2$ parameter decomposing the α viscosity prescription and the $\frac{H}{R}$ scale height for both flows in the best fit of the analytical propagation fluctuations model as listed in Table 3.3. The radii used are the outer radii of the respective flows. Outer flow is shown in blue (lower) and inner flow in orange (upper).

As inner disc edge has not been fixed it is interesting to note that the model allows this parameter to extend all the way to the white dwarf surface. This may be an indication AM CVn systems do not have inner hot and geometrically extended flow as that inferred in the CV MV Lyr by (Scaringi, 2014). Sandwich disc models where a geometrically thin flow exists within a geometrically thick one, have never been unambiguously confirmed, but Dobrotka et al. (2017) have shown that they are consistent with the data in high state nova-like system MV Lyrae. Another quite likely possibility is that any hot inner flow is either too small to be detected or is located in the region of the PSD that is strongly dominated by the white noise ($\leq 10^{-3}$ Hz).

In Figure 3.10 I show the constraints on α and $\frac{H}{R}$ independently for the two flows based on the analytical model fit. The viscosity α is limited to unity and is expected to be ~ 0.1 from MHD simulations (King et al., 2007; Penna et al., 2013; Yuan & Narayan, 2014; Coleman et al., 2018). With this assumption the best model fit infers a disc scale height between $\sim 5 \times 10^{-3}$ and $\sim 3 \times 10^{-2}$ for the outer flow and $\sim 10^{-1}$ for the inner flow making the disc geometrically thicker closer to the central white dwarf.

3.5.2 Limitations of the analytical model

The conclusions drawn on viscosity and disc scale height are subject to multiple assumptions. One of them is that the value of viscosity α is constant for the two separate flows. Further assumptions also follow from the model where a large part of the disc has a constant value of $\alpha\left(\frac{H}{R}\right)^2$. Thus it may be that the discrete difference in scale height and/or viscosity between the two flows is representative of a continuous variation instead. In any case it appears that the $\alpha\left(\frac{H}{R}\right)^2$ combination drops at larger disc radii.

As mentioned in Section 3.1 there can be two different implementations of τ_{dyn}, and these would result in a factor 2π in the inferred $\alpha\left(\frac{H}{R}\right)^2$ values for both flows. I have tested for the differences in the best fit model in these two cases. As expected the results presented in Figure 3.9 including the factor of 2π yields higher values of $\alpha\left(\frac{H}{R}\right)^2$ by the same amount. Importantly however, this has no effect on R_{in}, R_{tr} and R_{out} as they remain unaffected.

One further specific assumption of the model is the stressed boundary condition set at the inner disc edge, which in turn requires a hard surface at the innermost disc ring of the inner flow. Further limitations may also be related to the discretisation of two independent flows to characterise the low and high frequency breaks. This would affect not only the $\alpha\left(\frac{H}{R}\right)^2$ parameter estimation, but would also affect the damping prescription and disc emissivity profile inferred. Lastly it may be the case that the observed variability is related to an entirely different process and not associated with the accretion disk. Although I feel this to be unlikely, the source of flickering may be related to the mass transfer rate variations driven by the donor star alone. However, it is difficult to envisage how this would then relate to other previous studies of aperiodic variability which can be best explained by viscous fluctuations propagating through the disc (Uttley & McHardy, 2001; Arévalo & Uttley, 2006a; Scaringi et al., 2012a).

3.6 Conclusion

I present the first detection of a low frequency break in the PSD of an accreting white dwarf of the AM CVn type. I tentatively associate this break with the variability generated by the outer disc regions of a geometrically thin disc. Whereas the study of flickering in compact objects has yielded many results on the structure of the inner accretion region (Done et al., 2007; Buisson et al., 2019; Scaringi, 2014; Balman & Revnivtsev, 2012; Balman, 2019) the outer disc has remained elusive due to the associated long timescales of variability.

The compactness of AM CVn systems provide the ideal configuration where the outer disk regions may produce variability driven by viscous processes that are detectable by current high-cadence, high -precision, photometric surveys. I have used short cadence *Kepler* data of the AM CVn J1908 (Fontaine et al., 2011) to search for a low frequency break. To do this I have constructed a time-averaged PSD with a 11×60 day long segments to uncover two broad-band structures in the PSD.

I characterise the obtained PSD of J1908 through an empirical fit to obtain the characteristic frequency of each of the two components to be $\sim 6.8 \times 10^{-7}$ Hz and $\sim 1.3 \times 10^{-4}$ Hz. I verify the high level of detection significance of the low frequency component through simulations. My result suggests that similar searches for low-frequency variability components in other AM CVn-type systems may also reveal low frequency PSD breaks.

I have further attempted to adapt the analytical propagating fluctuations model based on Lyubarskii (1997) and Arévalo & Uttley (2006a) to fit the PSD by assuming the two observed PSD components originate from two distinct flows. In this case I infer different values of $\alpha \left(\frac{H}{R}\right)^2$ for each flow. I compared this to the $\alpha \left(\frac{H}{R}\right)^2$ values inferred by simply associating the characteristic break frequencies to the viscous frequency via $\nu_{visc} = \alpha \left(\frac{H}{R}\right)^2 \nu_{dyn}$. I find both methods to be consistent.

The characteristic frequency associated with the detection of the low frequency break in J1908 appears to be associated with the outermost regions of the disc. It is also clear that a consistent and comprehensive model to explain this specific feature, and the broad-band PSD overall, remains non-trivial. Future simulations of entire accretion discs that rely on MHD may provide further insight into the origin of low frequency breaks (e.g. Coleman et al. (2018)).

Chapter 4

Discovery of Persistent Quasi-Periodic Oscillations in Accreting White Dwarfs: A New Link to X-ray Binaries

Abstract

Almost all accreting black hole and neutron star XRBs exhibit prominent brightness variations on a few characteristic time-scales and their harmonics. These QPOs are thought to be associated with the precession of a warped accretion disc, but the physical mechanism that generates the precessing warp remains uncertain. Relativistic frame dragging (Lense-Thirring precession) is one promising candidate, but a misaligned magnetic field is an alternative, especially for neutron star XRBs. Here, I report the discovery of 5 AWDs that display strong optical QPOs with characteristic frequencies and harmonic structures that suggest they are the counterpart of the QPOs seen in XRBs. Since AWDs are firmly in the classical (non-relativistic) regime, Lense-Thirring precession cannot account for these QPOs. By contrast, a weak magnetic field associated with the white dwarf can drive disc warping and precession in these systems, similar to what has been proposed for neutron star XRBs. The observations confirm that magnetically driven warping is a viable mechanism for generating QPOs in disc-accreting astrophysical systems, certainly in AWDs and possibly also in (neutron star) XRBs. Additionally, they establish a new way to estimate magnetic field strengths, even in relatively weak-field systems where other methods are not available.

Co-author contribution

I have conducted the analysis as described in this Chapter and reported in Veresvarska et al. (2024b) under the supervision of Dr Simone Scaringi. Other co-authors have contributed with suggestions on analysis improvement and comments on the text of the paper. Dr John A. Paice has made the diagram shown in Figure 4.5.

4.1 Introduction

AWDs are binary systems in which a WD accretes material from a donor star. The properties of the most dominant population of AWDs - CVs, are described and reviewed in detail in Section 1.3. The effects of the intrinsic magnetic field of the WD accretor on the AD geometry are vital for the observable properties of the system. The accretor spin and its observational properties are summarised in Section 1.3.1.

QPOs are non-coherent brightness variations in the X-ray flux, widely recognised in XRBs, with their more detailed background being discussed in Section 1.5.2 and 1.5.2. There have been numerous QPOs reported in AWD systems in the literature (see e.g. Warner 2004 for review). The QPOs in the context of AWDs, as opposed to XRBs, usually refer to a transitional and temporary periodic signal in the optical whose amplitude can vary significantly. The first report of a QPO in an AWD was in Patterson et al. (1977), where a fast (∼50s) oscillation in the light curve was detected in the outburst of RU Peg.

Another type of quasi-periodic signals in AWDs are so-called dwarf novae oscillations (DNOs) (Warner & Robinson, 1972), which appear to display a somewhat more coherent period than QPOs in XRBs. One possible explanation is that these are associated with g-mode pulsations of the WD (Warner & van Zyl, 1998; Woudt et al., 2005; Townsley & Bildsten, 2004; Townsley et al., 2016). The DNO periods are usually quite fast (∼10 s) and follow a relation to the longer QPOs so that $P_{QPO} \approx 16 \times P_{DNO}$. In Warner et al. (2003), a further sub-type of DNOs (P_{DNO} ∼20s), the long period DNOs (lpDNOs with P_{lpDNO} ∼80−100s) are also discussed. These are thought to be empirically related to DNOs and QPOs such that $P_{lpDNO} \approx P_{DNO} \approx \frac{1}{4} P_{QPO}$ and are usually associated with high mass transfer rate systems and are sometimes detected as doubles.

Other types of QPOs in AWDs have been observed, such as the broad feature in the high state of magnetic AWD TX Col (Littlefield et al., 2021). The QPO in TX Col as observed by *TESS* spans from ∼10 to ∼20 d^{-1} and in width resembles the QPO in AM CVn SDSS J1908+3940 reported by Kupfer et al. (2015). These broad QPOs and their lack of harmonics resemble

a more broad-band feature of the PSD most likely associated with mass transfer variation in the accretion disc (see Scaringi 2014), rather then a quasi-coherent signal as in XRBs. Similarly to Warner et al. (2003), all of these QPOs have been detected in the optical, with no known X-ray counterparts. The study by Warner et al. (2003) extensively reports QPOs in AWD systems, drawing a comparison between the reported QPOs to those observed in XRBs (Wijnands & van der Klis, 1999). WZ Sge, a target in Warner et al. (2003) and also studied in this work, was reported to exhibit short-period DNOs at ∼27.87 s and 28.95 s and a ∼740 s QPO. While the 27.87 s signal has been linked to the spin of WZ Sge (Patterson, 1980), the QPO is attributed to the retrograde precession of a geometrically thick disc (Warner & Woudt, 2002). However, the absence of a ∼740 s QPO signal in WZ Sge from *TESS* short cadence data and other objects displaying QPOs in Warner et al. (2003) suggests these signals are transitional. It is also important to note that the reported correlation between AWDs and XRBs in Warner et al. (2003) is not based on broad-band features and QPO frequencies, but rather on transitional QPOs and DNOs, which may represent a separate class of signals. Therefore, the presence of these signals in AWDs could be driven by a different physical process than those observed in XRBs. A further important distinction between all of the above reported QPOs in AWDs and XRBs is that, unlike XRBs, there have never been reported harmonics of any kind of QPOs in AWDs.

Here I try to characterise QPOs in AWDs in direct analogy to those in XRBs using self-similar analysis techniques in order to better understand their physical origin. In doing so I report the discovery of 5 AWD systems showing persistent QPOs in optical detected by *TESS* at $\sim 1.3 - 3 \times 10^{-4}$ Hz ($1 - 2$ hours), which I use to revise the relation to XRBs. I also report on the first instance of harmonics being discovered for QPOs in AWDs in 3 of the 5 reported systems. *TESS* has an archival database of ∼1200 AWDs, with even more AWD candidates. After visually inspecting the closest sample of AWDs I recovered the 5 examples reported here. However, it is likely that many more are present in the TESS database and that many more could be uncovered with an instrument with a better signal-to-noise ratio. The observations used are described in Section 4.2. Section 4.3 discusses the methods and analysis used as well as the construction of the time-averaged power spectra (TPS) with a similar methodology to what is conventionally employed in analysis of QPOs in XRBs (Sections 4.3.1 and 4.3.2). I also discuss the statistical significance of the observed broad-band frequency features in the PSD used in the analysis (Section 4.3.3). In Section 4.4 I report that the QPOs and broad-band components of the TPS fit from Section 4.3.2 appear to follow the observational correlation between the QPO frequency and the low frequency

break from Wijnands & van der Klis (1999). In Section 4.5 I introduce a proposed model to explain the observed QPOs, based on magnetically driven precession of the inner accretion flow due to the interaction between a weak accretor magnetic field and its inner accretion flow. I then discuss the implications of these results with conclusions drawn in Section 4.6.

4.2 Observations

The data used in this work were obtained by *TESS* , with the detailed description of the telescope and data processing discussed in Chapter 2. The details of the number of *TESS* sectors available for each object studied here, as well as the chosen cadence, are presented in Table 4.1. The short cadence was used for the objects that had all the available sectors in 20 s cadence (WZ She and GW Lib). If the short 20 s cadence was only available for some of the sectors, 120 s cadence was used for those particular objects (CP Pup, T Pyx, and V3101 Cyg).

I attempt to convert these measurements using quasi-simultaneous ground-based observations from *ASAS-SN*, without accounting for any bolometric correction, as described in Section 2.3. Sufficient coverage was achieved only for CP Pup, as detailed in Veresvarska et al. (2024a). For the remaining targets no conversion is adopted, due to lack of quasi-simultaneous coverage by *TESS* and *ASAS-SN*. Whereas this does not pose a problem for the analysis presented in this Chapter, lack of ground-based calibration prohibits any measurements of the energetics being made. I note that with the advent of more synoptic sky surveys (e.g. BlackGEM Groot et al. 2024) space-based calibrations will be more easily achieved due to wider sky coverage.

There is a linear trend in the data of GW Lib and V3101 Cyg, which has been removed using a similar methodology as in Kupfer et al. (2015). Similar linear trends due to systematic effects have often been found to affect long-term data, especially in the *Kepler* and *K2* mission (Kupfer et al., 2015; Solanki et al., 2021). These trends can alter the flux levels over time and induce low frequency power excess and hence need to be removed. This is done by fitting a linear trend to the light curve smoothed on a 2 hr timescale which is subsequently subtracted from the original light curve. The correction was done for the whole sector for GW Lib and for each half sector for V3101 Cyg by fitting a straight line to the time-averaged light curve and correcting the non-averaged light curve for the obtained trend. The corrected light curve of CP Pup has already been reported in Veresvarska et al. (2024a), while the remaining targets are shown in Figure A.4. WZ Sge shows a greater amplitude of variability

Table 4.1: Summary of the *TESS* data of WZ Sge, CP Pup, GW Lib, T Pyx and V3101 Cyg with sector numbers and dates. The used exposure time of *TESS* sectors is noted for each sector, keeping it constant for each object. The optimal segment length p_0 used for constructing TPSs in 4.3.1 is noted as well as whether the *TESS* data is converted to flux in mJy or kept in *TESS* default $e^{-}s^{-1}$.

Name	TIC	Sector	Dates	t_{exp} (s)	p_0 (d)	Calibration
WZ Sge	86408822	41	20/07/21 - 20/08/21	20	6	–
		54	09/07/22 - 05/08/22	20	6	–
CP Pup	14560527	7	08/01/19 - 01/02/19	120	10	*ASAS-SN*
		8	02/02/19 - 27/02/19	120	10	*ASAS-SN*
		34	14/01/21 - 08/02/21	120	10	*ASAS-SN*
		35	09/02/21 - 06/03/21	120	10	*ASAS-SN*
		61	18/01/23 - 12//02/23	120	10	*ASAS-SN*
GW Lib	225798235	38	29/04/21 - 26/05/21	20	10	–
T Pyx	17897279	35	09/02/21 - 06/03/21	120	7	–
		62	12/02/23 - 10/03/23	120	7	–
V3101 Cyg	1974089138	55	05/08/22 - 01/09/22	120	10	–

akin to an envelope in sector 54. This is also seen in CP Pup (Bruch, 2022; Veresvarska et al., 2024a) and is thought to be an instrumental effect as it is displayed in multiple objects in the same sector, e.g. TIC 1909750039, TIC 1688054795 and TIC 1713691071 in sector 54 all show a similar envelope. This is not corrected for, but the analysis as described in Section 4.3 has been conducted on sectors 41 and 54 separately. Since it has been found that the results are robust to any changes between the 2 sectors, it is assumed that the effect of the envelope on the results is negligible.

For targets with more than 1 sector (WZ Sge and T Pyx) the combination of the different sectors using un-calibrated *TESS* absolute photometry is possible because the combination happens in frequency domain, where separate power spectra are combined after they have been rms normalised. In such a case the relative variability in separate sectors is conserved and does not affect the overall result. As a test I have conducted the same analysis on un-calibrated *TESS* data of CP Pup and found no significant differences.

4.3 Methods and Analysis

To draw an analogy to XRBs and the QPOs they exhibit, I attempt to reproduce their analysis as closely as possible. This involves construction of a Time-averaged Power Spectrum (TPS, as described in detail in Section 4.3.1 and shown in Figure 4.1) instead of inspecting a non-averaged and non-binned PSD (Figure A.5). The details of the broad-band PSD fits are described in Section 4.3.2, where the broad-band components of the TPS are fitted with

zero-centred Lorentzians akin to XRBs. Section 4.3.3 discusses the significance of the lowest frequency broad-band component of the fit from Section 4.3.2.

4.3.1 Broad-band Structure of the Time-averaged Power Spectrum

I here characterise the broad-band variability and QPOs using TPS as is conventionally done when studying XRBs (Belloni et al., 2002; Ingram & Motta, 2019). TPS are usually constructed by separating the light curve into non-overlapping segments of equal length and computing the Fourier transform for each segment. The resulting power spectra are then averaged and re-binned onto a coarser frequency grid to reduce uncertainty. The error on the normalised power in each frequency bin corresponds to the standard error on the mean. In XRBs the nature of X-ray timing requires the use of Fast-Fourier transform (FFT). Here I adopt the Lomb-Scargle (Lomb, 1976; Scargle, 1998) algorithm as the data obtained from *TESS* is not strictly evenly sampled due to gaps in the data from data downlinks and exclusion of some data points due to instrumental effects or other anomalous events. The Lomb-Scargle implementation used is `Astropy` v.5.3.4 with the limiting upper frequency set to the Nyquist frequency based on the sampling in Table 4.1 and the lower frequency set to $3 \times (L)^{-1}$, where L is the length of the light curve. The oversampling factor is set to 1. The resulting power spectrum is normalised so that the total power of the power spectrum corresponds to $\frac{\sigma}{rms^2}$, where σ is the variance of the light curve and rms the root mean square. The resulting TPSs of WZ Sge, CP Pup, GW Lib, T Pyx and V3101 Cyg are shown in Figure 4.1.

In Figure 4.1 the segment length that is used to construct the TPSs is specified for each object in Table 4.1. After testing the robustness of the fit in Section 4.3.2 by varying the segment length, the length with the best visualisation of the PSD features were chosen. A similar method was used to select the number of frequency bins ($N_{bins} = 90$), ensuring that the frequency resolution remains high enough to clearly distinguish QPOs from the broad-band PSD structure. This results in a rebinning factor of 270 for WZ Sge, 45 for T Pyx, 468 for GW Lib, 80 for V3101 Cyg and CP Pup.

The TPSs are also cleaned of the orbital signal, where present. This is not necessary for XRBs as most XRBs have orbital signals on the order of several hours, where the signal does not interfere with QPOs present on timescales of ∼seconds. The power originating from the orbital motion is removed after computing the Lomb-Scargle for each segment. For each segment the peak of the orbital period is identified and ∼25 points on each side of the peak are removed, varying the number as necessary according to the strength and width of the

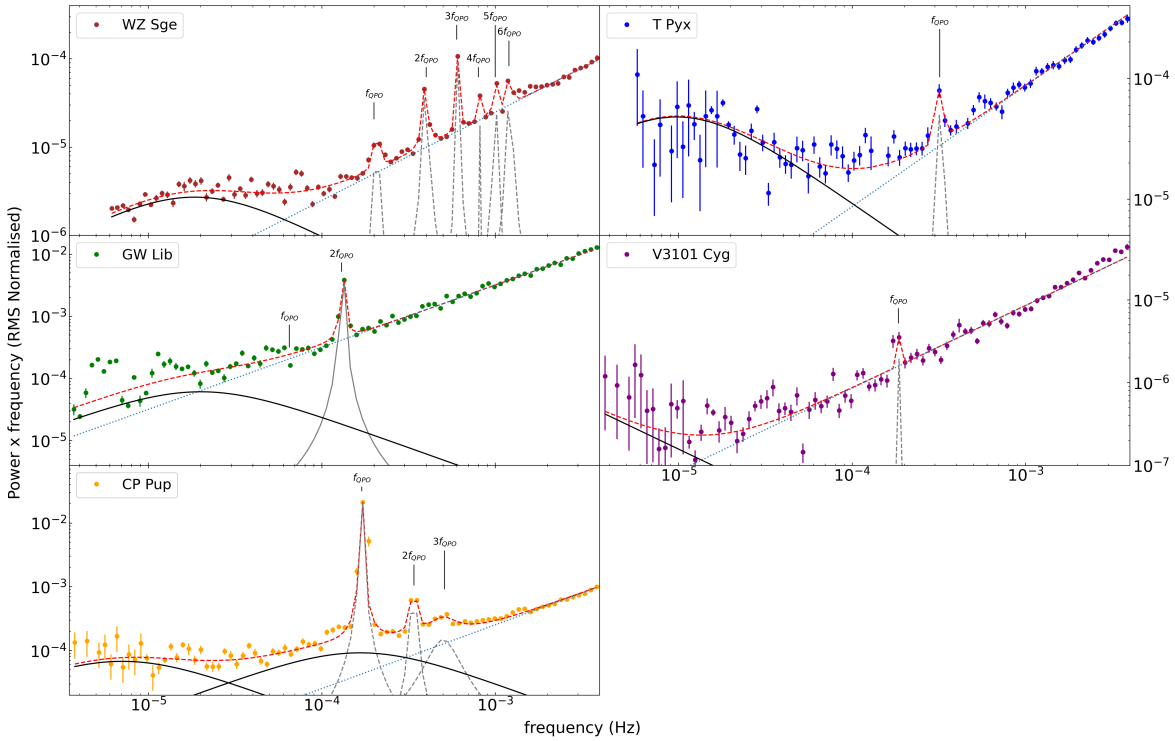

Figure 4.1: TPS of WZ Sge, GW Lib, T Pyx, V3101 Cyg and CP Pup averaged on the segment lengths specified in Table 4.1 with 90 logarithmicaly spaced bins. The empirical fit of the PSD is included here and comprises a Poisson noise power law (dotted line) in the high frequencies, one (in the case of WZ Sge, GW Lib, T Pyx and V3101 Cyg) or two (CP Pup) zero-centred Lorentzians (solid line) representing the broad band PSD structure and Lorentzians representing the QPOs and their harmonics (dashed line).

signal. The same process is then repeated for 10 following harmonics of the orbit, 20 in the case of WZ Sge. The number of removed points was chosen after visual inspection to confirm that this would not remove any variability intrinsic to the QPO or significantly affect the broad-band PSD. This process is chosen over pre-whitening the light curve to avoid any possible changes to the underlying broad band-variability. Figure 4.1 displays the TPSs with the orbital variability already removed for WZ Sge, T Pyx, and V3101 Cyg. The linear PSD with the orbital periods included can be seen in Figure A.5. The process was not necessary for GW Lib due to the low inclination of the system causing the orbital period to be only detectable spectroscopically (Thorstensen et al., 2002). Due to the lack of any periodic signals in the power spectrum of CP Pup and the uncertain nature of its orbital period (Veresvarska et al., 2024a), no orbital period variations were removed.

4.3.2 Time-averaged Power Spectra

The broad-band structure of systems that accrete via an accretion disc can usually be fitted well with a sum of Lorentzian components (Belloni et al., 2002):

$$P_L(\nu) = \frac{r^2\Delta}{\pi}\frac{1}{\Delta^2 + (\nu - \nu_0)^2}, \tag{4.3.1}$$

where $P_L(\nu)$ is the RMS normalised power, Δ the half width half maximum (HWHM) and r a normalisation factor proportional to the integrated fractional rms. ν_0 represents the centroid frequency, which is set to 0 in the case of zero-centred Lorentzians. In the case of non-zero centred Lorentzians, where $\nu_0 > 0$, the frequency of the peak of the PSD feature is given by:

$$\nu_{max} = \sqrt{\nu_0^2 + \Delta^2}. \tag{4.3.2}$$

Therefore the PSDs in Figure 4.1 are fitted with a number of non-zero centred Lorentzians corresponding to the number of quasi-periodic signals and their harmonics, plus one or two zero-centred Lorentzians representing the broad-band structure of the PSD. Two zero-centred Lorentzians were necessary only in the case of CP Pup. This is most likely due to the Poisson noise (see below) contributing mostly at high frequencies and intrinsic broad-band variability becoming dominant at $\sim 10^{-3}$ Hz. This can be seen in Figure 4.1 at the frequency where the Poisson noise component overtakes the zero-centred Lorentzian broad-band component. By contrast, this changeover occurs at $\sim 10^{-4}$ Hz for WZ Sge, GW Lib and V3101 Cyg.

The Poisson noise is another component of the PSD that needs to be considered. It can be represented by a constant, so that $P(\nu) = A$, where A represents the amplitude of the noise.

The PSD is fitted with all the free parameters for each object listed in Table 4.2. The overall PSD model is hence expressed as:

$$P_\nu = \sum_{i=0}^{N_{QPO}} P_L(r_i, \Delta_i, \nu_{0,i}, \nu) + \sum_{j=0}^{N_{L_0}} P_{L_0}(r_j, \Delta_j, \nu) + A. \tag{4.3.3}$$

Here, P_L is a non-zero centred Lorentzian representing the quasi-periodic signals and their harmonics, P_{L_0} corresponds to the zero-centred Lorentzians and A accounts for the Poisson noise.

The best fit parameters with the corresponding errors are shown in Table 4.2. The best fit is determined using the Levenberg-Marquardt least-squares fitting method with keeping all

parameters free. Given the number of free parameters in the fit (e.g. 21 for WZ Sge) it is not feasible to conduct a full parameter sweep to determine the true confidence contours. Instead an assumption that the correlation between individual parameters is not dominant is made. In such a case, a rough estimate of errors can be made by fixing all parameters to the best fit value and varying a single parameter to determine the one dimensional confidence contours of 99.7%. This technique was adapted from QPO fitting procedures in XRBs in cases where no strong correlations between PSD components can be assumed. This is applicable here due to the narrowness of the QPOs and the low number of zero-centred Lorentzians required to fit the individual PSDs. Further complications may however arise from the unevenly spaced data causing the frequency bins to not be strictly independent. Despite this it is important to note that the method cannot provide the exact 99.7% confidence contours, but can serve as a lower limit.

4.3.3 Break Significance

The uncertainty on the low frequency broad-band feature (break) measured in Table 4.2 is difficult to constrain due to several factors. One relates to the logarithmic spacing of the frequency bins resulting in a decrease of the number of points in the lower frequency bins, increasing their error. Therefore it is necessary to verify the presence of any break as opposed to a red-noise related power-law.

To generate light curves that follow a specific power-law pattern, I use an algorithm similar to the one described by Veresvarska & Scaringi (2023), based on the method developed by Timmer & König (1995). Given a PSD model, the algorithm will generate a simulated PSD by scattering the amplitudes and phases around the PSD model. The randomized PSD is then transformed back into the time domain using an inverse Fourier transform, creating a light curve with the desired PSD shape.

In this case, the PSD shape is almost the same as the one outlined in Table 4.2. However, the lowest frequency zero-centred Lorentzian is replaced by a power-law fit, as shown in Figure 4.3, where the power-law is defined by $P_{power-law} = A\nu^{\alpha}$. The Lorentzians corresponding to the QPOs are removed, and the other parameters from Table 4.2 are kept constant. The values for A and α are found using the Levenberg-Marquardt least-square method. The reduced χ^2_ν for the fits are also noted in Table 4.3. It is worth noting that all objects apart from V3101 Cyg have a significantly higher χ^2_ν for the power-law fit than when the zero-centred Lorentzians are used.

Table 4.2: Results of the empirical fit to the PSDs from Figure 4.1. The independent columns correspond to different objects and the rows correspond to model components: A − Poisson noise amplitude, r_i − integrated fractional rms of a given Lorentzian, Δ_i − half width half maximum of a given Lorentzian, $\nu_{0,i}$ − centroid frequency of a given Lorentzian (only Lorentzians representing QPOs and their harmonics have this component). The Q value for each Lorentzian representing a QPO is given as well and is denoted by Q_i. Broad-band component Lorentzians are zero-centred and their $\nu_0 = 0$ by default and is not denoted here. * denotes the lowest frequency zero-centred Lorentzian used in Figure 4.3 and 4.7.

	WZ Sge	CP Pup	GW Lib	T Pyx (s)	V3101 Cyg
A ($\times 10^{-2}$)	$2.5^{+0.2}_{-0.2}$	25^{+2}_{-2}	56^{+5}_{-5}	$8.5^{+0.8}_{-0.8}$	$8.7^{+0.8}_{-0.8}\times 10^{-2}$
r_1 ($\times 10^{-2}$)	$1.0^{+0.3}_{-0.4}$	59^{+10}_{-10}	6^{+4}_{-6}	7^{+3}_{-7}	$1.1^{+0.8}_{-1.1}\times 10^{-1}$
Δ_1 ($\times 10^{-8}$)	4^{+3}_{-3}	70^{+30}_{-30}	2^{+4}_{-2}	$0.7^{+0.9}_{-0.7}$	$0.1^{+0.2}_{-0.1}$
$\nu_{0,1}$ ($\times 10^{-4}$)	$2.07^{+0.05}_{-0.04}$	$1.70^{+0.1}_{-0.05}$	$1.33^{+0.01}_{-0.05}$	3^{+2}_{-2}	$1.8665^{+1}_{-0.0009}$
Q_1	~ 2600	~ 120	~ 3300	~ 21000	~ 93000
r_2 ($\times 10^{-2}$)	$0.21^{+0.05}_{-0.06}$	10^{+2}_{-2}	$1.0^{+0.3}_{-0.4}$	$1.7^{+0.2}_{-0.2}$	$1.9^{+0.8}_{-1.5}$
Δ_2 ($\times 10^{-5}$)	$0.7^{+0.7}_{-0.4}$	$7^{+4}_{-4}\times 10^{-3}$	$1.6^{+2.8}_{-1.2}$ *	$1.0^{+0.3}_{-0.5}$ *	$0.13^{+0.13}_{-0.13}$ *
$\nu_{0,2}$ ($\times 10^{-4}$)	$4.0^{+0.1}_{-0.1}$	$3.4^{+0.1}_{-0.1}$	–	–	–
Q_2	~ 30	~ 2500	–	–	–
r_3 ($\times 10^{-2}$)	$1.1^{+0.3}_{-0.4}$	$1.0^{+0.2}_{-0.3}$	–	–	–
Δ_3 ($\times 10^{-4}$)	$1.4^{+0.7}_{-0.7}\times 10^{-3}$	$1.0^{+2}_{-0.5}$	–	–	–
$\nu_{0,3}$ ($\times 10^{-4}$)	$6.1^{+0.2}_{-0.2}$	$4.9^{+0.6}_{-0.7}$	–	–	–
Q_3	~ 2200	~ 2.5	–	–	–
r_4 ($\times 10^{-2}$)	13^{4}_{-6}	$2.4^{+0.2}_{-0.3}$	–	–	–
Δ_4 ($\times 10^{-4}$)	$1.5^{+1}_{-1}\times 10^{-5}$	1.7^{+8}_{-5}	–	–	–
$\nu_{0,4}$ ($\times 10^{-4}$)	8^{+4}_{-7}	–	–	–	–
Q_4	~ 2.7	–	–	–	–
r_5 ($\times 10^{-2}$)	$1.7^{+0.5}_{-0.8}$	$2.1^{+0.4}_{-0.4}$	–	–	–
Δ_5 ($\times 10^{-7}$)	$1.0^{+0.7}_{-0.7}$	70^{+50}_{-30} *	–	–	–
$\nu_{0,5}$ ($\times 10^{-4}$)	$1.0^{+0.2}_{-0.2}$	–	–	–	–
Q_5	~ 500	–	–	–	–
r_6 ($\times 10^{-2}$)	$1.6^{+0.5}_{-0.7}$	–	–	–	–
Δ_6 ($\times 10^{-7}$)	3^{+2}_{-2}	–	–	–	–
$\nu_{0,6}$ ($\times 10^{-3}$)	$1.22^{+0.03}_{-0.02}$	–	–	–	–
Q_6	~ 200	–	–	–	–
r_7 ($\times 10^{-3}$)	$4.1^{+0.3}_{-0.3}$	–	–	–	–
Δ_7 ($\times 10^{-5}$)	$1.9^{+0.4}_{-0.3}$ *	–	–	–	–
χ^2_ν	6.16	3.41	1.95	1.52	5.26

Table 4.3: Results of the empirical fit to the PSDs from Figure 4.2. The independent columns correspond to different objects and the lines correspond to model components: A − power-law amplitude, α − power-law index.

	WZ Sge	CP Pup	GW Lib	T Pyx (s)	V3101 Cyg
A	$9^{+2}_{-2}\times 10^{-10}$	$2^{+8}_{-2}\times 10^{-8}$	$1\times10^{-4}{}^{+4}_{-1\times10^{-4}}$	$5^{+2}_{-2}\times 10^{-9}$	$1^{+13}_{-1}\times 10^{-13}$
α	$-1.756^{+0.003}_{-0.004}$	$-1.684^{+0.005}_{-0.004}$	$-0.883^{+0.004}_{-0.003}$	$-1.778^{+0.004}_{-0.005}$	$-2.248^{+0.010}_{-0.009}$
χ^2_ν	163	11.6	14.5	5.2	5.00

The parameters from Table 4.2, combined with the best-fit values of A and α, are used to generate artificial light curves. The components involved in this process are listed in Table 4.3. In this context, r_{last} and Δ_{last} refer to the parameters of the lowest frequency zero-centred Lorentzian for a given object in Table 4.2. The errors shown in Table 4.3 are calculated in the same way as those in Table 4.2, as detailed in Section 4.3.2.

The process of generating artificial light curves is repeated 1000 times, resampling the final output on the time stamps of the original *TESS* light curves, reproducing identical PSDs as in Figure 4.1. All the points in each frequency bin are examined and fitted with a χ^2 distribution. The optimal fit of the χ^2 distribution is obtained again with the Levenberg-Marquardt least-square method. The 3σ and 5σ confidence contours corresponding to 93.32% and 99.977% levels are extracted and shown in Figure 4.2. The envelopes determine the significance level of RMS in each frequency bin independently. Therefore any observed trend in deviation from a certainty envelope signifies a higher level of confidence that the input power law does not represent a viable model for the PSD.

The resulting certainty envelopes are shown for all objects in Figure 4.2. It is clear that WZ Sge contains a feature, that cannot be explained by a simple power-law, with a certainty over 5σ. Other deviations from the certainty envelope such as the QPO with its harmonics shows the significance of the QPO signal. Other such features similar to the bump at $7-8\times10^{-5}$ Hz represent broad-band features that were not included in the PSD fit. Similar deviations at frequencies $> 10^{-3}$ Hz are influenced by the remaining harmonics of the QPO that were not fitted as their corresponding frequency bins did not allow for separation of individual harmonics.

No significant deviation from the 5σ significance envelope is seen in any other objects apart from WZ Sge. The long-term TPS of AWDs are known to have a complex structure requiring multiple Lorentzians (Scaringi et al., 2012b). However, using the 3σ and 5σ confidence contours it is difficult to say to what extent this structure translates to the objects here, apart from the clear example of WZ Sge. Some structure is hinted at in GW Lib, but it is

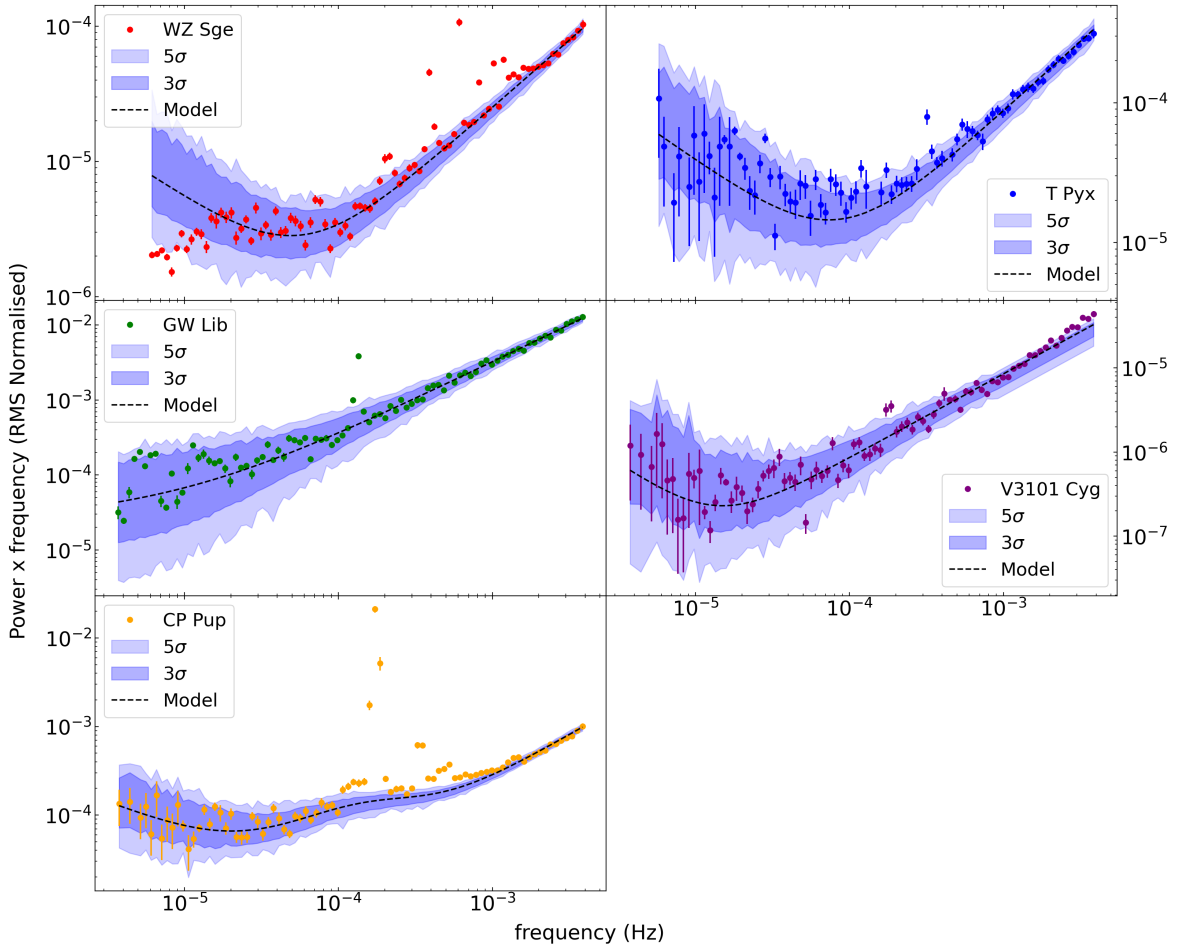

Figure 4.2: PSDs as shown in Figure 4.1. Shaded regions show confidence contours from Timmer & König (1995) algorithm. Dark shaded region corresponds to 3σ significance and light shaded region to 5σ significance. The data points outside of the shaded regions boundaries denote that the input power law (dashed line) cannot explain the underlying PSD shape to 3σ or 5σ significance.The QPOs are outside of the 3σ and 5σ significance since their respective Lorentzians have not been included in the model. This showcases their $>> 5\sigma$ significance above the underlying power-law.

obstructed by the dominant Poisson noise component and limited amount of data available (compared to WZ Sge and MV Lyr in Scaringi et al. 2012b).

Despite not being able to probe low enough frequencies to test the presence of a low frequency break with $\gtrsim 5\sigma$ significance in all the systems, the obtained significance combined with the χ^2 comparison of the 2 fits, shows evidence of self-similar empirical features to those in broad-band PSDs in XRBs. A zero-centred Lorentzian is used across all 5 systems, since the majority of the targets show a significantly lower χ^2 for the zero-centred Lorentzian fit. However, to err on the cautious side, the uncertainties on the break component are treated as an upper limit in all targets apart from WZ Sge.

4.4 Results

In this section the main results are outlined. The new QPOs in AWDs are reported in terms of the existing QPOs and broad-band low frequency break correlation from Wijnands & van der Klis (1999). The link to QPOs in XRBs is drawn from the broadness of the signal in the power spectrum as seen in Figure A.5 and explained further in Section 4.5.1. Another important characteristic of the new QPOs in AWDs is that it is the first instance in which QPOs in AWDs are reported to show harmonics as seen in Figure 4.1.

As mentioned before in Section 4.1, type-C and HBO QPOs in XRBs show a linear correlation with a low frequency break in their PSDs. The break corresponds to the nearest low zero-centred Lorentzian that is used in the fit of the broad-band PSD and was first reported in Wijnands & van der Klis (1999) with an overview available in Ingram & Motta (2019).

The results of taking the lowest zero-centred Lorentzian component from Table 4.2 (denoted by *) and plotting it against the characteristic QPO frequency as defined in Equation 4.3.2 is shown in Figure 4.3. Since for GW Lib the fundamental of the QPO signal reported by Chote et al. (2021) is not detected in *TESS* , half of the 2^{nd} harmonic frequency (Δ_1 and $\nu_{0,1}$ from Table 4.2) is used instead. Following from Section 4.3.3 only upper limits are used for the zero-centred Lorentzian in all systems apart from WZ Sge and are denoted by arrows. BH and NS QPOs with their corresponding low-frequency broad-band components (breaks) from Table 1 in Wijnands & van der Klis (1999) are also shown.

The points representing AWDs are clearly following the same empirical relation as the XRBs from Wijnands & van der Klis (1999). The AWDs are several orders of magnitude lower in both QPO and break frequency. To demonstrate the significance of this correlation a linear

fit is obtained using linear least-squares regression as implemented in `Scipy`. A Pearson correlation coefficient of 0.991 is obtained for all data shown in Figure 4.3 and 0.805 for XRBs only. The resulting linear trend is shown in Figure 4.3 as a solid line for all data and as a dashed line for solely XRBs. Bootstrapping is used to test the robustness of this correlation. This consists of randomising the QPO frequencies for corresponding break frequency values. In doing so, no correlation is expected and the Pearson correlation coefficient is expected to be ~ 0. Repeating this process 10^4 times then shows that the correlation is significant to 99.99% confidence. The resulting distribution of the Pearson correlation coefficient is then shown in the bottom panel of Figure 4.4. To constrain the uncertainty on these fits, N data points are randomly selected with replacement from the data set in Figure 4.3. The linear regression fit is then repeated and the Pearson coefficient is computed. The process is repeated 10^4 times resulting in the mean Pearson coefficient of 0.991 ± 0.005, a value consistent with the original Pearson correlation coefficient. This process is repeated for all data points in Figure 4.3 as well as only XRB points with the resulting distributions shown in Figure 4.4. The uncertainty in the linear regression fits performed during bootstrapping is shown in Figure 4.3 as the lightly shaded regions for all data points and for XRBs only. The correlation can hence be expressed as $log(\nu_{QPO}) = (0.87 \pm 0.03) log(\nu_{break}) + (0.72 \pm 0.05)$ for all data points and $log(\nu_{QPO}) = (0.86 \pm 0.06) log(\nu_{break}) + (0.73 \pm 0.05)$ for XRBs only.

4.5 Discussion

In this Section the implications of the QPO model as a potential tool for spin period and magnetic field strength measurement for weakly magnetised AWDs is discussed in Section 4.5.2. In Section 4.5.3 the QPO and break correlation for XRBs is discussed in the framework of AWDs and the implications for the driving mechanisms of the QPOs.

4.5.1 Possible interpretations of QPOs in AWDs

There are numerous signals which are present in AWDs in the frequency range displaying the QPO signals shown in Figure 4.1.

The PSDs in Figure 4.1 are already cleaned of any variability related to the orbital period of the systems. Inspecting the nature of the signals in the non-averaged and non-binned power spectra in Figure A.5 I find that the signals are phenomenologically different from the coherent signals usually present in AWDs, such as the orbital period or spin. The main

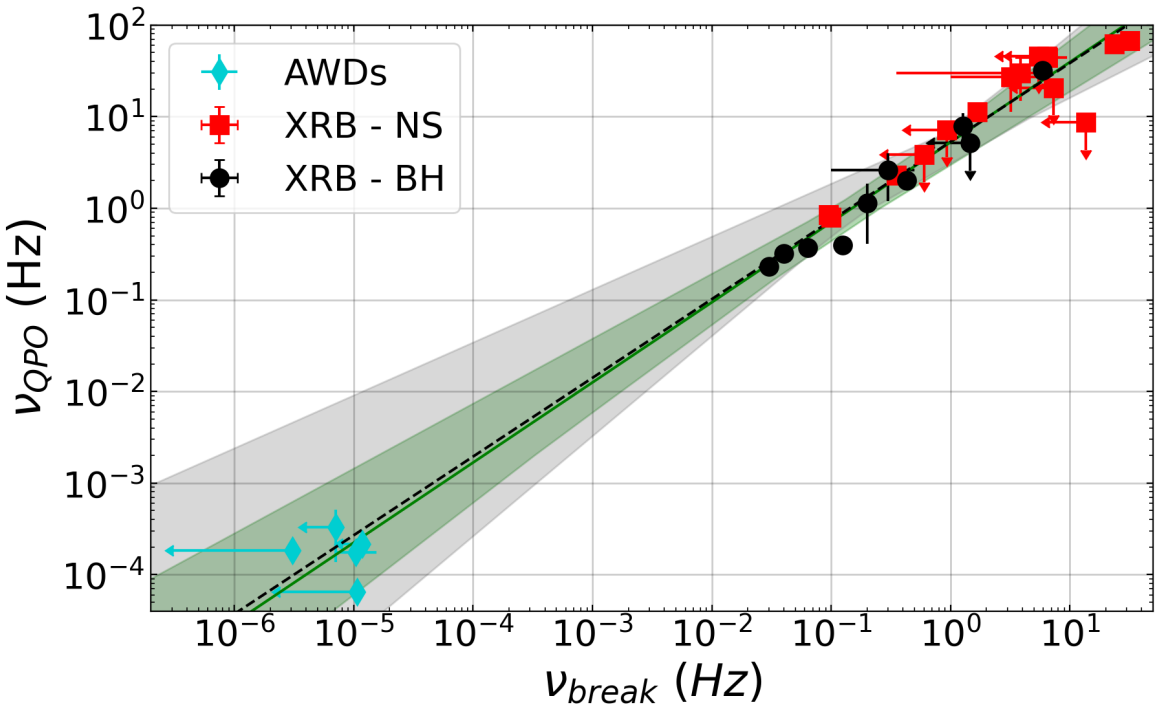

Figure 4.3: QPO frequency as a function of the break frequency. The observed QPOs with their corresponding low frequency breaks are denoted for AWDs in diamonds, for NS XRBs in squares and in filled circles for BH XRBs. For AWDs these are taken from the empirical fit in Section 4.3.2 and Table 4.2. The QPO frequency is the peak frequency as denoted in Equation 4.3.2 using Δ_1 and $\nu_{0,1}$. The only exception is GW Lib where the QPO frequency is taken as half that, since only the 1^{st} harmonic of the QPO is detected in *TESS* with its true fundamental being reported in Chote et al. (2021). The break frequencies are denoted in Table 4.2 by * for each object.The solid line represents the fit to the data from linear least-squares regression and the shaded darker area represents the uncertainty on the fit. The dashed line represents the fit to the data when AWDs are excluded, with the uncertainty being represented by the lighter shaded region.

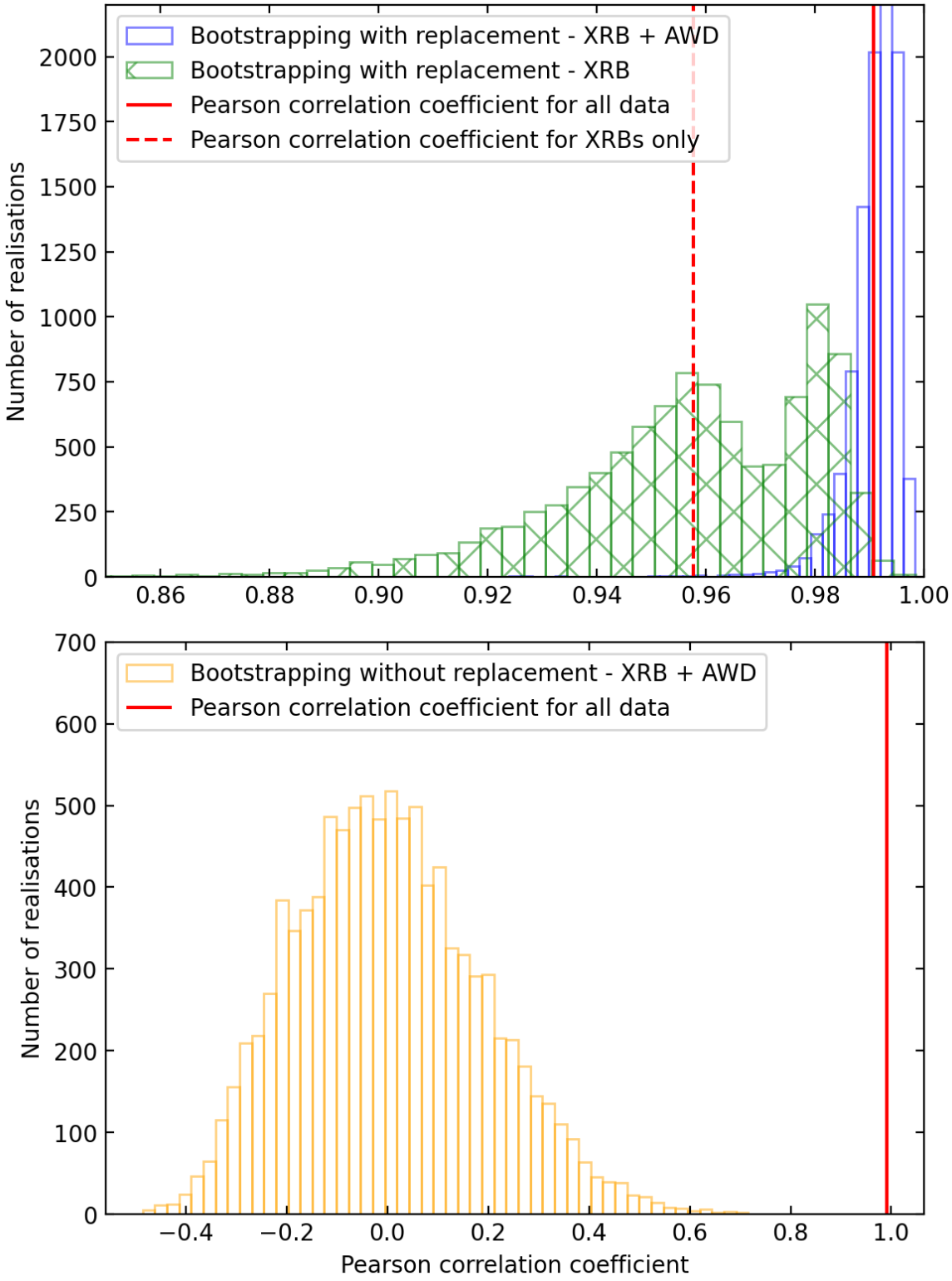

Figure 4.4: *Top*: Distribution of the Pearson correlation coefficient for the bootstrapping of data from Figure 4.3 with replacement. The clear distribution corresponds to bootstrapping of all data, whilst the hatched distribution only drew from the XRB sample from Figure 4.3. The solid line represents the Pearson correlation coefficient of of all data in Figure 4.3 and the dashed line corresponds to the value of the coefficient when AWDs are excluded. *Bottom*: The distribution of the Pearson correlation coefficient resulting from bootstrapping the data from Figure 4.3 without replacement and by randomising one of the axes. The zero-centred distribution shows the 99.99% significance of the correlation from Figure 4.3, with the solid line marking the value of the Pearson correlation coefficient of the data.

difference being the power peaks of the signals are broader than coherent periods. Where present, the signal from the orbital period is also indicated in Figure A.5.

Another type of coherent signal present in AWDs is usually due to negative and positive superhumps and their associated fundamental signals. In that case, the superhumps are present relatively close to the orbital period of the system. For a positive superhump, $\nu_{SH}^{+} < \nu_{orb}$, and the signal is associated with the tidal stresses exerted by the secondary on the disc. These cause the disc to become eccentric and undergo apsidal precession in the prograde direction (Lubow, 1991). In this scenario, only GW Lib and V3101 Cyg would qualify. In neither system is a fundamental frequency of the signal found at low frequencies. For the case of negative superhumps, where $\nu_{SH}^{-} > \nu_{orb}$, the signal is thought to be caused by the retrograde nodal precession of a tilted accretion disc (Wood et al., 2009), resulting in a 3:1 resonance. This is viable for WZ Sge and T Pyx. However, in the case of WZ Sge, CP Pup, GW Lib, and T Pyx, the QPO signal shows distinct harmonics, making a superhump explanation unfeasable. The presence of harmonics also rules out any other possibility of the signals being related to a beat between the orbit and spin.

Another peculiar feature of the signals is that they are not entirely coherent, as shown in Figure A.5. As opposed to the orbital signals, the QPO signals are broad, reaching a width of $\sim 2 \times 10^{-5}$ Hz. They also exhibit slight variations in central frequency, amplitude and shape. This has already been reported for CP Pup (Bruch, 2022; Veresvarska et al., 2024a). In GW Lib, the signal is revealed to be the first harmonic of the fundamental signal at $\sim$4 hours, interpreted as a quiescent superhump (Chote et al., 2021) similar to the transitional feature in EQ Lyn (Mukadam et al., 2013) and in V455 And (Araujo-Betancor et al., 2005). Since in *TESS* only the harmonic is detected, the fundamental is here inferred. This is similar behaviour to that of WZ Sge, where the subsequent harmonics are much stronger than the fundamental signal as is visible in Figure 4.1. A parallel may be drawn with the sub-harmonics of QPOs observed in XRBs, where the fundamental signal is the strongest, not the lowest frequency (Casella et al., 2005b). The overall unusual behaviour of these signals suggests the necessity of an alternative explanation.

QPOs in XRBs display strikingly similar properties. They show harmonics and time variability as well as general broadness of the signal itself (Ingram & Motta, 2019). This is apparent in the quality factor of the QPOs, which – depending on the type of XRB QPO – can be $Q \lesssim 3$ or $Q \gtrsim 6$. Due to the value of Q depending also on the variability of the signal during the observations, it may be expected that Q will be much larger for AWDs due to the slower

variability time scales. This is indeed the case as shown by the reported Q values in Table 4.2, where some QPOs have Q $\gtrsim$ 10000. This, whereas unusual for XRBs, would seem necessary for a signal to be detected above the Poisson noise dominated systems such as the ones shown here. However, despite such a high Q value the signals bear little similarity to other coherent signals such as the orbital period as described above and shown in Figure A.5.

4.5.2 Magnetically Driven Precession as QPO-driving Mechanism

QPOs in XRBs are generally explained by the relativistic effect of frame dragging modelled most commonly by Lense-Thirring precession (Stella & Vietri, 1998; Stella et al., 1999; Psaltis & Norman, 2000; Fragile et al., 2001; Ingram et al., 2009). While several possibilities have been presented, in particular for NS XRBs, Lense-Thirring precession is currently the most popular interpretation. However, since AWDs are indisputably non-relativistic, a different model is required to explain their QPOs. A model explored by Warner & Woudt (2002) proposes that a magnetospherically truncated accretion disc may give rise to QPOs from the interaction between twisted magnetic field lines and plasma in the disc. This may produce a dense and elevated region referred to as a "blob". The release of energy from the sudden reconnection of strained field lines within the blob is speculated to generate disturbances that propagate through the disc, potentially resonating with its natural oscillations and generating QPOs. In this scenario the frequency of the QPOs are associated with the recconection timescale estimated in Warner & Woudt (2002) to be on the order of $\sim$15 minutes for a non-resonant signal. The authors do not consider a resonant case as this would be too close to the orbital period and difficult to detect photometrically. The resulting frequency range thus corresponds to the QPOs and DNOs found by Warner et al. (2003), not the ones reported in this work which occur on longer timescales.

One alternative and intrinsically non-relativistic model for QPOs in neutron stars was proposed by Aly & Kuijpers (1990), where the QPOs are driven by interactions between the disc and accretor magnetic field. However, under such framework the QPOs can only occur at a radius where the magnetic fields strengths of the accretor and disc are equal (Equation 2 in Aly & Kuijpers 1990), which may not be a feasible scenario for accreting white dwarfs.

A further alternative model developed to explain QPOs in neutron stars and T Tauri stars was developed by Lai (1999). They suggest that QPOs may be associated with magnetically driven precession, a phenomenon where the orientation of the accretion disc surrounding a rotating magnetised star undergoes a periodic wobbling motion around the star's spin axis.

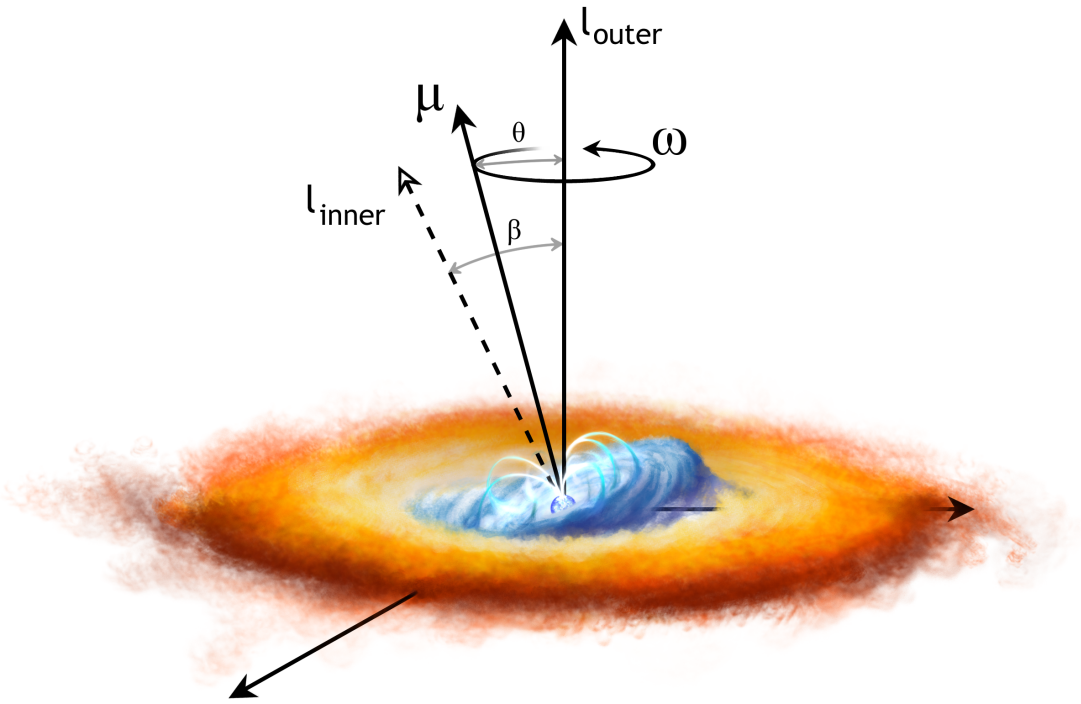

Figure 4.5: Diagram showing the disc geometry producing a QPO as described by (Lai, 1999; Pfeiffer & Lai, 2004). The accretor magnetic field vector μ and spin axis ω are misaligned to the angular momentum of the outer standard accretion disc (l_{outer}) leading to the precession of an inner part of the disc that is warped as a consequence (l_{inner}).

This interaction between the disc and the star's rotating magnetic field induces a warping effect on the disc, causing it to deviate from its original equatorial configuration and to precess around the star. The precession torque arises from the interaction between the surface current on the disc and the horizontal magnetic field produced by the star's dipole. The nonlinear evolution of the disc's state is then further explored by Pfeiffer & Lai (2004), and the model's applications to NS low-frequency QPOs are discussed in Shirakawa & Lai (2002a,c).

A schematic sketch of the model geometry is shown in Figure 4.5. In the framework of this model, as presented by Lai (1999), the star's rotational axis ω is tilted with respect to the disc's angular momentum (l) by an angle β.

The QPO is generated by the precession of the inner disk around the spin axis of the accretor. Lai (1999) approximate the precession frequency of the entire inner disk by multiplying the magnetic precession frequency of a ring at any specific characteristic radius r, $\nu_p(r)$, by a dimensionless constant A, such that the resulting QPO frequency can be expressed as

$$\nu_{QPO} = A\nu_p(r) = \frac{A}{2\pi^3}\frac{\mu^2}{r^7\ \Omega(r)\ \Sigma(r)}\frac{F(\theta)}{D(r)}, \tag{4.5.1}$$

where μ is the stellar magnetic dipole moment ($\mu = BR^3$, where B is the field strength and R is the stellar radius of the accretor), Ω is the Keplerian angular frequency, Σ is the disk surface density, and $F(\theta)$ and $D(r)$ are dimensionless functions defined in Appendix A.5 (where I discuss the model in more detail). Because of several degenerate parameters in this model, I here assume that the characteristic radius r is the disk inner radius $r_{\rm in}$ which I set equal to both the magnetospheric radius and the corotation radius such that $r = r_{\rm in} = r_{\rm m} = r_{\rm co}$. A more detailed description of the model and its parameters is given in the Appendix A.5.

Magnetic field strength, accretion rate, and spin estimation from QPOs in AWDs

Equation 4.5.1 depends on several free parameters. Amongst those are the accretor mass and size, the strength of the intrinsic magnetic field strength of the accretor B, the accretion rate of the system $\dot{M}$ and the dimensionless viscosity of the disc α. A different combination of these parameters can yield different QPO frequencies which may occur at different radii. The radius of the QPO is given by the relation between the magnetospheric radius r_M and the corotation radius r_{CO}. I here assume that $r_{in} = r_M = r_{CO}$, which allows to break some of the degeneracies in the model when inferring the accretor magnetic field and corresponding spin of the accretor.

To explore the validity of the model I employ a set of fiducial parameters as several of these would otherwise remain unconstrained. The effect of varying the B field and accretion rate is non-negligible, and no reasonable estimate can be made that would be applicable for all AWDs or NS XRBs. Therefore, I instead explore a range of these parameters for AWDs and NS XRBs as noted in Table 4.4. Hence, for a given magnetic field and accretion rate a specific combination of QPO frequency and spin period is obtained allowing for comparison to data for objects with QPO and spin period measurements.

Specifically for the purpose of comparing the model to the 2 observed QPOs in AWDs with spin period measurements, 2 separate values of viscosity are chosen. These correspond to the quiescent values of WZ Sge with $\alpha \sim 0.006$ and $\alpha \sim 0.003$ (Howell et al., 1995) for GW Lib, which are obtained from modelling of the recurrence timescales of the dwarf novae outbursts. For other objects the viscosity of WZ Sge as well as other values of fiducial parameters are used. The different fiducial parameters are due to the intrinsic differences between the systems. Despite both being dwarf novae with similar characteristics and recurrence times of the outbursts ($\sim$ years), the estimates of their viscosities from Howell et al. (1995) provide an important constraint on otherwise fully unconstrained fiducial parameters. Ideally, to truly

Table 4.4: Fiducial model parameters for the magnetically driven precession model for QPOs for AWDs and NS XRBs. For the main parameters that are varied through the model, the magnetic field of the accretor B and the accretion rate $\dot{M}$, the ranges are cited instead. For AWDs, 2 values of viscosity and η are given to represent WZ Sge and GW Lib like objects.

Model Parameter	AWDs	NS XRBs
M ($M_\odot$)	0.8	1.4
R	0.01 $R_\odot$	10 km
B (G)	$10^3 - 10^8$	$10^7 - 10^{10}$
$\dot{M}$ ($M_\odot yr^{-1}$)	$10^{-12} - 10^{-7}$	$10^{-12} - 10^{-7}$
α	0.006 (WZ Sge), 0.003 (GW Lib)	0.006
η	0.1 (WZ Sge), 0.05 (GW Lib)	0.1
θ (°)	45	45
A	0.6	0.6

apply the magnetically driven QPO model to its full extent a precise measurement of all parameters is required. With this not feasible, it is necessary to use these viscosity estimates. Since the estimated accretion rate of GW Lib from the literature (Hilton et al., 2007) is much smaller than that of WZ Sge, the fiducial parameters of WZ Sge are used in the treatment of the other objects showing QPO.

For the fiducial values of these parameters and each combination of B and $\dot{M}$ there is a characteristic QPO frequency ν_{QPO} with an associated spin period P_{spin}. A variation in the assumption of $r_{in} = r_M = r_{CO}$ would therefore result in variation of P_{spin} and ν_{QPO} pairs for corresponding B and $\dot{M}$ pairs.

Figure 4.6 demonstrates the dependence of the model on these 4 parameters. In the right hand side panels the QPO frequency is plotted as a function of P_{spin}. The dashed lines then show lines of equal B and the solid lines the lines of equal $\dot{M}$. A QPO measurement can in such a case be used to put constraints on B and and accretion rate for a given spin. Since there is a strong correlation between the B and accretion rate in the model, the same plots are also shown in the left hand side panels where P_{spin} is scaled by the magnetic field strength and the accretion rate.

By evaluating the magnetically driven precession model for the fiducial model values and the B and $\dot{M}$ ranges listed in Table 4.4 it is possible to estimate these parameters and the corresponding spin period of the accretor. The WD mass is fixed to 0.8 M_{WD} for all objects as a good approximation for the mean of the AWD accretor mass distribution Zorotovic et al. (2011); Pala et al. (2022). The WD radius is then derived from Hamada & Salpeter (1961); Nauenberg (1972b) using the WD mass. η, the parameter relating Alfvén and magnetospheric radius, is set to 0.1 and 0.05. For strongly magnetic systems such as NS and magnetic AWDs,

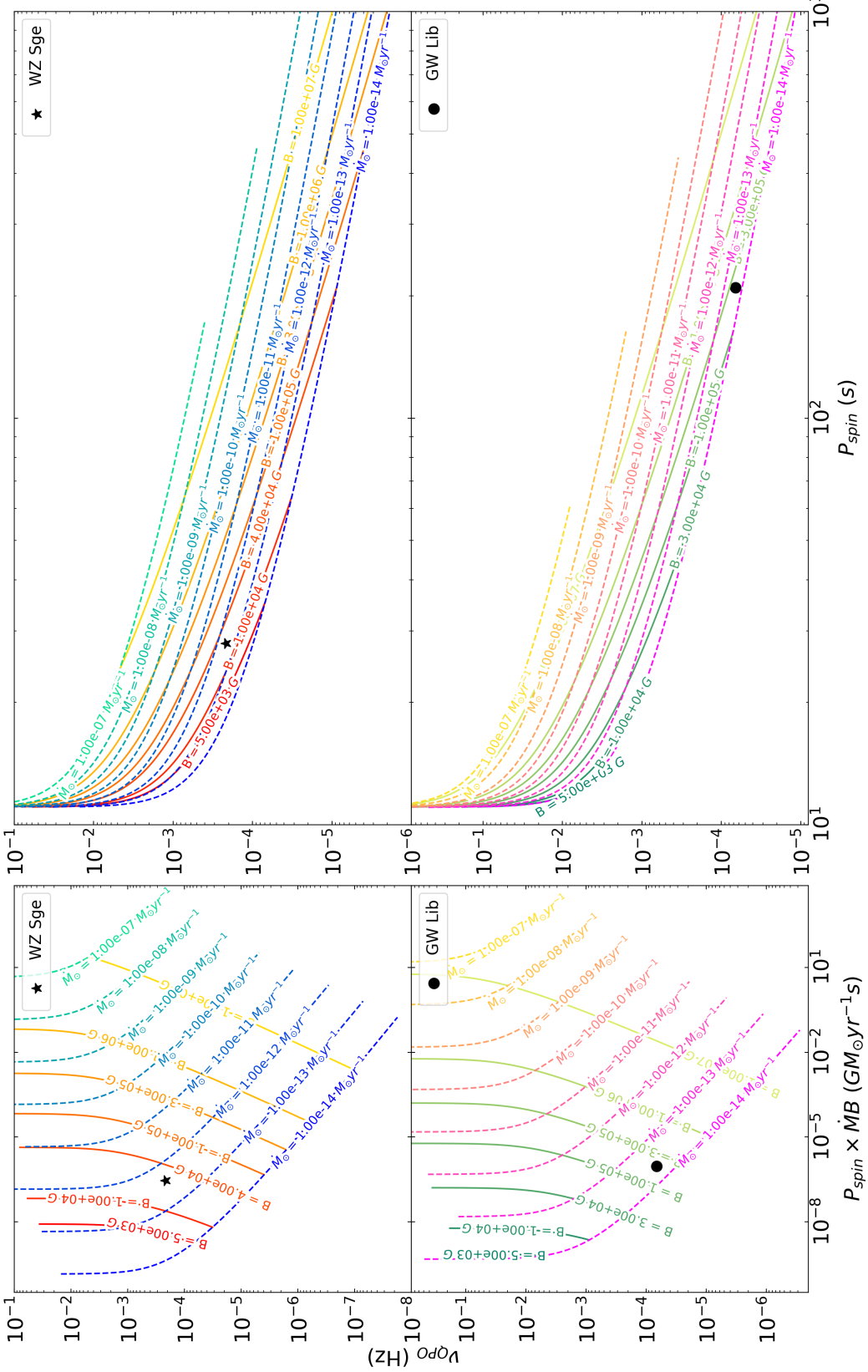

Figure 4.6: *Right*: Model QPO frequency as a function of the corresponding accretor spin. *Left*:Model QPO frequency as a function of the corresponding accretor spin scaled by the accretion rate and magnetic field strength of the accretor. In all panels the dashed lines denote lines of equal B field and solid lines denote lines of equal accretion rate. *Top panels*: Fiducial parameters corresponding to WZ Sge from Table 4.4. The star corresponds to the observed QPO and spin, scaled by B and accretion rate on the right. *Bottom panels*: Same as top panels but with fiducial parameters of GW Lib from Table 4.4. The filled circle represents the observed QPO and scaled spin of GW Lib.

it is by convention set to 0.5 (Ghosh & Lamb, 1979a; Mönkkönen et al., 2022). However, the model requires the magnetospheric radius to be equal to the co-rotation radius. This is not likely to always be the case and a smaller value of η required here may reflect that. θ is set to the midpoint value of 45°. A is fixed to 0.6 as this is the average of the range determined for the parameter in the framework of this model in Shirakawa & Lai (2002a).

To compare how successfully the model predicts B, $\dot{M}$, and spin for a particular QPO frequency, it is possible to use the cases of WZ Sge and GW Lib. To estimate B and $\dot{M}$ from the model a fine grid of B and $\dot{M}$ is computed with a pair of spin and QPO frequency corresponding to each pair of B and $\dot{M}$. Then for a given measurement of spin and QPO frequency with their corresponding uncertainties the corresponding range of B and $\dot{M}$ can be extracted.

WZ Sge has an estimated spin period of 27.87±0.01 s as measured by Patterson (1980). Later in Patterson et al. (1998) the magnetic field is invoked to be between $1 - 5 \times 10^4$ G. This is necessary to explain the disappearance of the potential spin frequency during an outburst when the accretion rate of a dwarf nova such as WZ Sge rises by a factor of ∼1000 from the quiescent rate of $\sim 1 \times 10^{-11}$ $M_{\odot} yr^{-1}$. With this information it is possible to compare the observables of WZ Sge to the parameter space in the top panel of Figure 4.6. The QPO and spin frequency with the assumed B range and $\dot{M}$ correspond to the correct range within the parameter space, showing that the model can reproduce reasonable results for the fiducial values of fixed parameters, with B = 2.5±0.1×10^4 G and $\dot{M}$ = 4.0±0.3×10^{-13} $M_{\odot} yr^{-1}$. This value is at odds with the previously reported quiescent accretion rate for WZ Sge. An important point to consider is that in the model the accretion rate represents the accretion rate onto the accretor, not the mass transfer rate from the donor. Furthermore, because there are a set number of fixed fiducial parameters, an error estimate on the model's parameter prediction is only meaningful when considering the potential variability of the free parameters that remain fixed. Hence the errors here only represent a snapshot of the real uncertainty contours and so should be treated as a lower limit on the real errors.

Similarly for GW Lib, the spin period was measured to be 209 s from the UV line widths (Szkody et al., 2012). As the recurrence timescale for GW Lib is very long (∼ years) the quiescent viscosity is also low (Howell et al., 1995). Adapting the fiducial model parameters from Table 4.4 the resulting B field and accretion rate estimate are B = 2.0±0.1×10^5 G and $\dot{M}$ = 2.2±0.3×10^{-14} $M_{\odot} yr^{-1}$. This leads to a higher magnetic field compared to WZ Sge and extremely low accretion rate. Nevertheless, such a low accretion rate has been reported

Table 4.5: Estimates of magnetic field strength, accretion rate and spin period from the magnetically driven precession model of QPO in AWDs. the values should be treated as possible ranges and not as best fit values. In the case of WZ Sge and GW Lib the parameters can be constrained better using the observational estimates of P_{spin}, which are noted in the table instead and denoted by *. For objects with unknown spin, an estimate of accretion rate is used so that ^{a} Veresvarska et al. (2024a), ^{b} Godon et al. (2018) and ^{c} $\sim 10^{-11} - 10^{-10}$ $M_\odot yr^{-1}$ as a representative value for the WZ Sge-type Dwarf Nova V3101 Cyg. CP Pup and T Pyx use the fiducial parameters of WZ Sge and V3101 Cyg of GW Lib.

Object	B (G)	$\dot{M}$ ($M_\odot yr^{-1}$)	P_{spin} (s)
CP Pup	$2 - 3 \times 10^5$	$1 - 2 \times 10^{-10}$ ^{a}	$72 - 84$
WZ Sge	$2.5^{+0.1}_{-0.1} \times 10^4$	$4.0^{+0.3}_{-0.3} \times 10^{-13}$	$27.87^{+0.01}_{-0.01}$ *
GW Lib	$1.97^{+0.14}_{-0.12} \times 10^5$	$2.2^{+0.3}_{-0.3} \times 10^{-14}$	209^*
T Pyx	$9 \times 10^6 - 1 \times 10^7$	$10^{-7} - 10^{-6}$ ^{b}	$148 - 345$
V3101 Cyg	$3 \times 10^3 - 1.2 \times 10^4$	$10^{-11} - 10^{-10}$ ^{c}	$99 - 165$

for quiescent state of GW Lib by Hilton et al. (2007). However given the lack of constraint on some of the model parameters, this should be treated more as a rough estimate. The parameter space for GW Lib and its adapted fiducial parameters are shown in the bottom panel of Figure 4.6.

As there are no estimates for spin period, B or $\dot{M}$ for any of the other systems, only very broad ranges can be provided for the model parameters, adopting α =0.006 and η =0.1. The only exception is V3101 Cyg, which has theoretically predicted $\alpha < 0.005$ (Hameury & Lasota, 2021) and so the fiducial parameters of GW Lib are used instead. In such a case it is impossible to provide reasonable constraint on any of the parameters. However, previously reported values of accretion rate can help constrain the estimates of B field and spin. The accretion rates used are $1 - 2 \times 10^{-10}$ $M_\odot yr^{-1}$ from Veresvarska et al. (2024a) for CP Pup, $\sim 10^{-7} - 10^{-6}$ $M_\odot yr^{-1}$ for T Pyx from Godon et al. (2018) and $\sim 10^{-11} - 10^{-10}$ $M_\odot yr^{-1}$ for V3101 Cyg which is a WZ Sge type Dwarf Nova. The corresponding B and spins are listed in Table 4.5, alongside the accretion rate estimates for WZ Sge and GW Lib. The obtained B field is below the standard values of confirmed magnetic systems, apart from T Pyx, and all estimated spin ranges are under 3 minutes, apart from T Pyx, where the range of possible spins reaches ∼6 minutes.

It is however necessary to note that all such deductions on the magnetic field strength and accretion rate are highly dependent on a good understanding of the system. As of now, there are no known systems in which there is sufficient certainty to constrain the values of the fiducial parameters. As a consequence all deduced constraints on B and $\dot{M}$ are simply a reflection of the constraints on the spin and QPO frequency measurements. Hence the results reported in Table 4.5 should be treated with extreme caution and mostly serve as a

prediction of the potential precision, subject to future precise measurements of parameters in Table 4.4.

QPO model implications for spin, B field and accretion rate measurement

Figure 4.6 shows that for the current set up of the model, all AWDs showing QPOs with similar characteristics as WZ Sge would be expected to have a relatively fast spin $\sim$20 $-$ 200 s WD. This is assuming a low magnetic field $B \lesssim 10^6$ G and low accretion rate $< 10^{-10}$ $M_{\odot} yr^{-1}$ and a similar frequency range for the QPOs as observed in the systems here. The extremely low accretion rates recovered by the model here should be taken as representative of the instantaneous accretion rate onto the accretor, not the mass transfer rate from the donor star. Hence such low values may not be unrealistic for the accumulation of mass between Dwarf Novae outbursts in WZ Sge and GW Lib, in particular in the case of GW Lib (Hilton et al., 2007).

For slowly spinning systems $\gtrsim$ 1000 s, the QPOs in weakly magnetised systems adopting parameters self-similar to the fiducial ones used here would yield QPO frequencies $\lesssim 10^{-6}$ Hz (278 hrs). This would provide a considerable observational challenge with the current data. New potential missions such as *PLATO* may help uncover these in the future. For magnetic systems, monitoring of close-by and bright magnetic systems, such as the Intermediate Polars V1223 Sgr or FO Aqr, may unveil new QPOs in systems with alternative values of B and direct spin observations to use for model verification. These potential detections could then be used to put a better constraint on some of the fiducial parameters in Table 4.4.

Given that the QPOs reported here are mostly observed in either dwarf novae or nova-likes the potential variability of the QPO with a large change of accretion rate could also provide important insight on the nature of the QPOs themselves and the systems in which they occur as well as their driving mechanism.

4.5.3 Break and QPO correlation in XRBs and AWDs and QPO driving mechanism implications

Type-C and HBO QPOs in XRBs bear several observational similarities to the QPOs reported here in AWDs. An important characteristic of these QPOs in XRBs is their correlation to a low-frequency break (Wijnands & van der Klis, 1999). The QPOs in AWDs reported here appear to follow the same correlation. Type-C and HBO QPOs in XRBs are usually explained

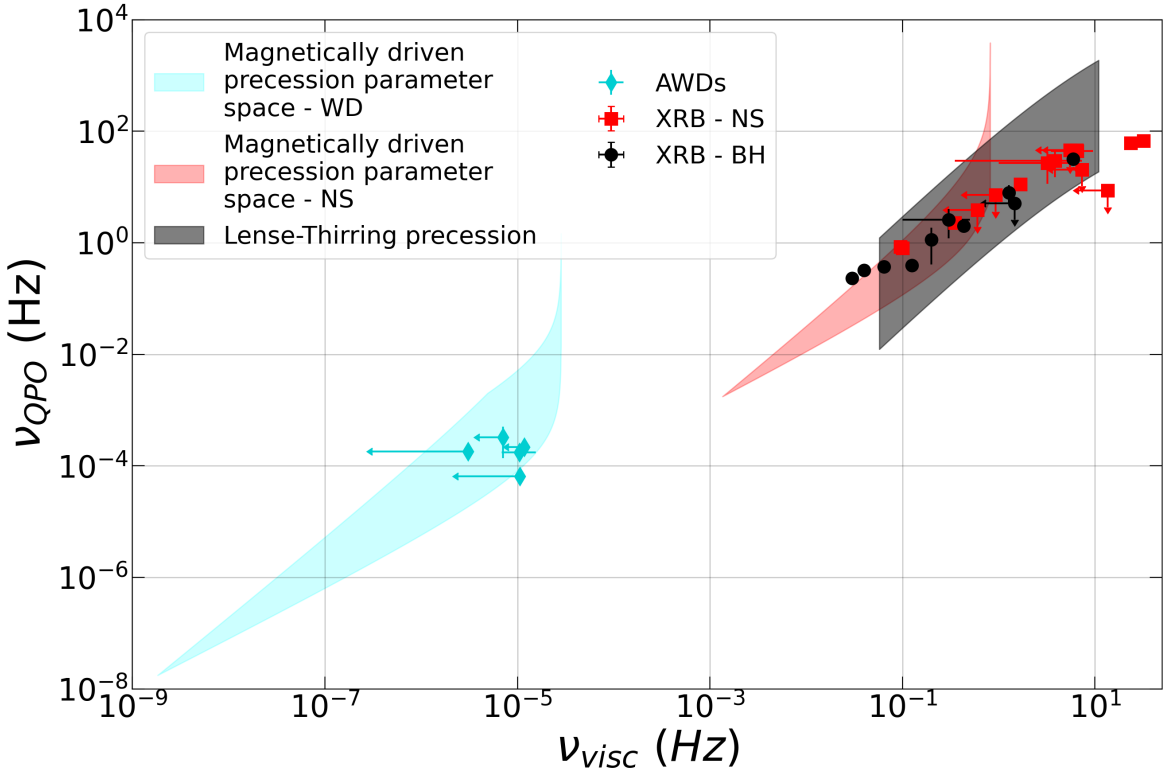

Figure 4.7: QPO frequency as a function of the viscous frequency at the QPO radius. The shaded regions correspond to the predicted model parameter space of QPOs and their viscous frequency. The lowest shaded region between $\nu_{visc} \sim 10^{-10} - 10^{-4}$ Hz represents the model parameter space of AWD QPOs as predicted by magnetically driven precession. For NS XRBs the magnetically driven precession model predicts a parameter space shown by the shaded region between $\nu_{visc} \sim 10^{-4} - 10^{0}$ Hz. The partially overlapping shaded region between $\nu_{visc} \sim 10^{-1} - 10^{2}$ Hz represents the parameter space of QPOs in BH XRBs as predicted by Lense-Thirring precession. The observed QPOs with their corresponding low frequency breaks (ν_{visc} are denoted for AWDs in diamonds, for NS XRBs in squares and in filled circles for BH XRBs.)

by the relativistic effect of frame dragging. In such a case it can be assumed that the PSD break is associated with the viscous frequency at the inner-edge of the precessing flow (Ingram et al., 2009; Ingram & Done, 2011b).

This cannot be the case in the non-relativistic AWDs. However in the framework of the magnetically driven precession model as described in Section 4.5.2 the observational characteristics of the QPOs are similar, despite a different driver behind the behaviour. A precessing inner flow of the accretion disc would also in this case be expected to produce a PSD break at the viscous frequency associated with the corresponding radius. This would have the effect of producing a break at a lower frequency than the QPO and a relation between the two quantities, as observed in Figure 4.7.

In Figure 4.7 I reproduce the data from Figure 4.3, but now overlay several models. As in Figure 4.3, the black circles represent the BH QPOs and their breaks from Wijnands & van der Klis (1999), the red squares represent the NS QPOs and their corresponding breaks from Wijnands & van der Klis (1999). The cyan diamonds represent the AWD QPOs and breaks from Table 4.2. The shaded regions represent the model parameter spaces for Lense-Thirring precession for BH XRBs, magnetically driven precession for NS XRBs and AWDs. The cyan shaded regions overlapping with the observed AWD QPOs represents the parameter space in which QPOs in AWDs can be explained by magnetically driven precession for all parameters shown in Table 4.4. The viscous frequency, ν_{visc}, was obtained from the dynamical frequency, ν_{dyn} at the QPO radius such that $\nu_{visc} = \alpha(\frac{H}{R})^2\nu_{dyn}$, and by assuming a value for $\alpha\left(\frac{H}{R}\right)^2 \sim 5 \times 10^{-5}$. $\alpha\left(\frac{H}{R}\right)^2$ is treated here as a standalone parameter, not a combination of viscosity α and the scale height ratio $\frac{H}{R}$. This is because in the context of AWDs there have been measurements of $\alpha\left(\frac{H}{R}\right)^2$ parameters that can be used to estimate this parameter (Scaringi, 2014; Veresvarska & Scaringi, 2023). Whereas estimates of α have been measured (Howell et al., 1995; Kotko & Lasota, 2012), no tangible constraint is known for $\frac{H}{R}$. Therefore treating $\alpha\left(\frac{H}{R}\right)^2$ as a single parameter based on previous measurements is deemed as the more appropriate assumption. The value is chosen as the middle of the expected range for this parameter for AWDs in quiescence. The potential range is considered for α to be between 10^{-3} for long recurrence dwarf novae such as GW Lib (Howell et al., 1995) up to 10^{-1} for high accretion rate systems (Kotko & Lasota, 2012), such as T Pyx. The estimated range for $\alpha\left(\frac{H}{R}\right)^2 \sim 1 \times 10^{-7} - 1 \times 10^{-3}$. The implications of the uniform assumption of $\alpha\left(\frac{H}{R}\right)^2 \sim 5 \times 10^{-5}$ with the range of $\alpha \sim 1 \times 10^{-3} - 0.1$ (Howell et al., 1995; Kotko & Lasota, 2012) is that the $\frac{H}{R} \sim 0.2 - 0.02$.

The x-axis of Figure 4.7 is the viscous frequency at the QPO radius. This demonstrates that all the QPOs reported here could be explained by the magnetically driven precession model, bearing in mind the upper limit on the break frequencies in all objects apart from WZ Sge. Therefore a potential test of this model and correlation would be the measurement of break frequencies for these systems and whether it deviates from the current limit by more than an order of magnitude. Such a test would however require more data, either an extension of the existing *TESS* time series or a new long-term mission such as *PLATO*.

The red shaded region overlapping with observed QPOs in XRBs and ranging from $\sim 10^{-4}$ $- 10^{0}$ Hz for the viscous frequency corresponds to the parameter space where the NS XRB QPOs and their PSD breaks can be explained by the magnetically driven precession. The parameter space was constructed for a NS with $M_{NS} \sim 2M_{\odot}$, $R_{NS} \sim 10$km, $B \sim 10^{7} - 10^{10}$ G, the same accretion rate range, θ and A as in Table 4.4. η was fixed to 0.1 and α to 0.006 for consistency with the AWDs. $\alpha \left(\frac{H}{R}\right)^{2}$ was assumed the same as in AWDs.

The black shaded region overlapping with QPOs in XRBs from $\sim 10^{-1} - 10^{2}$ Hz corresponds to the parameter space where the QPOs in XRBs can be explained by Lense-Thirring precession. QPOs driven by Lense-Thirring precession occur at a characteristic frequency which is related to the precession of a solid disc as detailed in Ingram et al. (2009) :

$$\nu_{LT} = \frac{(5-2\zeta)}{\pi\,(1+2\zeta)} \frac{a\left(1-\left(\frac{r_i}{r_o}\right)^{\frac{1}{2}+\zeta}\right)}{r_o^{\frac{5}{2}-\zeta} r_i^{\frac{1}{2}+\zeta}\left[1-\left(\frac{r_i}{r_o}\right)^{\frac{5}{2}-\zeta}\right]} \frac{c}{R_g} \tag{4.5.2}$$

where a is the BH spin, c is the speed of light in vacuum, r_i the inner radius of the precessing flow in the units of R_g and r_o the outer radius of the precessing flow in the units of R_g. R_g represents the gravitational radius $R_g = \frac{GM}{c^2}$. ζ is the index governing the radial dependence of surface density and is here fixed to 0 as from simulations as in Ingram et al. (2009). The mass range accounted for in the parameter space spans BH mass from $3 - 20\ M_{\odot}$ and spins from 0 to 0.998. The outer radius of the precessing region is considered between $1.01 - 50\ R_g$ and associated with r_o. The inner radius is here fixed to the innermost stable circular orbit (ISCO) based on the spin. This can predict larger QPO frequencies in black holes than are observed and the upper limit of the parameter space should be treated with caution. This is usually accounted for by setting the inner disc radius to the bending wave radius (Ingram et al., 2009) which would require the assumption of $\frac{h}{r}$ ratio. As this is unknown and could introduce another free parameter, the inner disc radius is here fixed at ISCO for simplicity. The viscous frequency is determined for radius r_o with $\alpha \left(\frac{H}{R}\right)^{2} \sim 10^{-3}$ as is usually assumed

for BH XRBs (Ingram et al., 2009).

For all the parameter spaces detailed above for Lense-Thirring precession and magnetically driven precession it is clear that that both follow the same observational trend behind the QPO and break relation, irrespective of the driver mechanism of the QPO. This unfortunately also means that the relation cannot be used to disentangle the nature of the driving mechanism for QPOs in XRBs since the 2 parameter spaces overlap. However, the non-relativistic AWDs show tentatively, whilst bearing in mind the uncertainty from the upper limits on most breaks in AWDs, that magnetically driven precession is a viable method for inducing QPOs in weakly magnetised AWDs.

4.6 Conclusions

QPOs are a well known characteristic in both XRBs and AWDs. In XRBs they are a well defined phenomena with different types according to their observational characteristics and correlation with broad-band structure. However, in AWDs, QPOs usually refer to unexplained, transitional and somewhat coherent signals observed in the light curves. Here I report 5 persistent QPOs in low magnetic field AWDs showing similar properties to type-C QPOs in XRBs, such as harmonics. A tentative link to the QPOs in XRBs is that the QPOs in AWDs seem to follow the correlation of XRB QPOs with a broad band low frequency break, when assuming that the upper limits on the break frequencies are representative of their true value. The break is usually associated with the viscous frequency of the outer part of the precessing flow of the disc where the QPOs are generated. Furthermore, the reported QPOs in AWDs show a low frequency broad-band structure, which can be fitted with a zero-centred Lorentzian as in XRBs or with a power-law, at a frequency where such a flow transition would be expected.

Due to the non-relativistic nature of AWD systems, I propose that the QPOs are driven by a weak magnetic field of the accretor being misaligned to the disc normal and causing precession of the inner part of the accretion disc. This model was previously considered for being part of the driving mechanism behind the low frequency QPOs in NS XRBs and potentially T Tauri stars. Here I show an implementation for AWDs, whose magnetic fields lie in between those of NS and T Tauri stars.

WZ Sge shows a QPO at $\sim 2 \times 10^{-4}$ Hz ($\sim$77 min) and GW Lib at $\sim 7 \times 10^{-5}$ Hz ($\sim$4.3 hrs), with both exhibiting harmonics. They are also the only systems in the sample with

spin period measurements. I report that the model prediction for a QPO at these frequencies requires accretion rate and spin that are consistent with the observationally reported values. This could present a possibility for magnetic field and spin estimates in weakly magnetic AWDs where direct measurements of these quantities are not yet possible. As an example I give estimates for these parameters for the rest of the sample. However, such predictions, together with the corresponding uncertainties, can only be obtained within the framework of the inherent assumptions of the model, once reasonable estimates on the fiducial parameters can be obtained. Therefore the results here can only serve as an illustration of the potential capabilities of the model, until a more detailed measurement of the fiducial parameters is obtained with the help of future missions such as *PLATO*.

4.7 Corrections

This Chapter discusses the results as reported in Veresvarska et al. (2024b). However, it has come to light that the PSD fits performed here in Section 4.3.2 were not done consistently with the fitting of QPOs in XRBs. The discrepancy comes from fitting the TPS as shown in Figure 4.1, and hence only the frequency bin centres are being fitted. Although this does not affect the results discussed in Veresvarska et al. (2024b) and in this Chapter (i.e. the frequency of the QPOs), it does affect the Q values of the individual QPOs and their resulting errors. The new values, i.e. updated version of Table 4.2, are reproduced here in Table 4.6. The new values of Q are still larger than standard Q values of Type C QPOs in XRBs, but they are not unrealistically different, with WZ Sge having a Q value of 10 for the fundamental.

Similarly, the new errors on the QPO measurements have a marginal effect on the Figures presented in this Chapter. The updated versions are shown below, with Figure 4.8 being the substitute for Figure 4.1, Figure 4.11 for Figure 4.4, Figure 4.10 for Figure 4.3 and Figure 4.12 for Figure 4.7. Figure 4.8 shows the direct reproduction of Figure 4.1, however some Lorentzian components are not clearly visible due to the model being evaluated on a finer frequency grid before then being re-binned to the sampling of the data when shown as a TPS. The full extent of the model (not as a TPS but as a non-averaged PSD) is shown in Figure 4.9. There may be some changes to the resulting estimates of the magnetic fields, accretion rates and spin ranges are reported in Table 4.5. However, considering the assumptions of the model and the resulting uncertainty on the inferred parameter ranges, these variations are negligible in comparison and hence not reported in detail here. A complete list of corrections

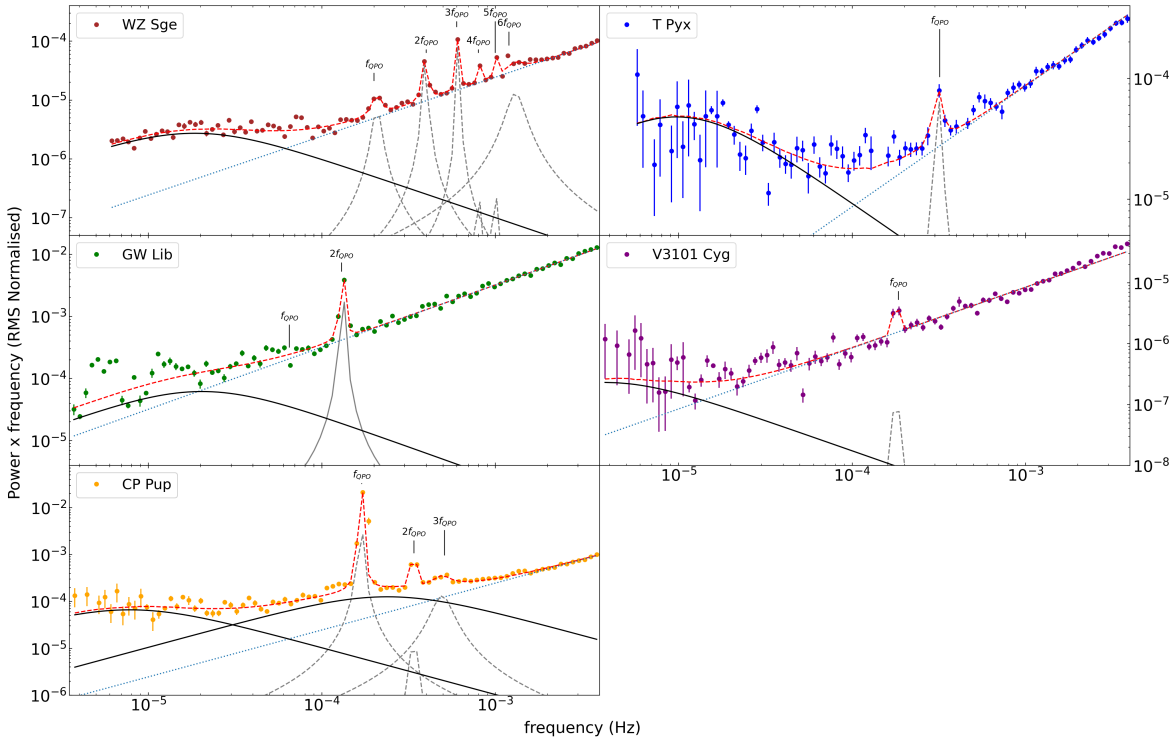

Figure 4.8: TPS of WZ Sge, GW Lib, T Pyx, V3101 Cyg and CP Pup averaged on the segment lengths specified in Table 4.1 with 90 logarithmicaly spaced bins. The empirical fit of the PSD is included here and comprises a Poisson noise power law (dotted line) in the high frequencies, one (in the case of WZ Sge, GW Lib, T Pyx and V3101 Cyg) or two (CP Pup) zero-centred Lorentzians (solid line) representing the broad band PSD structure and Lorentzians representing the QPOs and their harmonics (dashed line).

will be available in the erratum of Veresvarska et al. (2024b).

Table 4.6: Results of the empirical fit to the PSDs from Figure 4.1. The independent columns correspond to different objects and the rows correspond to model components: A − Poisson noise amplitude, r_i − integrated fractional rms of a given Lorentzian, Δ_i − half width half maximum of a given Lorentzian, $\nu_{0,i}$ − centroid frequency of a given Lorentzian (only Lorentzians representing QPOs and their harmonics have this component). The Q value for each Lorentzian representing a QPO is given as well and is denoted by Q_i. Broad-band component Lorentzians are zero-centred and their $\nu_0 = 0$ by default and is not denoted here. * denotes the lowest frequency zero-centred Lorentzian used in Figure 4.3 and 4.7.

	WZ Sge	CP Pup	GW Lib	T Pyx (s)	V3101 Cyg
A ($\times 10^{-2}$)	$2.4^{+0.6}_{-0.5}$	25^{+2}_{-2}	320^{+20}_{-20}	$8.6^{+0.8}_{-0.8}$	$8.5^{+0.8}_{-0.8}$
r_1 ($\times 10^{-3}$)	$1.1^{+0.9}_{-1.1}$	40^{+10}_{-10}	19^{+5}_{-7}	3^{+1}_{-3}	$6^{+4}_{-6}\times 10^{-1}$
Δ_1 ($\times 10^{-5}$)	1^{+1}_{-1}	$0.007^{+0.004}_{-0.004}$	10^{+20}_{-10}	$1.2^{+1.2}_{-0.1}$	$2^{+2}_{-2}\times 10^{-2}$
$\nu_{0,1}$ ($\times 10^{-4}$)	$2.1^{+1.2}_{-0.5}$	$1.67^{+0.13}_{-0.03}$	$1.32^{+0.06}_{-0.01}$	3^{+1}_{-2}	$1.8^{+0.2}_{-0.1}$
Q_1	~ 10	~ 160	~ 60	~ 15	~ 450
r_2 ($\times 10^{-3}$)	2^{+1}_{-2}	8^{+3}_{-3}	20^{+2}_{-3}	17^{+2}_{-2}	11^{+4}_{-11}
Δ_2 ($\times 10^{-5}$)	65^{+65}_{-64}	$2^{+100}_{-2}\times 10^{-2}$	$2.0^{+1}_{-0.6}$ *	40^{+30}_{-30} *	$4^{+4}_{-4}\times 10^{-3}$ *
$\nu_{0,2}$ ($\times 10^{-4}$)	$4.0^{+0.2}_{-0.2}$	$3.4^{+2}_{-0.3}$	–	–	–
Q_2	~ 30	~ 800	–	–	–
r_3 ($\times 10^{-3}$)	3^{+2}_{-3}	7^{+2}_{-3}	–	–	–
Δ_3 ($\times 10^{-5}$)	20^{+200}_{-20}	6^{+25}_{-4}	–	–	–
$\nu_{0,3}$ ($\times 10^{-4}$)	$6.1^{+0.2}_{-0.3}$	$4.9^{+0.6}_{-0.7}$	–	–	–
Q_3	~ 150	~ 4	–	–	–
r_4 ($\times 10^{-3}$)	1^{+1}_{-1}	$2.8^{+0.3}_{-0.3}$	–	–	–
Δ_4 ($\times 10^{-7}$)	3^{+3}_{-3}	$2.4^{+1}_{-0.6}$	–	–	–
$\nu_{0,4}$ ($\times 10^{-4}$)	8^{+8}_{-2}	–	–	–	–
Q_4	~ 1600	–	–	–	–
r_5 ($\times 10^{-3}$)	1^{+1}_{-1}	20^{+4}_{-4}	–	–	–
Δ_5 ($\times 10^{-7}$)	2^{+2}_{-2}	78^{+60}_{-40} *	–	–	–
$\nu_{0,5}$ ($\times 10^{-4}$)	$9.9^{+0.8}_{-0.1}$	–	–	–	–
Q_5	~ 2000	–	–	–	–
r_6 ($\times 10^{-3}$)	2^{+2}_{-2}	–	–	–	–
Δ_6 ($\times 10^{-4}$)	2^{+2}_{-1}	–	–	–	–
$\nu_{0,6}$ ($\times 10^{-3}$)	$1.3^{+1.3}_{-1.3}$	–	–	–	–
Q_6	~ 5	–	–	–	–
r_7 ($\times 10^{-3}$)	$4.1^{+0.7}_{-0.8}$	–	–	–	–
Δ_7 ($\times 10^{-5}$)	1.9^{+2}_{-1} *	–	–	–	–
χ^2_ν	6.20	2.94	12.5	2.92	5.15

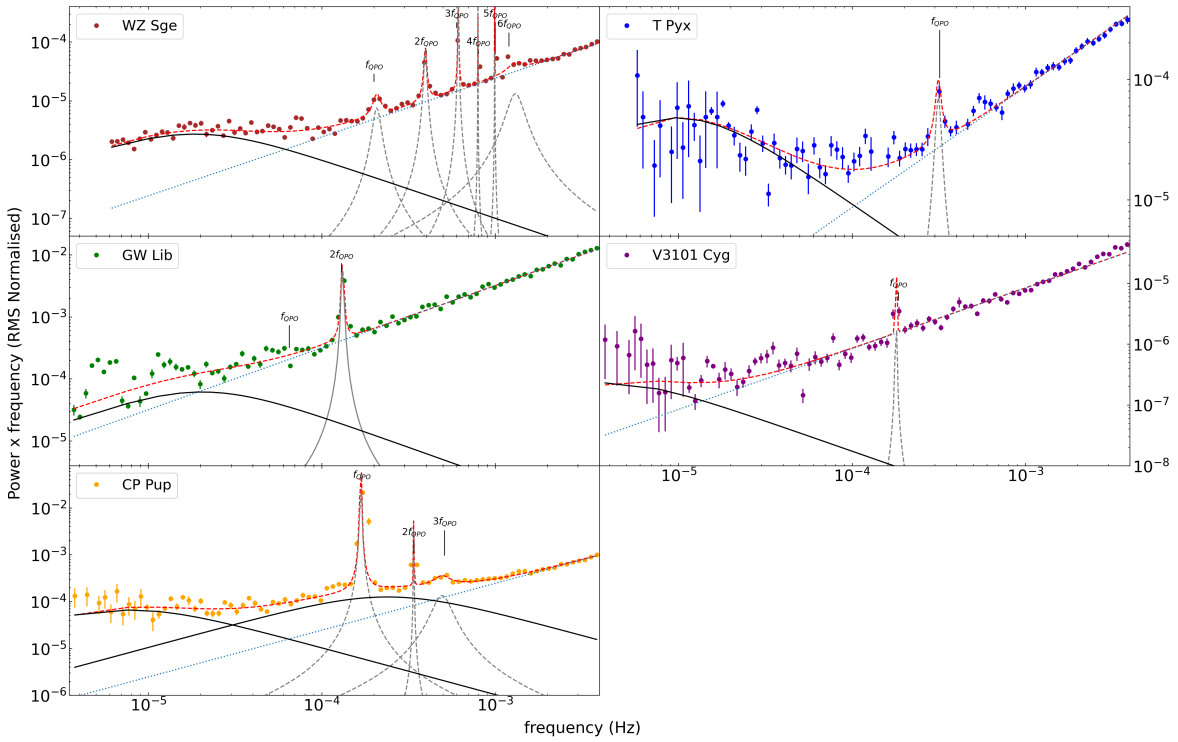

Figure 4.9: TPS of WZ Sge, GW Lib, T Pyx, V3101 Cyg and CP Pup averaged on the segment lengths specified in Table 4.1 with 90 logarithmicaly spaced bins. The empirical fit of the PSD is included here and comprises a Poisson noise power law (dotted line) in the high frequencies, one (in the case of WZ Sge, GW Lib, T Pyx and V3101 Cyg) or two (CP Pup) zero-centred Lorentzians (solid line) representing the broad band PSD structure and Lorentzians representing the QPOs and their harmonics (dashed line) and is evaluated on a fine non-averaged frequency range of the data.

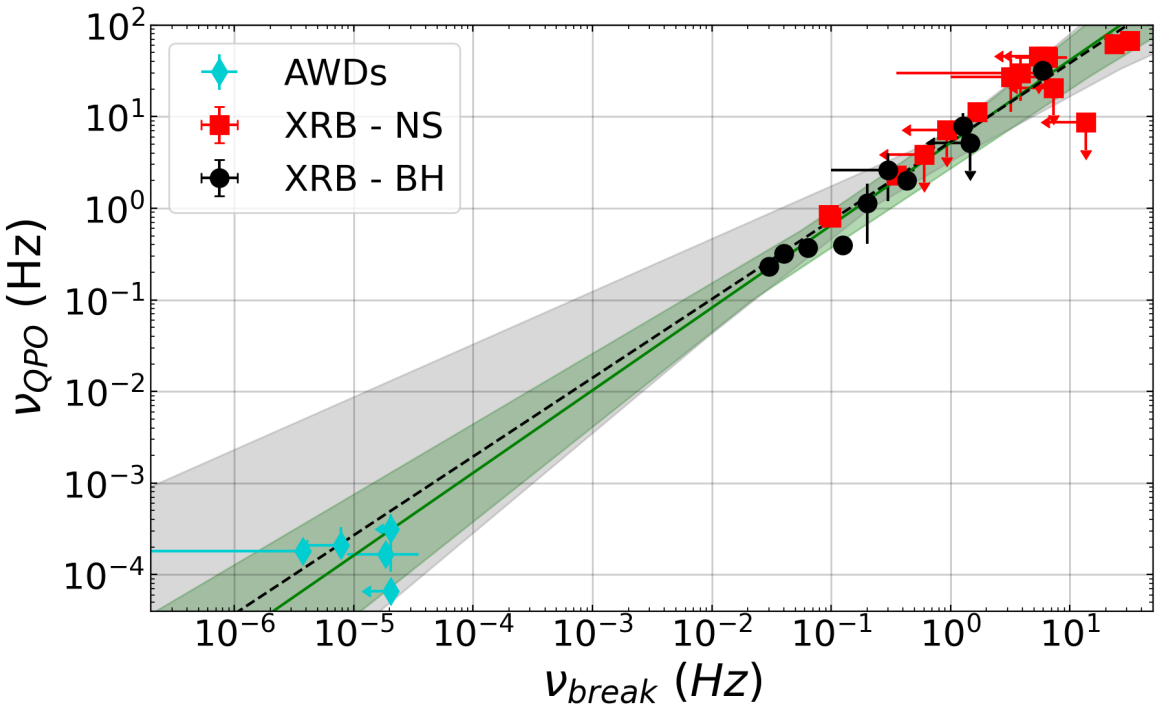

Figure 4.10: QPO frequency as a function of the break frequency. The observed QPOs with their corresponding low frequency breaks are denoted for AWDs in diamonds, for NS XRBs in squares and in filled circles for BH XRBs. For AWDs these are taken from the empirical fit in Section 4.3.2 and Table 4.6. The QPO frequency is the peak frequency as denoted in Equation 4.3.2 using Δ_1 and $\nu_{0,1}$. The only exception is GW Lib where the QPO frequency is taken as half that, since only the 1^{st} harmonic of the QPO is detected in *TESS* with its true fundamental being reported in Chote et al. (2021). The break frequencies are denoted in Table 4.6 by * for each object. The solid line represents the fit to the data from linear least-squares regression and the shaded darker area represents the uncertainty on the fit. The dashed line represents the fit to the data when AWDs are excluded, with the uncertainty being represented by the lighter shaded region.

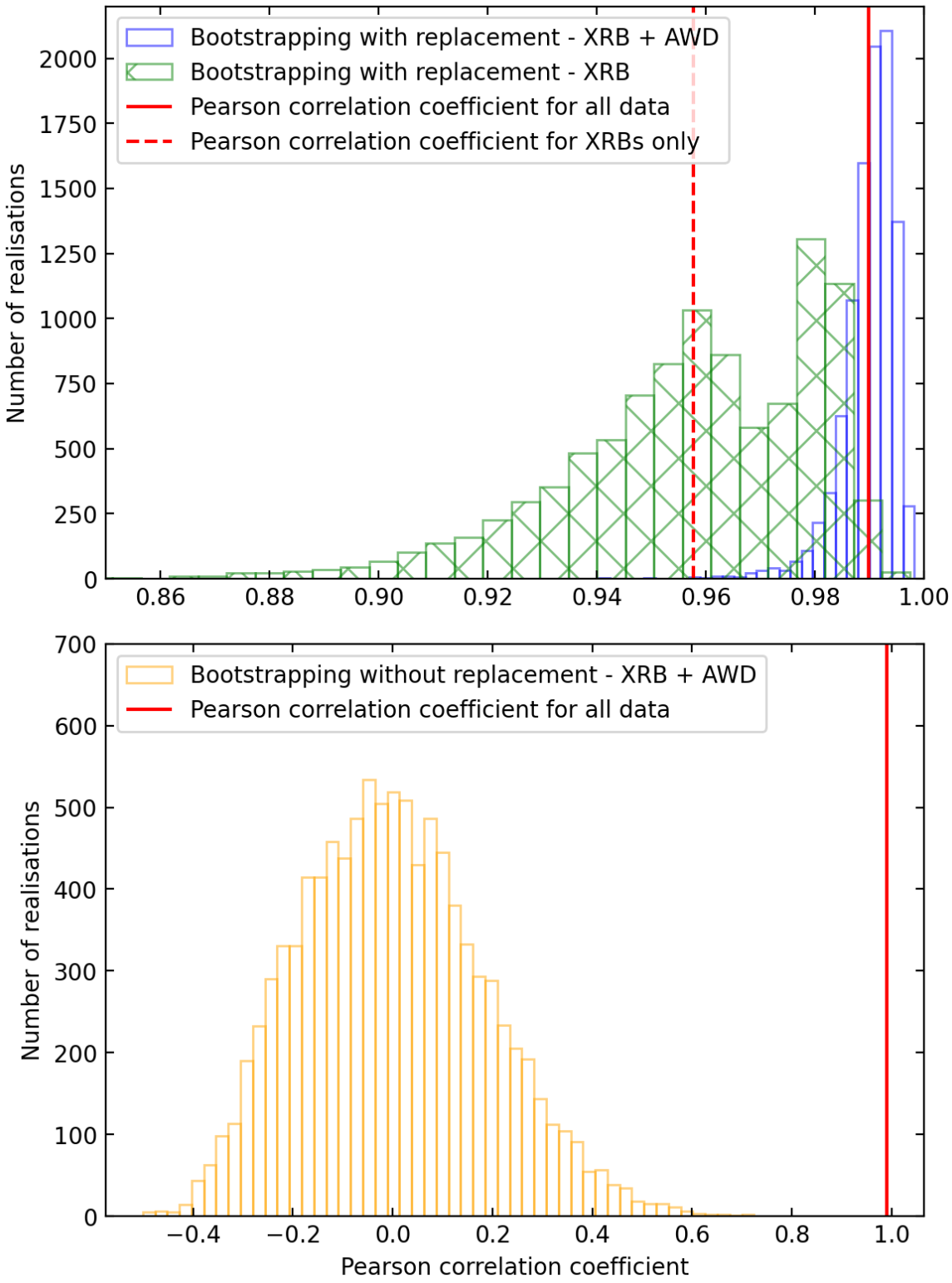

Figure 4.11: *Top*: Distribution of the Pearson correlation coefficient for the bootstrapping of data from Figure 4.10 with replacement. The clear distribution corresponds to bootstrapping of all data, whilst the hatched distribution only drew from the XRB sample from Figure 4.10. The solid line represents the Pearson correlation coefficient of of all data in Figure 4.10 and the dashed line corresponds to the value of the coefficient when AWDs are excluded. *Bottom*: The distribution of the Pearson correlation coefficient resulting from bootstrapping the data from Figure 4.10 without replacement and by randomising one of the axes. The zero-centred distribution shows the 99.99% significance of the correlation from Figure 4.10, with the solid line marking the value of the Pearson correlation coefficient of the data.

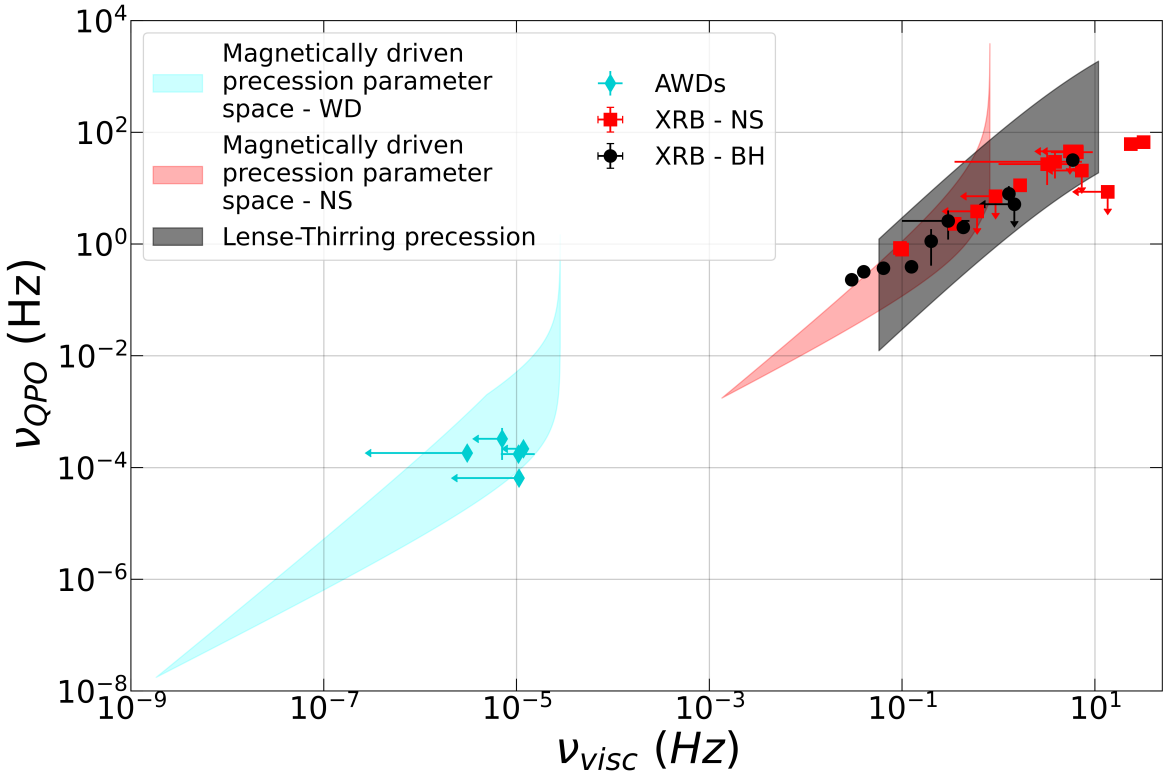

Figure 4.12: QPO frequency as a function of the viscous frequency at the QPO radius. The shaded regions correspond to the predicted model parameter space of QPOs and their viscous frequency. The lowest shaded region between $\nu_{visc} \sim 10^{-10} - 10^{-4}$ Hz represents the model parameter space of AWD QPOs as predicted by magnetically driven precession. For NS XRBs the magnetically driven precession model predicts a parameter space shown by the shaded region between $\nu_{visc} \sim 10^{-4} - 10^{0}$ Hz. The partially overlapping shaded region between $\nu_{visc} \sim 10^{-1} - 10^{2}$ Hz represents the parameter space of QPOs in BH XRBs as predicted by Lense-Thirring precession. The observed QPOs with their corresponding low frequency breaks (ν_{visc} are denoted for AWDs in diamonds, for NS XRBs in squares and in filled circles for BH XRBs.)

Chapter 5

Wobbling around the clock: magnetically-driven quasi-periodic oscillations in pulsating ultraluminous X-ray sources

Abstract

Ultraluminous X-ray sources (ULXs) are X-ray binary systems containing an accreting neutron star (NS) or black hole emitting at luminosities above the Eddington limit of a $10\,\mathrm{M}_{\odot}$ *black hole. Approximately 1900 (either confirmed or candidate) ULXs have been identified to date. Three systems have been confirmed to exhibit coherent signals consistent with NS spin frequencies and quasi-periodic oscillations (QPOs) in the mHz range. Several interpretations for generating such QPOs have been proposed, including general relativistic frame-dragging effects. In this work, I test if an alternative model in which magnetically-driven precession of the inner accretion flow can self-consistently reproduce the observed NS spin and QPO frequencies for reasonable values for accretion rates and NS magnetic field strengths. For a range of parameters, I recover family of solutions with accretion rates* $\approx 10^{-7}$–$10^{-5}\ M_{\odot}\ yr^{-1}$ *and surface magnetic fields* $\gtrsim 10^{12}\ G$*, in agreement with previous estimates. If validated, this interpretation could reconcile several observed properties of pulsating ULXs, including QPO frequencies and the observed high luminosities of these systems, in a self-consistent framework without requiring general relativistic effects and/or strong beaming due to specific viewing angles. Although the predictive power of the model is currently limited by parameter degeneracies and uncertainties, searching for and discovering more pulsating ULX systems will allow to further test or refute the proposed model.*

Co-author contribution

I have conducted the analysis as described in this Chapter and reported in Veresvarska et al. (2025a). The paper was written in collaboration with Dr Matteo Imbrogno, Dr Roberta Amato, Dr Simone Scaringi and Dr Gian Luca Israel. Other co-authors have contributed with suggestions on analysis improvement and comments on the text of the paper.

5.1 Introduction

Ultraluminous X-ray sources (ULXs) are a class of X-ray binaries with luminosities $L_{\rm X} \gtrsim 10^{39}\,{\rm erg\,s^{-1}}$, exceeding the Eddington limit ($L_{\rm Edd} \simeq 1.3 \times 10^{38} M/M_{\odot}\,{\rm erg\,s^{-1}}$, with M being the mass of the accretor) of a $\sim$10 $\rm M_{\odot}$ black hole (BH; see Kaaret et al., 2017; Fabrika et al., 2021; King et al., 2023; Pinto & Walton, 2023, for recent reviews). First detected by the *Einstein Observatory* in the off-nuclear regions of nearby galaxies (Fabbiano, 1989), they have been proposed to be possible intermediate-mass black hole (IMBH) candidates with $M_{\rm BH} \simeq 10^2 - 10^6\,{\rm M_{\odot}}$, accreting at sub-Eddington rates (see e.g. Colbert & Mushotzky, 1999). The presence of mHz quasi-periodic oscillations (QPOs) in some ULXs (see e.g. Strohmayer et al., 2007; Strohmayer & Mushotzky, 2009; Pasham et al., 2015; Atapin et al., 2019), interpreted as the low-frequency counterparts of QPOs in Galactic BH binaries (van der Klis, 1989), seemingly supported this hypothesis. Indeed, using the mass-frequency scaling derived from Galactic BH binaries (e.g. Aschenbach, 2004; Remillard & McClintock, 2006; Smith et al., 2018), the masses inferred from the QPO frequencies are found to be in the IMBH range (see e.g. Casella et al., 2008 and Figure 4 of Smith et al., 2018). However, some differences cast doubt on such simple analogies. For example, in the case of Galactic BH binaries, the QPO frequency $\nu_{\rm QPO}$ tightly correlates with a low frequency break $\nu_{\rm b}$, with $\nu_{\rm QPO} \approx 10\nu_{\rm b}$ (Wijnands & van der Klis, 1999). Such a correlation is not observed in ULXs with QPOs (see e.g. Middleton et al., 2011).

The detection in a few ULXs of coherent pulsations with $P \sim 0.1 - 10\,{\rm s}$ – known as pulsating ULXs (PULXs) – has demonstrated that at least some of these sources are powered instead by neutron stars (NSs) accreting at super-Eddington rates (King et al., 2001; Poutanen et al., 2007; Zampieri & Roberts, 2009). A few of these PULXs also show mHz QPOs at super-Eddington luminosities, providing additional evidence that care is needed when using the QPO frequency in a (P)ULX to estimate the mass of the accretor. A total of 12 (either confirmed or candidate) PULXs have been discovered (see Table 2 of King et al., 2023), with

luminosities up to $\sim 10^{41}\,\mathrm{erg\,s^{-1}}$ (Israel et al., 2017a). How these sources can reach such high luminosities is still unclear, with some arguing that the inferred luminosities (derived under the isotropic emission approximation) could be overestimated due to geometrical beaming (see e.g. King et al., 2017; Lasota & King, 2023).

In this Chapter, I focus on those PULXs that have shown mHz QPOs at (observed) luminosities $\gtrsim 10^{39}\,\mathrm{erg\,s^{-1}}$: M82 X-2 (Feng et al., 2010), M51 ULX-7 (Imbrogno et al., 2024) and NGC 7793 P13 (Imbrogno et al., in prep.). M82 X-2 was the first source identified as a PULX (Bachetti et al., 2014). With a luminosity $L_{\mathrm{X}} \simeq 10^{39} - 10^{40}\,\mathrm{erg\,s^{-1}}$ and an orbital period $P_{\mathrm{orb}} \simeq 2.5\,\mathrm{d}$, the NS powering M82 X-2 is found near spin equilibrium, with a spin period $P \simeq 1.37\,\mathrm{s}$. The source alternates between strong spin-up and spin-down phases over the years, despite less drastic changes in luminosity, and shows a spin evolution inconsistent with that expected from a slow rotator, as shown by Bachetti et al. (2020). M82 X-2 is also a good example of how the estimate of the mass of the accretor in a ULX from the QPO frequency can be misleading. The nature of the accretor was unknown when Feng et al. (2010) detected a QPO at $\nu \simeq 3\,\mathrm{mHz}$ in a few *Chandra* observations, leading the authors to conclude that the source was a good IMBH candidate, with $M \simeq 12000 - 43000\,\mathrm{M_\odot}$, $\sim$ four orders of magnitude larger than the real mass ($M \simeq 1.4\,\mathrm{M_\odot}$).

M51 ULX-7, whose spin pulsations at $P \simeq 2.8\,\mathrm{s}$ were first detected by Rodríguez Castillo et al. (2020), is the PULX with the shortest known orbital period ($P_{\mathrm{orb}} \simeq 2\,\mathrm{d}$; Hu et al., 2021; Vasilopoulos et al., 2021). It is also characterised by a super-orbital modulation, initially detected with a period $P_{\mathrm{so}} \simeq 38\,\mathrm{d}$, but later found to be gradually evolving towards a longer period $P_{\mathrm{so}} \simeq 45\,\mathrm{d}$ (Brightman et al., 2020; Vasilopoulos et al., 2020; Brightman et al., 2022). Recently, Imbrogno et al. (2024) detected a flaring-like feature in the light curve of three *XMM-Newton* observations of the source. A Fourier analysis of these data revealed the presence of a QPO at a frequency $\nu \simeq 0.5\,\mathrm{mHz}$. The same feature was detected also in *Chandra* archival observations. In both sources, the QPO is always present at the same frequency (Imbrogno et al., 2024).

Lastly, NGC 7793 P13 is the fastest known PULX, with a spin period $P \simeq 0.4\,\mathrm{s}$ (Fürst et al., 2016; Israel et al., 2017b). It is the only PULX with an identified optical counterpart (Motch et al., 2011). A peculiarity of this system is that the orbital periods estimated through optical ($P_{\mathrm{opt}} \simeq 64\,\mathrm{d}$) and X-ray ($P_{\mathrm{X}} \simeq 65\,\mathrm{d}$) are not compatible, an inconsistency which remains without a clear explanation (Fürst et al., 2018, 2021). Recently, a QPO at $\nu \simeq 10\,\mathrm{mHz}$ was detected in a few *XMM-Newton* observations of NGC 7793 P13 (Imbrogno et al., in prep.).

As for M51 ULX-7, the QPO is always found at a specific frequency and only when the system emits at super-Eddington luminosities.

Various models have been proposed to explain the presence of mHz QPOs in (P)ULXs. Middleton et al. (2019) proposed that mHz QPOs arise from a precessing inner flow of the disc. The general relativistic frame-dragging torque (inducing Lense-Thirring precession) is then communicated to the launched winds, whose precession is expected to cause the much longer super-orbital period seen in many (P)ULXs (see e.g. Kong et al., 2016; Walton et al., 2016; Fürst et al., 2018; Vasilopoulos et al., 2020; Brightman et al., 2020, 2022). Atapin et al. (2019), instead, proposed that the propagating fluctuations mechanism from Lyubarskii (1997) can explain both the QPO and the flat-topped noise observed in a sample of ULXs. Majumder et al. (2023) followed Das et al. (2021) to link the QPO frequency to the infall time towards the inner radius of the disc, and hence proposing to use the QPO frequency to infer the masses of the central object, assumed to be a BH. A similar mechanism for generating quasi-periodic variability, but for NSs, is also explored in Mushtukov et al. (2024).

Contrary to BHs, the presence of a magnetosphere and its dynamical importance to the accretion flow in PULXs can be substantial and is expected to exert additional torques on the inner flow. The effect of the magnetosphere through what I refer to here as the magnetically-driven precession model (MDP model hereafter) has been explored for both magnetised NSs and T Tauri stars by Lai (1999) and more recently for accreting white dwarfs (WDs) by Veresvarska et al. (2024a). In this Chapter, I explore the validity of applying the MDP model, presented in Sect. 5.2, to the mHz QPOs recently detected in a few PULXs. In particular, I want to verify if the MDP model can simultaneously match the spin and QPO periods observed in these PULXs for reasonable values of the accretion rate and the magnetic field. With this goal in mind, I apply the model to the PULXs showing QPOs and present the results in Sect. 5.3. Finally, I discuss the implications of my results, together with the strengths and limitations of the model in Sect. 5.4.

5.2 Magnetic precession model

The MDP model can in principle generate QPOs from magnetically driven precession, where the accretion flow surrounding a rotating magnetised star experiences a quasi-periodic wobbling motion around the star's spin axis. The interaction between the disc and the star's magnetic field induces a warping effect, causing the inner flow to deviate from its equatorial

plane and to undergo precession. This precessing motion is driven by the torque that arises from the interaction between the misaligned disc's surface currents to the star's magnetic field, generated by its dipole, in the plane of the accretion disc.

The MDP model further explores the non-linear evolution of the warped disc, as detailed by Pfeiffer & Lai (2004). The application of this model to low-frequency QPOs in NSs is also examined in Shirakawa & Lai (2002b,a). Within this framework the global precession of the disc can generate the observed QPOs, offering insights into the underlying mechanisms driving these oscillations in various accreting systems, including WDs and NSs.

Lai (1999) estimates the precession frequency of the entire inner flow by scaling the magnetic precession frequency of a specific ring at a characteristic radius, r, $\nu_{\rm p}(r)$, with a dimensionless constant A. The value of the constant A depends on the disc structure. Shirakawa & Lai (2002b,a) estimate A in the range $0.3-0.85$ and here I fix this to a fiducial value of 0.65 (close to the midpoint of the quoted range). This leads to the expression for the QPO frequency:

$$\nu_{\rm QPO} = A\nu_p(r) = \frac{A}{2\pi^3}\frac{\mu^2}{r^7\ \Omega(r)\ \Sigma(r)}\frac{F(\theta)}{D(r)}, \tag{5.2.1}$$

where μ represents the stellar magnetic dipole moment ($\mu = BR^3$, with B as the surface magnetic field strength and R the stellar radius), Ω is the Keplerian angular frequency, and Σ is the surface density of the disc (here assumed to be represented by Equation 5.41 in (Frank et al., 2002b)) as adopted for the NS application of the MDP model in Lai (1999); Shirakawa & Lai (2002a).

The dimensionless function $F(\theta)$ is defined such that $F\left(\theta\right) = 2f\cos^2\theta - \sin^2\theta$, where θ is the angle between the magnetic moment of the accretor and the angular momentum of the disc. The dimensionless number f ($0 \leq f \leq 1$) determines what part and how much of the vertical magnetic field is being screened out; here, I take $f = 0$ as in Pfeiffer & Lai (2004); Veresvarska et al. (2024a), so that only the spin-variable vertical field is screened out (for $f = 1$ all the vertical field is screened out). $D\left(r\right)$ is a dimensionless function given by

$$D\left(r\right) = \max\left(\sqrt{\frac{r^2}{r_{\rm in}^2} - 1}, \sqrt{\frac{2H\left(r\right)}{r_{\rm in}}}\right), \tag{5.2.2}$$

where $H\left(r\right)$ is the half-height of the disc at radius r and $r_{\rm in}$ is the magnetospheric radius from Eq. 1.3.2. In the first applications to NS in Lai (1999); Shirakawa & Lai (2002a) and the WD application in Veresvarska et al. (2024a) of the MDP model the disc half-height is assumed from Equation 5.41 in Frank et al. (2002b). Here I retain this height prescription.

The overall sub-Eddington treatment of the model here is anchored in the assumption that $r_{\rm M} > r_{\rm sph}$, where $r_{\rm sph}$ is the spherisation radius, defined as the radius at which the inflow starts to be supercritical (Poutanen et al., 2007) and $r_{\rm M}$ is the magnetospheric radius.

An alternative half height prescription which could lead to exploration of the model within the spherisation radius is detailed in (Lipunova, 1999). Compared to the thin disc prescription, the steeper dependence of disc height on accretion rate results in a $\frac{H}{R} \sim 1$ at $\dot{M} \sim 10^{-6} - 10^{-5} M_{\odot} yr^{-1}$ for a $1.4 M_{\odot}$ NS with 10 km radius. This prescription for the half-height of the disc in Lipunova (1999) results in the inverse dependence of QPO frequency on accretion rate as opposed to the direct dependence for a thin-disc prescription. However, implementation of the super-Eddington regime would also require further changes to the model, namely in the surface density and the condition of $r_{\rm M} < r_{\rm sph}$. Exploration of this implementation is the subject of future work and beyond the scope of this Chapter.

Table 5.1 lists all the parameters adopted in this study together with the explored ranges, where some are set to fixed fiducial values. Although some of the parameter ranges can be constrained from the work of Chashkina et al. (2017, 2019) (where $\alpha \sim 0 - 0.2$ for M82 X-2), I here explore all parameter ranges given in Table 5.1 for completeness.

In order to reduce several parameter degeneracies, I here assume spin equilibrium such that the co-rotation ($r_{\rm co}$) and magnetosphere ($r_{\rm M}$) radii are equal. This is a reasonable assumption in the case of M82 X-2, as already discussed in the Introduction, while it comes with some caveats for NGC 7793 P13 and M51 ULX-7, which are currently spinning up (see Fürst et al., 2021, 2025; Brightman et al., 2022 and the Discussion).

Assuming spin equilibrium, I can anchor the QPO radius to the spin and magnetic field, reducing the degeneracy between them. Thus, $r = r_{\rm M} = r_{\rm co}$, where the co-rotation radius is defined as:

$$r_{\rm co} = \left(\frac{G M P_{\rm spin}^2}{4\pi^2} \right)^{\frac{1}{3}}, \tag{5.2.3}$$

where $P_{\rm spin}$ is the spin period of the NS, M its mass and G the gravitational constant. Similarly, the magnetospheric radius is here defined as:

$$r_{\rm M} = \eta \left(\frac{2\pi^2}{\mu_0^2} \frac{\mu^4}{G M \dot{M}^2} \right)^{\frac{1}{7}}, \tag{5.2.4}$$

where μ_0 is the vacuum permeability. η is generally assumed to be 0.5 (Wang, 1987; Ghosh & Lamb, 1979b; Campana et al., 2018), however a wider range of values (Table 5.1) are explored here. Implications of this assumption on the model are further discussed in Section 5.4. A

Table 5.1: Model parameters for the magnetically driven precession model for QPOs in NS XRBs. Parameters with their explored ranges are given. For some cases they are fixed to a fiducial value, where only that one is given and denoted by *.

Model Parameter	Value
M* ($M_\odot$)	1.4
R* (km)	10
B (G)	$10^8 - 10^{15}$
$\dot{M}$ ($M_\odot yr^{-1}$)	$10^{-10} - 10^{-3}$
α	$10^{-3} - 1$
η	$10^{-2} - 1$
θ (°)	0 - 90
A*	0.65

parameter of the MDP model is the mass accretion rate $\dot{M}_{\rm acc}$ onto the compact object, which can differ from the mass loss rate from the donor star through the L1 point (see Section 5.4). I can obtain a rough estimate of $\dot{M}_{\rm acc}$ through the gravitational energy released assuming most is emitted at X-ray wavelengths:

$$\dot{M}_{\rm acc} = \frac{2bR_{\rm NS}L_{\rm obs}}{GM_{\rm NS}} \tag{5.2.5}$$

where b is the beaming factor (such that $b = 1$ corresponds to no beaming), $L_{\rm obs}$ is the observed isotropic luminosity of the source, $M_{\rm NS}$ and $R_{\rm NS}$ are the mass and radius of the NS. Note that the $L_{\rm obs}$ does not distinguish between the luminosity of the different components of the system (i.e. accretion disc, winds, etc.), but represents the observed luminosity as an upper limit. Furthermore, the linear relation between accretion rate and luminosity is used, as opposed to Equation 4 in (Middleton et al., 2023), since within the framework of the assumptions made here, it is expected that $r_{\rm M} > r_{\rm sph}$. In such cases super-Eddington accretion can be sustained for high magnetic field strengths (Gúrpide et al., 2021).

5.3 Results

I apply the model described in Section 5.2 and explore the parameter space as detailed in Table 5.1 to three PULXs, namely M82 X-2, M51 ULX-7 and NGC 7793 P13, for which both the spin and QPO periods have been detected.

The parameter space in Table 5.1 presents a wide array of combinations leading to a family of solutions with the same QPO and spin. To explore this non-linear parameter space and recover families of solutions that can reproduce the observed spin and QPO frequencies, I first generate 10^8 model realisations using parameter combinations randomly drawn from a

Table 5.2: List of observational parameters present in literature and the B field inferred form the MDP model, for the three PULXs considered in this work

Source	References	$P_{\rm spin}$ (s)	$\nu_{\rm QPO}$ (mHz)	$-\dot{M}_\star$ ($10^{-7}\,{\rm M}_\odot\,{\rm yr}^{-1}$)	$\dot{M}_{\rm acc}/b$	b	$B_{\rm MDP}$ ($10^{13}\,{\rm G}$)
M82 X-2	[1,2,3]	1.32−1.39	2.77−3.98	47(2)	20−40	1	> 0.8
					2−4	0.1	> 0.3
M51 ULX-7	[4,5,6]	2.79−3.28	0.53−0.56	–	5−12	1	> 2
				–	0.5−1.2	0.1	> 0.7
NGC 7793 P13	[7,8,9,10]	0.406−0.420	11−15	–	5−8	1	> 0.3
				–	0.5−0.8	0.1	> 0.1

Notes. Reference values for $P_{\rm spin}$, $\nu_{\rm QPO}$ and (in the case of M82 X-2) $\dot{\rm M}_\star$, the overall mass-transfer rate from the companion, taken from: [1] Feng et al. (2010); [2] Bachetti et al. (2022); [3] Liu (2024); [4] Rodríguez Castillo et al. (2020); [5] Imbrogno et al. (2024); [6] Earnshaw et al. (2016); [7] Fürst et al. (2016); [8] Israel et al. (2017b); [9] Fürst et al. (2021); [10] Imbrogno et al. (in prep). The reported values of the mass-accretion rate $\dot{\rm M}_{\rm acc}$ for b=1 have been inferred from the X-ray luminosities (typically in the 0.3–10 keV band) of the datasets where QPOs have been detected.

flat distribution in log space (apart from θ as the range spans fewer orders of magnitude than the other parameters) within the ranges given in Table 5.1. I then retain those parameter combinations for which both the model-predicted QPO and spin are within the 1σ errors of their measured values as reported in Table 5.2. In the case of M82 X–2, where several QPO measurements exist, I take the average of the individual QPO measurements from Table 1 of Feng et al. (2010). In the case of M51 ULX-7, the QPO was fitted with two separate Lorentzians in Imbrogno et al. (2024). Here I assume that the Lorentzian at lower frequency with larger $Q = \frac{\nu}{\Delta\nu} \geq 2.1$ is the QPO, whilst the higher frequency Lorentzian corresponds to the "broad component". Finally, in the case of NGC 7793 P13 I found that one Lorentzian was enough to model the QPO (Imbrogno et al., in prep.) and I took the average value of the QPO frequency.

The model realisations (under the assumption of no beaming i.e. $b = 1$) which reproduced the QPO frequencies and spin periods within their errors are shown in Figure 5.1 for M82 X-2 and in Figure A.6 and A.7 for M51 ULX-7 and NGC 7793 P13 respectively, as grey points. Figures 5.1, A.6 and A.7 show a corner plot displaying a parameter sweep through all combinations.

I first consider the case of M82 X-2, since it is also the only PULX for which an estimated measurement mass-transfer rate from the donor star ($\dot{M}_\star$) has been inferred from the derivative of the orbital period (Bachetti et al., 2022) (although note King & Lasota (2021) associate this signal to stochastic variability). Assuming the orbital period derivative is indeed driven by the mass-transfer rate from the donor, I can reduce the number of family of solutions that can

reproduce the QPO and spin of M82 X-2. The red diamonds in Figure 5.1 represent another set of model realisations in which all parameters are randomly drawn from flat distributions as for the grey points, but are additionally constrained by a uniform distribution within the range of $\dot{M}_\star$ in Table 5.2. With this additional constrain a correlation between B and η is observed, where lower B requires higher η (Figure 5.1). A similar relation is found between B and $\dot{M}$, where higher $\dot{M}$ provides reasonable constraints for higher B, when not considering the $\dot{M}$ constraint from Table 5.2. Therefore, limiting $\dot{M}$ for M82 X-2 yields a smaller set of family of solutions with a lower limit on $B \gtrsim 1 \times 10^{13}$G. Furthermore the observed X-ray luminosity can be explained with no beaming with the assumed mass accretion rate. Nevertheless, I show in Table 5.2 the effects on the recovered B field assuming a moderate beaming of $b = 0.1$. I also explored the effects of moderate beaming, likely due to the geometry of the inner part of the accretion disk and the presence of a wind component often observed in ULXs (Middleton et al., 2015; Pinto et al., 2016; Pinto & Kosec, 2023). It is worth noting that the MDP model does not directly include beaming but only mass accretion rate. Thus in producing the red points in Figure 5.1, b is set to the minimum luminosity required to justify the observed $\dot{P}$. The effect of varying the beaming factor (for $b = 0.1$) is shown by the blue diamonds in Figures A.6 and A.7. This has the effect of lowering the required accretion rate (see Eq. 5.2.5), which allows for a factor ≈ 3 lower B fields. The other parameters remain largely unaffected. In either case, the dipolar magnetic field B is found to be larger than 10^{12} G for all three sources.

5.4 Discussion and conclusions

The magnetic torque exerted by the NS on the accretion disc generates a precession of the innermost regions, potentially giving rise to the observed mHz QPOs. Other torques have been invoked to explain these QPOs, as well as the superorbital periodicities observed in several ULXs. For instance, the Lense-Thirring precession model has been applied to the non-pulsating NGC 5408 X-1, to interpret both its QPOs and time lags (Middleton et al., 2019). Other possible mechanisms that can induce precession are asymmetries in the NS with respect to its spin axis (free-body precession, Jones & Andersson, 2001), magnetic or self-induced warping (Lai, 2003; Pfeiffer & Lai, 2004; Pringle, 1996), tidal torque from the donor star (Frank et al., 2002b) and warping of an inclined disc due to the relativistic Bardeen-Petterson effect (Bardeen & Petterson, 1975). Two or more of these mechanisms could in principle be competing. This would explain, for instance, the presence of (magnetically-induced) QPOs

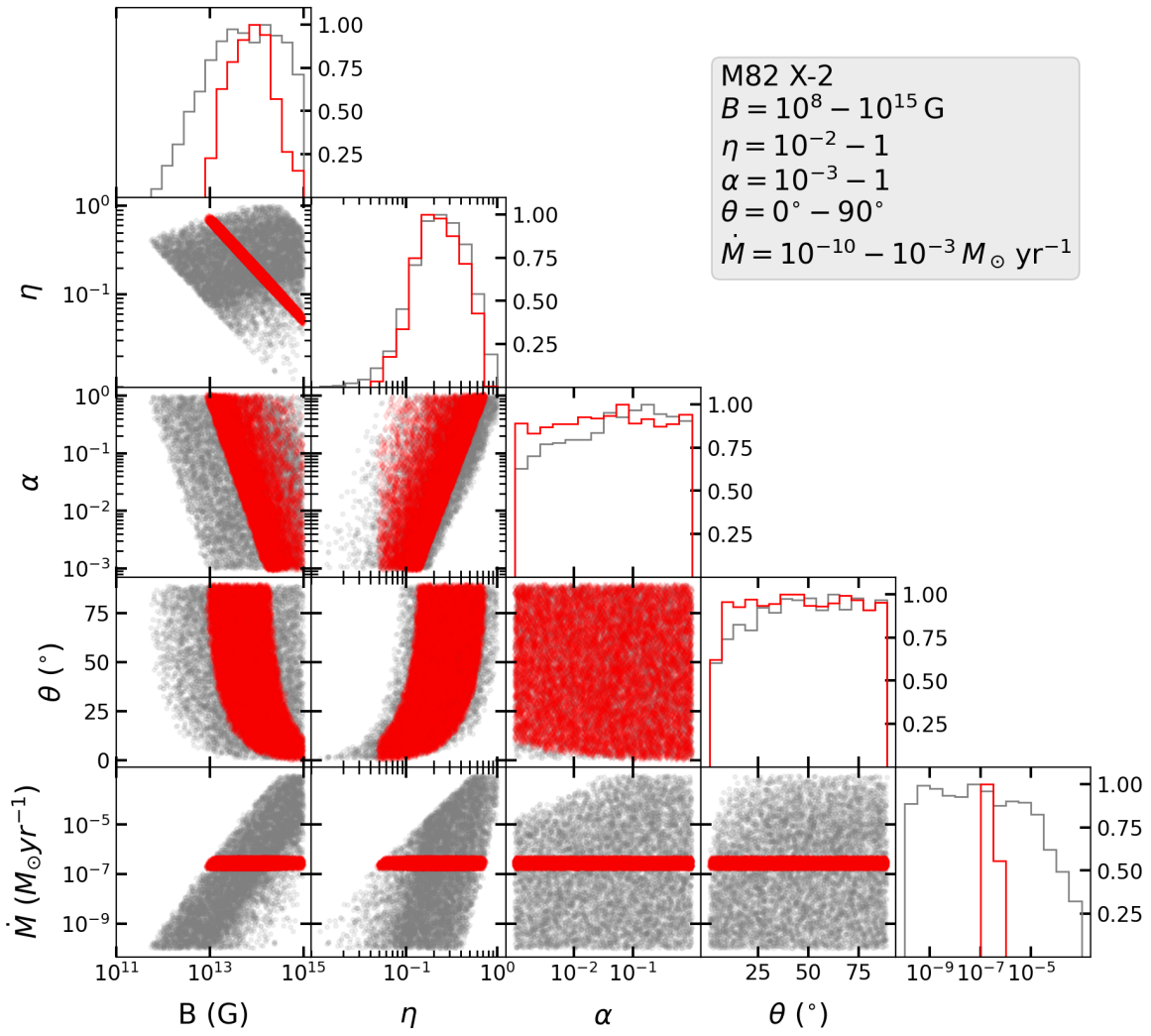

Figure 5.1: Parameter space of the MDP model with all parameter combinations (in grey circles) producing QPO frequency and spin within the observed errors as noted in Table 5.2. All the solutions which also reproduce accretion rate within the range given by the observed $\dot{P}$ are given in red diamonds. Distributions of all parameters are provided, with all being scaled to unity. The explored parameter ranges are noted as also shown in Table 5.1.

and superorbital periods observed in all three PULXs discussed in this work. Middleton et al. (2018) discussed the relative strengths of magnetic and Lense-Thirring torques in ULXs, concluding that the magnetic torque would be negligible for $B \sim 10^{10-11}$ G and $\alpha \sim 0.01$. However, for larger B, as considered here (Table 5.2) and larger α, the magnetic torque is expected to be more dominant and becomes a viable option for generating QPOs. Another relativistic effect that can be present concurrently with magnetic warping is the Bardeen-Patterson effect (Bardeen & Petterson, 1975; King et al., 2005; Ingram & Motta, 2019). In such a case, an inner tilted disc is warped towards the orbital plane of the system at similar scales as the Lense-Thirring precession. However, a lower limit on the QPO frequency caused by this effect can be set at $\sim 3\,\mathrm{Hz}$ (Fragile et al., 2001). This is significantly higher than the frequencies of the QPOs reported in this work in Table 5.2, making it unlikely that the Bardeen-Petterson effect and the magnetically induced warp can counteract one another on the same scale size in the disc.

Despite the complexity of the phenomena that can generate QPOs, in this work I focussed on the effects of a misaligned NS magnetic field to the accretion disc (MDP model) and recovered reasonable family of solutions. In the following Sections, I discuss and outline the most important aspects and limitations of the model when applied to the QPOs in PULXs (Section 5.4.1), the effects of beaming on the accretion rate of the systems, the implications on the preferred model parameters (Section 5.4.2), the implications of the model on the properties of the PULXs, as well the potential avenues for identifying future candidates of mHz QPOs that can test the MDP model further (Section 5.4.3).

5.4.1 Limitations of the model

Given the number of free parameters in Table 5.1 any conclusions drawn from the model application should be treated with caution. Apart from the lack of direct observational evidence for the viability of the inferred parameters, it is also important to discuss other assumptions used by the model. One of them is the systems are in spin-equilibrium, such that $r = r_{\rm in} = r_{\rm M} = r_{\rm co}$. This is not necessarily the case for any system with an observed secular spin-up or spin-down (Fürst et al., 2021). By analogy however, accreting WDs that are thought to be in spin-equilibrium do display both spin-up and/or spin-down around the equilibrium point (Patterson et al., 2020). Nonetheless, the adopted spin-equilibrium assumption adopted here conveniently removes several parameter degeneracies. As already mentioned, this assumption is likely correct only by M82 X-2 at present - but crucially not

when the QPOs were detected. I further note that the model is very sensitive to parameters α and θ, whose combinations are degenerate in all ULXs as seen in Figures 5.1, A.6 and A.7. As shown in Figure 5.1 for M82 X-2, high accretion rates rule out low viscosity α and low angles θ.

The MDP model is also very sensitive to changes in η. However constraining the mass accretion rate significantly constrains η. The standard value of $\eta \sim 0.5$ used in literature for magnetic accretors (Wang, 1987; Ghosh & Lamb, 1979b; Campana et al., 2018) is used as the fiducial value and reproduces reasonable results, for $\alpha \gtrsim 0.1$ and B on the lower end of the range given in Table 5.2 for most systems. However M82 X-2 has been reported to be out of spin-equilibrium during some of the QPO measurements (Liu, 2024). It is thus not surprising that families of solutions with $\eta < 0.5$ can reproduce the observed accretion rate in Table 5.2.

Similarly, NGC 7793 P13 is known to be out of spin-equilibrium (see the long-term evolution of the spin period discussed by Fürst et al., 2021 and Fürst et al., 2025). Following the example of M82 X-2, $\alpha \sim 0.1 - 0.2$ would require setting $\eta \sim 0.3$ to reproduce the observed accretion rates $\dot{\mathrm{M}}_{\mathrm{acc}}/b$, well below the observational limit for the mass loss of the known donor (see below). Naturally, a higher value of α would then also allow for $\eta = 0.5$.

The present model does not take into account all key aspects of super-Eddington accretion physics (e.g. Shakura & Sunyaev, 1973; Poutanen et al., 2007), but it is interesting nonetheless that it can recover reasonable families of solutions.

For a NS accreting at super-Eddington rates, the magnetospheric radius, r_{M}, is usually smaller than r_{sph}, depending on the magnetic field strength and accretion rate, as also shown in numerical simulations (Chashkina et al., 2017, 2019), also inferred from the application of the MDP model to the three considered PULXs. Using the equation for spherisation radius from Poutanen et al. (2007) and the measured spin periods of the 3 PULXs considered here, the spherisation radii for the sources considered here are $\sim 990\ R_{\mathrm{g}}$, $\sim 165\ R_{\mathrm{g}}$ and $\sim 330\ R_{\mathrm{g}}$ for M82 X-2, M51 ULX-7 and NGC 7793 P13 respectively, with R_{g} being the gravitational radius. However the associated magnetospheric radii based on the observed spins and $r_{\mathrm{M}} = r_{\mathrm{CO}}$ are $\sim 990\ R_{\mathrm{g}}$, $\sim 1700\ R_{\mathrm{g}}$ and $\sim 450\ R_{\mathrm{g}}$ for M82 X-2, M51 ULX-7 and NGC 7793 P13 respectively. This suggests that $r_{\mathrm{M}} \sim r_{\mathrm{sph}}$ only for M82 X-2. For M51 ULX-7 and NGC 7793 P13 $r_{\mathrm{M}} > r_{\mathrm{sph}}$, as also suggested by Gúrpide et al. (2021) for high magnetic fields. This would imply the model applied here is self-consistent, at least for M51 ULX7 and NGC 7793 P13 and justifies my assumption of ignoring mass-loss.

5.4.2 Beaming factor

The MDP model requires a mass accretion rate, which can be converted to an observed luminosity assuming a beaming factor (Eq. 5.2.5). As already discussed in Section 5.3, beaming is likely present and should be considered. Whether this beaming is moderate or extreme is still a matter of debate (see e.g. Israel et al., 2017a and King & Lasota, 2020 for both scenarios).

For M82 X-2, strong beaming is not required to reconcile the observed X-ray luminosity with the mass accretion rate inferred by Bachetti et al. (2022) through the secular orbital period derivative $\dot{P}_{\rm orb}$. In the case of M51 ULX-7 and NGC 7793 P13, the available X-ray data do not allow a $\dot{P}_{\rm orb}$ measurement, and therefore an estimate of $\dot{\rm M}_\star$. However, the latter can be inferred from the observed luminosity, as $L_{\rm obs} = L_{\rm acc}/b$. Some recent observational results suggest that if the beaming is present, it should be relatively small (see e.g. Israel et al., 2017a; Rodríguez Castillo et al., 2020). This is also the case for another PULX, NGC 5907 ULX-1, for which a luminosity of 10^{41} erg s^{-1} has been inferred from its surrounding nebula, suggesting that it is a genuine super-Eddington accretor with no need of (strong) beaming (Belfiore et al., 2020). Additionally, the morphology and strength of He II, Hβ and [O I] emission regions in the nebula surrounding Ho II X-1 and NGC 1313 X-1 strongly argue against the presence of extreme beaming (Kaaret et al., 2004; Gúrpide & Castro Segura, 2024). Moreover, the inferred mass-transfer from the companion $\dot{M}_{\rm orb}$ in M82 X-2 shows that the mass available for accretion onto the NS is $\sim$150 M$_\odot$yr^{-1}, high enough to account for the observed luminosity (100 times the Eddington limit) without invoking (strong) beaming (Bachetti et al., 2022). Finally, as already emphasised, strong beaming would imply a too small torque on the NS to account for the observed $\dot{P}$. Because of this I explored moderate beaming factors (>1/10), resulting in a reduction of the predicted B field by about a factor of ~ 4. For M82 X-2 and M51 ULX-7 this still poses a lower limit on the $B \gtrsim 10^{13}$ G within the MDP model assumptions and $B \gtrsim 10^{12}$ G for NGC 7793 P13.

5.4.3 Implications of the model and future perspectives

As discussed in Section 5.4.1, the MDP model is based on the standard accretion theory for an optically thick, geometrically thin disc (Shakura & Sunyaev, 1973), with a modification for the disc thickness to mimic a supercritical accretion disc, but without taking into account any further element specific to super-Eddington accretion (winds, thick disc, radiation pressure, etc.). When applied to the sample of PULXs, the model yields reasonable families of solutions

with mass-accretion rates, spin and QPO frequencies consistent with those obtained from observations. Within the recovered families of solutions, the inferred dipolar magnetic fields are found to be between a few 10^{12} G and a few 10^{13} G, also consistent with the literature estimates (Fürst et al., 2016; Israel et al., 2017b; Rodríguez Castillo et al., 2020; Bachetti et al., 2022), and of the same order of magnitude to the known X-ray pulsars in HMXBs in our Galaxy and in the Magellanic Clouds.

A potential implication of the MDP model may be the transitional behaviour of QPOs and spin pulses in M51 ULX-7, where the QPO is observed when the spin signal is absent and vice versa, without significant spectral variations in the source (see Imbrogno et al., 2024 for details). Within the MDP model, this may suggest that the tilted, precessing inner flow could partially or fully obscure the neutron star's accretion column. In this case, large values of θ would cause a drop in pulse coherence, while when $\theta \sim 0$, the alignment minimises obscuration, leading to increased pulse coherence and the absence of QPOs, due to the inner disc symmetry. It is worth clarifying that while the lack of spin pulses is attributed to the precession of the inner disc, θ relates to the tilt of the outer parts of the disc (Veresvarska et al., 2024a). This suggests that the outer disc may also precess to some extent, potentially influencing the overall dynamics of the system, as noted in Imbrogno et al. (2024). A more detailed investigation of how the outer and inner disc regions interact and contribute to observed variability could provide further insights into the coupling between QPOs, spin pulses, and disc precession.

Further implication arises from the expected observational correlations depending on the assumed disc half-height prescription. As mentioned above, assuming a thin disc from Shakura & Sunyaev (1973) yields a positive correlation between the QPO frequency and the accretion rate. On the other hand, the disc half-height prescription more appropriate for a geometrically thick ULX inner disc (Lipunova, 1999) yields a negative correlation. Therefore, with sufficient data on a given QPO in different states, the QPO frequency is expected to change based on the underlying accretion rate, with the variations being driven by the type of inner accretion flow. A QPO with a non-varying frequency throughout different states would thus rule out the MDP model. However, such data is not available, with M51 ULX-7 showing very little variation in QPO frequency over ~ 10 year period where state changes have not been observed (Imbrogno et al., 2024).

In principle, the MDP model could provide a direct way to estimate the magnetic field strength from the QPO and spin frequencies. However, the dependence on other uncon-

strained model parameters (α, θ and accretion rate) make this challenging. Despite this, new and independent measurements of the magnetic field strength, could lead to a new method to constrain η and potentially α.

Furthermore, with M82 X-2 in spin equilibrium and based on the assumptions that spin equilibrium implies $\eta \sim 0.5$ and $r_{\rm M} \sim r_{\rm CO}$, the MDP model predicts that the QPO should move to lower frequencies for the same spin and accretion rate ($\sim 5 \times 10^{-4}$ Hz assuming the viscosity remains unchanged).

Of all the analysed PULXs, NGC 7793 P13 is the only one with a known companion star (B9Ia class, Motch et al., 2014). The estimated mass-loss rate of the star can be as high as $\sim 10^{-5}$ $\rm M_\odot\,yr^{-1}$ (El Mellah et al., 2019). Adopting this value as an upper limit on the mass-transfer rate in ULXs, I can place limits on the expected spin period and magnetic field strength of other candidate PULXs showing mHz QPOs. As an example, 2CXO J140314.3+541816 (Urquhart et al., 2022) and 4XMM J111816.0-324910 (Motta et al., 2020) have been suggested to host accreting NSs due to a hard spectrum and large variation in the luminosity, respectively. Using the same model set-up and adopting the fiducial parameters from Table 5.1, I explore the family of solutions adopting the strict upper limit for the mass-transfer rate of $\dot{M}$ $<10^{-5}$ $\rm M_\odot\,yr^{-1}$. For the QPO in 2CXO J140314.3+541816 at 1.35−1.92 mHz I infer 0.5 ms $\lesssim P_{\rm spin} \lesssim$ 8 s and $B > 3 \times 10^9$ G, consistent with the previously suggested $B \sim 10^{10}$G and $P_{\rm spin} \sim$ 5ms (Urquhart et al., 2022). Similarly for 4XMM J111816.0-324910 I infer 0.5 ms $\lesssim P_{\rm spin} \lesssim$ 4 s and $B \sim 10^{10}$G for QPO frequency ∼0.3 mHz. I note that these limits only pertain to the specific case of the fiducial parameters from Table 5.1. Nevertheless, assuming the magnetically driven precession model as the mHz QPO driver suggests a spin period range for potential new pulsation detections. Obtaining new independent measurements of the dipolar magnetic field of the NSs could help remove some of the degeneracies in the model. This could then potentially open up an avenue of independent constraint on the elusive nature of viscosity α.

5.5 Parameter space exploration for QPOs in AWDs

The new parameter space exploration implemented in this Chapter and in Veresvarska et al. (2025a) was developed after the publication of the QPOs in AWDs in Veresvarska et al. (2025a) (Chapter 4). Hence the QPO properties exploration in Chapter 4 was kept as published. In this Section I will outline a more detailed parameter space exploration of the QPOs

Table 5.3: Model parameters for the magnetically driven precession model for QPOs in AWDs. Parameters with their explored ranges are given. For some cases they are fixed to a fiducial value, where only that one is given and denoted by *.

Model Parameter	Value
M* ($M_\odot$)	0.8
R* ($R_\odot$)	0.01
B (G)	$10^3 - 10^{11}$
$\dot{M}$ ($M_\odot yr^{-1}$)	$10^{-15} - 10^{-4}$
α	$10^{-6} - 1$
η	$10^{-5} - 1$
θ (°)	0 - 90
A*	0.65

in AWDs from Chapter 4 as was done for QPOs in PULXs this Chapter and Sections 5.3 and 5.4. In particular, the results of the parameter exploration are outlined in Section 5.5.1 and they are discussed in Section 5.5.2.

5.5.1 Results: AWDs

Chapter 4 details the discovery of new type of QPOs in AWDs, with analogous observational properties to the type-C QPOs in XRBs(Wijnands & van der Klis, 1999; Ingram & Motta, 2019) as well as an application of the MDP model as a potential explanation of their driving mechanism. However, in Chapter 4, the model is only explored in terms of fixed fiducial values as specified in Table 4.4. In order to explore the parameter space of this model in a more general fashion, I implement a random sampling technique using flat log and normal priors as described in Section 5.3.

Sampling the parameter space for the AWD QPOs requires several changes to the parameter space sampling from Section 5.3. The main change pertains the lack of spin period measurement or estimate in most of the AWD systems. To account for this, the spin period is also extracted with each model realisation and saved with the other parameters. Hence when reproducing Figure 5.1, another line of plots is added at the bottom, corresponding to the parameter space of the spin period with respect to the other model parameters. Therefore, only the QPO frequency with its error is used as a constraint here. Furthermore, the sampled parameter ranges are altered appropriately for AWDs, and are detailed in Table 5.3. There, all parameter ranges are sampled randomly from a uniform logarithmic distribution 10^8 times, recording all solutions returning a QPO frequency within the error specified in Table 4.2.

Table 5.4: Accretion rates assumed here for AWD systems showing type-C analogous QPOs along with the corresponding publications. The only system where a single value is quoted without an error is GW Lib, for which purposes a 10% error margin is assumed.

System	$\dot{M}$ $(M_{\odot} yr^{-1})$	Reference
WZ Sge	$7.4 \pm 1.3 \times 10^{-11}$	Pala et al. (2020)
GW Lib	7×10^{-14}	Hilton et al. (2007)
CP Pup	$1 - 2 \times 10^{-10}$	Veresvarska et al. (2024a)
T Pyx	$10^{-7} - 10^{-6}$	Godon et al. (2018)
V3101 Cyg	$10^{-11} - 10^{-10}$	Veresvarska et al. (2024b)

A further constraint, similarly to PULXs is also taken from the accretion rate estimates. Another set of 10^8 model realisations are completed with parameters drawn in the same manner from a logarithmic (and normal for θ) uniform distributions, with the $\dot{M}$ range boundaries being limited to the observational values and estimates. These are summarised in Table 5.4.

Only WZ Sge and GW Lib have estimates of their spin period, as discussed in Chapter 4. Therefore, here I use these estimates to further constrain the families of viable model solutions. This is done through the samples drawn with $\dot{M}$ range quoted in Table 5.4 and selecting only the solutions consistent with the spin estimates. These values are 27.87 ± 0.01 s for WZ Sge (Patterson, 1980) and $\sim 209 \pm 21$ s for GW Lib (Szkody et al., 2012). The error on the spin of WZ Sge is as quoted in (Patterson, 1980), whereas a 10% error margin has been assumed on the spin of GW Lib.

The families of solutions reproducing the observed QPOs for WZ Sge and GW Lib are shown in Figures 5.2 and Figure 5.3. The grey points represent families of solutions that can reproduce the QPO, the red diamonds represent the families of solutions drawn from the range of observed accretion rate in Table 5.4 and the blue squares represent a subset of the red points that also return the observed spin. The parameter spaces of CP Pup, T Pyx and V3101 Cyg, for which no spin estimates are available are shown in Figures A.8, A.9 and A.10.

5.5.2 Discussion: AWDs

Considering the wider exploration of the parameter space of the MDP model in the AWD application it is necessary to re-evaluate the conclusions of Chapter 4 and discuss new implications. Similarly to the PULXs the overall distributions of individual parameter values across all families of solutions for the QPO can provide limits on specific parameters. These limits, mostly drawn from the $\dot{M}$ constraint family of solutions relies therefore not only on the

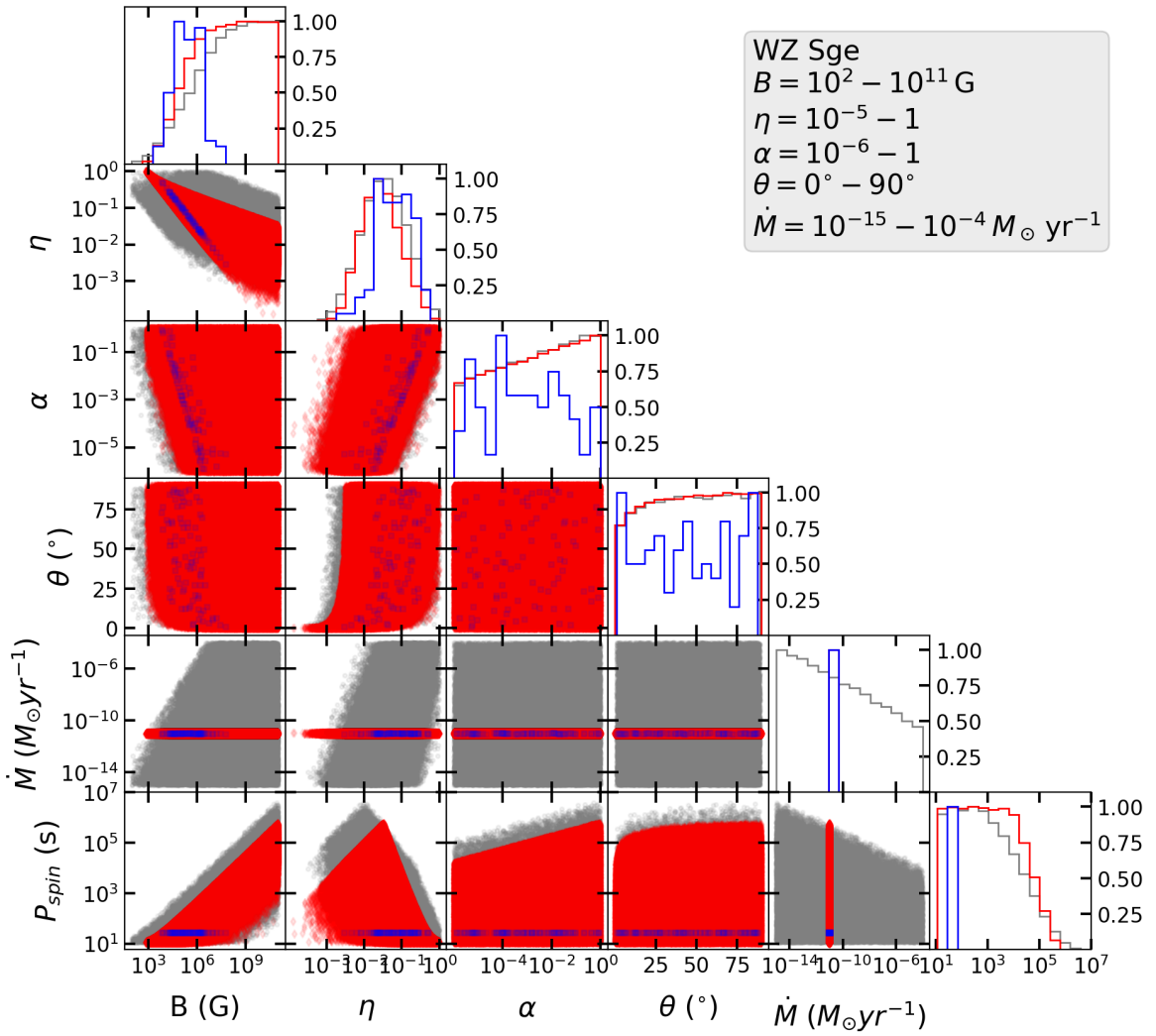

Figure 5.2: Parameter space of the MDP model with all parameter combinations (in grey circles) producing QPO frequency and spin within the observed errors as noted in Table 4.2 and 5.4. All the solutions which also reproduce accretion rate within the range given in Table 5.4 are given in red diamonds. The blue squares represent fractions of family of solutions of the red diamonds, that also reproduce the spin of WZ Sge within its error as given in (Patterson, 1980). Distributions of all parameters are provided, with all being scaled to unity. The explored parameter ranges are noted as also shown in Table 5.3.

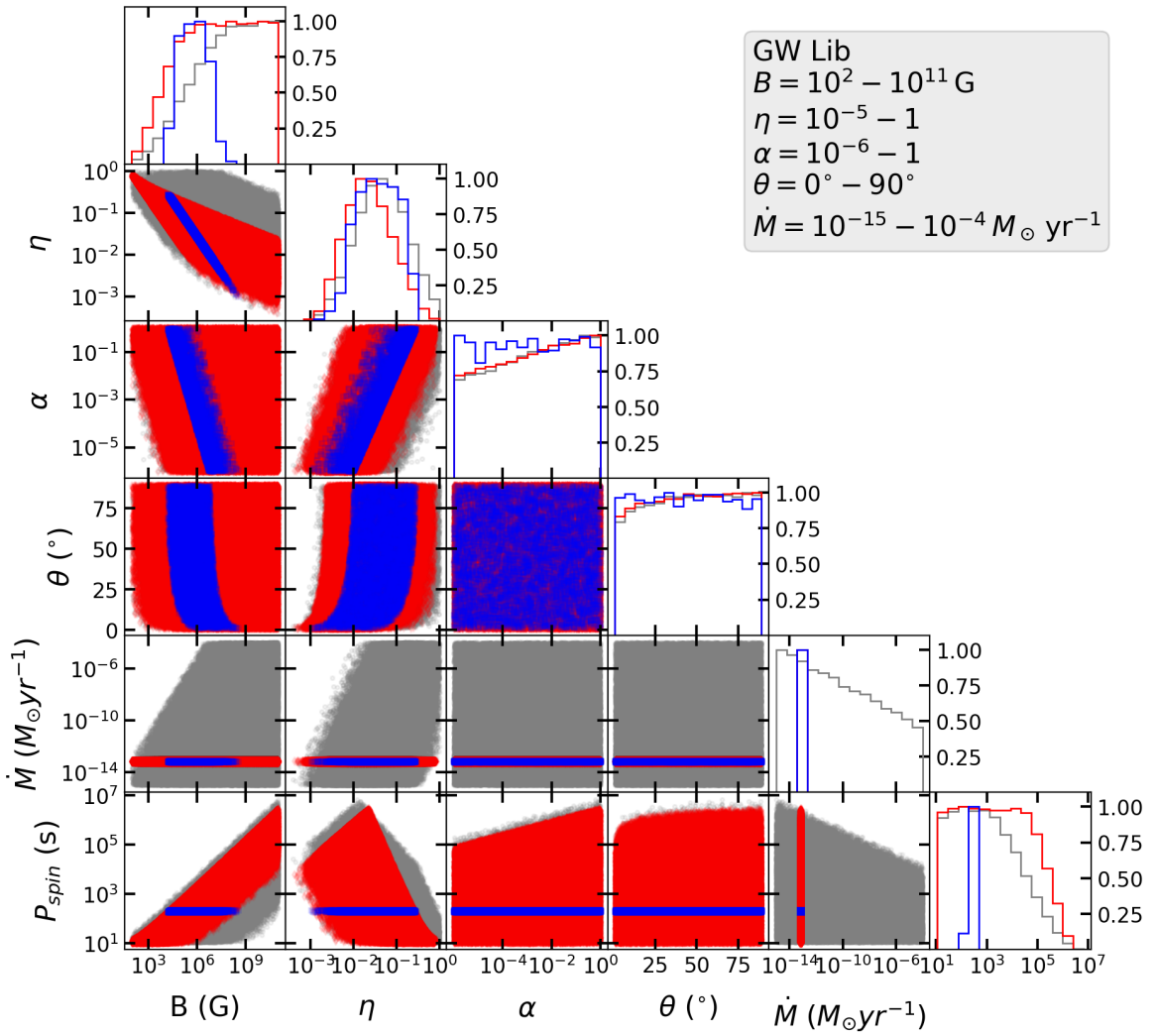

Figure 5.3: Parameter space of the MDP model with all parameter combinations (in grey circles) producing QPO frequency and spin within the observed errors as noted in Table 4.2 and 5.4. All the solutions which also reproduce accretion rate within the range given in Table 5.4 are given in red diamonds. The blue squares represent fractions of family of solutions of the red diamonds, that also reproduce the spin of GW Lib as given in (Szkody et al., 2012). Distributions of all parameters are provided, with all being scaled to unity. The explored parameter ranges are noted as also shown in Table 5.3.

Table 5.5: Limits and ranges for MDP model parameters for QPOs in AWDs. B lower limit is derived using the $\dot{M}$ constraint, whereas $log(B)$ range uses the spin limitation as well, where available. $log(\eta)$ is the range as obtained from the entire parameter space, and the $\dot{M}$ constraint is marked by * and adding spin constraint as well is denoted by †.

Model Parameter	CP Pup	WZ Sge	GW Lib	T Pyx	V3101 Cyg
B (G)	$> 3 \times 10^3$	$> 7 \times 10^2$	$> 1 \times 10^3$	$> 8 \times 10^4$	$> 9 \times 10^2$
$log(B)$ $(log(G))$	–	5.4 ± 0.8	5.8 ± 0.8	–	–
$log(\eta)$	-1.5 ± 0.6	-1.5 ± 0.6	-1.4 ± 0.6	-1.5 ± 0.6	-1.5 ± 0.6
$log(\eta)^*$	-1.4 ± 0.5	-1.6 ± 0.5	-1.6 ± 0.5	-1.1 ± 0.5	-1.5 ± 0.5
$log(\eta)^\dagger$	–	-1.2 ± 0.5	-1.4 ± 0.5	–	–

model assumptions but also on the $\dot{M}$ measurement. However, using this limit it is possible to extract lower limits on the B for all systems, and even constrain a range of possible values. The range, given by the mean and standard deviation of the distribution in Figures 5.2 and 5.3 is constrained using the spin period. The respective values of the limits and ranges are summarised in Table 5.5. Similar estimates can also be provided for the η parameter and are also summarised in Table 5.5.

Fixing specific parameters in the MDP model to fiducial values like in Chapter 4 allowed me to make rough estimates on the spin periods of the systems without a pre-existing measurement. However, when considering a larger parameter space for the MDP model as in this section, this is not possible, bar a very rough upper limit. Overall, without a separate handle on some of the other parameters, such as α or B, the spin estimates for these systems may remain elusive.

Chapter 6

The Peculiar Bursting Nature of CP Pup

Abstract

The classical nova CP Puppis has been observed to have particularly puzzling and peculiar properties. In particular, this classical nova displays occasional bursts in its long-term ASAS-SN light curve. Here I report on 5 sectors of TESS data displaying 2 of these rapid bursts, lasting $\sim$ 1 day. Based on the estimated lower energy limits of the bursts I discuss whether the bursts may be examples of micronovae resulting from localised thermonuclear explosion. Furthermore, its orbital period remains uncertain, with several inconsistent periodic signals appearing in spectroscopic and photometric observations at various wavelengths. Although I cannot unambiguously unravel the physical origin of the signals, the previously suggested nature of CP Puppis as a long orbital period system may be a viable explanation. The recurrence time of the bursts in CP Puppis, together with the unexplained variable modulations make it a prime candidate for intense monitoring.

Co-author contribution

I have conducted the analysis as described in this Chapter and reported in Veresvarska et al. (2024a) under the supervision of Dr Simone Scaringi. Dr Scott Hagen has conducted the analysis of XMM-Newton data used in this paper. Other co-authors have contributed with suggestions on analysis improvement and comments on the text of the paper.

6.1 Introduction

CP Puppis (CP Pup hereafter) is a well studied CV that has undergone a nova explosion in 1942. It is an unusually bright and fast example of a nova explosion, with the difference in amplitude of apparent magnitude of $\sim$ 17 mag (Payne-Gaposchkin, 1964). It is also a particularly fast nova with $t_3 \sim 6.5$ d (Payne-Gaposchkin, 1964), where t_3 represents the time it takes for the nova luminosity to decline by 3 magnitudes. It has been reported that since the nova explosion the brightness levels of the nova have yet to return to the pre-burst quiescence level (Schaefer & Collazzi, 2010). Similarities can be drawn between CP Pup and V1500 Cyg (Della Valle & Livio, 1998), which is also uncharacteristically brighter and has also remained brighter post eruption. CP Pup is also suggested to have a magnetic accretor (Balman et al., 1995; Orio et al., 2009; Mason et al., 2013).

One of the main peculiarities of CP Pup is its elusive orbital period. There have been spectroscopic (Bianchini et al., 1985; Duerbeck et al., 1987; O'Donoghue et al., 1989; White et al., 1993; Bianchini et al., 2012; Mason et al., 2013) and photometric (Warner, 1985; O'Donoghue et al., 1989; Diaz & Steiner, 1991; White et al., 1993; Bruch, 2022) periods reported between 0.06115 days and 0.06834 days. A summary of all these is provided in Bruch (2022). Both spectroscopic and photometric periods reported in literature lie in a similar range, with most of the spectroscopic periods being shorter. Furthermore, the spectroscopic periods have been reported to show large scatter in the folded radial velocity curve (Bianchini et al., 2012). It is worth noting that the spectroscopic and photometric periods in the literature are inconsistent with each other (Diaz & Steiner, 1991). Orio et al. (2009) has further reported 3 periods from *XMM-Newton* data. However, due to the large uncertainty, the periods quoted in Orio et al. (2009) are consistent with each other, as well as consistent with previously reported spectroscopic and photometric periods (see summary by Bianchini et al. (2012) and Bruch (2022)). [2]

If taken at face value as the orbital period, all the reported values are short for known classical novae and non-magnetic nova-likes in general ($\sim$ 3 hours), making CP Pup one of a handful of novae with a potential period reported below the period gap (Bianchini et al., 1985; Marelli et al., 2018). It has thus been suggested that CP Pup is a system whose disc is always hot and bright, and often exhibits superhumps persisting in a state similar to SU UMa

[2] Note that this signal is interpreted as a new type of QPO, as discussed in Chapter 4 and Veresvarska et al. (2024b). However this work precedes this interpretation and is hence not discussed in this Chapter.

type dwarf novae during superoutburst (Warner, 1985; Patterson & Warner, 1998; Patterson et al., 2013).

Further interpretations of the period assigned it to the spin of the magnetic white dwarf, suggesting a white dwarf slightly out of spin-orbit synchronism (Warner, 1985; Diaz & Steiner, 1991; Balman et al., 1995). Asynchronous polars are not the only option for the magnetic interpretation of CP Pup. Orio et al. (2009) and Mason et al. (2013) consider the hypothesis of CP Pup being an intermediate polar. However, there is a lack of conclusive evidence for either interpretation.

The peculiar nature of CP Pup extends to other observations too. The relatively recent nova explosion, with its characteristics such as peak absolute magnitude, suggests a high mass white dwarf (WD), due to the smaller physical accretor size resulting in higher pressure, making it more favourable to trigger a nova explosion (Prialnik & Kovetz, 1995). However, White et al. (1993) points out that the reported values of $K_1 \sim 70-146$ kms^{-1} require a WD mass $< 0.2M_{\odot}$. This is in contradiction to the nova nature of CP Pup. Some more recent studies adopting higher WD mass of 1.1 $M_{\odot}$ have instead obtained better fits to optical spectra with an accretion rate in the range of $3.3-7.3\times10^{-10}M_{\odot}yr^{-1}$ (Mason et al., 2013). Also assuming a high mass WD, $M_{WD} > 1.1M_{\odot}$, Orio et al. (2009) derived an upper limit on mass transfer rate $\lesssim 1.6\times10^{-10}M_{\odot}yr^{-1}$. However, this estimate assumes a distance of 1600 pc, more than double the distance of 780 $\pm$ 11 pc inferred from the *Gaia* parallax (Gaia Collaboration et al., 2016, 2023). Orio et al. (2009) also quotes a 3σ upper limit $\lesssim 8\times10^{-11}M_{\odot}yr^{-1}$ at 850 pc, as determined by Cohen & Rosenthal (1983). Other estimates of the accretion rate adopting the more precise *Gaia* parallax measurement have been made. Selvelli & Gilmozzi (2019) reports a considerably higher value of $10^{-9.22\pm0.32}$ $M_{\odot}$yr^{-1}. This is related to the unusually high extinction of $A_v \sim 0.6$ mag, which they adopt.

In this Chapter I report on the analysis of 5 sectors of *TESS* data of CP Pup (Section 6.2). In Section 6.3 I discuss 2 rapid bursts observed as well as the phenomenology of the cluster of periods found in the *TESS* light curves. Reanalysis of *XMM-Newton* data of CP Pup is also discussed here and the new WD mass estimate is derived. In Section 6.4 I discuss the observed rapid bursts in the context of the micronova model (Scaringi et al. (2022c); Scaringi et al. (2022d).

Table 6.1: Summary of the *TESS* data of CP Pup, with sector numbers and dates. If a sector contains a burst, the corresponding date in Barycentric Kepler Julian date, duration in days and energy is noted. The details of energy calculation are described in Section 6.3.1.

Sector	Dates (BTJD-2457000)	burst dates (BTJD-2457000)	Duration (d)	Energy (erg)
7	1491.6 - 1516.1	1491.6 - 1492.2	~ 0.6	1.2×10^{38}
8	1518.0 - 1542.0	–	–	–
34	2229.0 - 2254.1	2229.0 - 2234.4	~ 1	6.3×10^{37}
35	2255.7 - 2280.0	–	–	–
61	2964.0 - 2988.1	–	–	–

6.2 Observations

The data used in this work was obtained by *TESS* with the detailed description of the telescope and data processing discussed in Chapter 2. *TESS* observed CP Pup over 5 sectors amounting to ~ 5 months of observations at 2 minute cadence. The last sector 61 also contains 20 second cadence data. The detailed description of the data with the burst characteristics is provided in Table 6.1.

The *TESS* data shows a modulation of the shape of the light curve in the form of a larger envelope, where the variance and flickering temporarily varies on timescales of $\lesssim 10$ days (see Fig. 6.1). The same envelope is present to a greater extent in the 20 s cadence data of Sector 61 in *TESS* . The Lomb-Scargle periodogram of the 20 s data shows a QPO-like feature at ≈ 1500 cycles/day. This is also present in all the neighbouring stars in the field of CP Pup and hence assumed to not be intrinsic to the CP Pup itself, but rather a common systematic. Similar behaviour is also observed in other *TESS* 20 s observations in Sector 61 (such as TIC 260266504, TIC 289113766 and TIC 289113764). This points to an instrumental origin of the QPO and is hence disregarded. As no other new signals are found in the 20 s cadence data of Sector 61, the 2 minute cadence is used throughout for consistency.

TESS data is converted to the ground-based *ASAS-SN* flux using the technique described in 2.3 and particularly Equation 2.3.1. The corresponding values of the coefficients for each half-sector are specified in Table 6.2 to account for any deviations in data due to the gap in the middle of *TESS* sectors.

There are 2 cases where the calibration between *TESS* and *ASAS-SN* fails. The first is in Sector 8, where the *TESS* light curve shows a drop in flux inconsistent with the ground-based *ASAS-SN* observations. This is also reported in Bruch (2022). Another similar case occurs in Sector 35 where the *TESS* data shows an uncharacteristic rise in flux, but this

Table 6.2: Summary of the conversion coefficients from *TESS* flux in e^{-s} to *ASAS-SN* flux in mJy for CP Pup. As the conversion is done twice per *TESS* sector, all corresponding coefficients are listed.

Sector	Sector half	A $\left(\frac{mJy}{e^{-}s^{-1}}\right)$	C (mJy)
7	1	0.0241 ± 0.0007	-1.2 ± 0.1
	2	0.016 ± 0.002	-0.0 ± 0.3
8	1	0.011 ± 0.001	-0.9 ± 0.4
	2	0.011 ± 0.001	-0.9 ± 0.4
34	1	0.0209 ± 0.0008	-11.1 ± 0.5
	2	0.011 ± 0.001	-4.6 ± 0.9
35	1	0.015 ± 0.001	-2.2 ± 0.4
	2	0.014 ± 0.003	-1.8 ± 0.9
61	1	0.013 ± 0.001	-1.8 ± 0.4
	2	0.008 ± 0.002	-0.5 ± 0.7

appears to be shared within the entire region surrounding CP Pup and I attribute this to poor background correction. Consequently both segments of Sectors 8 and 35 where the calibration to *ASAS-SN* fails are discarded. The final result is shown in Figure 6.1, where the light curve is also corrected for the distance of 780 ± 11 pc inferred from *Gaia* DR3 parallax. Despite the high extinction in *Gaia* passband, no bolometric correction has been applied, as mentioned in Section 2.3. This is to avoid any effects due to a potential change in the SED between quiescent and bursting parts of the light-curve, which would affect any bolometric correction. As a result the obtained luminosity of CP Pup should be treated as a lower limit. It is however possible to estimate the effect the bolometric correction could have on the luminosity. The X-ray luminosity in Section 6.3.4 is estimated to be $L_X \sim 1.1 \times 10^{33}$ erg s^{-1}. Similarly, Orio et al. (2009) estimated the UV luminosity to be $L_{UV} \sim 2 \times 10^{33}$ erg s^{-1}. Alongside with the mean *TESS* luminosity of $L_{TESS} \sim 1 \times 10^{33}$ erg s^{-1} the total bolometric luminosity is expected to be of the order of $\sim 4 \times 10^{33}$ erg s^{-1}. Therefore the lower limits on the luminosity are expected to represent about $\sim 4\times$ lower values than the total bolometric values.

Further data used in this work has been obtained by *XMM-Newton* on 4^{th} of June 2005 and reported in Orio et al. (2009). As described in greater detail in Orio et al. (2009), the data was obtained with EPIC-pn, MOS-1 and MOS-2 with $\sim$ 50 ks exposure. Grating spectrum with low SNR was also obtained with RGS and reported in Orio et al. (2009). The spectrum is shown in Orio et al. (2009) in Figure 3. The reduced data is available online at `heasarc`[6]. However, the data reanalysed here, is only the data taken with the most sensitive EPIC-pn

[6] `https://heasarc.gsfc.nasa.gov/cgi-bin/W3Browse/w3browse.pl`

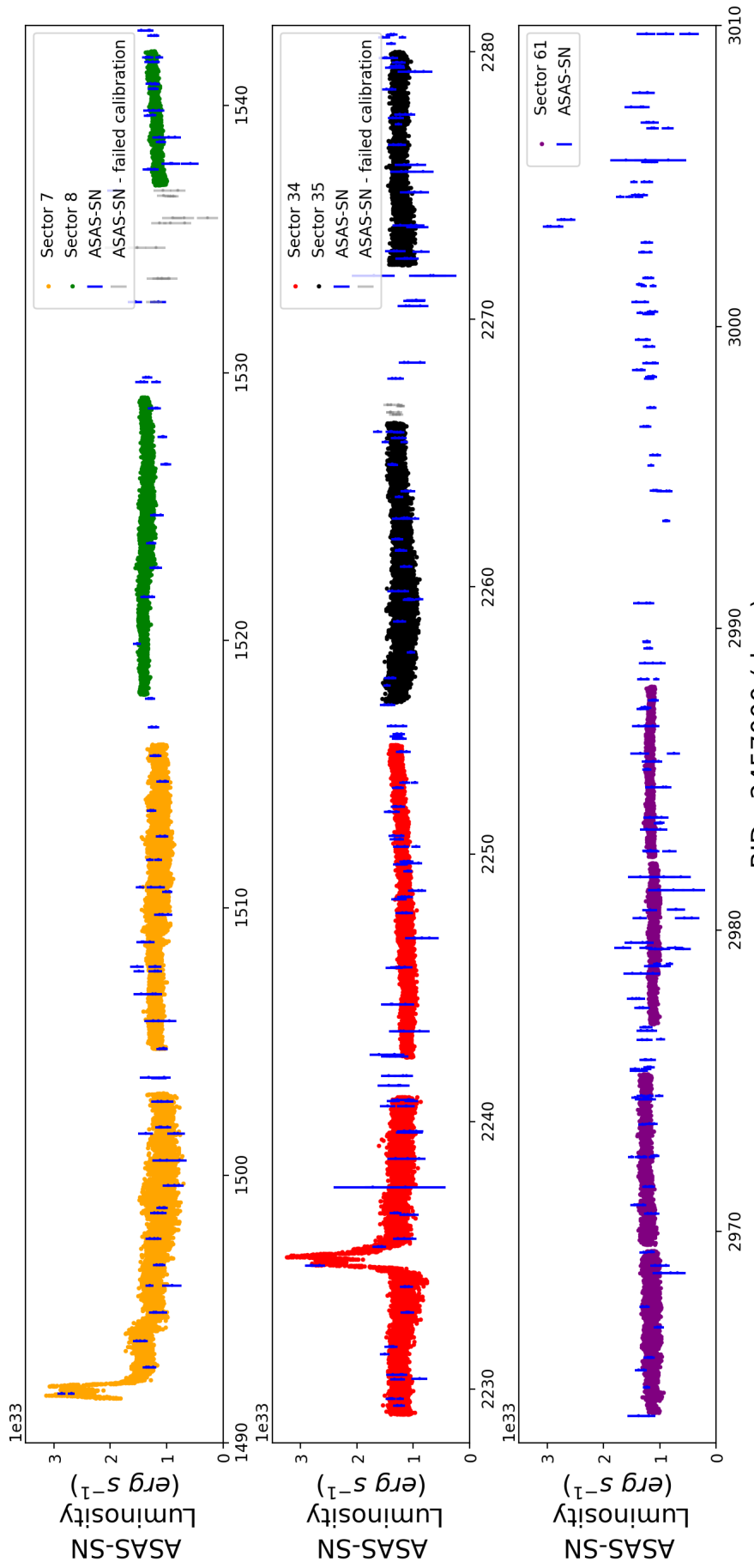

Figure 6.1: Light curve of CP Pup showing all 5 sectors of *TESS* data as described in Table 6.1 (orange, green, red, black and purple consecutively for sectors 7, 8, 34, 35 and 61). Overlaid (in blue) is the *ASAS-SN* light curve used for calibration. The grey points are data from *ASAS-SN* for which calibration failed and hence were excluded. The flux of both *TESS* and *ASAS-SN* light curves is converted to erg s^{-1} using the *Gaia* parallax.

instrument.

6.3 Results

In this section I report the bursts found in 2 of the 5 available *TESS* sectors in Section 6.3.1. I further report on the observed variable cluster of frequencies found in the power spectrum of CP Pup in Section 6.3.2. The *XMM-Newton* spectrum reported in Orio et al. (2009) and the new model fit is presented in Section 6.3.4

6.3.1 Bursts

The *TESS* light curve from all sectors is displayed in Figure 6.1, where two bursts are detected in Sector 7 and 34 with the corresponding times in Table 6.1. The bursts have also been reported in Bruch (2022), however they are disregarded in the analysis. The recorded bursts in Sectors 7 and 34 all lasted $\lesssim 1$ day, with the overall amplitude increasing by a factor of > 2, from $\sim 1.5 \times 10^{33}$ erg s^{-1} to $> 3.0 \times 10^{33}$ erg s^{-1}. A detailed version of the bursts is shown in Figure 6.2. Only Sector 34 contains both the immediate pre-burst and post-burst observation. Sector 7 started during the rise of the burst and contains the post-burst part only. It is worth noting an additional burst of similar nature in the long term *ASAS-SN* light curve at ~ 3005 BTJD in Figure 6.1. Unfortunately there are no *TESS* observations around that date. Another interesting characteristic of the bursts is their shape, showing 2 distinct peaks with ~ 0.35 d separation.

To understand the origin and nature of the bursts, their energy has to be determined. This is done by integrating the luminosity under the calibrated light curve after subtracting the baseline luminosity level. I estimate the baseline luminosity using the pre- and post burst data only. I use these to compute a running mean and interpolate in between the two with a spline function. The resulting energy in ergs is reported in Table 6.1. The most energetic burst in Sector 7 releases in excess of 1.2×10^{38} erg. The energy released by the burst in Sectors 34 is $> 6.3 \times 10^{37}$ erg. I note that the aforementioned data gaps, as well as the lack of a bolometric correction allows us to only provide lower limits to the burst energies.

6.3.2 Phenomenology of the period cluster

A peculiar feature of CP Pup is the cluster of periods between ~ 14 cycles/d and ~ 15 cycles/d ($\sim 1.5 - 1.6$ hr). In the 5 *TESS* sectors reported here all show this variability.

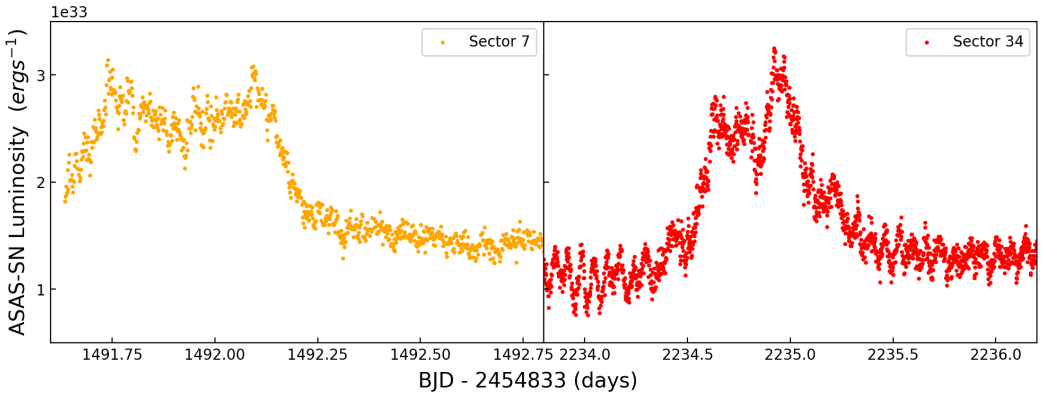

Figure 6.2: Zoom in on the bursts shown in Figure 6.1 and described in Table 6.1. The energy of each burst is 1.2×10^{38} erg for sector 7 and 6.3×10^{37} erg for sector 34.

This time-dependent variability is discussed in detail in Bruch (2022). The persistent signal reported from 4 *TESS* sectors in Bruch (2022) is at $\sim$ 16.29 cycles/d. Independently redoing the period analysis on all 5 *TESS* sectors also reveals a single identical persistent signal in the cluster at 16.29 $\pm$ 0.04 cycles/d.

In Figure 6.3 the cluster is shown right before and after the burst present in sector 34. There is no apparent connection between the burst and the position or shift of the cluster frequencies. However, it is evident that there is considerably more rms power in the cluster before the bursts than after. For sector 34 the peak power of the cluster is at $\sim$ 590 RMS, whereas after burst it is at $\sim$ 110 RMS, excluding the power of the signal at $\sim$ 16.29 cycles/d at $\sim$ 200 RMS. Similarly, sector 7 shows a significant quasi-periodic variability as well. However lack of data pre-burst does not allow for similar comparison as in sector 35.

Orio et al. (2009) also reports only one coherent period in the light curve of CP Pup of 16 $\pm$ 2 cycles/d ($\sim$90 minutes). I recover the same signal from the *XMM-Newton* data. The signal is marked by the dashed grey line in Figure 6.3. Furthermore, this period also corresponds to the only persistent signal in *TESS* light curve.

6.3.3 The potential nature of the orbital period

The signal at 1.473 hr is interpreted in literature as the orbital period of CP Pup. Using the evolutionary tracks of Knigge et al. (2011) I can estimate the temperature of the donor to be $\sim$ 2700 K with radius of $\sim$ 0.131 $R_{\odot}$ for a system with an orbital period of $\sim$ 1.473 hr. The corresponding white dwarf temperature according to Knigge et al. (2011) would be 11 000 K with radius following from the WD mass in Section 6.3.4. In such a case the SED of

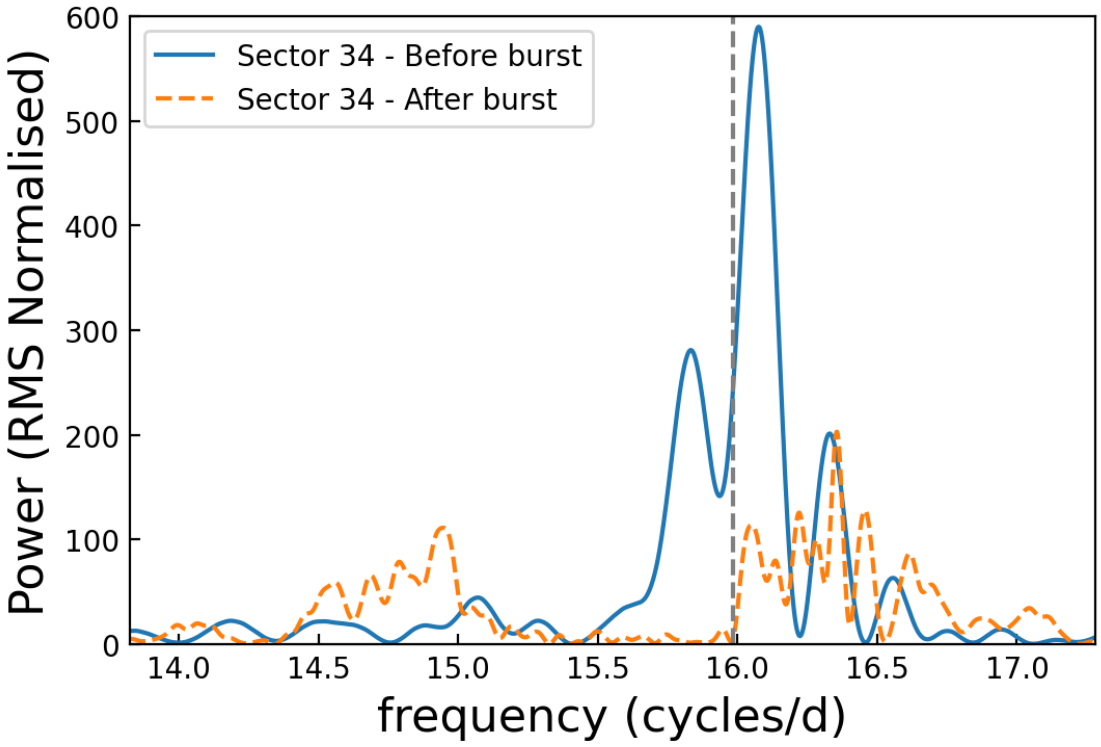

Figure 6.3: PSD of sectors 34 divided into pre-burst (blue) and post-burst (orange) parts. Grey dashed line shows the coherent *XMM-Newton* period at ~ 16 cycles/d.

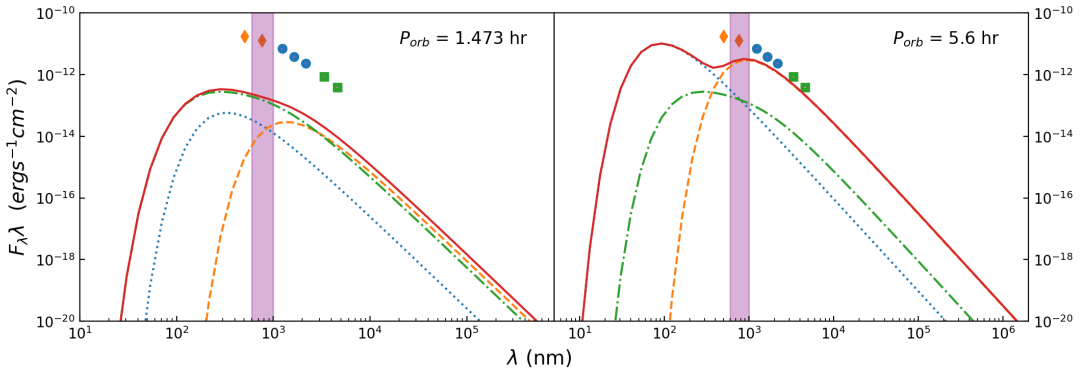

Figure 6.4: *Left:* model SED of CP Pup for an estimated orbital period of 1.473 hr with the dotted (blue) line representing the WD, dashed (orange) line the secondary and the dashed-dotted (green) line the accretion disc. The total SED is shown in solid (red) line. For comparison the measurements from *WISE* W1 and W2 are shown (green squares) as well as the *2MASS* filters (blue dots) and the *Gaia* measurements (orange diamonds). The *TESS* bandpass is shown in the shaded (pink) region. *Right:* Same SED components and data as in the left panel but for orbital period of ~ 5.6 hr, the longest orbital period included in the evolutionary tracks in Knigge et al. (2011).

the system can be roughly approximated by two spheres radiating as blackbodies with the corresponding radii and temperatures. Another possible dominant SED component would be the accretion disc. Taking the X-ray derived accretion rate of $\sim 1 \times 10^{-10}$ $M_{\odot}\mathrm{yr}^{-1}$ (Section 6.3.4) at face value, a standard Shakura-Sunyaev (Shakura & Sunyaev, 1973) accretion disc from the WD surface to the tidal radius at $\sim$0.31 $R_{\odot}$ is assumed. The resulting SED is hence shown in the left hand side panel of Figure 6.4. It is evident that there is a deficit in flux across all observed wavebands that cannot be corrected by either an increase in accretion rate or by correcting for extinction ($A_V \sim 0.6$ mag (Selvelli & Gilmozzi, 2019), A_H =0.107 mag and A_J =0.173 mag (Cardelli et al., 1989) and A_{W1} =0.203 mag and A_{W2} =0.157 mag (Fitzpatrick, 1999; Indebetouw et al., 2005).

Mason et al. (2013) discusses the possibility that CP Pup may be a long orbital period CV. Despite no other photometric signal being detected, Mason et al. (2013) reports a substantial power at low frequencies ($\sim$ 2.38 cycles/d). Their Hβ RV curve produces a fit of 9.8 hr. They point out a large uncertainty of 1 day, making this a lower limit on the potential signal. The longest orbital period I can use from the evolutionary tracks of Knigge et al. (2011) at an orbital period of 5.6 hr provides an estimated donor temperature of $\sim$ 3900 K and radius of $\sim$ 0.63 $R_{\odot}$. Assuming the same parameters for the WD and accretion disc as previously (with the slight correction for tidal radius being at $\sim$ 0.19 $R_{\odot}$) the estimated SED is as shown in the right panel of Figure 6.4. This is more consistent to the observed *2MASS* and *WISE* absolute magnitudes of CP Pup, suggesting a hotter and larger donor than previously anticipated. Since the evolutionary tracks in Knigge et al. (2011) do not include orbital periods above 5.6 hr, the right panel in Figure 6.4 represents an estimate, not a fit, of the effect a longer orbital period would have on the SED. This also tentatively suggests a longer orbital period for CP Pup than reported in the past, but a more intensive radial velocity campaign is required to unravel the problem of the orbital period of CP Pup.

6.3.4 Revisiting the WD mass and mass accretion rate with X-Rays

The reanalysis of the X-ray spectrum in this section is motivated by the inconsistent estimates of the WD maximal temperature T_{max} in the literature (Orio et al., 2009; Mason et al., 2013), leading to an uncertain WD mass and unconstrained accretion rate. This is also exacerbated by the pre-*Gaia* distances used in past X-ray analyses. More specifically Orio et al. (2009) infer large values of T_{max} following from the used models for non-magnetic systems and a simplified model of magnetic systems. Exploring the possibility of micronova eruptions

present in CP Pup, the model implemented in this work is adapted specifically for magnetic accreting WD with an accretion column.

Figure 6.5 shows the archival *XMM-Newton* spectrum of CP Pup taken on 4th June 2005, reported in Orio et al. (2009). Orio et al. (2009) fit the RGS spectrum using MKCFLOW model (Mushotzky & Szymkowiak, 1988) model which describes the emission from a cooling multi-temperature plasma and the EPIC-pn spectrum with a multi-temperature APEC model. However their analysis does not include the combination with a complex absorber which is instead characteristic of magnetic CVs (Lopes de Oliveira & Mukai, 2019; Islam & Mukai, 2021) while they use a single simple absorber.

Orio et al. (2009) also uses APEC multi-temperature model to fit the *XMM-Newton* EPIC-pn spectrum. The APEC model consists of 3 temperature components and obtains a spectrum for a collisionally-ionized diffuse gas. For an IP or polar one can expect the presence of a magnetically confined accretion flow onto the magnetic pole (or poles) of the accretor. In this case the impacting material generates a shock heated plasma, which cools towards the surface of the WD, and generates the X-ray emission. This is similar to the multi-temperature APEC model used by Orio et al. (2009).

Testing the possibility that the bursts can be explained by micronova requires a magnetic accretor. Therefore, I fit the spectrum using XSPEC version 12.13.0 (Arnaud, 1996), and specifically use the CEMEKL model (Singh et al., 1996) which describes the emission from a multi-temperature plasma. The geometry of an accretion stream onto a WD surface can be approximated as cylindrical (see Figure 1 in Done & Magdziarz 1999). X-rays emitted on the far side of the stream (with respect to the observer) encounter a larger effective column-density to the observer compared to those emitted on the side facing the observer. To account for this I convolve CEMEKL with the absorption model PWAB (Done & Magdziarz, 1998), which calculates the emission assuming the non-uniform absorption profile arising from a cylindrical emitter. I further convolve the model with RELFECT (Magdziarz & Zdziarski, 1995), which calculates the reflected emission from neutral material. The use of the REFLECT component follows from the presence of the Fe-Kα line. Additionally I add two components to model, the fluorescence lines Fe-Kα (~ 6.4 keV), and O VII (~ 0.58 keV). The strong O VII line might be due to the wind from the nova shell, as noted in Orio et al. (2009). Finally, I also include TBABS to account for interstellar absorption as obtained from the visual extinction from Table 1 in (Selvelli & Gilmozzi, 2019), using the optical extinction to H column density relation (Guver & Ozel, 2009). The final XSPEC model is then: TBABS*PWAB*REFLECT*(CEMEKL +

GAUSSIAN(FE-Kα) + GAUSSIAN(O VII)). The best fit model is shown in Figure 6.5, and the corresponding model parameters are shown in Table 6.3.

Table 6.3 shows the resulting best fit parameters. In particular, $T_{\rm max} = 29.3^{+9.4}_{-7.4}$ keV, significantly lower than ~ 64 keV for the multi-temperature APEC model and ~ 78 keV for the MKCFLOW model discussed in Orio et al. (2009). Although $T_{\rm max}$ is loosely constrained it does not approach the maximum allowed limit of the model. I attribute the main difference between this fit and that of Orio et al. (2009) to the inclusion of the PWAB component, which represents an approximation for the accretion column. The new estimate is consistent with the range determined by Mason et al. (2013) using *Chandra* data, which has considerably softer coverage. I note that although $N_{h,\rm max}$ is unconstrained its effect on the overall fit is negligible. This particular behaviour of $N_{h,\rm max}$ is also reported in Done & Magdziarz (1998) for BY Cam. Similarly for reflection, which is loosely constrained but with negligible effect on the final value of $T_{\rm max}$. The possibility of fixing reflection to 1 is also explored. It was found that a fixed value of reflection changes $T_{\rm max}$ to $T_{\rm max} = 29.3^{+10.4}_{-7.1}$ keV, however all variations of the temperature are well within the errors, making a fixed value of reflection unnecessary. Done & Magdziarz (1998) explored the possibility of fixing $\alpha = 1$, however found that the best fit is obtained for $\alpha < 1$. This is also the case for CP Pup and is indicative of multiple sources of cooling, not only Bremsstrahlung, most likely cyclotron.

To infer the WD mass and mass accretion rate it is here assumed that CP Pup is a magnetic system. This choice was based on partial evidence as presented in Mason et al. (2013) and other works, but also in order to explore the micronova nature of the bursts. From the updated X-ray fit I first isolate the plasma component from the model spectrum, extrapolating it over the energy range for which the model is defined ($5 \times 10^{-3} - 60$ keV) and integrating it. This results in a bolometric flux of $\sim 1.5 \times 10^{-11}$ erg s^{-1}cm-2. Using the *Gaia* inferred distance of $D = 780 \pm 11$ pc, this gives $L_x \sim 1.1 \times 10^{33}$ erg s^{-1}. The WD mass is derived from $T_{\rm max}$ using Equation 1, relating the shock temperature to the WD mass in magnetic cataclysmic variables, in Orio et al. (2009) following from Wu et al. (2003) and references therein. The resulting mass is $M_{WD} \sim 0.73 M_{\odot}{}^{+0.12}_{-0.11}$ with the corresponding radius $R_{WD} \sim 0.011 R_{\odot}{}^{+0.001}_{-0.002}$, assuming the mean molecular weight from the abundance in Table 6.3.

Assuming the inferred M_{WD} is correct, I find a mass accretion rate $\dot{M} = 1{-}2{\times}10^{-10}\, M_{\odot}\, {\rm yr}^{-1}$. The accretion rate is quite low, however estimating the optical luminosity from *Gaia* magnitude yields $\sim 8.8 \times 10^{32}$ erg s^{-1}. Therefore estimating the accretion rate from the optical luminosity would lead to similarly low values. As it is likely that the accretion luminosity is

not solely constrained to X-rays it is reasonable to assume that the accretion rate above is a lower limit.

Another method of estimating the accretion rate is through the optical to NIR SED. Using the photometric observations of CP Pup available in vizier[7], the peak of the SED is placed at *XMM-Newton* optical Monitor at $\sim$ 543 nm with 2.26 $\pm$ 0.06 mJy. This translates to a luminosity of 2.53 $\pm$ 0.02 $\times$ 10^{33} erg s^{-1} using a distance of 780 $\pm$ 11 pc. Assuming that the luminosity corresponds to the accretion luminosity $L_{acc} = \frac{GM_{WD}\dot{M}}{2R_{in}}$, the estimated accretion rate is $\dot{M} \sim 6 \times 10^{-10}$ - 6×10^{-9} $M_{\odot}$yr^{-1}. The range of estimated accretion rate depends on the possible truncation of the inner accretion disc. The values taken into account here estimated $R_{in} \sim R_{WD} - 10 \times R_{WD}$, where $10 \times R_{WD}$ is a value representative of the estimated truncated disc radii in IPs from (Suleimanov et al., 2019) for systems of similar mass to CP Pup. Whereas this only represents a very rough estimate of the accretion rate, it corresponds to the same order of magnitude as the X-ray accretion rate. Integrating the entire available SED, with a cut-off after W_2 *WISE* band, would result in total luminosity of $\sim 4 \times 10^{34}$ erg s^{-1}. This would correspond to $\dot{M} \sim 9 \times 10^{-9}$ - 9×10^{-8} $M_{\odot}$yr^{-1}, a significantly higher value than previous estimates. The excess may be accounted for if part of the SED is dominated by the donor star as suggested in Section 6.3.3. In such a case the approximation of accretion luminosity through the SED peak provides a more accurate estimate.

It is important to note that I do not have sufficiently high spectral coverage to confidently determine the maximum plasma temperature, $T_{\rm max}$, which sets the roll-over in the spectrum, and should therefore also affect the derived luminosity. Hence, the above estimates should be treated with caution, noting the model dependence. Furthermore, the accretion rate range above is an lower limit determined by the underlining assumptions.

6.4 Discussion and Conclusions

In this section I discuss the interpretation of the nature of the bursts detected in CP Pup. A connection is drawn in Section 6.4.1 with micronova, where the details of the model are discussed as well as its limitations and application to CP Pup. The recurrence timescale is determined from the model and compared to that observed from *ASAS-SN* data. As mentioned in section 6.3.4, the interpretation of the nature of the bursts, as well as the

[7] `https://vizier.cfa.harvard.edu/vizier/sed/`

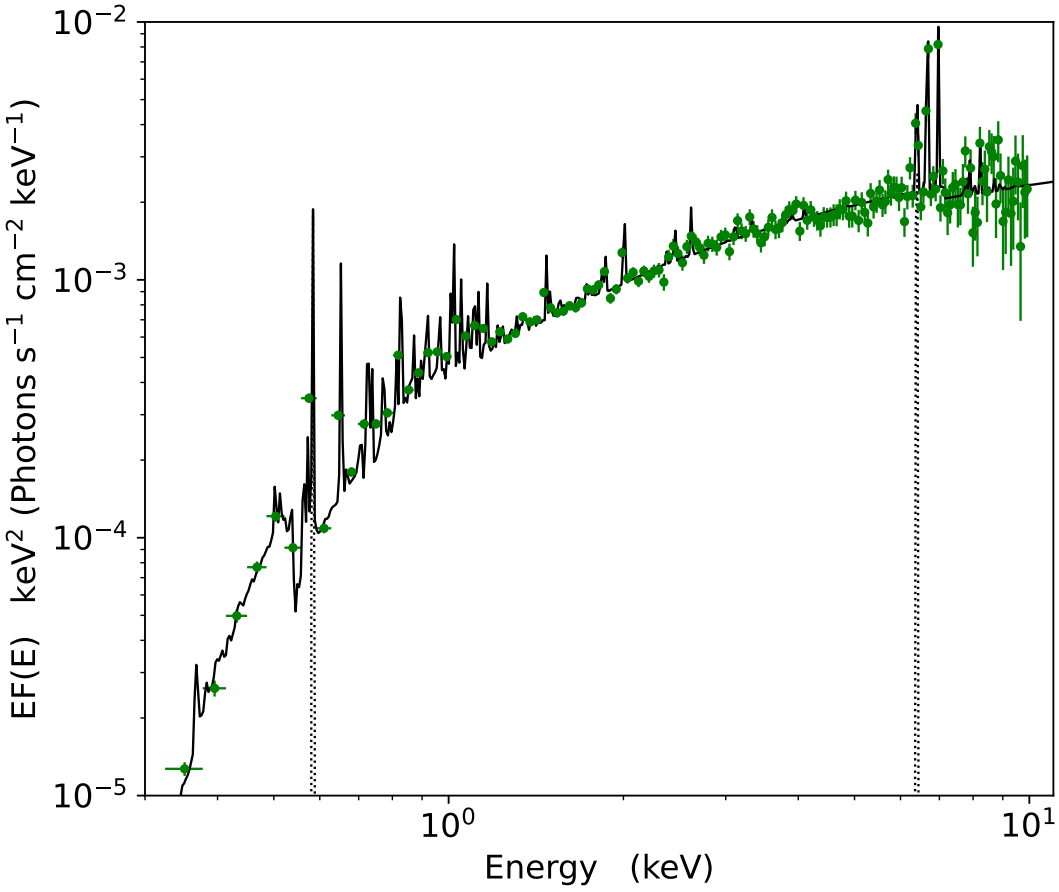

Figure 6.5: Unfolded XMM Epic-PN X-Ray spectrum of CP Pup. The green points show the data, while the solid black line shows the total model. The dotted gaussians show the two additional lines needed to fit the spectrum. These are (from left to right): O VII and Fe-Kα

Parameter	Units	Value
	TBABS	
N_H	$10^{22}\,\mathrm{cm}^{-2}$	0.16
	PWAB	
$N_{h,\mathrm{min}}$	$10^{22}\,\mathrm{cm}^{-2}$	$1^{+1625}_{-1} \times 10^{-7}$
$N_{h,\mathrm{max}}$	$10^{22}\,\mathrm{cm}^{-2}$	$7.34^{+\mathrm{inf}}_{-2.32}$
β		$-0.86^{+0.04}_{-0.09}$
	REFLECT	
rel_refl		$1.06^{+0.94}_{-1.04}$
Redshift		0
abund		$0.57^{+0.11}_{-0.11}$
Fe_abund		1
$\cos(i)$		0.5
	CEMEKL	
α		$0.60^{+0.10}_{-0.04}$
T_{max}	keV	$29.3^{+9.4}_{-7.4}$
n_h	cm^{-3}	1
abund		$0.57^{+0.11}_{-0.11}$
Redshift		0
switch		1
norm	10^{-3}	$5.9^{+0.9}_{-0.7}$
	GAUSSIAN (Fe-Kα)	
E	keV	6.4
EW	keV	0.07
σ	keV	10^{-2}
norm	10^{-6}	$4.56^{+1.73}_{-1.73}$
	GAUSSIAN (O VII)	
E	keV	$0.584^{+0.011}_{-0.010}$
EW	keV	0.072
σ	keV	10^{-3}
norm	10^{-5}	$2.2^{+0.4}_{-0.4}$
χ^2_ν	$148.22/159 = 0.93$	

Table 6.3: The best fit parameters to the *XMM-Newton* EPIC-pn spectrum of CP Pup, with errors representing 90% confidence limits. Values with no error were kept frozen during the fitting process, and values with no units are dimensionless. For completeness I also include the switch parameter that were used throughout and determine whether the spectrum is computed via interpolating or pre-computed tables. The abundances used correspond to the 'angr' Table (`https://heasarc.gsfc.nasa.gov/xanadu/xspec/manual/node116.html`).

accretor mass and accretion rate are here dependent on the assumption that CP Pup is a magnetic system.

6.4.1 The CP Pup bursts as micronova eruptions?

The energy and shape of bursts shown by CP Pup resemble at least phenomenologically the bursts reported in Scaringi et al. (2022d) and Schaefer et al. (2022). In Scaringi et al. (2022d) the bursts are interpreted as micronova bursts, somewhat analogous to Type I X-ray bursts in neutron stars. Micronovae are hypothesised to be the result of a thermonuclear runaway effect in a relatively small magnetically confined accretion column. The objects so far reported to show these bursts are TV Col, EI UMa and ASASSN-19bh, with burst energies ranging from 9×10^{37} erg to 1.2×10^{39} erg. TV Col in particular has been observed at UV wavelengths during one of the bursts by Szkody & Mateo (1984), displaying high ionisation helium and nitrogen lines strengthening during the burst as well as clear P-Cygni profiles suggesting outflow velocities in excess of 3500km s^{-1}. The bursts in TV Col and EI UMa have been compared to those in V1223 Sgr (Hameury et al., 2022). In Hameury et al. (2022) the bursts reported in V1223 Sgr are interpreted by the magnetic-gating accretion instability model as observed in other accreting WDs (Scaringi et al. (2017b, 2022b); Littlefield et al. (2022)), but draws no definite conclusion on the nature of bursts in other IPs. Although magnetic gating may explain some observables for V1233 Sgr, it may not explain the large outflows observed by Szkody & Mateo (1984) in TV Col. The recurrent nova V2487 Oph has also been reported to display fast bursts that appear phenomenologically similar (Schaefer et al. (2022)), but their interpretation has been argued to be attributed to flares due to magnetic recconection events within the accretion disc.

If these are indeed related to the micronova events, then I can attempt to compute the burned/ejected mass during one of these events. The average conversion rate of Hydrogen during the CNO cycle in a standard nova explosion (Bode & Evans, 2008; José et al., 2020) is $\approx 10^{16}$ erg g^{-1}. With this assumption the observed energies convert to ejected masses of $> 6.2 \times 10^{-12} M_{\odot}$ and $> 3.2 \times 10^{-12} M_{\odot}$ for sectors 7 and 34 respectively, somewhat lower than those reported for TV Col and EI UMa in Scaringi et al. (2022d) of $1.8 - 5.8 \times 10^{-11} M_{\odot}$. I note that all these estimates should be considered lower limits as no colour and bolometric corrections have been applied. Hence the energies, and consequently ejected mass would most likely be larger under this interpretation.

From the micronova model (Scaringi et al., 2022c), the recurrence of the bursts is simply

associated with the time it takes for a confined column of material to reach thermonuclear runaway conditions. In the simplest scenario the burst recurrence time is given by $t_{\rm rec} = \frac{M_{\rm ejected}}{\dot{M}_{\rm acc}}$, where $M_{\rm ejected}$ represents the ejected mass during the burst and $\dot{M}_{\rm acc}$ the accretion rate of the system. The mass accretion rate estimated from the fit to the *XMM-Newton* spectra is between 1×10^{-10} to $2 \times 10^{-10} M_{\odot} yr^{-1}$. This assumes a WD mass of $M_{WD} \sim 0.73 M_{\odot}{}^{+0.12}_{-0.11}$, as estimated in Section 6.3.4. Hence the estimated recurrence time would be $t_{\rm rec} \approx 7 - 23$ days. For comparison the accretion rates quoted above from literature and the one determined in this work are all compared in Table 6.4 alongside with the corresponding recurrence times. Most of the accretion rates in Table 6.4 are also derived from fits to X-ray spectra and in such case the $T_{\rm max}$ and appropriate model are given as well. The table also notes if the model has a constraint on the $T_{\rm max}$ parameter and hence the accretion rate. This is judged by the constraint placed on the $T_{\rm max}$ by the model boundaries of the parameter.

The long-term *ASAS-SN* light curve may also constrain the recurrence timescale of the bursts. Figure 6.1 reveals an additional burst not observed by *TESS* after the ones detected in Sector 7 and 34 around $\sim$ 3005 BTJD. Along with the 2 bursts observed by *TESS* this suggests a recurrence timescale of $\sim$ 60 days. Considering the entire long-term *ASAS-SN* light curve from $\sim$ 1020 BTJD to $\sim$ 3020 BTJD the recurrence time can be roughly estimated to be $\sim 30 - 60$ days. The lower limit of the range is consistent with the predicted recurrence timescale using the accretion rate from Section 6.3.4. I do note that the data gaps could potentially make this an upper limit on the recurrence time. Beyond the long-term *ASAS-SN* data it is difficult to estimate if the recurrence holds.

Given the 1942 classical nova eruption, it is plausible to assume that up until then the WD in CP Pup had accreted $\approx 10^{-5} M_{\odot}$ during the preceding centuries, and that this fresh Hydrogen material would be spread across the entire WD surface. On the other hand, from the *ASAS-SN* long-term light curve it appears that fast burst events have been recurring in CP Pup for at least $\sim$4 years. Assuming these events are indeed micronova eruptions, the amount of mass used by the micronova events would then constitute only $\sim$0.005% of the mass required to trigger the next classical nova. It is of course also possible that micronova events have been occurring since the 1942 nova explosion. In this case, the consumed mass from micronovae would represent about 0.1% of the required mass to trigger the next classical nova. It is unclear how the recurrence timescales of micronovae and classical nova in the same system relate to each other, but I point out that the two types of explosions do not necessarily need to be mutually exclusive. The magnetic confinement criteria required may not be attained for long enough time to build up enough material to trigger a micronova,

allowing lateral spreading of freshly accreted material. The exact conditions for this remain unclear and it is possible that the bursts have not always been present in the system, for example if the conditions for magnetically confined accretion are fulfilled only temporarily. In such a case one or multiple micronova may be triggered. Cessation of micronova events could happen if the magnetic confinement of the accretion column is broken. Whether the accretion column can stay magnetically confined is thought to depend on the combination of multiple parameters, such as the strength of the magnetic field, the column height and footprint area as described in detail in Scaringi et al. (2022c).

Assuming a micronova interpretation, the lower limit of the recurrence deduced from the long term *ASAS-SN* light curve $t_{\rm rec} \approx 30$ days, the expected ejected mass would convert to $\sim 3 - 6 \times 10^{-11} M_{\odot}$, consistent with those reported in Scaringi et al. (2022d). This however would imply that the released energy in the *TESS* passband underestimates the bolometric release of energy by a factor of 3 or more. It is however possible that lower mass transfer rates could yield consistent burst recurrence times and energies.

All the recurrence timescales in Table 6.4 are however either shorter or on the lower boundary of the recurrence timescale deduced from the long term *ASAS-SN* light curve. This might be due to the number of necessary conditions for micronova to occur. For example the magnetic pole can change the size of its footprint on the surface of the WD before enough material is accreted for a micronova to be triggered. In such a case the recurrence timescale would become longer. The recurrence timescales could also be underestimated due to the WD mass. The same underestimation can be applicable in the recurrence timescale using accretion rate from other papers, see Table 6.4. For the mass of the WD to be better constrained however, a wider spectral coverage is necessary, such as that of *NuSTAR*.

Table 6.4: Summary of accretion rate estimates for CP Pup from literature and the parameters used to determine it. The recurrent timescale range is computed for the ejected masses above and compared to the results in this work.

Paper	Data	Model	$T_{\max}$ keV	Distance pc	M_{WD} $M_\odot$	$\dot{M}_{\rm acc}$ $\times 10^{-10}$ $M_\odot {\rm yr}^{-1}$	$t_{\rm rec}$ days	Constrained
Orio et al. (2009)	*XMM-Newton*	APEC	64	1600	>1.1	$\lesssim 1.6$	7.3 - 14	No
Mason et al. (2013)	*Chandra*	VMCFLOW	$36.5^{+19.2}_{-16.3}$	1600	$0.8^{+0.19}_{-0.23}$	4^{+3}_{-1}	$1.6 - 6.9$	Yes
Selvelli & Gilmozzi (2019)	–	Livio (1992)	–	795 ± 13	1.16 ± 0.2	$6.0^{+6.6}_{-3.1}$	$0.9 - 7.8$	–
This work	*XMM-Newton*	CEMEKL	$29.3^{+9.4}_{-7.4}$	780 ± 11	$0.73^{+0.12}_{-0.11}$	$1 - 2$	$7 - 23$	Yes

Another important parameter of the micronova model is the fractional area on which material is being accumulated. From the ejected masses $M_{\rm ejected}$ the fractional area f can be derived from Figure 1 in Scaringi et al. (2022d). For $M_{\rm ejected}$ and WD mass quoted above the expected f is $\sim 2 - 9 \times 10^{-7}$. This is particularly low for triggering micronova and may point to the bombardment scenario suggested for polars (Frank et al., 2002a). In that case, inhomogeneous accretion of dense blobs penetrate into the WD photosphere and radiate most of their energy in a form of soft X-rays. In such a scenario in Frank et al. (2002a), the accretion rate is constrained by $\lesssim 1.6 \times 10^{-11}\ M_{\odot}{\rm yr}^{-1}$. This is much lower than the estimated accretion rate for CP Pup and argues against the micronova interpretation. The only way out from this potential problem with the model is that the WD mass has been underestimated in the X-ray spectral analysis.

Further photometric, polarimetric and high-time resolution spectroscopic follow-up observations, of the peculiar behaviour displayed by CP Pup will provide additional constraints to unravel its true nature. Specifically the lack of consistent results when it comes to CP Pup, coupled with the lack of a coherent model to explain its behaviour, may warrant a dedicated observing campaign.

Chapter 7

DW Cnc: a micronova with a superhump

Abstract

Magnetic accreting white dwarfs in cataclysmic variables have been known to show bursts driven by different physical mechanisms; however, the burst occurrence is much rarer than in their non-magnetic counterparts. DW Cnc is a well-studied intermediate polar that showed a burst with a 4-magnitude amplitude in 2007. Here I report on a recent burst in DW Cnc observed by ASAS-SN that reached a peak luminosity of 6.6 $\times$ 10^{33} erg s^{-1}, another 4 mag increase from its quiescent high state level. The released energy of the burst suggests that these are micronovae, a distinctive type of burst seen in magnetic systems that may be caused by a thermonuclear runaway in the confined accretion flow. Only a handful of systems, most of them intermediate polars, have a reported micronova bursts. I also report on the reappearance of the negative superhump of DW Cnc as shown by TESS and OPTICAM data after the system emerges from its low state and immediately before the burst. I further report on a new phenomenon, where the spin signal turns "on" and "off" on the precession period associated with the negative superhump, which may indicate pole flipping. The new classification of DW Cnc as a micronova as well as the spin variability show the importance of both monitoring known micronova systems and systematic searches for more similar bursts, to limit reliance on serendipitous discoveries.

Co-author contribution

I have conducted the analysis as described in this Chapter and reported in Veresvarska et al. (2025b) under the supervision of Dr Simone Scaringi. The OPTICAM data was taken by Dr Federico Vincentelli and Section 7.2.2 was contributed by the members of the OPTICAM team

as well as the OPTICAM data reduction. Other co-authors have contributed with suggestions on analysis improvement and comments on the text of the paper.

7.1 Introduction

CVs are the most common type of AWD consisting of a binary system in which a WD accretes mass from a low-mass star via Roche lobe overflow. For an in-depth review of CVs and their history see Warner (2003) and Knigge et al. (2011), with a summary in Section 1.3.1.

CVs and how their accretion geometry is moulded by the magnetic field of the accretor are also reviewed in Section 1.3.1. This Section also offers explanation of the resulting observational effects of strong magnetic field, e.g. accretor spin. Section 6.3.1 offers an overview on the bursting and transient behaviour of CVs, with relation to the strength of their magnetic field as well.

DW Cnc is a well studied IP (Stepanyan, 1982; Rodríguez-Gil et al., 2004) which is known to undergo periods of low states as also observed in other IPs (Duffy et al., 2022; Covington et al., 2022). It has a reported spectroscopic orbital period of 86.1 minutes (Patterson et al., 2004; Rodríguez-Gil et al., 2004) and a 38.6 minute spin (Rodríguez-Gil et al., 2004). The spin signal has been known to disappear during the low state (Segura Montero et al., 2020; Covington et al., 2022), only to emerge after the system recovers to its pre-low state levels (Ramírez et al., 2022a; Duffy et al., 2022). There is also evidence of both hydrogen and helium in the accretion disc of DW Cnc; Segura Montero et al. (2020) reports double peaked Hα and He λ5876 Å lines with the latter showing a spiral structure in the disc. The authors associate this feature to a similar behaviour seen on several other systems including IP Peg, U Gem, EC 21178-5417 and the IP system DQ Her (Steeghs et al., 1997; Groot, 2001; Bloemen et al., 2010; Ruiz-Carmona et al., 2020) where such structures are considered to signify an enlarged accretion disc whose outer regions are being affected by the tidal forces of the donor e.g. Steeghs et al. (1997). Furthermore, DW Cnc has been known to show short duration (<1 day) bursts (Crawford et al., 2008). These bursts detected in 2007 correspond to a brightening of $\sim$ 4 mag. Disc instabilities and mass-transfer enhancements have been suggested as causes (Crawford et al., 2008), but their nature remains unknown.

Here I present new *Transiting Exoplanet Satellite Survey* (*TESS*) photometric observations of DW Cnc showing 2 coherent periods that persist throughout the *TESS* monitoring. I associate these coherent periods with the spin and beat between the WD spin and the orbital

period of the system. I present these results in Section 7.3.1 along with the appearance of a negative superhump in *TESS* sectors 71 and 72 accompanied by variable spin in Section 7.3.2. I further report a burst observed in *All-Sky Automated Survey for Supernovae* (*ASAS-SN*) coverage of DW Cnc reaching a maximum observed luminosity of $\sim 6.6 \times 10^{33}$ erg s^{-1}. I present these results in Section 7.3.3 and their interpretation as micronova in Section 7.4.1.

7.2 Observations

In this section, I discuss the data used for this work. *TESS* data and its calibration with *ASAS-SN* and *ATLAS* is discussed in Section 7.2.1, while the ground-based OPTICAM data is detailed in Section 7.2.2.

7.2.1 *TESS* and simultaneous ground-based *ASAS-SN* and *ATLAS* observations

The data analysed in this work were obtained from *TESS* and *ASAS-SN*. *TESS* observed DW Cnc over five sectors from October 12$^{\text{th}}$, 2021, to December 30$^{\text{th}}$, 2021 (sectors 44, 45 and 46), and from October 16$^{\text{th}}$, 2023, to December 7$^{\text{th}}$, 2023 (sectors 71 and 72). *ASAS-SN* observed DW Cnc from February 16$^{\text{th}}$, 2012, to November 29$^{\text{th}}$, 2018, in the V band, and from October 7$^{\text{th}}$, 2017, to May 28$^{\text{th}}$, 2024, in the g band. All relevant observations are displayed in Figure 7.1.

TESS data access and processing is described in detail in Chapter 2. *TESS* data is calibrated to ground-based *ASAS-SN* flux using the method detailed in Section 2.3 and Equation 2.3.1, with no bolometric correction. The coefficients for each half-sector, accounting for data deviations due to the gap in the middle of *TESS* sectors, are specified in Table 7.2.

Figure 7.1 shows the luminosity corresponding to the *TESS* and *ASAS-SN* data corrected for the distance of 209 ± 2 pc inferred from *Gaia* DR3 parallax (Gaia Collaboration et al., 2023). Additionally, Figure 7.1 shows the *ATLAS* o and c band forced-photometry light curve (Tonry et al., 2018; Heinze et al., 2018; Smith et al., 2020), corrected for the distance inferred from *Gaia* DR3 parallax. The *ATLAS* forced photometry was obtained through the web interface (Shingles et al., 2021)[4]. Combined *ATLAS* and *ASAS-SN* photometry improve the sampling of the observations and constraint on transient events not detected by only one survey (see right inset panel in Figure 7.1).

[4] `https://fallingstar-data.com/forcedphot/`

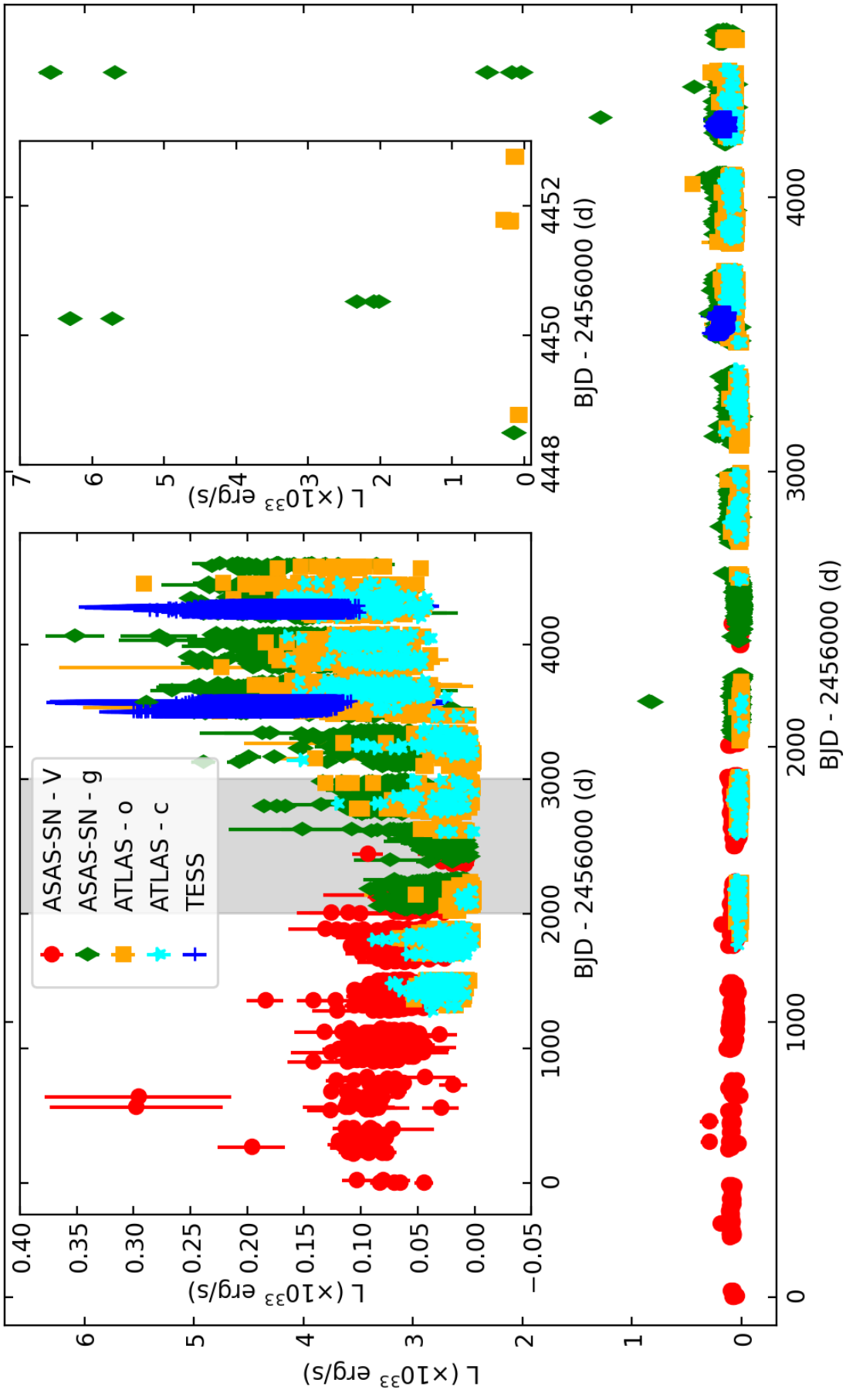

Figure 7.1: *ASAS-SN* , *ATLAS* , and *TESS* light curve of DW Cnc. Circles and diamonds denote the *ASAS-SN* V and g bands respectively. Similarly, the *ATLAS* o and c bands are denoted by squares and stars respectively. The crosses correspond to *TESS* sectors 44, 45, 46, 71 and 72. The left inset panel shows an enlargement in the luminosity axes, with the low state being marked by the shaded region. The right inset panel shows a zoom-in on the burst with $\sim 6.6 \times 10^{33}$ erg s^{-1} peak observed luminosity.

Table 7.1: Log of multi-band OPTICAM observations. All observations presented in the table were carried out using the filters g', r', and i' simultaneously, with an exposure time of 20 seconds.

Date (UT)	HJD (start time)	Effective Exposure (h)
2022-12-10	2459924.8052	2.22
2022-12-15	2459928.8021	2.84
2023-02-05	2459980.6460	4.58
2023-02-06	2459981.8040	4.59
2023-02-10	2459985.7215	5.58
2023-02-14	2459989.6513	7.42
2024-01-10	2460319.6720	8.02
2024-01-12	2460321.7719	6.00
2024-01-14	2460323.6973	7.56

7.2.2 OPTICAM

High-time resolution, triple-band optical observations with OPTICAM [5] (Castro et al., 2019, 2024) were conducted using the 2.1 m telescope at the Observatorio Astronómico Nacional San Pedro Mártir (OAN-SPM). The log of observations made with OPTICAM is shown in Table 7.1. All observations carried out with OPTICAM used the filters g', r', and i' simultaneously, with an exposure time of 20 seconds. Data were reduced following standard procedures using various tasks in NOIRLab IRAF v2.18[6] (Fitzpatrick et al., 2024). Star J075900.5+161647.1[7] was used as a reference. According to the GAIA synthetic photometry catalogue, this star has magnitudes $g' = 15.32, r' = 14.78$ and $i' = 14.62$ (Gaia Collaboration, 2020).

7.3 Results

In Section 7.3.1 I report all the coherent signals found in new *TESS* photometry of DW Cnc. In Section 7.3.2 the variable nature of the spin signal of DW Cnc as seen in *TESS* is shown. I further report on the burst of DW Cnc observed by *ASAS-SN* on the 19$^{\text{th}}$ of May 2024 in Section 7.3.3.

[5] `https://www.southampton.ac.uk/opticam`
[6] https://iraf.noirlab.edu/
[7] also SDSS J075900.5+161646.5 with g=15.47; r=15.01 and i=14.84

Table 7.2: Summary of the conversion coefficients from *TESS* flux in $e^{-}s^{-1}$ to *ASAS-SN* flux in mJy for DW Cnc. As the conversion is done twice per *TESS* sector, all corresponding coefficients are listed.

Sector	Sector half	$A\left(\frac{\text{mJy}}{e^{-}s^{-1}}\right)$	C (mJy)
44	1	0.021 ± 0.002	-0.5 ± 0.4
	2	0.021 ± 0.002	-0.5 ± 0.4
45	1	0.035 ± 0.004	0.9 ± 0.4
	2	0.036 ± 0.004	0.8 ± 0.4
46	1	0.027 ± 0.003	-0.4 ± 0.5
	2	0.03 ± 0.01	0 ± 2
71	1	0.032 ± 0.001	-0.2 ± 0.2
	2	0.032 ± 0.001	-0.2 ± 0.2
72	1	0.031 ± 0.002	-0.4 ± 0.3
	2	0.032 ± 0.009	-1 ± 2

7.3.1 *TESS* Data Analysis

The *TESS* light curve of DW Cnc as described in Section 7.2 can be divided into 2 semi-continuous sections. One represents sectors 44 to 46 immediately after DW Cnc returned from a low state and before any of the reported bursts in Section 7.3.3 took place. The Lomb-Scargle (Lomb, 1976) periodogram of this $\sim$ 3-month light curve is shown in the bottom panel of Figure 7.2. In all instances in this work, the Lomb-Scargle implementation used is `Astropy` v.5.3.4, with the high limiting frequency corresponding to the Nyquist frequency of the given time series and the low frequency to the $\frac{3}{L}$, where L represents the length of the time series. There are only 3 signals recovered from this light curve at 37.3 c d^{-1}, 20.6 c d^{-1} and 41.2 c d^{-1} and they are listed in Table 7.3.

The other semi-continuous light curve is constructed from sectors 71 and 72, immediately before the small burst at $\sim$ 2460287 BJD. The Lomb-Scargle periodogram of the light curve is shown in the top panel of Figure 7.2. The periodogram also shows all the signals present in sectors 44 through 46. However, on top of these signals, numerous new signals appear. All the signals are listed in Table 7.3 with their corresponding errors and sectors in which they are present.

The errors in Table 7.3 are determined via bootstrapping of the original light curve, similar to Paice et al. (2024b). This consists of randomly selecting with replacement N number of data points from the light curve, where N is the original number of data points. Then the same Lomb-Scargle periodogram is constructed and the peak of the signal is extracted. A distribution of the peaks after 5×10^4 repetitions is constructed. A Gaussian fit to the resulting distribution gives the mean value of the signal and its error corresponding to a 1σ

Table 7.3: List of all coherent signals extracted from *TESS* data of DW Cnc and their relation to one another with the sectors in which they are present. The spin period is noted as $P_{\rm spin}$. The beat between the spin period and the undetected orbital period ($P_{\rm orb} = 16.7245$ c d^{-1}) is noted as $P_{\rm b}$ with its first harmonic $2P_{\rm b}$. The negative superhump associated with the retrograde nodal precession of a tilted accretion disc is noted as $P_{\rm nSH}$ with its first harmonic $2P_{\rm nSH}$. The beats between these frequencies and their harmonics are denoted by their combination.

Frequency (c d^{-1})	Origin	*TESS* sectors
3.66860(5)	$P_{\rm b} - P_{\rm nSH}$	71 & 72
13.2602(7)	$2P_{\rm nSH} - P_{\rm b}$	71 & 72
16.9276(2)	$P_{\rm nSH}$	71 & 72
20.5962(2)	$P_{\rm b} = P_{\rm spin} - P_{\rm orb}$	all
30.189(1)	$3P_{\rm nSH} - P_{\rm b}$	71 & 72
33.85669(8)	$2P_{\rm nSH}$	71 & 72
37.32166(7)	$P_{\rm spin}$	all
37.52541(3)	$P_{\rm nSH} + P_{\rm b}$	71 & 72
41.2024(2)	$2P_{\rm b}$	all

deviation of the distribution.

7.3.2 Spin Variability

Figure 7.3 shows the dynamical power spectral density (PSD) of *TESS* sectors 71 and 72, with zoom-ins showing the light curves of several sections folded on the spin period from Table 7.3. The dynamical PSD is constructed by taking Lomb-Scargle periodograms, as in Section 7.3.1, of 0.5-day long non-overlapping sections of the light curve. While a strong signal is present throughout the 2 sectors, there is also a significant time-dependent variability, with 2 distinct states, that are not seen in the previous *TESS* sectors 44−46: An "on" state, where the spin signal is showing significant power and lasts ~ 3 days centred around BJD − 2457000 3235, 3242, 3247, 3255, 3267, 3272, 3279 and 3285; and an "off" state in between these, when the power at $P_{\rm spin}$ drops significantly to the background level of Poisson noise $P_{\rm RMS\ normalised} \lesssim 200$. This latter state is much shorter (~ 1 day) in duration and occurs around BJD - 2457000 3238, 3244, 3252, 3258, 3260, 3270, 3277 and 3282. To demonstrate the change in spin state, examples of phase-folded light curves are provided for the “on” (top panels of Figure 7.3) and “off" (bottom panels of Figure 7.3) states. The examples of the phase-folded light curves correspond to the 0.5-day segments of the light curve at instances indicated by the red arrows. As seen from the phase-folded light curves, the flux level remains constant in both states and there is no significant change in the spin period $P_{\rm spin}$ detected over the course of the *TESS* sectors with respect to the ephemeris reported by Patterson et al. (2004). As seen in the spin pulse profiles in Figure 7.3 only shows 1 peak, which is also true of other signals detected in

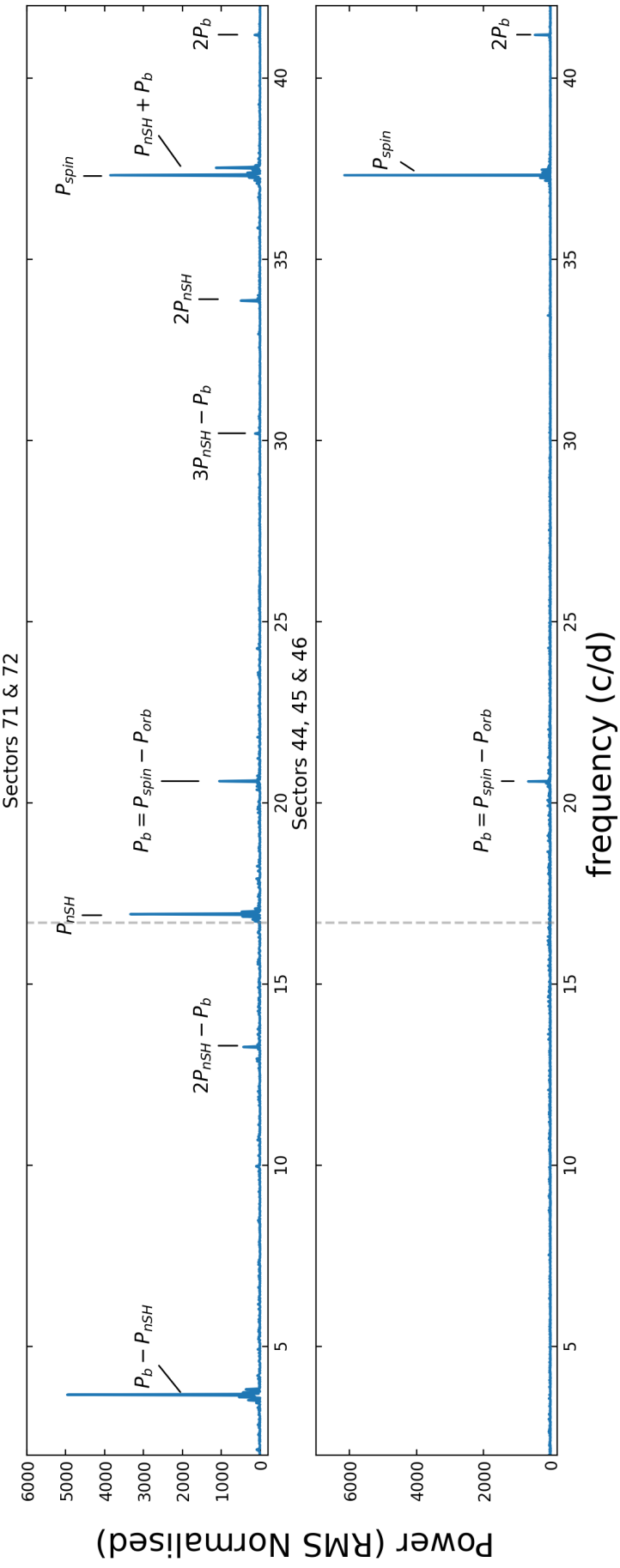

Figure 7.2: Lomb-Scargle power spectra of *TESS* sectors of DW Cnc zoomed in on all identified signals. The top panel shows the periodogram of the combined light curves of sectors 71 and 72 whilst the bottom panel shows the periodogram for the combined light curve of sectors 44 to 46. The position of the orbital period, which is not detected here, is marked by a dashed line.

Sectors 71 and 72. However, when examining the shape of the spin-orbit beat pulse profile over the course of the negative superhump period from Table 7.3 shows a $\sim 180°$ phase shift. This is demonstrated in Figure 7.4, where the spin period (left hand-side) and spin-orbit beat period (centre) pulse profiles are shown as a function of the negative superhump cycle, similarly to Littlefield et al. (2019, 2021, 2023). Figure 7.4 demonstrates a dynamical representation of phase folded light curves on a signal at different phases of another signal. This allows us to identify the changes in positions of the peaks and troughs of the phase-folded light curves on a given period with respect to the phase of another one. Hence, a diagonal pattern signifies a phase shift between the given signals, as seen in the middle and right panel of Figure 7.4. Furthermore, the $\sim 180°$ phase drift in spin cycle is also visible during the precession cycle associated with the negative superhump identified in Table 7.3.

To quantify the "on" and "off" states, I measure the power at $P_{\rm spin}$ for each of the 0.5-day segment for sectors 71 and 72 from Figure 7.3. The resulting time series of the $P_{\rm spin}$ variability is shown in Figure 7.5. From Figure 7.5 the Spin-off state is hence defined as when the $P_{\rm spin}$ power is below twice the average power at frequencies below $P_{\rm spin}$. These thresholds are indicated in Figure 7.5 by a dotted line for sector 71 and a dashed line for sector 72.

Figure 7.6 shows a Lomb-Scargle periodogram of the time series, to search for periodic modulation of the spin power (the data shown in Figure 7.5). The PSD shows shows a single peak at ~ 0.2 c d^{-1}, which is consistent with the fundamental precession frequency associated with the negative superhump observed in *TESS* data $1/P_{-} = 1/P_{\rm nSH} - 1/P_{\rm orb} = 0.2028(9)$c d^{-1}. The error on the signal is determined using the same method as described in Section 7.3.1 for the signals in *TESS* data.

I also separated the light curves of sectors 71 and 72 into the "on" and "off" states based on the thresholds in Figure 7.5, producing distinct light curves with and without the spin variability. The resulting Lomb-Scargle of these light curves are shown in Figure 7.7. I see only negligible power in the "off" state and a significant decrease in power amplitude at other frequencies present in the overall Sector 71 and 72 (see Figure 7.2 top panel).

Furthermore, a time-averaged power spectrum (TPS) is computed for several sections of *TESS* data and shown in Figure 7.8. The TPS is constructed by separating the light curve into 0.5-day segments. A segment of 0.5 days is chosen to be consistent with the segment length in Figure 7.3. A Lomb-Scargle of each of the segments is then computed, before the individual PSDs are averaged together and binned onto a coarser frequency bin ($N_{\rm bins} = 50$).

To estimate further constraints on the spin variability seen in *TESS* data of DW Cnc I

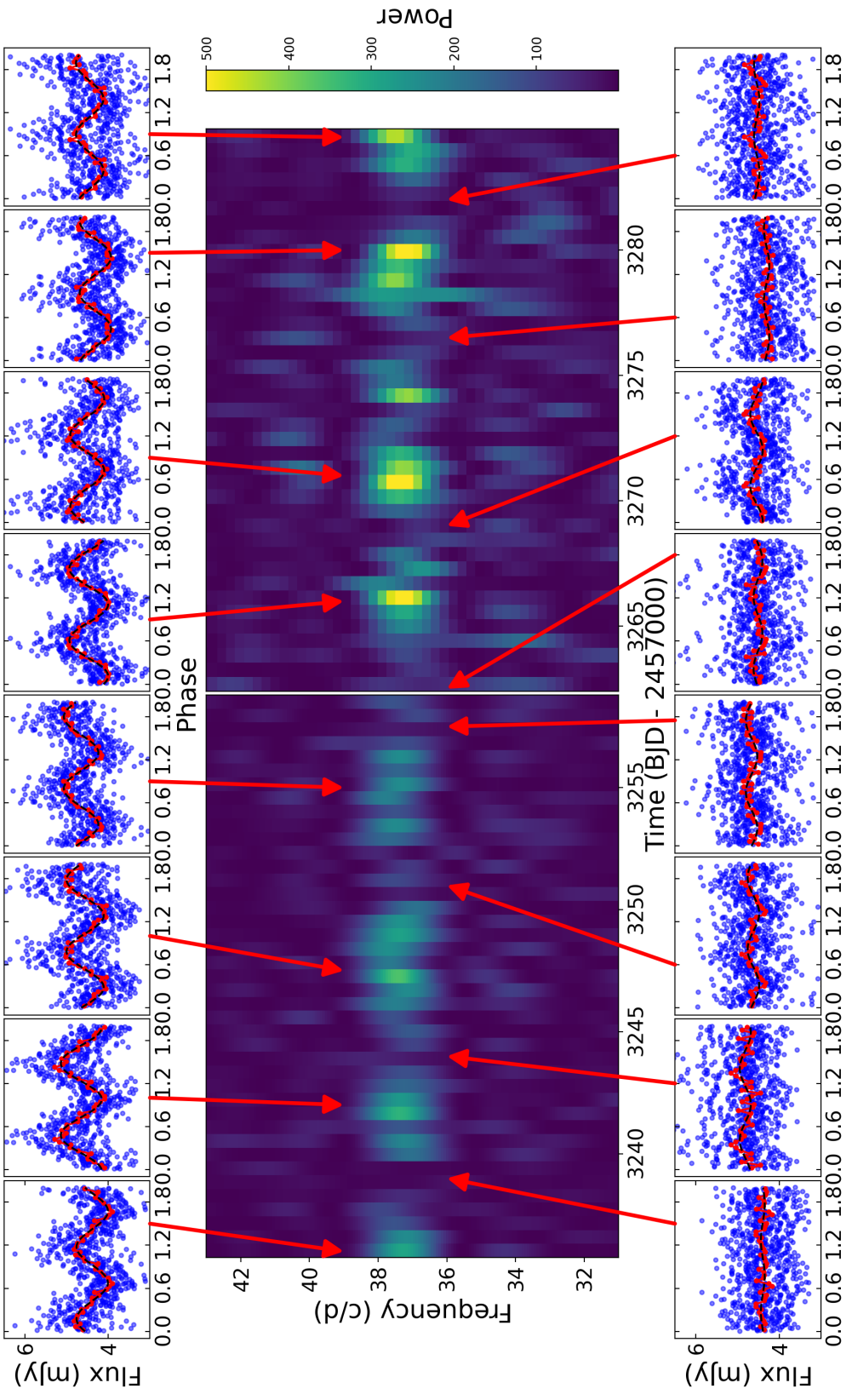

Figure 7.3: Dynamical Lomb-Scargle power spectra of *TESS* sectors 71 and 72 of DW Cnc zoomed in on the spin signal at 37.32166(7) c d^{-1} showing semi-periodic turning "on" and "off" of itself. The top and bottom panels show a phase folded light curve on the spin period of 0.5 *d* long segment as indicated by the arrows. The top panels are selected at the peak spin power in a given cycle on the spin being "on". The bottom panels show the minimum power segment in the "off" segment.

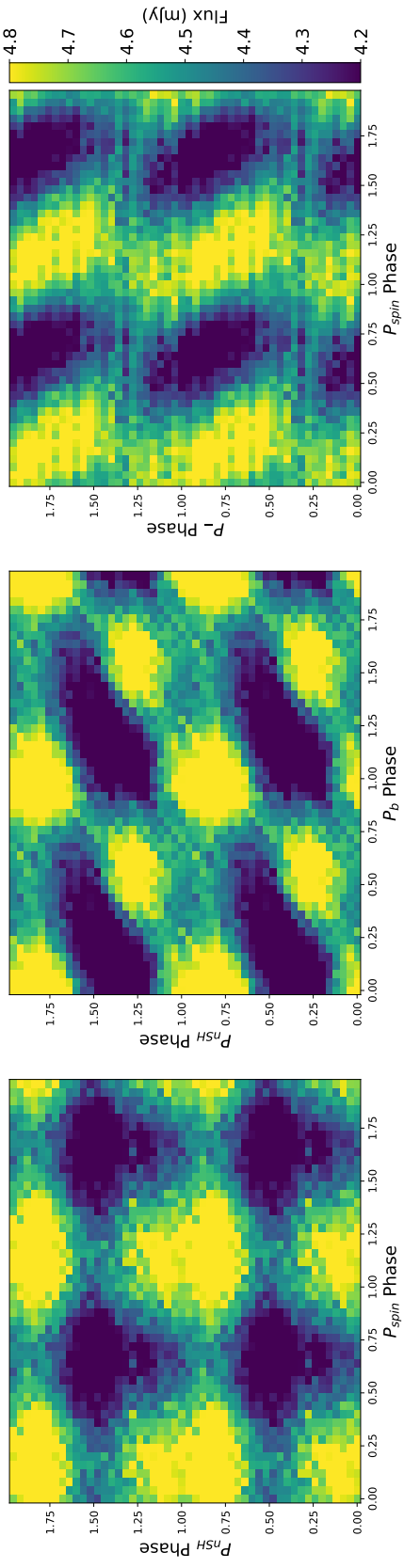

Figure 7.4: 2D profiles of the spin and beat pulses across the superhump cycle and spin profile across the fundamental precession cycle. The beat profile shows a $\sim 180°$ jump for half of the superhump cycle similarly to the $\sim 180°$ phase shift in spin phase over the precession cycle, indicating that the tilt of the disk determines which magnetic pole is dominant.

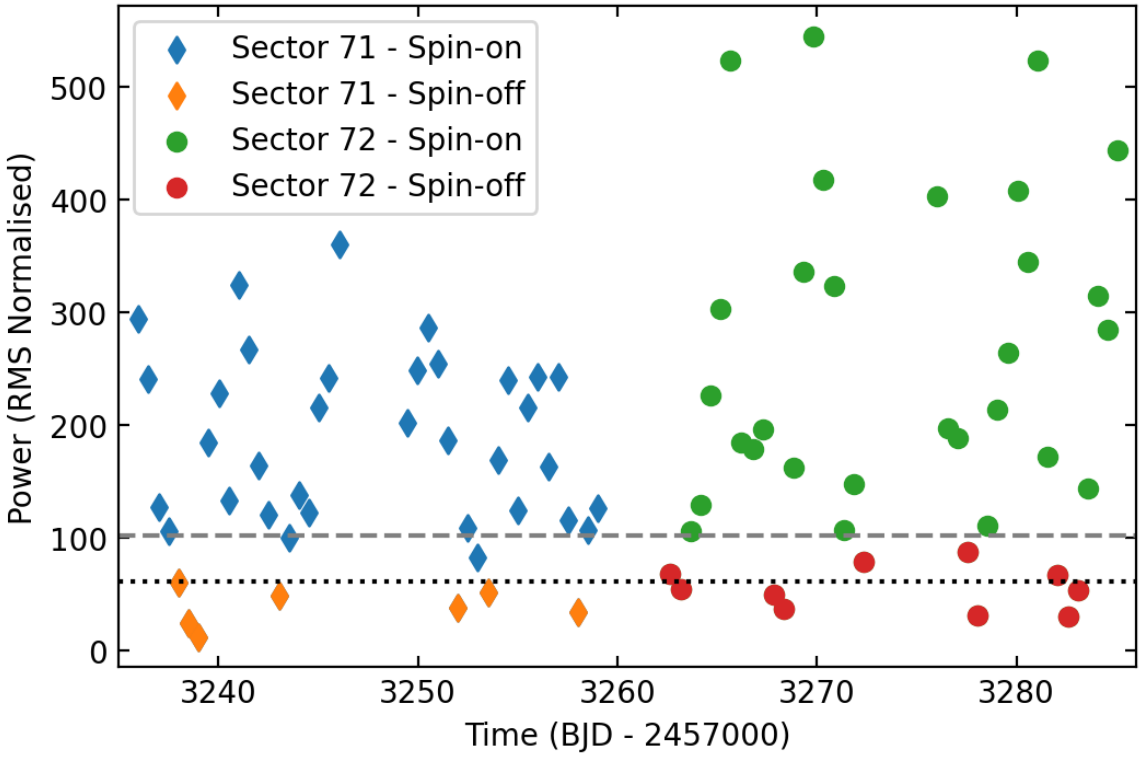

Figure 7.5: Time dependent evolution of power at $P_{\rm spin}$ for DW Cnc *TESS* data of sectors 71 and 72. The dotted line indicates the threshold for sector 71 at which the spin power is considered not significant. Similarly, the dashed line indicates a significance threshold for sector 72.

Table 7.4: OPTICAM observations corresponding to Table 7.1. $f_{\rm low}$ represents the lowest possible frequency probed by the observation, defined as $1/effective\ exposure$ from Table 7.1. The following columns indicate if the spin period $P_{\rm spin}$ and the negative superhump $P_{\rm nSH}$ were detected in the given observation.

Date (UT)	$f_{\rm low}$ (c d^{-1})	$P_{\rm spin}$	$P_{\rm nSH}$
2022-12-10	10.81	✓	x
2022-12-15	8.45	x	x
2023-02-05	5.24	✓	x
2023-02-06	5.22	✓	x
2023-02-10	4.30	✓	x
2023-02-14	3.23	x	✓
2024-01-10	2.99	✓	✓
2024-01-12	4.00	✓	✓
2024-01-14	3.17	✓	✓

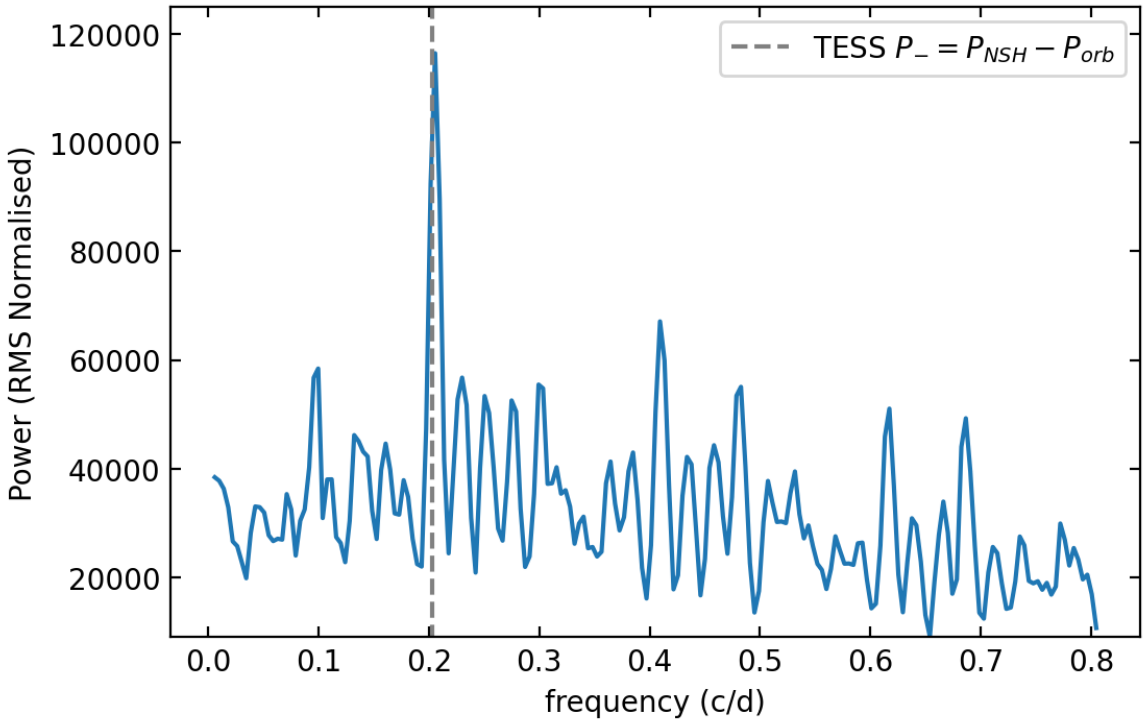

Figure 7.6: Lomb-Scargle periodogram of the time dependent variations of power at $P_{\rm spin}$ as shown in Figure 7.5. The dashed line corresponds to the frequency inferred for the precession fundamental precession frequency associated with the negative superhump reported in Table 7.3.

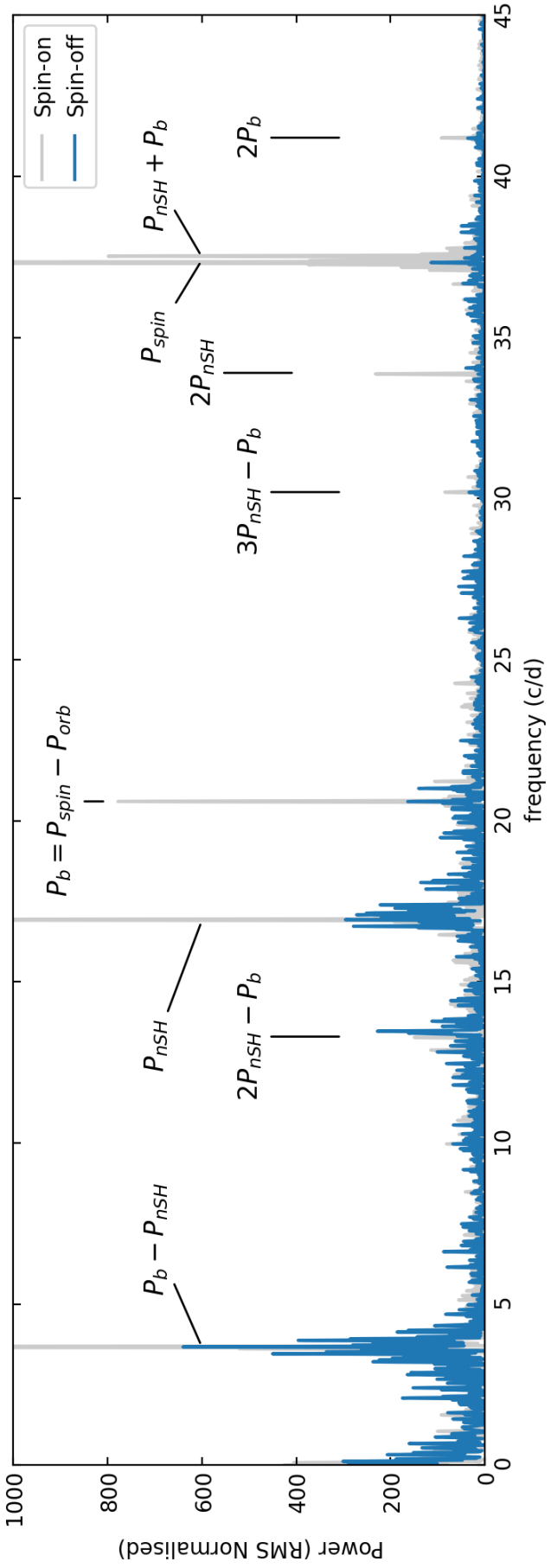

Figure 7.7: Lomb-Scargle power spectra of the separate "on" and "off" light curves from *TESS* sectors 71 and 72. The signals present in these sectors are marked as in Figure 7.2.

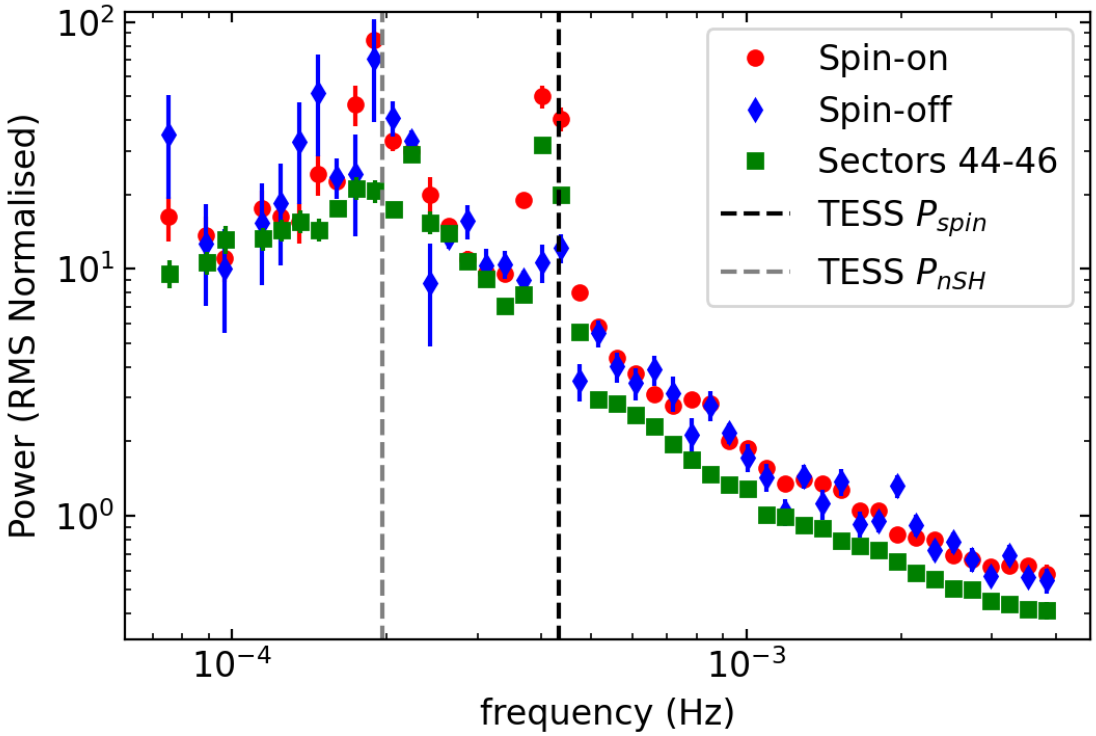

Figure 7.8: Time averaged power spectrum of *TESS* data. The squares correspond to Sectors 44 to 46, whilst sectors 71 and 72 are divided into the "on" (circles) and "off" (diamonds) spin state based on Figure 7.5. The positions of $P_{\rm spin}$ and nSH from Table 7.3 are indicated by the dashed lines.

introduce the OPTICAM data as detailed in Section 7.2.2. The 3-band optical photometry was taken on multiple nights at different cadence and lengths (see Table 7.1 for further details). An example of the multi-band light curves is shown in the top panels of Figure 7.9. In Figure 7.9 I choose to show examples of DW Cnc light curves from Table 7.1, with the results from all the data being detailed in Table 7.4.

Figure 7.10 shows the combined PSD of the OPTICAM data from Table 7.1. The PSD is obtained as described in detail in Section 7.3.1. The signals in *TESS* data are marked by vertical lines, confirming the presence of spin of DW Cnc, the negative superhump and the beat between the spin-orbit beat and the negative superhump. To verify if all of these signals are always present in the OPTICAM data, the Lomb-Scargle is computed for all OPTICAM data and bands, with examples shown in the middle panels of Figure 7.9. Given the shorter duration of the individual OPTICAM observations and the limiting lowest frequency, I use the frequencies in Table 7.3 as guidelines to mark the likely presence of signals in the OPTICAM data. The presence of the signals detected in Figure 7.10 in separate OPTICAM observations is marked in Table 7.4. I note that the spin signal wasn't detected during several observations, similar to the behaviour seen in *TESS* sectors 71 and 72.

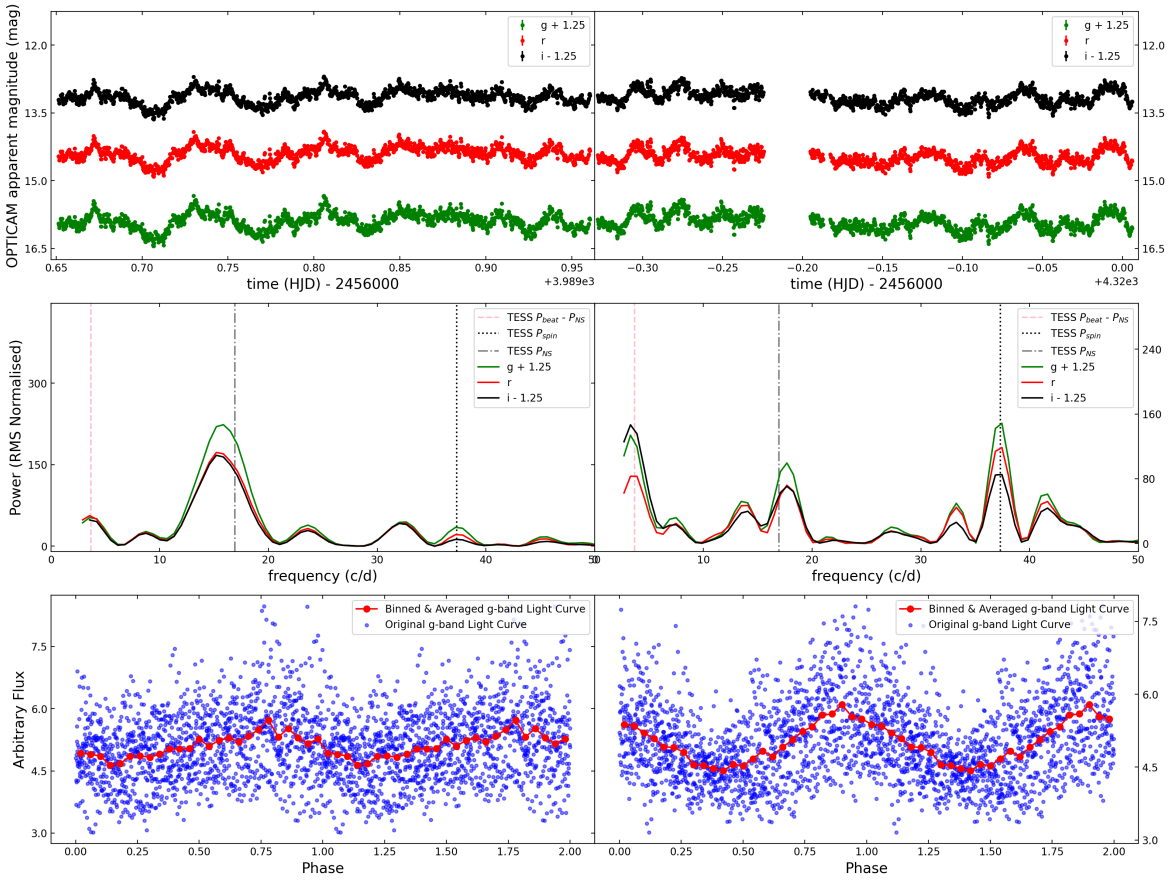

Figure 7.9: Examples of OPTICAM data from 2023-02-14 (left panels) and 2024-01-10 (right panels). The *Top*: The top panels show a g, r and i band light curves of DW Cnc on given nights with a specified offset. *Middle*: The middle panel shows a PSD corresponding to the light curves from the top panel with selected periods from *TESS* ($P_{\rm spin}$, $P_{\rm nSH}$ and $P_{\rm b} - P_{\rm nSH}$). *Bottom*: The bottom panel shows a phase-folded *g*-band light curve, folded on the spin period $P_{\rm spin}$ from *TESS* data as noted in Table 7.3.

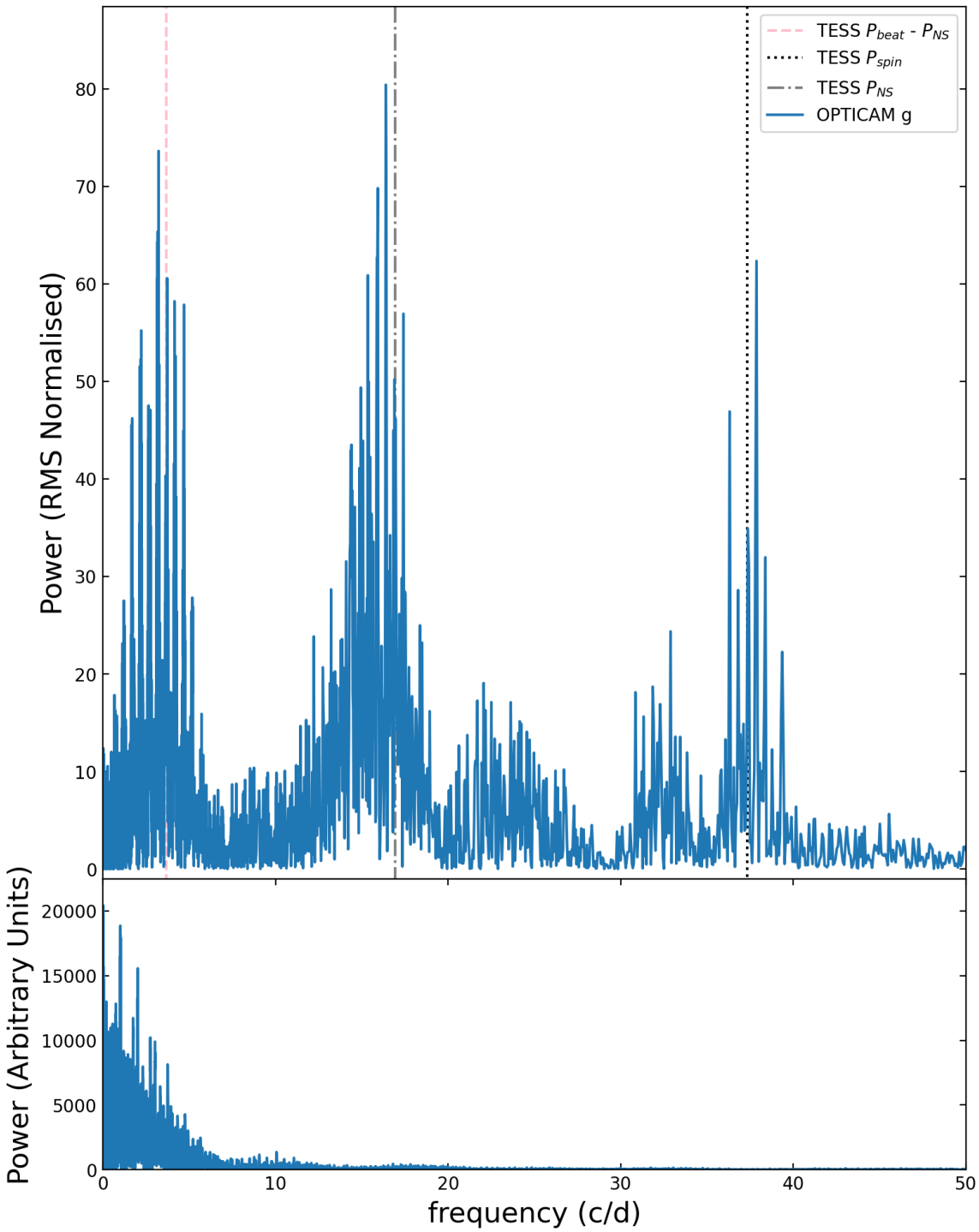

Figure 7.10: *Top:* PSD of the combined OPTICAM g-band data from Table 7.1. The vertical lines indicate the spin $P_{\rm spin}$, negative superhump $P_{\rm nSH}$ and the beat between the spin-orbit beat and the negative superhump $P_{\rm b} - P_{\rm nSH}$. *Bottom:* PSD representing the window function used.

The 2 columns in Figure 7.9 represent examples of when the spin signal is not present (left) and where is it detected (right). There is also a clear power excess seen at the frequencies corresponding to the negative superhump frequency from 14$^{\text{th}}$ of February 2023 (almost a year before sector 71) until the last measurement on the 14$^{\text{th}}$ of January 2024 ($\sim$ month after the end of sector 72). To demonstrate the switching of spin between the "on" and "off" state is present in the OPTICAM data as well, phase-folded light curves of g-band OPTICAM data are included in the bottom panels in Figure 7.9. There, the OPTICAM data is folded on the *TESS* spin as shown in Table 7.3.

7.3.3 Bursts

The long-term *ASAS-SN* and *ATLAS* light curve of DW Cnc covers its variability from 16$^{\text{th}}$ of February 2012. There are only a couple of instances in this time when the luminosity of DW Cnc rises above its average levels, showing distinct bursts akin to those reported in Crawford et al. (2008). At $\sim$ 2456600 BJD there are 2 data points at $\sim 3 \times 10^{32}$ erg s^{-1} in *ASAS-SN* V-band. However, in both cases, these are single-point measurements and considering the uncertainty of the measurements the validity of these points as an outburst may be less reliable.

The data show two low-amplitude outbursts that I will not consider further here. These appear immediately before the low state between $\sim$ 2458000 BJD and 2459000 BJD (Covington et al., 2022) (shaded region in Figure 7.1), at 2458164 BJD reaching peak luminosity at $\sim 8.8 \times 10^{32}$ erg s^{-1} lasting for about a day in *ASAS-SN* . However, *ATLAS* observed DW Cnc in quiescence in the middle of the *ASAS-SN* bursts. Therefore, the outburst is either not real or a sequence of multiple $\sim$0.5 day bursts. In any case, this is not considered here due to the low significance. A similar amplitude burst is seen in *ASAS-SN* at $\sim$ 2460287 BJD with peak luminosity of $\sim 1.3 \times 10^{33}$ erg s^{-1} and also about a day long duration.

However, a truly analogous burst to those reported in Crawford et al. (2008) is seen in *ASAS-SN* at HJD 2460450. The peak luminosity of this burst is recorded at 6.6×10^{33} erg s^{-1}, corresponding to a brightening of 4 magnitudes from its quiescent levels. By combining the *ASAS-SN* and *ATLAS* light curves it is possible to obtain an upper limit on the duration of the burst; Due to the *ASAS-SN* light curve sampling, the upper limit on the duration of the burst would be $\sim$ 6 days, when a measurement at quiescent level confirms the end of the burst after a $\sim$ 4-day data gap. However, considering the *ATLAS* c-band measurements as seen in the right inset plot in Figure 7.1, the upper limit on the duration is $\sim$3 days. The burst has

been completely missed by *ATLAS* and only serendipitously picked up by *ASAS-SN* . This raises an important question, how many similar shorter-length bursts have been missed in DW Cnc since the start of monitoring and in other systems as well? Therefore, with the rise of higher-cadence surveys such as *BlackGEM* and the Rubin Observatory (Ivezić et al., 2019), the frequency of detecting the short-duration bursts in AWDs should allow us to understand them better and constrain their recurrence with greater precision.

The total energy released during the burst is determined by integrating the luminosity under the light curve after subtracting the baseline luminosity of the light curve. The baseline is determined from a fit to the mean of the pre-burst long-term light curve about ~ 100 days before the burst. This reveals an energy release of $> 6 \times 10^{38}$ erg when using a linear interpolation between the first quiescent point before and after the burst from the combined *ASAS-SN* and *ATLAS* light curve. A lower limit here is used as no bolometric correction is used and energy that may have been released in other parts of the spectrum has not been considered. A more conservative lower limit, only integrating the energy of the points above the quiescence level, would produce an energy of $> 9 \times 10^{37}$ erg.

7.4 Discussion

In Section 7.4.1 I discuss the interpretation of the bursts in DW Cnc as a micronova, as well as the related implications with this interpretation. In Section 7.4.2 I discuss the interpretation of signals detected in *TESS* data of DW Cnc with the physical and geometrical consequences for the system. Section 7.4.3 details the interpretation of the spin variability seen in DW Cnc.

7.4.1 Burst Nature

There are several possible explanations for bursts observed in magnetic AWDs, such as dwarf nova outbursts, micronovae, and magnetically gated bursts. A diagnostic diagram that attempts to distinguish among these possibilities has been introduced by Iłkiewicz et al. (2024), where the burst integrated energy, peak luminosity, recurrence time and burst duration appear to separate different burst types (see Figure 1.6 for more detail). Adopting a peak luminosity for the burst observed in DW Cnc of $\approx 6.6 \times 10^{33}$ erg s^{-1}, an integrated energy of $> 6 \times 10^{38}$ erg, and a bust duration of < 3 days, it appears that the burst in DW Cnc most closely matches the properties of ASASSN−19bh (Scaringi et al., 2022d) and PBC

J0801.2−4625 (Irving et al., 2024) which have both been interpreted as a particularly energetic micronovae events.

As discussed in Scaringi et al. (2022c) micronovae may occur if mass accretion occurs onto magnetically confined polar regions of AWDs, where accreted mass is magnetically confined and accumulates until thermonuclear ignition conditions are reached, triggering a runaway micronova explosion. Under these assumptions the recurrence time of micronova events on any one system can be estimated from the mass accretion rate $\dot{M}_{acc}$ together with the total mass required to thermonuclear ignite the magnetically confined accretion column.

Adopting a mass to energy conversion rate of hydrogen burning during the CNO cycle of $\approx 10^{16}$ erg g^{-1} (Bode & Evans, 2008; José et al., 2020), the observed $> 6 \times 10^{38}$ erg burst in DW Cnc would convert to $M_{\rm col} > 3 \times 10^{-11} {\rm M}_{\odot}$. Assuming this amount of mass has been accumulated onto a magnetically confined polar region since the last burst an estimate of the mass accretion rate onto DW Cnc can be obtained from $\dot{M}_{\rm acc} = M_{\rm col}/t_{\rm rec}$. The $M_{\rm col}$ represents the mass that is ejected from the accretion column during the burst and $t_{\rm rec}$ the recurrence time of the bursts. The *ASAS-SN* light curve in Figure 7.1 reveals a recorded (small amplitude) burst ≈ 6 years earlier, which I assume to be a partially observed micronovae event to obtain a mass accretion rate onto DW Cnc of $5 \times 10^{-12} {\rm M}_{\odot} {\rm yr}^{-1}$.

This estimate can be compared to the mass transfer rate of DW Cnc assuming the optical and X-ray luminosities are a reliable tracer for accretion luminosity through

$$L_{\rm acc} = \frac{G M_{\rm WD} \dot{M}}{2 R_{\rm in}} \approx L_{\rm opt} + L_{\rm X\text{-}rays} \tag{7.4.1}$$

where $M_{\rm WD}$ is the WD mass, assumed to be $\sim 0.8\ M_{\odot}$, $\dot{M}$ is the mass transfer rate, G the gravitational constant and $R_{\rm in}$ the inner disc radius. I set the inner disk radius to the WD radius, $R_{\rm in} = R_{\rm WD} = 0.01 R_{\odot}$ as any X-ray emission from accretion curtains should also be considered. Adopting the optical luminosity $L_{\rm opt} = 9.8 \times 10^{31}$ erg s^{-1} from the *ASAS-SN* light curve (excluding bursts), together with the X-ray luminosity of $L_{\rm X} = 8.7 \times 10^{31}$ erg s^{-1} in the *XMM-Newton* $0.3 - 10$ keV range as inferred by Nucita et al. (2019), yields a mass transfer rate $\dot{M} \approx 3.9 \times 10^{-11}\ M_{\odot} {\rm yr}^{-1}$, consistent with other IPs at similar orbital periods (Knigge et al., 2011; Duffy et al., 2022).

It is important to note that while the the optical and X-ray luminosities provide an estimate of the secular disk mass *transfer* rate, the burst energetics provide an estimate of mass *accretion* rate onto the WD magnetically confined polar regions. Although these can be the same in some cases, they do not strictly have to be. As also discussed in Scaringi et al. (2022c)

the mass transfer and mass accretion rates would not necessarily be the same since some of the material may experience either lateral spreading at the base of the magnetically confined polar region or be accreted outside of the magnetically confined region (or both). In any case I emphasise that the interpretation of Scaringi et al. (2022c) and related methodology applied here to DW Cnc requires further testing through observational evidence and theoretical modelling.

7.4.2 *TESS* Signals

The Lomb-Scargle of the *TESS* light curves as presented in Figure 7.2 shows many periodic signals reported in Table 7.3. Only 3 signals are always present in the *TESS* data. One of them, at 37.32166(7) c d^{-1} is consistent with the spin period of the systems previously reported (Rodríguez-Gil et al., 2004). This confirms what was found in Covington et al. (2022), i.e. that the spin signal has recovered after its disappearance in the low state (Segura Montero et al., 2020). Another period that is always present in the *TESS* light curve is the 20.5962(2) c d^{-1} signal. This signal has been observed before and after the low state (Segura Montero et al., 2020; Covington et al., 2022) and is associated with the beat between the spin and the orbital period of the system. The orbital period is not recovered due to the likely low inclination of the system. The last signal present during all *TESS* sectors is the first harmonic of the beat, at 41.20 c d^{-1}.

Sectors 71 and 72 see the appearance of new signals. One of them is the 16.9276(2) c d^{-1} signal. This is very close to the spectroscopic period of the system at 16.72441(6) c d^{-1} (Segura Montero et al., 2020). Given the close frequencies of the signals, I propose that 16.9276(2) c d^{-1} is the negative superhump of the system associated with the retrograde precession of a tilted accretion disc. This is similar to another low inclination system MV Lyr, which also displays negative superhump (Bruch, 2023). No precession frequency has however been recovered. TV Col, another intermediate polar showing micronova bursts, has also shown negative superhump (Scaringi et al., 2022d); and even showed a positive superhump in the pre-burst stage. This peculiar behaviour suggests that DW Cnc may also show similar behaviour before undergoing a burst and thorough monitoring is necessary to confirm this for future bursts.

The other signals represent beats with the harmonics of the superhump and the spin-orbit beat, as described in Table 7.3.

7.4.3 Spin variability as evidence of pole flipping?

As described in Section 7.3.2 and shown in Figure 7.3 the spin period is showing semi-periodic changes between "on" and "off" states in *TESS* sectors 71 & 72, with evidence that the behaviour started as early as February 2023 from the OPTICAM observations. The change between states occurs on 0.2028(9) c d^{-1} timescale, consistent with the fundamental superorbital period expected at $\frac{1}{P_{\text{-}}} = \frac{1}{P_{\text{nSH}}} - \frac{1}{P_{\text{orb}}} = 0.2028$ c d^{-1} ~ 4.9 days, as seen in Figure 7.3 and 7.6. Unfortunately, this period is not detected in the *TESS* data but can be recovered from the variability of power at P_{spin}.

One possible explanation for this behaviour is a modulation of accretion, where accretion ceases during the "off" states. This would resemble the low state previously observed in DW Cnc (Segura Montero et al., 2020) but occurring on much shorter timescales. However, in contrast to Segura Montero et al. (2020), no significant drop in flux is observed, suggesting that accretion persists even during the "off" states. This raises the possibility that the modulation is related to accretion geometry rather than an outright cessation of accretion.

The hypothesis that pole flipping occurs in DW Cnc must be treated with caution. In asynchronous polars (APs), pole flipping is driven by accretion from an azimuthally asymmetric stream directly interacting with the white dwarf's magnetosphere (Ferrario & Wickramasinghe, 1999). This scenario is known to occur in APs, where the central white dwarf accretes via magnetically confined stream, but the orbit and spin period are slightly out of sync. In these systems, particularly BY Cam and CD Ind (Littlefield et al., 2019), where both accretion poles are visible, the switch from one to another can be detected by a phase shift of the spin during the beat cycle. In APs, pole-switching is accompanied by a phase shift of 180° in the spin cycle during half the spin-orbit beat cycle. This is observed in FO Aqr (Norton et al., 1992) as well as CD Ind (Littlefield et al., 2019) and BY Cam (Mason et al., 2022). Such behaviour is unlikely in DW Cnc, where the presence of a negative superhump implies accretion via a tilted, precessing accretion disc. Unlike APs, where pole flipping occurs at the beat frequency between the spin and orbital periods, any pole modulation in DW Cnc would likely occur at the disc's precession period. This distinction underscores that pole flipping in DW Cnc, if present, would be fundamentally different from that in APs.

The observed spin variability may instead reflect changes in the accretion flow alignment with the white dwarf's magnetic poles, modulated by the disc's tilt and precession. Figure 7.4 shows a similar phase shift of $\sim 180°$ in the beat during the negative superhump cycle and in the spin phase during the precession cycle, suggesting that the tilt and precession of the

disc influence the accretion flow. Furthermore, before the discontinuous jump of spin phase at ~ 0.3 and ~ 1.6 precession phase there is a continuous shift in the spin over ~ 0.5 cycle of the precession. This modulation could lead to periodic shifts in the dominant accreting pole. Unlike classical pole flipping, which depends on direct interaction with a stream, this process would be driven by the precession of the disc itself, which modifies the effective area of interaction between the disc and the magnetic field. Furthermore, the process needs not to be discrete, but rather a continuous change of accretion power fraction between the magnetic poles, as indicated by the right panel in Figure 7.4.

The non-detection of a photometric modulation at the orbital period suggests the inclination is fairly low. If that is the case, the "off" state may correspond to either accretion onto only one magnetic pole permanently obscured by the WD, or a gradual change of power accreted onto either pole. Such a gradual change may be supported by Figure 7.4 and in the remnants of sinusoidal variations in phase folded light curves of the spin in the "off" state in *TESS* data (Figure 7.3) and OPTICAM data (Figure 7.9). These phase-folded light curves on the *TESS* spin period show a single peaked shape consistent with majority accretion onto a single magnetic pole. Furthermore, there is no expectation of the geometry of the accretion disc changing, as seen in Figure 7.8. This figure shows, that the broad-band shape of the PSD in DW Cnc is the same during "on" and "off" states as well as prior to the appearance of the negative superhump. Considering the relatively red bandpass of *TESS* data, this is not surprising as the bandpass would be only probing the outer edges of the accretion disc. Nucita et al. (2019) observed DW Cnc with *XMM-Newton* in 2012 and found that the spin signal is present, and shows no energy dependence, further suggesting that only one pole is visible.

Using OPTICAM data, I can further constrain that the negative superhump was present in the system almost a year prior to *TESS* sector 71. With the lack of spin in the OPTICAM data from 14^{th} of February 2023, during which the negative superhump is detected for the first time, it may be possible to assume that the spin variability and negative superhump are coupled. However, the only other instance in which the spin is not detected (15^{th} of December 2022) is before the appearance of the negative superhump, this is most likely due to the lower data quality and substantial gaps in the dataset. Furthermore, the OPTICAM data suggests a continuation of this behaviour after the end of Sector 72 for at least another month, up to 4 months before the 4 magnitude burst.

A hypothetical scenario may then suggest that once a sufficient amount of material has been

accreted on one pole a micronova burst can be triggered. Assuming that similar behaviour occurs before a burst, the recurrence time during which material actively accretes onto one magnetic pole to trigger a micronova is at least half of the time between the observed bursts. However, without at least a very precise recurrence timescale of the bursts, this cannot be verified. Similar IPs, such as EX Hya could therefore eventually exhibit such behaviour. With similar amplitude bursts reported (Bond et al., 1987; Hellier et al., 1989, 2000), EX Hya is a prime candidate for monitoring to find another system with variable spin and test the relation of its variability as pre-cursor of micronova bursts.

7.5 Conclusions

DW Cnc is a well-studied intermediate polar which has been known to show bursts of unexplained nature in the past. Here I present new *TESS* and ground-based *ASAS-SN* , *ATLAS* , and OPTICAM data of DW Cnc. I report a new 4-magnitude burst in the *ASAS-SN* , light curve, which I interpret as a micronova burst. I present the similarities of DW Cnc behaviour with other magnetic systems showing micronovae as well as categorising it using the diagnostic diagrams from Iłkiewicz et al. (2024) (shown here in Figure 1.6). I also report the appearance of a negative superhump in 2 of the 5 *TESS* sectors which I retrospectively confirm has appeared at least a year earlier in the OPTICAM data. Along with the negative superhump I report a variability in the spin amplitude on the precession period associated with the negative superhump. I do not observe any changes in the geometry of the accretion disc or flux levels during the times at which the spin amplitude is negligible. However, I observe a decrease in the amplitude of all the other signals present in the PSD. I associate this behaviour to several possible scenarios, where in the "off" state the accretion mostly occurs onto the accretion pole obscured by the WD. An observed $\sim 180^{\circ}$ shift in the spin phase over the precession cycle of the disc as well as $\sim 180^{\circ}$ shift in the beat phase over the negative superhump cycle further suggests that the accreting poles are switching and that this phenomena is linked to the tilt of the accretion disc. I am not able to distinguish this unequivocally, but I propose that the geometry could be verified with fast time-resolved spectroscopy to separate "on" and "off" states.

Chapter 8

Conclusions & Future prospects

In this Chapter I outline an overview and summary of the main findings of this thesis (in Section 8.1) as well as present the currently unpublished ongoing and future work where I would like to take my research (Section 8.2). I finish this Chapter and this thesis with final concluding remarks in Section 8.3.

8.1 Summary of Thesis Contribution

In this Section I review the individual content and contribution of the Chapters of this thesis, focusing on those whose results have lead to publications, i.e Chapters 3 to 7. In order to do this, I discuss the Chapter summaries in the broader context of their results. Hence, the results pertaining to Chapter 3 are summarised in Section 8.1.1, where the overarching theme is the implications of broad-band variability on the geometry of ultra-compact white dwarf binaries. Keeping with the geometry theme, Section 8.1.2 concerns the summary of Chapters 4 and 5. These Sections are connected by a common interpretation of AWD and PULX QPOs as driven by magnetic precession, the model implication for the accretor magnetic field strength and the resulting inner flow geometry. Section 8.1.3 details the findings of Chapters 6 and 7, pertaining the discovery of 2 new micronova bursts and the consequences for the behaviour of the systems.

8.1.1 Broad-band variability in AWDs

Broad band variability offers insights into the physical properties and geometry of accreting systems, from XRBs to AWDs (Lyubarskii, 1997; Arévalo & Uttley, 2006b; Done et al.,

2007; Ingram & van der Klis, 2013; Revnivtsev et al., 2011; Balman & Revnivtsev, 2012; Scaringi, 2014). In this thesis, in particularly in Chapter 3, I showed an application of the propagating accretion rate fluctuation model (Lyubarskii, 1997; Arévalo & Uttley, 2006b; Ingram & van der Klis, 2013; Scaringi, 2014) to an AM CVn system J1908. The 3-year long *Kepler* light curve of J1908 with 60 s cadence offers an unprecedented view of flickering in an AM CVn, or an AWD system, across many orders of magnitude sampled in temporal frequency. This expansive frequency range then translates to a scale size spanning across most of the AD.

In Veresvarska & Scaringi (2023) (and hence Chapter 3) I have shown that the time-averaged power spectrum of this light curve does encompass most of the this accretion disc including its very outer most regions. The TPS shows 2 distinct breaks at $\sim 6.8 \times 10^{-7}$ Hz and at $\sim 1.3 \times 10^{-4}$ Hz. Following the assumptions outlined in Chapter 1 that these breaks represent the viscous frequency I associate the lower frequency break to the outer disc region, signifying the first detection of an outer disc edge.

In order to reinforce this conclusion I apply a modified version of the propagating fluctuations model to the TPS of J1908. The adjustments to the model represent the constant treatment of the $\alpha \left(\frac{H}{R}\right)^2$ parameter, similarly to Scaringi (2014). However, here I have split the model into 2 separate flows with both being characterised by an independent and constant value of $\alpha \left(\frac{H}{R}\right)^2$. By fitting this model to the TPS I independently recover the low frequency break is associated with the outer disc edge. The agreement between the purely observational and the semi-analytical method is demonstrated in Figure 3.9. Furthermore, the model predicts that $\alpha \left(\frac{H}{R}\right)^2$ for the breaks are 4×10^{-4} and 7×10^{-3} for the low and higher frequency break respectively. This suggests that $\alpha \left(\frac{H}{R}\right)^2$ increases through the AD from outside in.

For α and the $\frac{H}{R}$ ratio this implies that in order for α to be constant in the AD, the disc has to be much thicker in the outer regions. Or rather in a more realistic scenario, if the $\frac{H}{R}$ does not change dramatically in the outer disc, within the range that we are sensitive to, then the α viscosity prescription is smaller in the outer disc regions.

Overall this first detection of the outer region of a thin AD and its properties presents insights into thin AD behaviour. It can also prove useful for future comprehensive full AD MHD simulations.

8.1.2 Quasi-periodic variability

In Chapter 4 and Chapter 5 I discuss a new type of QPO in AWDs and a rare type of QPO in PULXs which are connected by a common interpretation of their origin by the MDP model (Lai, 1999; Pfeiffer & Lai, 2004).

In Chapter 4 I present a new type of QPO in AWDs, which is analogous in behaviour to type C QPOs in XRBs. The similarities are rooted in the broadness of the QPOs, i.e. their Q value, but also in the fact that the QPOs show harmonics, which has never been observed in AWD QPOs before. Furthermore, the QPOs with the broad band structure of their TPSs represented by Lorentzian-like breaks follow the same relation as the XRB QPOs (Wijnands & van der Klis, 1999). To explain these QPOs in the strictly non-relativistic AWD regime I apply the MDP model which relies on generating the QPOs by magnetically driven precession of a warped disc. Whereas the model relies on many free parameters, the model could in the future provide a stronger handle on B in classically non-magnetic AWDs. Furthermore the model predicts that the precessing flow will manifest as a break in the TPS, at the viscous frequency corresponding to the QPO radius (the outer radius of the precessing flow). Under this assumption the MDP model shows that the linear correlation between QPO and break frequencies can be reproduced theoretically. This suggests that the link between QPO and break frequencies consequence of the geometry of the precessing flow, not the underlying physics driving it.

In Chapter 5 I present an application of the MDP model to 3 examples of mHz QPOs in PULXs. These rare ultraluminous systems show QPOs that struggle to be explained by Lense-Thirring precession classically invoked in XRBs. Whereas the MDP model also struggles with a definite and unambiguous model solution Figures 5.1, A.6 and A.7 present a family of viable solutions capable of reproducing both the observed QPO frequency and NS spin. Furthermore all the families of solutions require a high magnetic field $B \gtrsim 10^{12}$ G for all 3 systems, ruling out the necessity for strong beaming to explain their behaviour. Whereas a lot of testing is necessary for the MDP model, it is providing a new avenue into exploring the scale invariance of accretion.

8.1.3 Transient phenomena in AWDs

High cadence all-sky monitoring missions, such as *TESS* have allowed new insights into fast ($\lesssim 1$ d) transient bursts in AWDs (Scaringi et al., 2022d; Scaringi et al., 2023; Veresvarska

et al., 2024a; Irving et al., 2024), showing that such short duration phenomena are much more common than previously thought. In Chapters 6 and 7 I discuss results from 2 publications (Veresvarska et al., 2024a, 2025b) detailing the detections of 2 new systems showing micronova bursts.

In Chapter 6, the micronovae have been detected in an old nova CP Pup by *TESS* , showing detailed multi-peaked structure of the $\lesssim 1$ d bursts. More examples of these bursts have also been retrospectively identified in the long-term *ASAS-SN* light curve, leading to a reassessment of other system parameters such as the WD mass and its orbital period.

In Chapter 7 I report on the detection of 4 mag burst in a well known IP DW Cnc, which hasn't been detected in the system since 2007 (Crawford et al., 2008). Furthermore, DW Cnc shows peculiar behaviour in the new *TESS* data after the system has emerged from the low state, where the spin signal has disappeared (Segura Montero et al., 2020; Covington et al., 2022). After the new state the spin reappeared (Ramírez et al., 2022b; Duffy et al., 2022) which is also seen in the *TESS* data from Sectors 44 to 46. However, in Chapter 7 I also report on the appearance of a negative superhump in Sectors 71 and 72, shortly followed by the 4 mag burst. Also preceding the burst is a strong variability in the power level in the spin signal, causing it to turn "on" and "off". This behaviour is also shown to be modulated on the precession frequency associated with the new superhump. I associate this to the gradual change in accretion from one pole to the other as demonstrated by the 180° phase flip shown in Figure 7.4.

8.2 Future prospects and research plans

Accreting white dwarfs are crucial to understanding accretion in astrophysical systems, from stellar-mass black holes to active galactic nuclei. With accretion present across all mass scales, one of the main draws of AWDs is that they are among the closest accreting objects, with thousands within 1000 pc (Rodriguez, 2024). They play a significant role in supernova Ia progenitors, galactic transients, and contributing to the gravitational wave background for missions like *LISA* (Scaringi et al., 2023). Many similarities in structure and behaviour exist between various types of accreting systems (Uttley et al., 2005; McHardy et al., 2006; Körding et al., 2007; Scaringi et al., 2012b, 2015; Veresvarska et al., 2024b), suggesting that studying simpler systems like AWDs can illuminate complex ones like XRBs and AGNs. Many of these links between different accreting scales are tied to the broad-band TPS of these objects

and the breaks in their TPS (McHardy et al., 2006; Körding et al., 2007; Scaringi et al., 2015) (see Section 1.5.1 for more detail). In this Section I describe my currently ongoing and future projects focusing on leveraging AWDs in order to understand the geometry and physics driving the variability of the different accretion flows surrounding compact objects.

8.2.1 Systematic study of broad-band variability of accreting white dwarfs in *TESS*

In *TESS* there are approximately 3000 AWDs and AWD candidates with at least one sector of 20s or 2-minute photometry. Exploring such a vast archive of broad band features is challenging, however it has led to some serendipitous discoveries throughout my PhD, such as the findings shown in Chapters 4, Chapter 6 and Chapter 7. The main focus of this Section is the systematic search and analysis of broad-band variability, particularly for high frequency TPS breaks, similar to the ones in Chapter 3. It is expected that all AWDs with a disc to show these breaks at frequencies of $\sim 10^{-3}$ Hz (see Section 1.5.1), however for a break to be detected, a very high signal to noise ratio is required, limiting the number of suitable sources. In order to select these sources, I visually inspected all the data and selected 130 targets showing a clear, unambiguous break in at least one Sector at high ($\gtrsim 10^{-5}$ Hz) frequencies. To qualify as *the* high frequency break, the source has to have negligible Poisson noise to observe clear drop in power after the break. The TPS of each individual Sector is then constructed as described in Chapter 4, with $N = 90$ frequency bins, such that each Sector is divided into 5 day segments whose power spectra are averaged and re-binned. In order to quantify the breaks the resulting TPS are fitted with 1 to 3 Lorentzians, after all periodic signals have been removed, analogously to Chapter 4. Including the Poisson noise component the overall equation for the final TPS fit is:

$$P_\nu = \sum_{i=0}^{N_L} P_L\left(r_i, \Delta_i, \nu_{0,i}, \nu\right) + A. \tag{8.2.1}$$

where P_L represents the power of each Lorentzian as defined in Equation 4.3.1 and A corresponds to the Poisson noise level normalisation. The characteristic frequency of the high frequency break is then represented by the peak frequency of the highest frequency Lorentzian defined in Equation 4.3.2. The required number of Lorentzians used in each Sector and system is decided on an individual basis, with the default value being 2. The number of Lorentzians is then increased if the fit to the TPS with 2 Lorentzians produces $\chi^2_\nu > 10$. If only 1 Lorentzian is used, it is decided based on a visual inspection. The fitting method and error computation

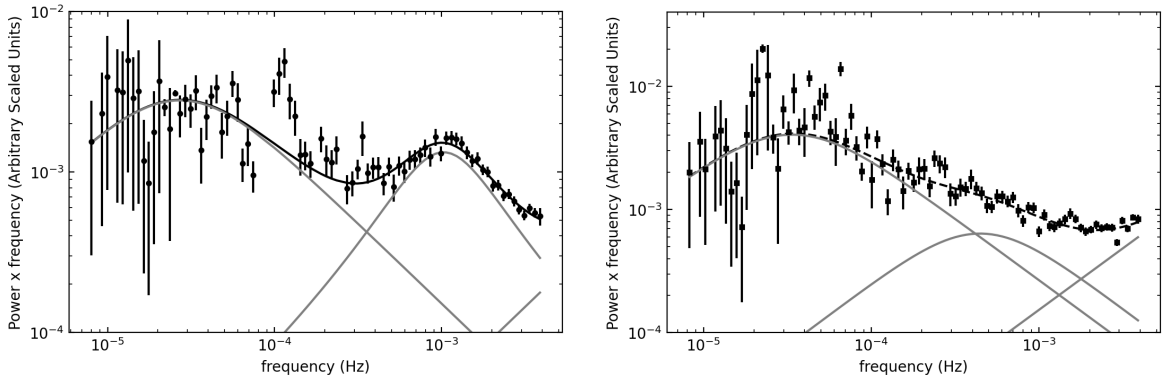

(a) MV Lyr (NL) *TESS* break example (b) AB Dra (DN) *TESS* break example

Figure 8.1: Examples of breaks of a NL and DN for 2 *TESS* Sectors for ML Lyr (NL) and AB Dra (DN). The TPS fit is shown, with the individual Lorentzians indicated in grey as well as the Poisson noise level.

is performed using the same techniques as described in Chapter 4. The final list of targets with their corresponding Sectors and break frequencies can be found in Table A.2. Examples of these fits are shown in Figure 8.1.

The distribution of the breaks, with treating systems with multiple Sectors as several independent measurements is shown in Figure 8.2. In the cases of DNs, only the quiescent data is used, with the burst being manually excluded. The main classes of interest here are DNs and NLs, which do not have the added complication of magnetically truncated disc like IPs, or more complex accretion stream in polars. Naturally, this test is subject to the assumptions and biases that affected this sample. One of the main systematic factors is the number of Sectors for each system being affected by the system's position in the sky and *TESS*'s observational strategy, combined with the target selection bias. To minimise this, I reproduce the distribution from Figure 8.2 such that each system with multiple Sectors is represented by the mean value of all the measurements. The resulting distributions are shown in Figure 8.3. This may partially mitigate the bias in statics caused by *TESS* observational strategy, however, it cannot correct for the sample selection bias. Further bias is also introduced by the fact, that for a high frequency break to be observed in a system, a high signal to noise ratio is required. Therefore a natural bias towards luminous targets and NLs in particular is expected. To quantify the effects of these biases, further work is required, such as for example, using a volume limited sample (Pala et al., 2020). However, for the purpose of the discussion in this Section, the current sample of averaged breaks is used.

I note that the average of NL break frequencies is higher than the DN average. The Kolmogorov-Smirnov test for goodness of fit returns a p-value of $\sim 7 \times 10^{-6}$ when com-

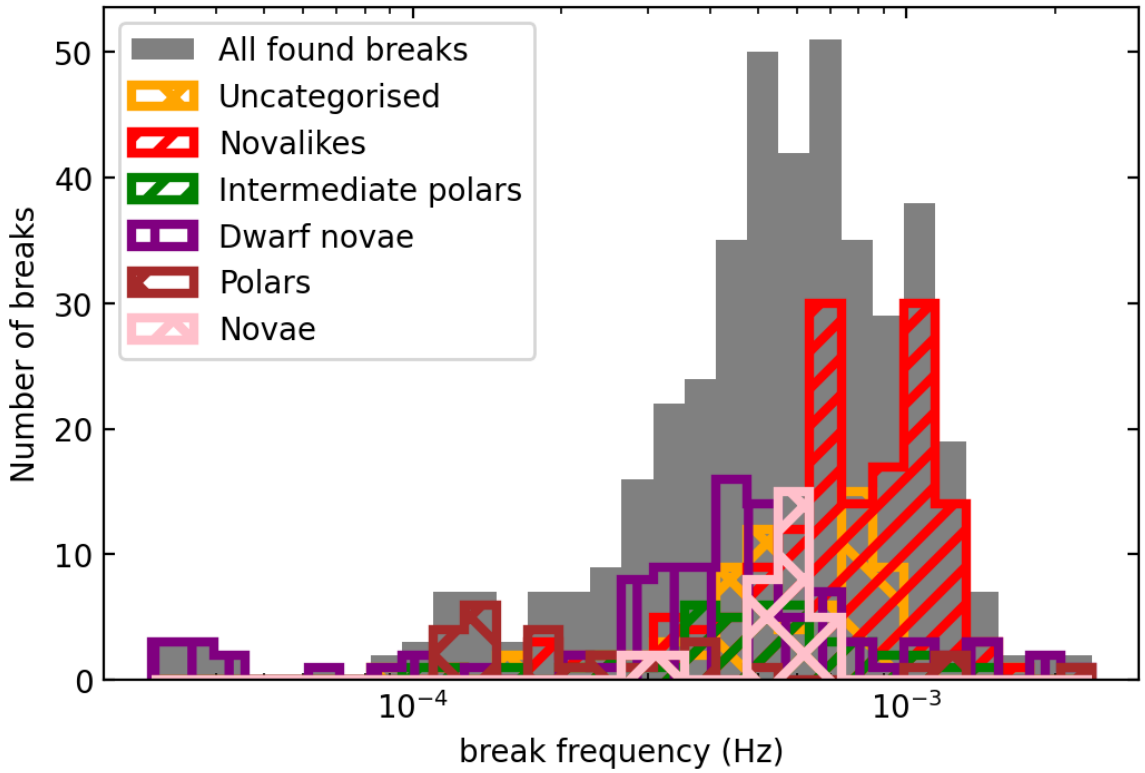

Figure 8.2: Distribution of TPS high frequency breaks in *TESS* Sectors for a sample of AWDs. Distributions of separate AWD classes, based on the Ritter & Kolb (2003) classification are also shown. Here, multiple measurements of a break in the same system in different *TESS* Sectors are treated as individual measurements.

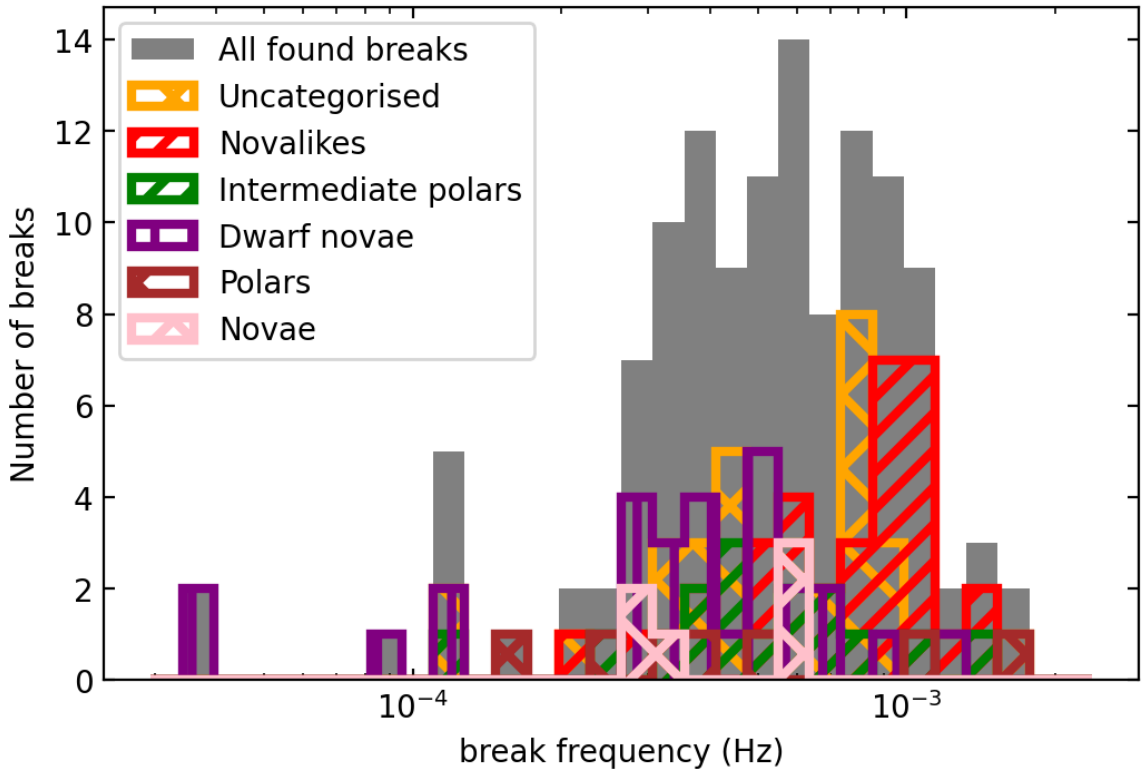

Figure 8.3: Distribution of TPS high frequency breaks in *TESS* Sectors for a sample of AWDs. Distributions of separate AWD classes, based on the Ritter & Kolb (2003) classification are also shown. Here, multiple measurement of the break in different *TESS* Sectors are averaged to produce one measurement per system.

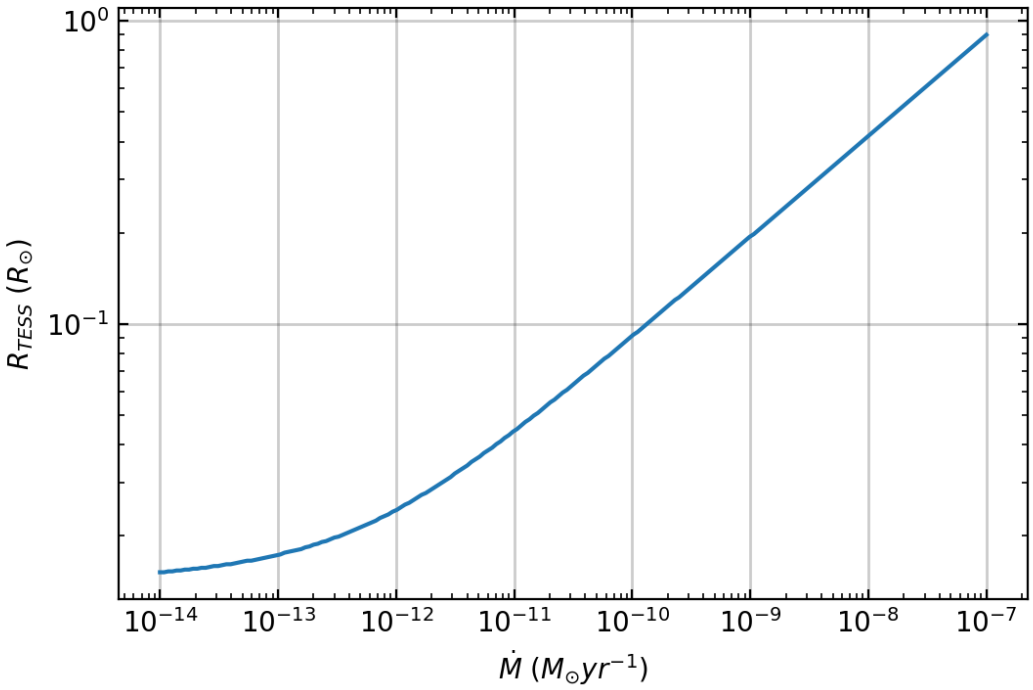

Figure 8.4: *TESS* effective radius as a function of $\dot{M}$ for a standard Shakura-Sunyaev AD.

paring the NL and DN distributions in Figure 8.3. This suggests that they are 2 separate distributions with different geometry and behaviour of the inner accretion flow, within the framework of the aforementioned biases and assumptions.

There are several factors which can affect the high break frequency, with the $\dot{M}$, $\alpha\left(\frac{H}{R}\right)^2$ and bandpass in which the break is observed among the main ones of interest. The bandpass and $\dot{M}$ are linked, such that the higher the $\dot{M}$ the further parts of the accretion disc emit in a fixed bandpass. Therefore, under the assumption of standard Shakura-Sunyaev AD, the "effective" radius contributing the most energy emitted in *TESS* bandpass is a function of the systems' $\dot{M}$. Their dependence is shown in Figure 8.4.

Therefore, if the high frequency break is dynamical, the DN high frequency breaks should be higher in frequency than the NL ones for a fixed bandpass. This follows from Equation 1.1.8, if the radius in Equation 1.1.8 is not the inner AD radius, but the effective radius contributing the most power to a given bandpass, R_{TESS} in this case. NLs on average accrete at much higher rates than DNs. This translates to their effective radii being further out than for DNs. Assuming limited effect from the WD mass and an AD extending all the way towards the WD, the effective radius is the only factor affecting the value of the dynamical frequency of

each system in a given passband. Hence, for larger effective radii in NLs, the corresponding dynamical frequency is lower, than those of DNs. Naturally in the case of a truncated disc this becomes more complex and it is necessary to consider beyond what accretion rates the bandpass becomes dominated by either the inner or outer regions of the AD. However, this is subject of future work and for the purpose of discussion here, I limit myself to the assumption of a geometrically thin AD extending to the WD surface.

However, if the break is viscous then the $\alpha \left(\frac{H}{R}\right)^2$, and hence the nature of the inner flow affects this prediction. Scaringi (2014) suggests, that a break in a well known NL is consistent with a optically thin and geometrically thick flow. In particular this is expected to result in a high value of $\alpha \left(\frac{H}{R}\right)^2$, as supported by the propagating fluctuations model fit in Scaringi (2014). Assuming a presence of an inner flow, whose boundary is determined by the $\dot{M}$, such that for higher $\dot{M}$ the geometrically thin AD pushes closer in to the accretor. Hence for a DN, the boundary between the 2 flows, representing the break would be at larger radii (and in lower frequencies). In order to try and quantify the $\alpha \left(\frac{H}{R}\right)^2$ for each system and Sector, I estimate an accretion rate for each system using Equation 5.2.5, such that L_{obs} corresponds to *TESS* luminosity after calibration with *ASAS-SN* data (see Chapter 2). This approximation is very crude and among future work of this project is to improve this estimate. One attempt to improve the $\dot{M}$ estimate was to use $\dot{M}$ values derived from DIM implemented in Dubus et al. (2018). However, not all systems from Table A.2 were included in this sample. To enhance the accuracy for other systems not included in Dubus et al. (2018), I plan X-ray to mid-IR SED fitting using databases like *Gaia*, *WISE*, *GALEX*, and *eROSITA* similar to Veresvarska et al. (2024a), and employing observed links between the orbital period of the system and donor properties Knigge et al. (2011) to estimate WD and donor temperatures from the *TESS* orbital period. Verification of these accretion rates can be cross-checked using the DIM with DNs and NLs from Dubus et al. (2018).

With more precise accretion rates, I can use my code for the standard accretion disc model (McHardy et al., 2023) to determine the disc radius with the dominant contribution in the *TESS* (or any other) bandpass. This effective radius can be assumed to correspond to the viscous timescale associated with the frequency break in a given bandpass. Thus, with the accretion rate and radius, it is possible to measure the viscosity scale-height $\alpha(\frac{H}{R})^2$, the last (currently) variable for the parameter space to model the inner flow in AWDs. A semi-analytical model of $\alpha(\frac{H}{R})^2$ as a function of accretion rate and disc radius would then allow inference of the general properties and behaviour of $\alpha(\frac{H}{R})^2$ across the disc as a function of radius R. Such parameter space is displayed in Figure 8.5.

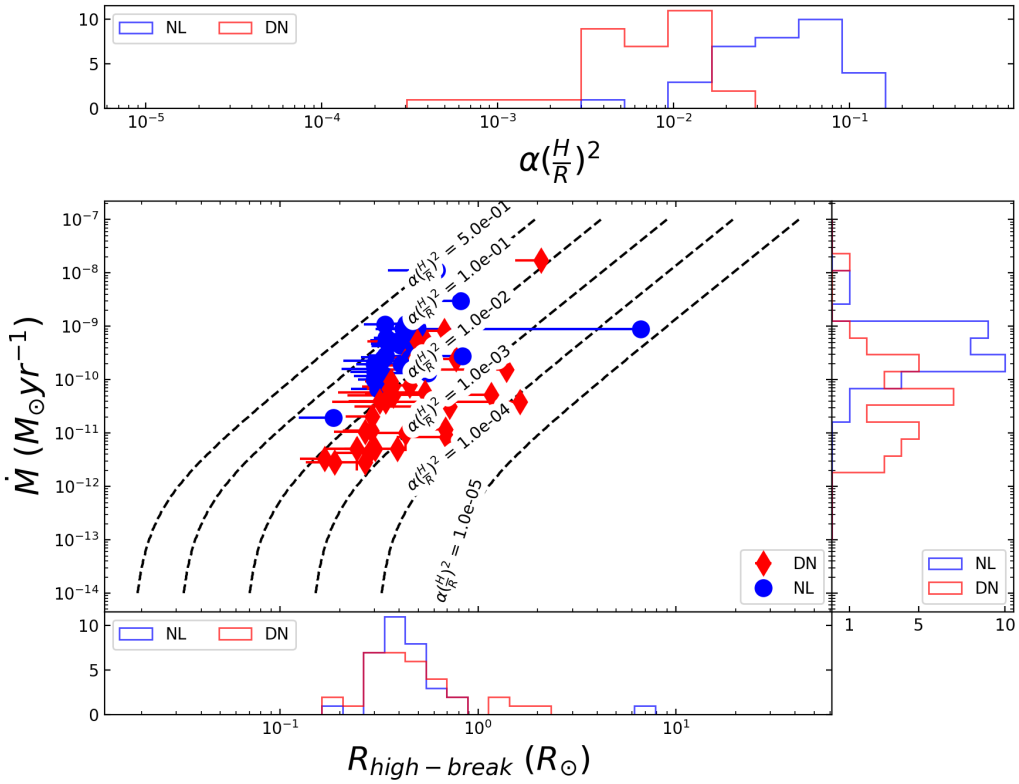

Figure 8.5: $\dot{M}$ as a function of effective radius associated with the *TESS* bandpass. Lines of constant $\alpha(\frac{H}{R})^2$ are given in dashed lines. The corresponding measured *TESS* $\dot{M}$ and radius are given in red diamonds for DNs and in blue circles for NLs. Corresponding distributions of $\alpha(\frac{H}{R})^2$ for DNs and NLs are given in the top panel with the $\dot{M}$ distributions on the right and effective radius of the high frequency break at the bottom.

Figure 8.5 suggests that the difference in $\alpha(\frac{H}{R})^2$ between DNs and NLs may be one of the main drivers of the difference in break frequencies, coupled with smaller bandpass and accretion rate effects. However, a more thorough $\dot{M}$ estimate is needed to draw any quantitative conclusions. Another, not negligible issue arising from the Figure 8.5 is the assumption of the effective radius.

With the current estimates of accretion rate the effective radius for NLs and DNs peaks at $\sim 0.4R_{\odot}$. However, assuming that the disc doesn't extend beyond the tidal radius, which should be a reasonable assumptions for all systems not showing positive superhumps, the tidal radius ranges between $\sim 0.3 - 0.48R_{\odot}$ based on the evolutionary tracks in Knigge et al. (2011). Therefore, a new approach considering the standard Shakura-Sunyaev AD is necessary to decipher the inner flow geometry. To attempt it, I plan to extend the *TESS* analysis to test the semi-analytical model and characterize the radial dependence of $\alpha(\frac{H}{R})^2$ across different accretion rates and wavelengths. The details of this extensions are outlined in the following Sections.

8.2.2 Accreting White Dwarfs as a Laboratory for Testing Accretion Flows

In the following months *XMM-Newton* will observe an archetypal AWD BB Dor in X-ray and UV for 40 ks, during 4 month *TESS* optical monitoring. This simultaneous multi-wavelength data will probe the origin of variability components and reveal processes like reflection and accretion rate fluctuation. This analysis may help constrain semi-analytical models of flow variability and thus underlying system geometry.

An important parallel between other compact systems and AWDs is illustrated in Scaringi et al. (2013), where 2 NLs, were observed simultaneously in 3 optical *ULTRACAM* bands. However, no significant difference in break frequency was detected, with only a time and phase delay between the bands, referred to as Fourier-dependent phase and time lags. This highlights the necessity for a broader wavelength coverage to uncover the fundamental differences in accretion flow structure.

Frequency-dependent phase/time lags were first detected and characterized at X-ray wavelengths in both XRBs and AGNs across a wide frequency range (Vaughan & Nowak, 1997; Fabian et al., 2009; de Marco et al., 2011; Uttley et al., 2011). Generally observations show that X-ray hard/bluer wavelengths lag the X-ray soft/redder ones at low frequencies (by ≈hours for AGNs and by ≈seconds for XRBs), while the opposite is observed at higher frequencies (by <1 hour for AGNs and by <1 second for XRBs). The frequency where the lags

invert sign can depend on several factors such as source intensity and/or hardness/colour, but is nonetheless generally associated with a characteristic size within the accretion disc (Reig et al., 2000; De Marco et al., 2013). The origin of the hard lags is yet not well understood, but it is well established in AWDs, that the lags are too long to be explained by reprocessing from the inner hot flow on the geometrically thin accretion disc or donor star as they are larger than the light travel time of the binary systems Scaringi et al. (2013); Aranzana et al. (2018). Whereas Scaringi et al. (2013) and Aranzana et al. (2018) detected these lags in AWDs, the ground based optical data did not allow to probe low enough frequencies to resolve the turn-over frequency and to probe lags between optical bands. There have been lags reported between X-ray and UV in AWDs Balman & Revnivtsev (2012) with X-ray lagging the UV band by 100-200 s. However the quality of the data did not allow to study frequency or phase dependence of lags. The extension to optical wavelength was not performed though, preventing to disentangle the energy dependence - still unknown - of the lags. This leaves open a fundamental question: What drives variability of the inner accretion disc in AWDs?

This project is a joint strictly-simultaneous *XMM-Newton* and *TESS* pilot study of an archetypal examples of novalike AWD to test the physics behind variability of accreting systems on different timescales. I propose to do this in 2 steps:

1. **How does the PSD shape depend on wavelength, and what implications does this have on the disk geometry?**

   PSD breaks are a key indicator of accretion scale invariance. In 8.2.1, a study of broadband variability in AWDs shows that high and low accretion rate sources have different PSD structures and breaks at various frequencies. Similarly, Dobrotka et al. (2020) reviewed previously reported breaks, finding a strongly bimodal distribution, likely caused by combining optical and X-ray data. This contradicts Balman & Revnivtsev (2012), who found no difference in breaks between EPIC-pn and OM in archival *XMM-Newton* data, showcasing the need for a wider simultaneous X-ray to UV and optical coverage.

   According to Shakura-Sunyaev accretion disc theory, breaks should vary with wavelength, depending on the accretion rate and viscosity. These conflicting results highlight a gap in understanding inner accretion flow in AWDs. By measuring breaks with two independent instruments in 3 different bandpasses, I will determine if optical/near IR (nIR), UV and X-ray breaks arise from the same flow or different regions and physical conditions.

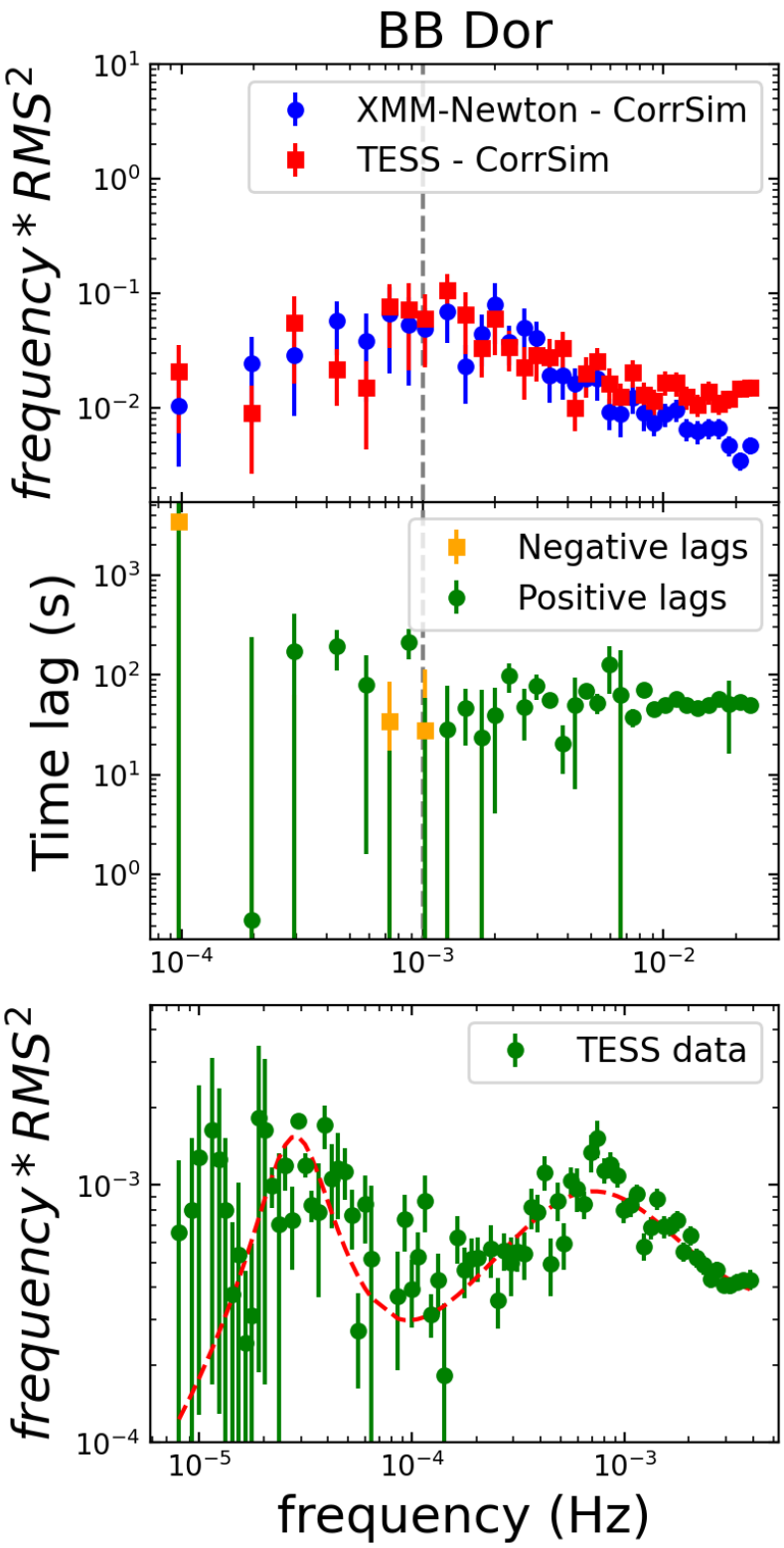

Figure 8.6: *Top: Simulated XMM-Newton and TESS PSDs for BB Dor showing the observability of the PSD break modeled by* `CorrSim` *Paice et al. (2024a). Middle: Simulated lag spectra for the simulated PSDs from the top panel with an artificial lag of 50s. Bottom: Examples of archival TESS data of targets showing PSD breaks and respective fits.*

The synergy between *XMM-Newton* and *TESS* is crucial; long-term *TESS* monitoring (covering a dynamic range from $\sim 3{\times}10^{-3}$ Hz to $\sim 10^{-7}$ Hz) reveals broad-band structure, which can be compared with simultaneous X-ray and UV bands from *XMM-Newton* to create a spectral energy distribution. This comparison will inform not only the broad-band structure but also the activity level. It will allow us to infer the energy dependence of the breaks and study the spectral energy distribution of the accretion flow components. Additionally, multi-wavelength measurements at different accretion rates will inform predictions for future missions like *PLATO*.

2. **What are the optical/UV/X-ray time-lag properties in AWDs and how does this inform disk geometry?**

   Accretion systems have multiple components, each contributing to variability from different physical processes. Understanding these is key to grasping accretion physics. Fourier lags help identify which process dominates at various timescales and radii. In Balman & Revnivtsev (2012), UV to X-ray lags of around 100 s were reported for low accretion rate dwarf novae in quiescence, too long to be consistent with reprocessing off the accretion disc. This hence raises the question of what is driving this variability and what other part of the accretion disc and hence wavelength range does it extend to? I will extend to the *TESS* band for for an archetypal novalike AWD. With this source, I will relate these lags to differences in breaks (see Section 8.2.1). Fourier-based time and phase lags will directly test the propagating accretion rate fluctuations model. Lag behaviour as a function of frequency can also be compared in the future to XRBs, further testing accretion properties across different scales.

Simultaneous X-ray, UV, and optical/nIR observations with *XMM-Newton* and *TESS* could study the variability in AWDs at an extended wavelength and timescale range. Since it is not possible to observe such a wavelength range simultaneously with *XMM-Newton* alone, through combining with the cadence and baseline of *TESS* I can combine the optimal wavelength coverage with *TESS*'s long-term observing capability.

8.2.3 Multiwavelength broad-band variability of accreting white dwarfs in *PLATO*

ESA M-class mission PLAnetary Transits and Oscillation of Stars (*PLATO*) is panned to launch in 2026 (Rauer & Heras, 2018). The primary science case of *PLATO* consists of

studying planets in the habitable zone of Sun-like stars, and characterising these stars. With 26 cameras and fastest cadence of 2.5 seconds in 2 visible bands *PLATO* will bring more opportunities to understand variability in AWDs.

PLATO will provide a unique opportunity with its high cadence, long-term, and simultaneous multiband observations, enabling time-domain techniques not previously available in optical astronomy on this scale. I will extend the proposed *TESS* analysis to test the semi-analytical model and characterize the radial dependence of $\alpha(\frac{H}{R})^2$ across different accretion rates. *PLATO* will enable this in two simultaneous bands.

Understanding the origin and phenomenology of power spectral breaks is challenging due to the lack of simultaneous multi-band studies in AWDs. A parallel can be drawn to Scaringi et al. (2013), where 2 NLs were observed simultaneously in 3 optical *ULTRACAM* bands. However, no significant difference in break frequency was detected, only a time and phase delay between the bands, referred to as Fourier-dependent phase and time lags. The origin of the frequency-dependent phase/time lags is unclear, but they are too long to be explained by reflection from the inner hot flow on the geometrically thin accretion disc or donor star (Scaringi et al., 2013; Aranzana et al., 2018). While Scaringi et al. (2013); Aranzana et al. (2018) detected these lags in AWDs, the ground-based data couldn't probe low enough frequencies to resolve the turnover frequency.

Measuring the Fourier lags with *PLATO* will allow me to probe frequencies down to $\approx 10^{-6}$ Hz, 3 orders of magnitude lower than previously measured Scaringi et al. (2013); Aranzana et al. (2018), spanning ~ 5 orders of magnitude compared to the usual $2 - 3$ in XRBs and AGN. TPS spanning this many orders of magnitude in frequency have been previously shown in AM CVn J1908 (Veresvarska & Scaringi, 2023). Therefore, *PLATO* will also allow for general broad-band monitoring of accreting sources and potentially detecting an outer region of an AD in a CV, providing a stationary light curve in a system with sufficiently high signal to noise ratio.

I will propose to observe the sample of bright targets from Section 8.2.1, to expand the existing sample and incorporate it into the model from Section 8.2.1. There are 28 bright targets in the currently planned southern *PLATO* field of view, with a mean *Gaia* g magnitude of 14.6 mag, with 8 in the multi-band fast cameras field of view. Since the required signal-to-noise ratio for broad-band variability is lower than that for exoplanet transit detection, all targets are sufficiently bright for *PLATO*. Among the 28 targets, there are 11 DNs and 9 NLs, including the closest AWD, VW Hyi, at 54 pc, which shows a DN burst about once a month.

This sample offers excellent candidates to measure Fourier lags, not only in NLs and one DN in quiescence as done previously Scaringi et al. (2013); Aranzana et al. (2018), but also in DNs in outburst, which has never been attempted before.

8.3 Concluding remarks

In this thesis I have hoped to provide a detailed overview of my work during the past four years. Not all that I have learned and that I would have wished to include made it in to this thesis. However, I have strived to include a complete picture of my published work, which I hope has provided new insights into the geometry of accreting compact objects and the physical processes driving their variability.

I have reported on the first detection of an outer disc edge using a TPS of an AM CVn system J1908+3940. The application of the propagating accretion rate fluctuations have consistently shown that the broad band variability of J1908+3940 is consistent with an accretion disc with an outer edge around the tidal radius and a variable $\alpha \left(\frac{H}{R}\right)^2$ parameter value through the accretion disc. Furthermore I have discovered new type of QPO in AWDs, which show direct analogies to type-C QPOs in XRBs. Modelling these QPOs with the magnetically driven precession model has allowed to explain the empirical relation with broad-band structure connecting them to the QPOs in XRBs. The model has also proved helpful in interpreting the QPOs in PULXs. I have shown that it can be used to derive an lower limit on the magnetic field of the NSs and provide a viable alternative to Lense-Thirring precession. With my reports of two new micronova systems I have also shown peculiar pole-switching behaviour in an AWD DW Cnc, immediately prior to a micronova burst.

Highlighting this unusual behaviour in close proximity to the burst showcases the importance of understanding the geometry of accreting systems individually and in the broader context of accretion around compact objects. Overall, this is the message which I wish to convey through this thesis, in particular with the new possibilities brought to us by the new and planned instruments. With more data and information at our disposal then ever before, we have the hope for an in depth understanding of the Universe and the fundamental laws that drive it.

Appendix A

A.1 Neighbouring *Kepler* targets

In order to verify that the low frequency break associated with the outer disc edge cannot be produced by instrumental effects of *Kepler* the analysis is reproduced on 3 neighbouring *Kepler* sources. The selected stars are all rotating variable stars, namely KOI-625, TYC 3124-850-1 and Kepler-475. KOI-625 was observed by *Kepler* between Quarters 7 and 14. It is ~ 3 mag brighter than J1908 in g band and $\sim 25'$ away from J1908 with its rotational period of 5 ± 1 days (Mazeh et al., 2015). Similarly, TYC 3124-850-1 was observed between Quarters 2 and 10. It is substantially brighter than J1908 by ~ 6 mag in g band and is at a distance of $\sim 30'$ from it. Kepler-475 was observed by *Kepler* between Quarters 3 and 14. It is of similar brightness as KOI-625 in g band and is about $\sim 32'$ from J1908. It's corresponding rotational period is at 42 ± 2 days (Mazeh et al., 2015).

The time-averaged PSDs of these objects are shown in Figure A.1. It is clear that the stars show little variability as expected (Reinhold et al., 2014), with the level of RMS variability at $\sim 10^{-7}$. However, the stars also show no significant break at low frequencies that is not associated to the binning and construction of the time-averaged PSD. The masked out data points denote frequencies whose power is affected by the length of the segment, as described in Section 3.3.1. The main increase in the power in these systems is associated with the rotational periods in A.1 for KOI-625 and Kepler-475 with their rotational periods being reported in Mazeh et al. (2015). TYC 3124-850-1 is not included in Mazeh et al. (2015), but considering the similarity in the increase in power at the frequency range between the rotational period of the other 2 systems ($\sim 3 \times 10^{-7} - 2 \times 10^{-6}$ Hz) it is assumed that the rotational period of TYC 3124-850-1 is roughly at ~ 6.8 days in Figure A.1. Kepler-475 also shows a clear feature at $\sim 5 \times 10^{-7}$ Hz that is not associated with the length of the segments. Since the rotational period of Kepler-475 is $\sim 3 \times 10^{-7}$ Hz, I suggest that this broad-band

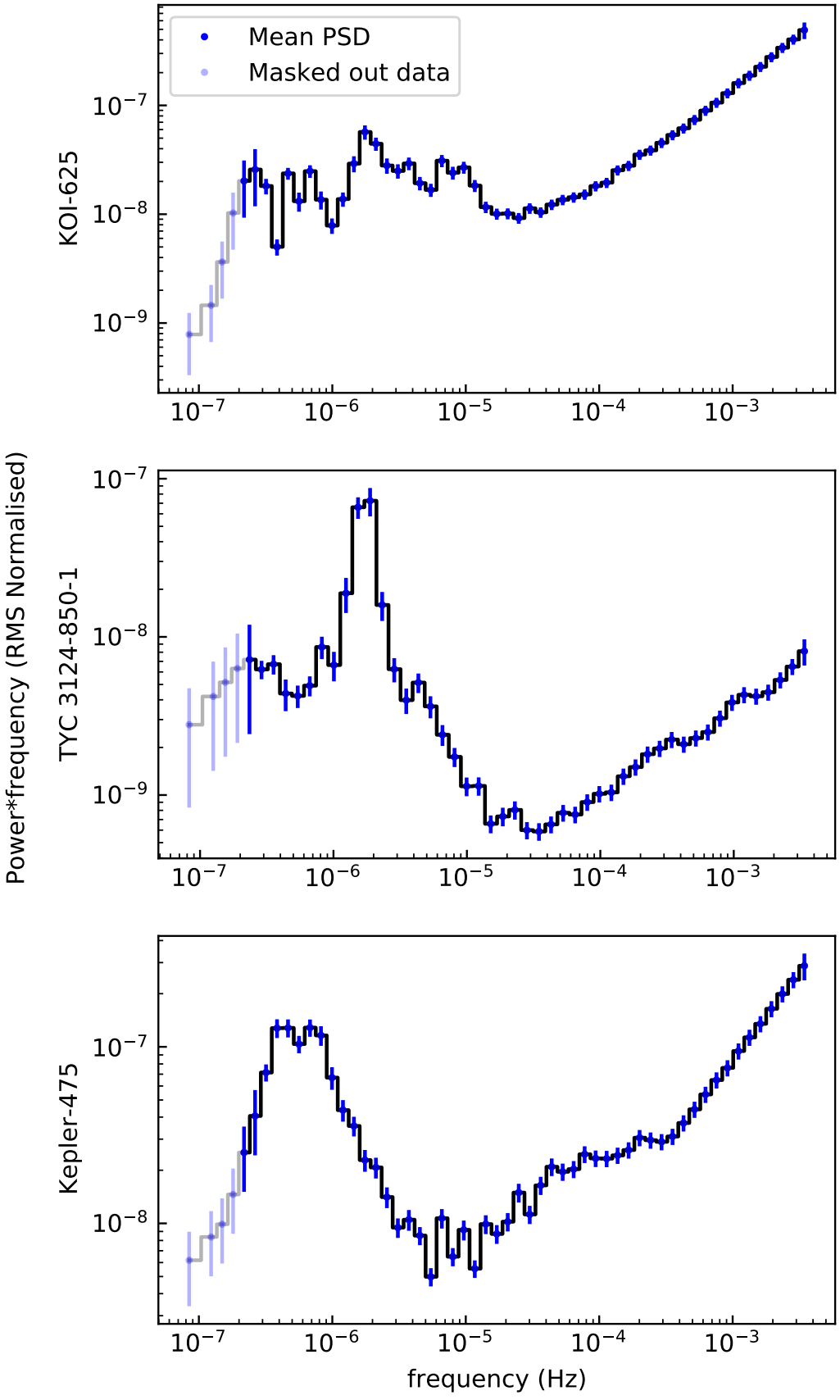

Figure A.1: Time-averaged PSD of neighbouring rotating variable stars KOI-625, TYC 3124-850-1 and Kepler-475. The masked out data denotes the frequencies below the segment sensitivity limit.

variability feature is intrinsic to this target and possibly associated to the rotational period of the star. It is important to note that although the break in Kepler-475 appears similar to that of J1908, it does not occur at the same frequency. Furthermore, the shape of the broad-band feature in Kepler-475 is also clearly different (possibly double-peaked), further distinguishing it from that of SDSS J1908+3940.

A.2 Robustness, stability and stationarity of the PSD segments

It is possible that structure in the disc evolve over time and this can in turn change the location and amplitude of features within the PSD. An obvious scenario that would alter the stationarity oif the PSD are thermal-visous outbursts observed in several AM CVn systems lasting about $\sim 1 - 10$ days (Rivera Sandoval et al., 2021). J1908 does not display any outbursting behaviour over the 3 year period it has been observed with *Kepler*. However this does not necessarily imply that the PSD is stationary across the entire observation length.

To test for stationarity I have performed empirical model fits to the individual 11 segments using the same model as described in Section 3.3.2. The results are tabulated in Table A.1. Model fits, together with the individual PSDs are also shown in Figure A.3. Although not all segments find an acceptable χ^2_ν, all model fits seem to be qualitatively well described by the same 4 components. More importantly, the recovered characteristic frequencies for the low and high Lorentzians are found to be consistent across the 11 observations (see Figure A.3), supporting the assumption of stationarity for these components.

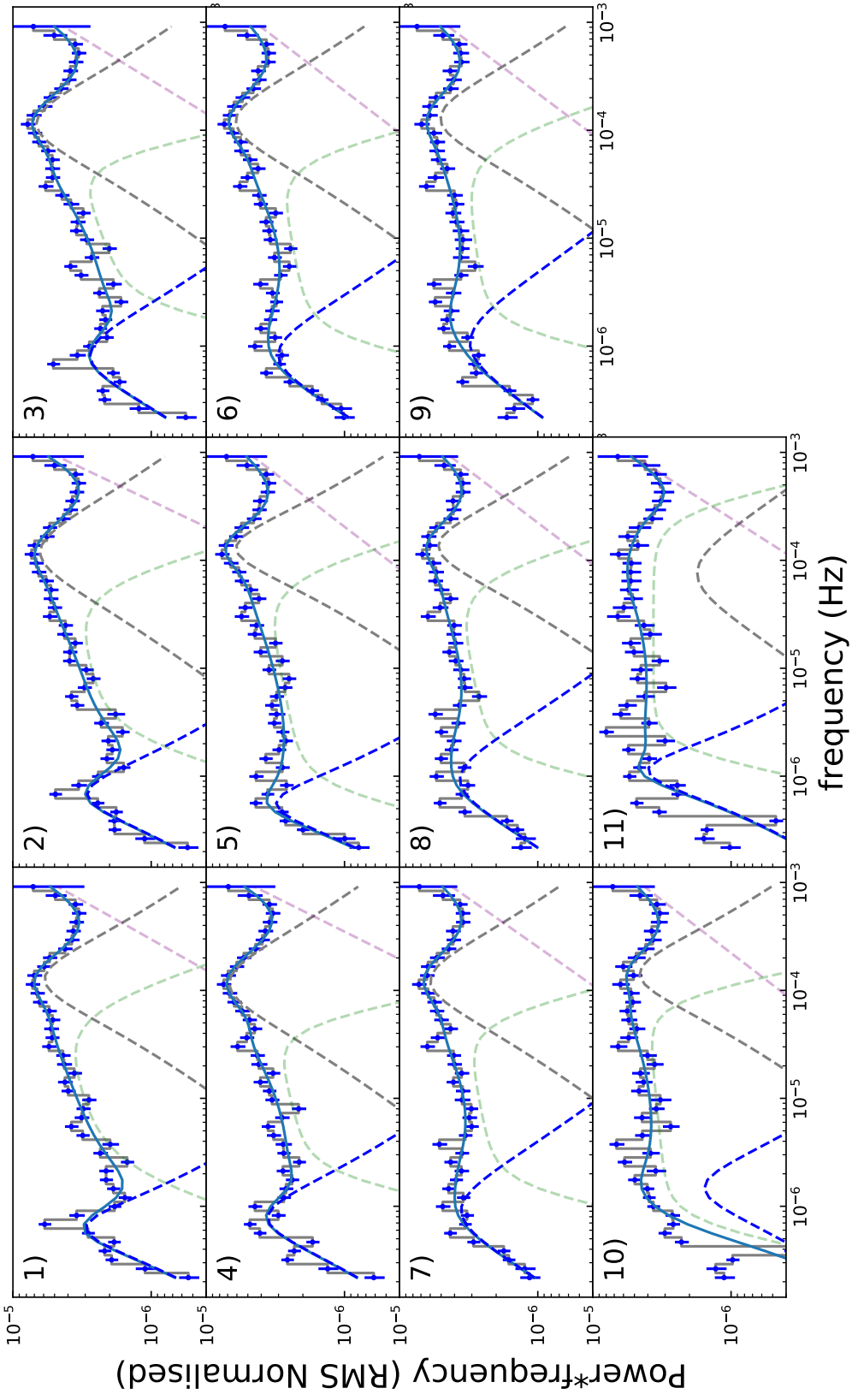

Figure A.2: Low and high frequency break as fitted by the empirical fit for separate segments. Separate dashed lines denote the 2 Lorentzian components, the central power-law and a white noise component. The best fit values of all parameters with the appropriate χ^2_ν are shown in Table A.1.

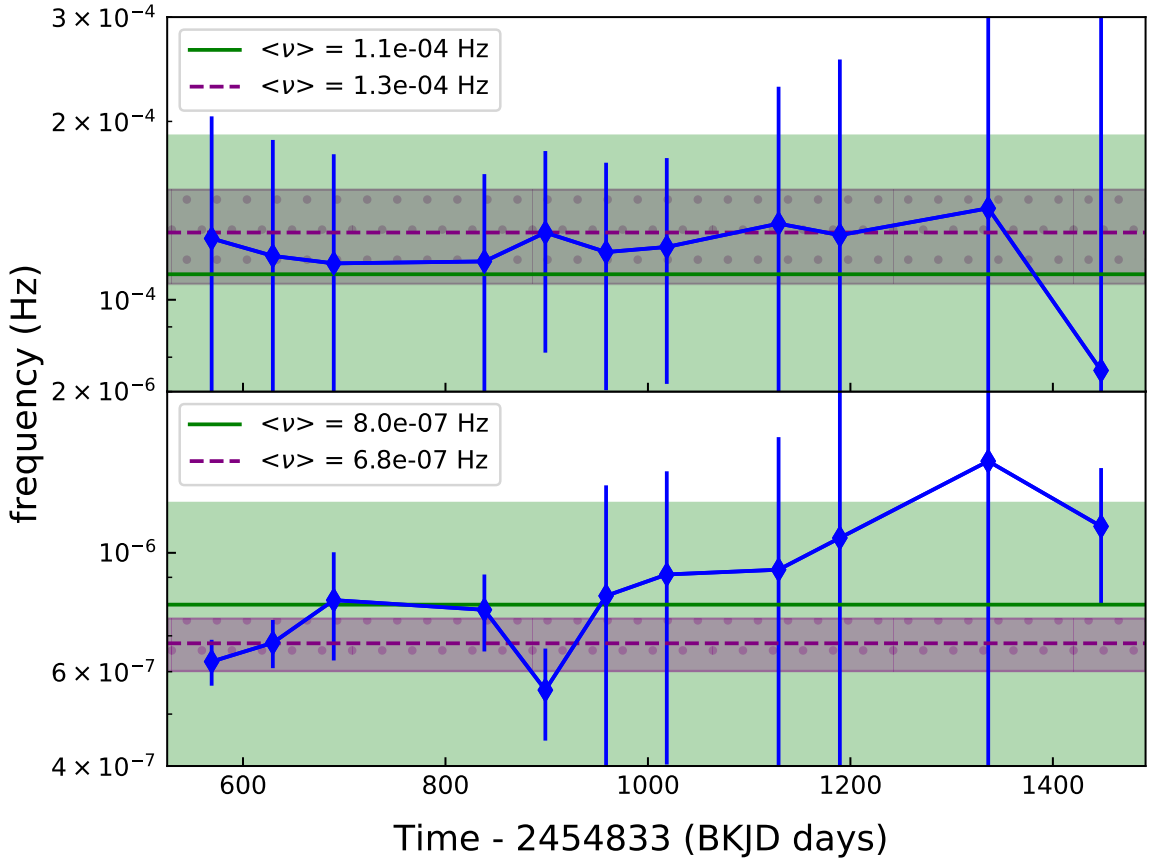

Figure A.3: Low and high frequency break as fitted by the empirical fit for separate segments as a function of time. Blue diamonds denote the frequency of the break, with the low frequency break in the bottom panel and high frequency in the top one. The weighted non-logarithmic mean is denoted by a green horizontal line, with the uncertainty limit on the weighted mean being marked in the light green shaded region. The weights used to compute the mean are based on the individual χ^2_ν values of each fit. The break frequencies from the overall empirical fit of the time-averaged PSD as reported in Table 3.2 are shown in dashed purple line with the shaded dotted region representing the uncertainty.

Table A.1: Free parameters of the empirical fit of the time-averaged PSD of J1908 as described in section 3.3.2. The the best fit value of the parameters for the central power law: A, power law amplitude, a_{1-3}, bending power law indexes when going from low to high frequency and ν_{1-2}, bending power law frequencies at which the power law transitions between the different indexes. For the Lorentzian components the parameters are r_{1-2}, integrated fractional RMS power of the Lorentzian components of the fit, $\Delta\nu_{1-2}$, HWHM of the Lorentzians and $\nu_{0,1-2}$, central frequency of the Lorentzians. For the white noise components the parameters are β, white noise power law index, and P_0, white noise normalisation.

Segment	Time - 2454833 (BKJD days)	A (RMS Normalised)	a_1	a_2	a_3	ν_1 (Hz)	ν_2 (Hz)	r_1
1	$539-599$	$0\pm5\times10^{-4}$	-0.2 ± 0.9	-3 ± 4	0 ± 12	$0.2\pm8\times10^{-5}$	$6.19\pm0.02\times10^{-5}$	$4\pm5\times10^{-3}$
2	$599-659$	$0\pm2\times10^{-4}$	-0.2 ± 0.9	-3 ± 4	0 ± 11	$0.2\pm7\times10^{-5}$	$5.56\pm0.02\times10^{-5}$	$5\pm4\times10^{-3}$
3	$659-719$	$1\pm5\times10^{-4}$	-0.3 ± 0.6	-4 ± 6	0 ± 13	$0.2\pm7\times10^{-5}$	$5.17\pm0.03\times10^{-5}$	$4\pm3\times10^{-3}$
4	$808-868$	$0\pm1\times10^{-4}$	-0.2 ± 0.5	-4 ± 6	0 ± 12	$0.2\pm6\times10^{-5}$	$4.62\pm0.03\times10^{-5}$	$5\pm2\times10^{-3}$
5	$868-928$	$2\pm4\times10^{-5}$	-0.2 ± 0.2	-4 ± 8	0 ± 11	$0.1\pm7\times10^{-5}$	$6.72\pm0.02\times10^{-5}$	$4\pm2\times10^{-3}$
6	$928-988$	$1\pm8\times10^{-5}$	-0.1 ± 0.5	-4 ± 6	0 ± 10	$0.1\pm6\times10^{-5}$	$5.33\pm0.05\times10^{-5}$	$4\pm2\times10^{-3}$
7	$988-1048$	$2\pm9\times10^{-5}$	-0.2 ± 0.5	-4 ± 5	0 ± 10	$0.1\pm6\times10^{-5}$	$5.42\pm0.07\times10^{-5}$	$4\pm2\times10^{-3}$
8	$1099-1159$	$0\pm1\times10^{-4}$	-0.2 ± 0.7	-4 ± 7	0 ± 13	$0.1\pm9\times10^{-5}$	$6.74\pm0.06\times10^{-5}$	$4\pm4\times10^{-3}$
9	$1159-1219$	$0\pm2\times10^{-4}$	-0.1 ± 1	-4 ± 6	0 ± 16	$0.1\pm10\times10^{-5}$	$7.1\pm0.1\times10^{-5}$	$4\pm8\times10^{-3}$
10	$1306-1366$	$1\pm6\times10^{-5}$	-0.08 ± 0.6	-4 ± 5	0 ± 13	$0.1\pm14\times10^{-5}$	$8.2\pm0.1\times10^{-5}$	$3\pm6\times10^{-3}$
11	$1418-1477$	$0\pm9\times10^{-5}$	-0 ± 0.2	-4 ± 18	0 ± 27	$0.2\pm17\times10^{-5}$	$2.758\pm0.005\times10^{-4}$	$3\pm3\times10^{-3}$

Segment	$\Delta\nu_1$ (Hz)	$\nu_{0,1}$ (Hz)	r_2	$\Delta\nu_2$ (Hz)	$\nu_{0,2}$ (Hz)	β	P_0 (RMS normalised)	χ^2_ν
1	$9\pm4\times10^{-5}$	$0.9\pm1\times10^{-4}$	$2.4\pm0.3\times10^{-3}$	$3.5\pm0.8\times10^{-7}$	$5.2\pm0.5\times10^{-7}$	0 ± 1	0 ± 2	2.9
2	$10\pm4\times10^{-5}$	$0.7\pm1\times10^{-4}$	$2.5\pm0.3\times10^{-3}$	$4.2\pm0.9\times10^{-7}$	$5.3\pm0.5\times10^{-7}$	0 ± 7	0 ± 2	2.4
3	$9\pm4\times10^{-5}$	$0.7\pm0.8\times10^{-4}$	$2.9\pm0.4\times10^{-3}$	$7\pm2\times10^{-7}$	$5\pm1\times10^{-7}$	0.0 ± 0.5	0 ± 2	3.4
4	$9\pm3\times10^{-5}$	$0.7\pm0.7\times10^{-4}$	$3.0\pm0.4\times10^{-3}$	$5\pm2\times10^{-7}$	$5.7\pm0.7\times10^{-7}$	0 ± 4	0 ± 2	3.1
5	$8\pm3\times10^{-5}$	$1\pm0.6\times10^{-4}$	$2.5\pm0.9\times10^{-3}$	$3.1\pm0.8\times10^{-7}$	$5\pm1\times10^{-7}$	0.01 ± 0.05	0 ± 1	1.7
6	$9\pm3\times10^{-5}$	$0.7\pm0.7\times10^{-4}$	$3\pm1\times10^{-3}$	$7\pm6\times10^{-7}$	$4\pm3\times10^{-7}$	0.01 ± 0.05	0 ± 1	1.4
7	$10\pm3\times10^{-5}$	$0.8\pm0.7\times10^{-4}$	$3\pm1\times10^{-3}$	$8\pm6\times10^{-7}$	$5\pm2\times10^{-7}$	0.0 ± 0.1	0 ± 1	1.4
8	$10\pm5\times10^{-5}$	$0.9\pm1\times10^{-4}$	$4\pm2\times10^{-3}$	$8\pm8\times10^{-7}$	$5\pm3\times10^{-7}$	0.01 ± 0.08	0 ± 2	2.4
9	$10\pm6\times10^{-5}$	$0.8\pm2\times10^{-4}$	$4\pm3\times10^{-3}$	$1\pm2\times10^{-6}$	$4\pm5\times10^{-7}$	0.0 ± 0.1	0 ± 2	2.4
10	$10\pm12\times10^{-5}$	$1\pm3\times10^{-4}$	$2\pm2\times10^{-3}$	$1\pm1\times10^{-6}$	$10\pm10\times10^{-7}$	0.0 ± 0.1	0 ± 3	6.7
11	$7\pm53\times10^{-5}$	$0.3\pm6\times10^{-4}$	$3\pm2\times10^{-3}$	$6\pm2\times10^{-7}$	$10\pm3\times10^{-7}$	0.0 ± 0.8	0 ± 5	7.6

A.3 *TESS* light curves

Figure A.4 shows the *TESS* light curves of AWDs used in this work apart from CP Pup as noted in Table 4.1. To demonstrate more clearly the variability on the QPO timescale a running average of the light curve is overlaid on top of the data in solid black line.

A.4 Linear PSDs of QPOs

Figure A.5 shows the linear non-averaged PSD of the light curves from Table 4.1. The PSDs are zoomed in on the frequency range where the QPOs and their harmonics are the most dominant. In this case the orbital period signals are not removed to demonstrate the difference between the QPOs and a coherent orbital period. For WZ Sge the first harmonic of the QPO is not visible due to the first harmonic of the orbit. Other high frequency harmonics of the QPO and orbit are present but not shown in the frequency range displayed here. For GW Lib only the first harmonic of the QPO is shown as the fundamental of the signal observed in Chote et al. (2021).

A.5 QPO Model: Magnetically Driven Precession Model

The magnetically driven precession model of QPOs discussed in this Section was developped by Lai (1999) for the purpose of explaining QPOs in NSs and T Tauri stars. In this frame work the accretor's spin axis is misaligned to the angular momentum of the accretion disc causing magnetic and warping torques. These torques warp the inner part of the disc which then precesses around.

The magnetospheric radius at which the accretion flow is disrupted by the accretor's magnetic field B is given by

$$r_M = \eta \left(\frac{2\pi^2}{\mu_0^2} \frac{\mu^4}{GM\dot{M}^2} \right)^{\frac{1}{7}}, \tag{A.5.1}$$

where η is a dimensionless parameter describing the geometry of the accretion flow and the relation between the Alfvén and magnetospheric radius. It is usually set to 0.5 for magnetic systems, but a lower value could indicate that the assumption of $r_M = r_{CO}$, typically assumed for magnetic systems, is not valid (i.e. for a low magnetic field). Such a scenario (low value of η) could also be possible for a system with high inclination. μ is the stellar magnetic

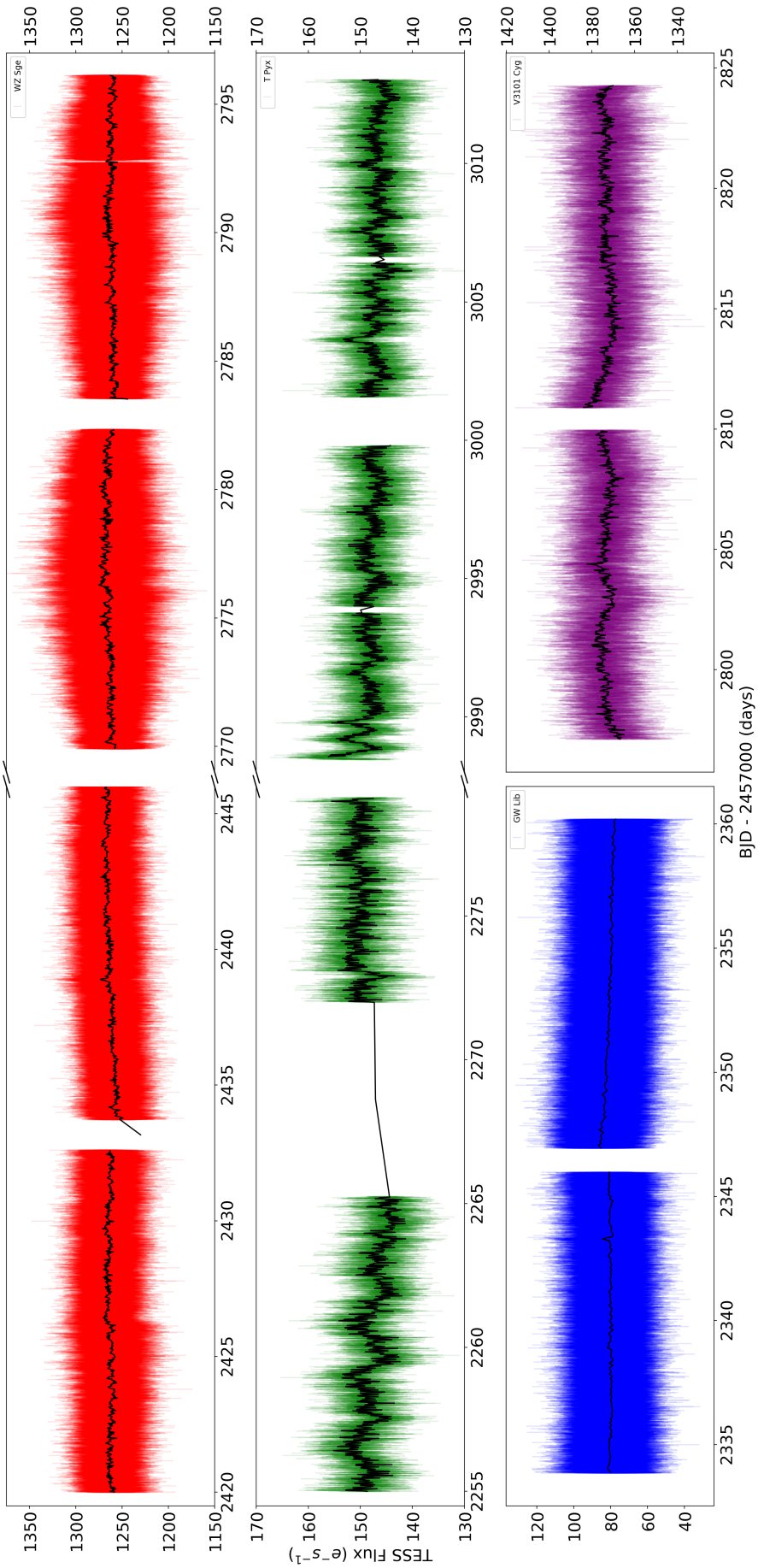

Figure A.4: Light curve of WZ Sge, GW Lib, T Pyx and V3101 Cyg showing all sectors of *TESS* data as described in Table 4.1 (CP Pup is shown in Figure 1 of Veresvarska & Scaringi 2023). The gap between the individual *TESS* sectors in WZ Sge and GW Lib has been excluded. The solid line in each panel denotes the running average of the light curve on the QPO timescale.

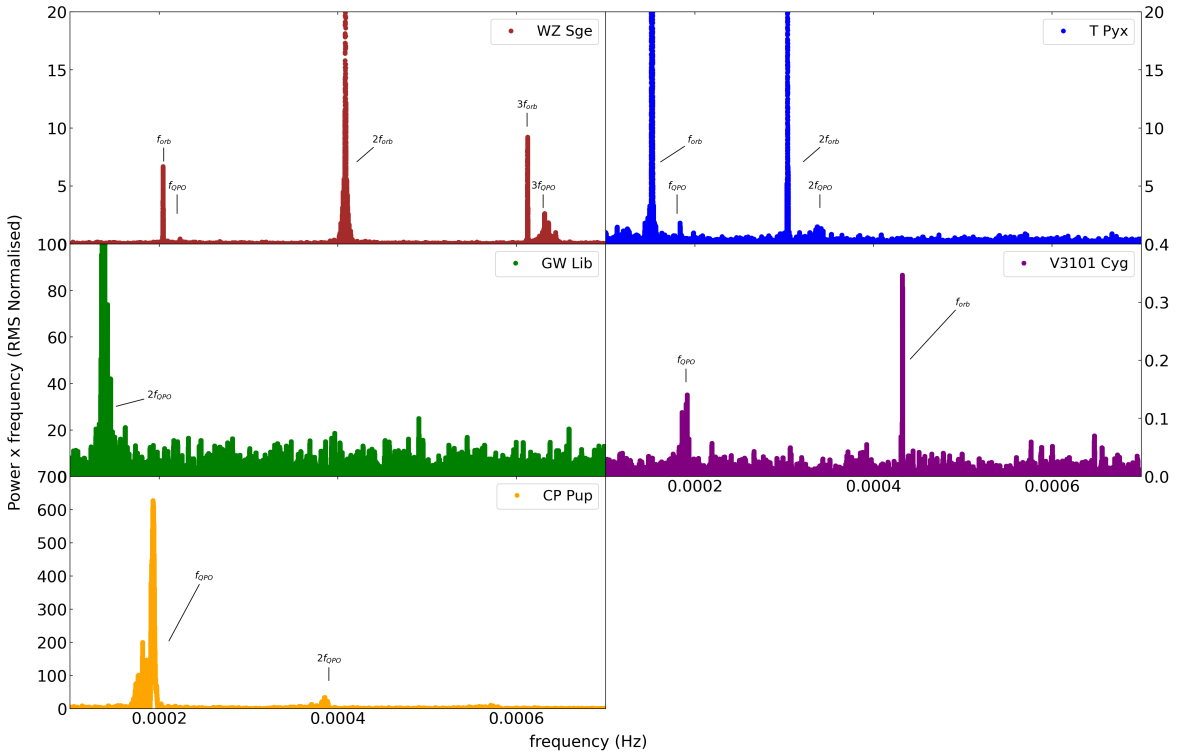

Figure A.5: A zoom-in on a section of PSD of light curves from Table 4.1 with labelled QPO and orbital period signals. The frequency range is fixed to be the same for all panels. Some of WZ Sge harmonics were excluded for better visualisation.

dipole moment such that $\mu = BR^3$, M the accretor mass, R the accretor radius, $\dot{M}$ its accretion rate, G the gravitational constant and μ_0 the vacuum permeability. Following Lai (1999); Pfeiffer & Lai (2004), the magnetospheric radius from A.5.1 is set to be equal to the co-rotation radius:

$$r_{CO} = \left(\frac{GMP_{spin}^2}{4\pi^2} \right)^{\frac{1}{3}}, \tag{A.5.2}$$

where P_{spin} is the spin period of the accretor. This assumption of co-rotation radius being equal to magnetospheric radius is a simplification and may not be entirely realistic. This radius is also set to be equal to the inner disc radius r_{in}. With these assumptions, the global precession frequency of the inner flow is given by

$$\nu_{QPO} = A\frac{\Omega_p\left(r_{in}\right)}{2\pi} = \frac{A}{2\pi}\frac{\mu^2}{\pi^2 r^7 \Omega\left(r\right)\Sigma\left(r\right)D\left(r\right)}F\left(\theta\right), \tag{A.5.3}$$

where A is related to the offset between the global precession frequency and the magnetically driven precession frequency. Depending on the details of the disc structure at $r_{in} = r_M$, $A \simeq 0.3 - 0.85$ as determined by Shirakawa & Lai (2002c). $\Omega\left(r\right)$ is the Keplerian frequency

at a radius r, $\Sigma(r)$ is the surface density as determined in Equation 5.41 in Frank et al. (2002a). $D(r)$ is a dimensionless function given by

$$D(r) = max\left(\sqrt{\frac{r^2}{r_{in}^2} - 1}, \sqrt{\frac{2H(r)}{r_{in}}}\right), \tag{A.5.4}$$

where $H(r)$ is the half-height of the disc at radius r, as defined in Equation 5.41 in Frank et al. (2002a). $F(\theta)$ is a function that depends on the dielectric property of the disc, so that $F(\theta) = 2fcos^2\theta - sin^2\theta$, where θ is the angle between the magnetic moment of the accretor and the angular momentum of the disc. f is a dimensionless number between 0 and 1, so that for $f = 1$ all the vertical field is screened out by the disc, whereas for $f = 0$ only the spin-variable vertical field is. I follow Pfeiffer & Lai (2004) in taking $f = 0$ throughout this work for simplicity.

Though the QPO can happen at any radius r the degeneracy this would create would not allow to test the model through observations. However, assuming $r_{in} = r_M = r_{CO} = r$ mitigates this. Through $r_{in} = r_M = r_{CO}$, the precession and QPO frequency depend on the spin of the accretor, providing a potential handle on the spin period of systems in which it cannot be directly measured, such as weakly magnetic AWDs. Naturally the model is dependent on many other parameters, chiefly among them the strength of the intrinsic magnetic field strength of the accretor B, the accretion rate of the system $\dot{M}$ and the viscosity of the disc α.

A.6 Magnetic precession model parameter space for M51 ULX-7 and NGC 7793 P13

A.7 Magnetic precession model parameter space for CP Pup, T Pyx and V3101 Cyg

A.8 *TESS* systems with high frequency breaks

Table A.2: *TESS* systems with high frequency breaks for all available Sectors and errors.

System Name	TESS Sector	ν_b (Hz)	ν_b low error (Hz)	ν_b high error (Hz)

IGR J14536-5522	11	0.0012	0.0002	0.0012
	12	0.0015	0.0004	0.002
	38	0.001	0.0012	0.0014
[PK2008] J102442.03-4	36	0.0007	0.0002	0.0002
VX Ret	29	0.0001	9e-05	7e-05
	30	0.0001	4e-05	4e-05
	31	0.00013	7e-05	8e-05
	35	0.0001	3e-05	7e-05
	62	0.00018	8e-05	0.00081
	65	0.0001	3e-05	8e-05
VV Pup	34	0.00049	0.0002	0.00046
VAR Ret	29	0.00035	0.00015	0.00023
	30	0.0006	0.0002	0.0003
	31	0.0009	0.0005	0.0011
	32	0.0005	0.0002	0.0003
	35	0.00037	0.00015	0.00023
	38	0.00042	0.00016	0.00026
	62	0.00028	8e-05	0.00012
	65	0.00022	6e-05	8e-05
	68	0.00017	6e-05	9e-05
	69	0.00023	7e-05	8e-05
V834 Cen	38	0.00024	5e-05	9e-05
V795 Her	25	0.0012	0.0003	0.0003
	26	0.0011	0.0002	0.0002
	79	0.0009	0.0006	0.0004
V751 Cyg	15	0.0008	0.0003	0.0003
	55	0.001	0.0002	0.0002
	56	0.0009	0.0003	0.0002
	75	0.0008	0.0002	0.0002
	76	0.0008	0.0002	0.0002
V592 Cas	17	0.0012	0.0004	0.0004
	24	0.0013	0.0003	0.0003

	57	0.0011	0.0002	0.0001
	58	0.0012	0.0002	0.0002
V533 Her	26	0.0007	0.0003	0.0002
	40	0.0006	0.0003	0.0003
	52	0.0006	0.0003	0.0003
	53	0.0006	0.0002	0.0002
	54	0.0006	0.0002	0.0002
	74	0.0005	0.0002	0.0002
	79	0.0006	0.0003	0.0003
V405 Aur	19	0.00035	9e-05	0.00012
	59	0.0005	0.0001	0.0001
	73	0.00044	0.00012	0.00018
V3885 Sgr	13	0.0007	0.0001	0.0001
	27	0.0006	0.0003	0.0008
	67	0.0009	0.0002	0.0009
V378 Peg	57	0.0006	0.0001	0.0001
V2709 Cyg	15	0.00046	0.00015	0.00022
	16	0.0006	0.0003	0.0003
	41	0.0006	0.0001	0.0001
	56	0.0006	0.0001	0.0001
	75	0.0006	0.0002	0.0002
	76	0.0006	0.0001	0.0001
V2690 Cyg	14	0.00048	0.00014	0.00018
	41	0.0012	0.0004	0.0007
	54	0.0006	0.0002	0.0002
	55	0.0008	0.0004	0.0004
	74	0.0006	0.0002	0.0003
	75	0.00031	5e-05	5e-05
V1193 Ori	5	0.001	0.0003	0.0005
	32	0.0012	0.0002	0.0002
V1084 Her	51	9e-05	8e-05	9e-05
	52	0.0008	0.0004	0.0003

	78	0.001	0.0005	0.0004
	79	0.001	0.0002	0.0002
V1068 Per	58	0.00037	0.00016	0.00015
V1033 Cen	37	0.0015	0.0004	0.0026
	38	0.0014	0.0004	0.0018
V0704 And	17	0.0009	0.0005	0.0005
	57	0.0013	0.0002	0.0002
V504 Cen	38	0.0011	0.0003	0.0003
V0436 Cen	36	0.0013	0.0006	0.0005
	63	0.001	0.0003	0.0004
V0391 Hya	36	0.00025	6e-05	8e-05
	63	0.00037	0.00017	0.00016
V* WX Ari	42	0.0005	0.0001	0.0002
	43	0.0005	0.0001	0.0002
	44	0.0007	0.0002	0.0002
	70	0.0007	0.0003	0.0005
	71	0.0006	0.0002	0.0002
V* V923 Cyg	40	0.0008	0.0002	0.0002
	41	0.0009	0.0002	0.0002
	54	0.00047	0.00059	0.0005
	74	0.00012	5e-05	0.0001
	75	0.0001	6e-05	0.00013
UU Aqr	42	0.0005	0.00017	0.0002
	55	0.001	0.0005	0.0011
KR Aur	43	0.001	0.0002	0.0003
	44	0.0011	0.0003	0.0003
	45	0.0011	0.0002	0.0002
	72	0.0001	2e-05	4e-05
TX Col	5	0.0014	0.0008	0.0013
	6	0.0006	0.0002	0.0003
	32	0.0008	0.0003	0.0003
	32	0.0008	0.0003	0.0003

	33	0.0005	0.0001	0.0001
	33	0.0005	0.0001	0.0001
TW Pic	1	0.0012	0.0005	0.0005
	2	0.0012	0.0007	0.0006
	3	0.0011	0.0007	0.0007
	4	0.001	0.0007	0.0005
	5	0.0009	0.0004	0.0004
	6	0.001	0.0006	0.0005
	7	0.001	0.0005	0.0005
	8	0.0011	0.0006	0.0006
	9	0.0008	0.0002	0.0003
	10	0.0006	0.0002	0.0004
	11	0.001	0.0005	0.0014
	12	0.001	0.0007	0.0007
	13	0.0011	0.0006	0.0006
	32	0.00018	5e-05	5e-05
	31	0.00018	6e-05	5e-05
	30	0.0012	0.0006	0.0005
	33	0.001	0.0003	0.0004
	28	0.00025	7e-05	6e-05
	27	0.0009	0.0004	0.0004
	29	0.0005	0.0002	0.0002
	34	0.001	0.0004	0.0004
	35	0.001	0.0009	0.0007
	36	0.0012	0.0006	0.0005
	37	0.0006	0.0002	0.0002
	38	0.0012	0.0005	0.0004
	39	0.0011	0.0006	0.0006
	69	0.0007	0.0003	0.0003
	68	0.0009	0.0003	0.0004
	67	0.0009	0.0006	0.0005
	66	0.0006	0.0002	0.0002

	62	0.001	0.0005	0.0004
	64	0.0009	0.0005	0.0006
	63	0.0008	0.0003	0.0003
	61	0.0011	0.0005	0.0005
	65	0.0007	0.0003	0.0004
TT Ari	42	0.0009	0.0003	0.0003
	43	0.0009	0.0003	0.0003
	70	0.0007	0.0001	0.0001
	71	0.0008	0.0002	0.0002
SS Aur	60	0.00046	0.00017	0.00014
	73	0.00041	0.00011	0.0001
SERIV 90	40	0.00034	0.00019	0.0002
	41	0.00032	8e-05	0.00041
	54	0.0005	0.0002	0.0002
	55	0.0005	0.0002	0.0002
SDSS J225831.18-09493	42	0.00021	7e-05	8e-05
	70	0.0001	2e-05	3e-05
SDSS J083751.00+383012.5	47	0.0006	0.0002	0.0002
SDSS J075844.17+12015	34	0.00026	0.0001	0.00044
	44	0.0006	0.0002	0.0003
	45	0.0007	0.0002	0.0004
	46	0.00049	0.00016	0.00027
	61	0.00046	0.00018	0.00033
	71	0.0007	0.0003	0.001
RZ Gru	28	0.0004	0.0001	9e-05
	68	0.0008	0.0003	0.0004
RW Tri	18	0.0014	0.0004	0.0017
	58	0.0006	0.0002	0.0008
RR Pic	2	0.00033	0.00017	0.00026
	3	0.0006	0.0002	0.0005
	4	0.0006	0.0002	0.0005
	5	0.0006	0.0001	0.0004

	6	0.00031	0.00014	0.00016
	7	0.0006	0.0001	0.0004
	8	0.0006	0.0002	0.0006
	9	0.0006	0.0007	0.0004
	10	0.0006	0.0008	0.0004
	12	0.0005	0.0002	0.0007
	13	0.0005	0.0006	0.0004
	32	0.0006	0.0001	0.0005
	31	0.0006	0.0001	0.0004
	33	0.0005	0.0001	0.0004
	29	0.0007	0.0002	0.001
	27	0.0006	0.0001	0.0005
	30	0.0005	0.00012	0.00035
	34	0.0005	0.0001	0.0004
	35	0.0005	0.0001	0.0005
	36	0.0005	0.00011	0.00037
	37	0.0005	0.0001	0.0004
	39	0.0006	0.0009	0.0004
	69	0.0006	0.0003	0.0007
	68	0.0006	0.0001	0.0006
	67	0.0005	0.0002	0.0007
	66	0.0005	0.0002	0.0008
	63	0.0006	0.0002	0.0007
	64	0.0006	0.0001	0.0008
	62	0.0006	0.0001	0.0006
	65	0.0006	0.0002	0.0008
QU Car	37	0.0005	0.0001	0.0001
	38	0.00048	0.00013	0.00011
	64	0.00019	0.00013	9e-05
	65	0.00017	7e-05	6e-05
QQ Vul	41	0.0012	0.001	0.0012
	54	0.0012	0.0011	0.0012

	55	0.0024	0.0015	0.0052
Q Cyg	15	0.0006	0.0002	0.0002
	16	0.0007	0.0002	0.0001
	56	0.0006	0.0001	0.0001
	76	0.0006	0.0002	0.0002
OR And	16	0.001	0.0011	0.001
	17	0.0009	0.0013	0.0011
	57	0.0008	0.0005	0.0004
	77	0.0007	0.0008	0.0006
MU Cam	19	0.0009	0.0003	0.0011
	20	0.00043	0.0002	0.00031
	26	0.00041	0.00015	0.00022
	40	0.0005	0.0001	0.0002
	53	0.0006	0.0003	0.0003
	59	0.0006	0.0002	0.0002
	60	0.0006	0.0002	0.0003
	73	0.0006	0.0003	0.0003
	79	0.00046	0.00011	0.00013
MT Pup	34	0.0011	0.0002	0.0015
	61	0.0007	0.0002	0.0015
MT Dra	14	9e-05	7e-05	0.00015
	15	0.00022	0.00011	0.00035
	16	0.00014	6e-05	0.00012
	18	0.00018	8e-05	0.00016
	19	0.00013	6e-05	0.0001
	20	0.00018	0.0001	0.00025
	26	0.0002	8e-05	0.00016
	23	3.6e-05	3.4e-05	0.000544
	25	0.00019	6e-05	0.00011
	21	0.0002	7e-05	0.00014
	22	0.00018	3e-05	5e-05
	40	0.00019	6e-05	0.00013

	41	0.00033	0.00012	0.00021
	56	0.00013	3e-05	5e-05
	60	0.00013	3e-05	6e-05
	59	0.00012	3e-05	4e-05
	58	0.00013	4e-05	7e-05
	57	0.00013	3e-05	4e-05
	55	0.00012	3e-05	4e-05
	53	0.00014	3e-05	5e-05
	49	0.00023	7e-05	0.00014
	48	0.00029	0.00012	0.0003
	54	0.00011	2e-05	4e-05
	75	0.00021	7e-05	0.00014
	76	0.00012	4e-05	7e-05
	74	0.0013	0.0011	0.0021
MR Ser	24	0.00032	0.00025	0.00032
	25	0.0004	0.00034	0.0004
MGAB-V202	34	0.001	0.0002	0.0001
	35	0.0009	0.0001	0.0001
	61	0.0009	0.0002	0.0002
	62	0.001	0.0001	0.0001
MASTER OT J072703.91-	27	0.0008	0.0003	0.0003
	28	0.0008	0.0003	0.0003
	30	0.0007	0.0002	0.0002
	31	0.0008	0.0002	0.0002
	32	0.0008	0.0002	0.0002
	33	0.0007	0.0002	0.0002
	34	0.0009	0.0003	0.0003
	35	0.0009	0.0002	0.0003
	36	0.0011	0.0004	0.0003
	37	0.0008	0.0002	0.0002
	38	0.00029	7e-05	9e-05
	69	0.0011	0.0003	0.0002

	68	0.0009	0.0002	0.0002
	67	0.0009	0.0002	0.0002
	66	0.001	0.0003	0.0003
	61	0.00018	7e-05	0.0001
	64	0.001	0.0003	0.0003
	63	0.001	0.0003	0.0003
	62	0.0012	0.0007	0.0008
	65	0.0009	0.0002	0.0002
LX Ser	24	0.00022	0.00012	0.00014
	78	0.00043	0.00034	0.00062
LS Peg	55	0.0007	0.0002	0.0003
LQ Peg	55	0.00033	9e-05	0.00015
LN UMa	14	0.00031	0.00026	0.00023
	20	0.0006	0.0004	0.0004
	21	0.0006	0.0004	0.0004
	40	0.0006	0.0004	0.0005
	41	0.0005	0.0002	0.0007
	47	0.0008	0.0003	0.0004
	74	0.00045	0.00025	0.00024
Karachurin 15	42	0.0017	0.0017	0.0018
	70	0.0014	0.0008	0.0007
KV Dra	14	0.00032	3e-05	0.00037
	15	0.0005	0.0004	0.0029
	16	3e-05	1e-05	3.1e-05
	21	3.9e-05	2.6e-05	2.1e-05
	22	3.1e-05	1.4e-05	1.4e-05
	41	2e-05	7e-06	9e-06
	48	3.5e-05	1.5e-05	2e-05
	49	3.7e-05	3.6e-05	2.7e-05
	50	4.1e-05	3.1e-05	2.6e-05
	76	2.5e-05	1e-05	1.3e-05
	77	3.7e-05	6e-06	8e-06

KT Eri	32	0.00034	0.0004	0.00022
KQ Mon	34	0.0008	0.0003	0.0003
J2124+0502	55	0.0008	0.0002	0.0002
J202921+180925	55	0.00012	3e-05	3e-05
J1858+4914	14	0.00029	8e-05	9e-05
	15	0.00028	9e-05	0.00011
	26	0.0011	0.0003	0.0009
	40	0.0005	0.0002	0.0004
	41	0.00041	0.00011	0.00013
	54	0.00047	0.0002	0.00037
	55	0.0008	0.0003	0.0006
	74	0.00026	0.00012	0.00013
	75	0.0006	0.0007	0.0007
J1831+6511	14	0.0005	0.0001	0.0013
	16	0.0009	0.0002	0.0024
	17	0.0006	0.0008	0.0006
	18	0.0006	0.0003	0.0019
	19	0.0005	0.0002	0.0006
	20	0.00033	0.00013	0.00021
	26	0.00018	7e-05	0.00011
	24	0.00029	0.00013	0.00022
	25	0.00034	0.00014	0.00053
	21	0.00028	9e-05	0.00012
	23	0.00025	0.00015	0.00028
	40	0.0014	0.0005	0.0018
	41	0.0014	0.0003	0.0022
	47	0.00014	6e-05	0.0001
	55	0.0014	0.0001	0.0019
	60	0.00021	0.00012	0.00026
	59	0.0002	0.0001	0.00032
	58	0.00028	0.00015	0.00036
	57	0.00032	0.00015	0.00031

	54	0.0014	0.0006	0.0019
	53	0.0014	0.001	0.0012
	52	0.001	0.0003	0.0016
	51	0.0014	0.0005	0.0026
	48	0.00017	6e-05	0.00016
	73	0.00016	9e-05	0.00016
	79	0.0014	0.0003	0.0015
	76	0.001	0.0004	0.002
	77	0.001	0.0002	0.0019
	75	0.00027	3e-05	0.0005
	74	0.001	0.001	0.001
	78	0.00014	0.00014	0.00056
J172710+614527	14	0.00024	0.00018	0.00049
	15	1.4e-05	1.2e-05	2e-05
	16	0.00028	0.00028	0.00062
	17	3.3e-05	3e-05	6.3e-05
	19	0.00021	0.00016	0.00043
	20	8e-05	8e-05	0.00085
	26	0.00021	0.0002	3e-05
	24	0.01	0.01	0.01
	25	4.2e-05	4e-05	8.2e-05
	22	0.00018	0.00017	0.00062
	21	0.00034	0.00032	0.00034
	23	0.00017	0.00017	4e-05
	40	2e-05	0.000534	0.000559
	41	4e-05	4e-05	0.000105
	47	0.0006	0.0006	0.0006
	56	6e-05	2e-05	2e-05
	60	0.001	0.0002	0.0003
	59	0.0008	0.0002	0.0003
	58	0.0006	0.0002	0.0003
	57	0.0005	0.0002	0.0002

	55	0.0002	0.0002	0.00117
	53	4.3e-05	4.3e-05	0.000695
	52	0.0005	0.0004	0.0005
	51	0.0001	0.0001	9e-05
	50	5e-05	5e-05	4e-05
	49	0.0003	0.0003	0.00011
	48	4e-05	4e-05	8.7e-05
	54	1.6e-05	1.6e-05	5.4e-05
	73	0.0007	0.0002	0.0004
	76	0.0004	0.00011	0.00014
	78	0.00039	0.00015	0.00023
	77	0.00042	0.00016	0.00024
	74	0.0006	0.0002	0.0002
	79	0.00042	0.00014	0.00023
J0746-0934	7	0.00029	0.00017	0.00026
	34	0.00037	0.00013	0.00016
	61	0.0008	0.0003	0.0002
J0742-1049	34	0.00024	5e-05	7e-05
	61	0.00042	0.0001	0.00013
J071202+322641	20	0.00022	0.00023	0.00027
	44	0.0007	0.0003	0.0002
	45	0.0005	0.0001	0.0005
	47	0.00023	0.0001	0.00032
	60	0.0008	0.0003	0.0002
	71	0.0007	0.0002	0.0005
	72	0.0008	0.0002	0.0002
IX Vel	8	0.0003	0.00011	0.0001
	9	0.00035	0.00015	0.00013
	34	0.0005	0.0005	0.0002
	35	0.00045	0.00023	0.00019
	36	0.00048	0.00037	0.00023
	61	0.00012	4e-05	5e-05

	62	0.00031	9e-05	8e-05
IU Leo	46	0.00028	9e-05	0.00027
	72	0.00042	6e-05	0.00047
IR Gem	44	0.00031	0.00015	0.00013
	45	0.00028	0.00012	0.00012
	71	0.00018	0.00011	0.00041
	72	0.0006	0.0007	0.0005
HV And	57	0.0008	0.0003	0.0003
HS 0002+0901	42	0.00034	0.0002	0.00025
	43	0.0002	6e-05	0.00011
HR Lyr	40	0.0003	7e-05	0.00011
	53	0.00017	7e-05	0.00031
	54	5e-05	4e-05	0.00016
	74	0.00028	8e-05	0.0002
HR Del	55	0.0003	8e-05	7e-05
Gaia 18dnm	33	4.8e-05	3.5e-05	2.9e-05
	34	4.2e-05	2.2e-05	4.6e-05
	61	3.5e-05	1.6e-05	1.5e-05
Gaia 16bnz	18	0.00028	9e-05	0.00012
	59	0.0005	0.0002	0.0002
GZ Cnc	46	9e-05	3e-05	3e-05
	72	0.0001	3e-05	0.00018
GSC 08944-02101	36	0.0009	0.0002	0.0002
	37	0.0009	0.0002	0.0002
	62	0.0009	0.0002	0.0002
	63	0.0008	0.0002	0.0002
	64	0.0008	0.0002	0.0002
GSC 06742-00051	38	0.00034	0.00014	0.00023
	64	0.0005	0.0002	0.0003
GSC 03285-01142	18	0.00046	0.0001	0.0001
	58	0.00042	7e-05	7e-05
FO Aqr	42	0.00044	0.00014	0.00022

EX Hya	10	0.00041	0.00016	0.00028
	37	0.00022	6e-05	8e-05
	64	0.00036	0.00013	0.00021
EK TrA	38	3.4e-05	1.3e-05	1.6e-05
	39	4.3e-05	2.1e-05	1.6e-05
EF Tuc	27	0.00024	7e-05	8e-05
	28	0.00045	0.0002	0.0002
	68	0.0002	4e-05	4e-05
DX Oct	27	0.00015	4e-05	4e-05
	39	9e-05	6e-05	6e-05
	66	0.00013	6e-05	5e-05
	67	0.00018	0.00011	9e-05
DW Cnc	44	0.0004	0.0001	0.00014
	45	0.00036	0.0001	0.00014
	46	0.0007	0.0003	0.0004
	71	0.00032	8e-05	0.00012
	72	0.00036	0.0001	0.00015
DO Dra	20	0.0009	0.0002	0.0002
	21	0.0009	0.0005	0.0005
	40	0.0005	0.0001	0.0001
	41	0.0007	0.0001	0.0001
	47	0.00049	8e-05	0.0001
	48	0.0007	0.0001	0.0001
	74	0.0015	0.001	0.0042
	75	0.0005	0.0002	0.0004
DDE 79	33	0.0007	0.0001	0.0001
DDE 75	14	0.0008	0.0002	0.0002
	20	0.0007	0.0002	0.0001
	21	0.0008	0.0002	0.0002
	26	0.0007	0.0002	0.0002
	40	0.0008	0.0002	0.0002
	41	0.0008	0.0002	0.0002

	47	0.0008	0.0002	0.0002
	48	0.0008	0.0003	0.0003
	60	0.0008	0.0003	0.0003
	73	0.0009	0.0003	0.0003
	74	0.0008	0.0003	0.0003
	75	0.0007	0.0002	0.0003
CH UMa	14	0.00031	0.00015	0.00031
	20	0.00028	8e-05	0.00015
	21	0.00041	0.00016	0.00023
	40	0.00031	7e-05	7e-05
	41	0.00031	9e-05	9e-05
	47	0.00033	8e-05	7e-05
	74	0.00031	0.00661	0.00713
CD-35 9665	38	0.0009	0.0002	0.0002
	65	0.0009	0.0004	0.0003
BZ UMa	20	0.00047	0.00021	0.00037
	47	0.0007	0.0001	0.0001
	60	0.0006	0.0001	0.0002
	74	0.0009	0.0003	0.0003
BZ Cam	19	0.0007	0.0002	0.0006
	20	0.0005	0.0005	0.0005
	26	0.0007	0.0001	0.0005
	40	0.00047	0.00047	0.00047
	53	0.0006	0.0006	0.0006
	59	0.0008	0.0008	0.0007
	60	0.0005	0.0005	0.0005
	73	0.0005	0.0005	0.0005
BL Hyi	1	0.00027	0.00015	0.00014
	2	0.00037	0.00018	0.00028
	29	0.00037	0.0003	0.00037
	68	0.00022	8e-05	0.00017
	69	0.00043	0.00017	0.00059

BB Dor	1	0.0006	0.0002	0.0002
	2	0.0007	0.0002	0.0002
	3	0.0007	0.0002	0.0002
	4	0.0007	0.0003	0.0003
	5	0.0007	0.0002	0.0002
	6	0.0007	0.0003	0.0002
	7	0.0007	0.0002	0.0002
	8	0.0007	0.0002	0.0002
	9	0.0007	0.0003	0.0003
	10	0.0008	0.0004	0.0003
	11	0.0007	0.0003	0.0003
	12	0.0007	0.0003	0.0003
	13	0.0007	0.0003	0.0003
	33	0.0007	0.0002	0.0002
	31	0.0007	0.0002	0.0002
	30	0.0007	0.0002	0.0002
	32	0.0007	0.0002	0.0002
	28	0.0007	0.0002	0.0002
	27	0.0006	0.0002	0.0002
	29	0.0009	0.0005	0.0004
	34	0.0007	0.0002	0.0002
	36	0.0007	0.0002	0.0002
	37	0.0009	0.0005	0.0005
	38	0.0007	0.0003	0.0003
	39	0.0006	0.0002	0.0002
	69	0.0007	0.0003	0.0003
	68	0.0007	0.0004	0.0003
	67	0.0008	0.0004	0.0003
	66	0.0007	0.0003	0.0003
	63	0.0008	0.0002	0.0002
	64	0.0007	0.0002	0.0002
	62	0.0008	0.0002	0.0002

	61	0.0008	0.0002	0.0002
	65	0.0007	0.0002	0.0002
AT Cnc	21	0.00045	0.00041	0.00038
	44	0.00024	7e-05	0.00012
	45	0.0007	0.0003	0.0002
	46	0.00032	7e-05	8e-05
	47	0.00026	6e-05	7e-05
	71	0.00029	0.00012	0.00011
	72	0.0006	0.0001	0.0012
ASASSN-V J210752.24+4	15	0.00049	0.0002	0.00028
	16	0.0008	0.0005	0.0004
	55	0.0006	0.0002	0.0002
	56	0.0007	0.0003	0.0002
	75	0.0009	0.0005	0.0004
	76	0.00045	0.00013	0.00015
ASASSN-14kc	27	0.00037	0.00017	0.00015
	29	0.00043	0.0002	0.00021
	31	0.00047	0.0003	0.00026
	32	0.00044	0.0002	0.00021
	33	0.00028	0.00012	0.00018
	38	0.00048	0.00011	0.00011
	37	0.00044	0.00012	0.00011
	39	0.0006	0.0002	0.0006
	35	9e-05	4e-05	6e-05
	34	0.0007	0.0001	0.0019
	36	0.00039	0.00017	0.00017
	61	0.00041	0.00013	0.00015
	62	0.0006	0.0003	0.0003
	63	0.00035	0.00012	0.00018
	64	0.00042	0.00018	0.00025
	65	0.00049	0.00015	0.0002
	66	0.0006	0.0003	0.0003

	69	0.00037	0.00011	0.0001
ASAS J071404+7004.3	20	0.0005	0.0001	0.0001
	26	0.00044	7e-05	8e-05
	40	0.00043	9e-05	0.00012
	47	0.00025	3e-05	3e-05
	53	0.00016	4e-05	4e-05
	60	0.00035	0.00011	0.00015
	73	0.00033	9e-05	0.00011
	74	0.00039	9e-05	0.00011
AQ Men	1	0.00046	0.00014	0.00022
	5	0.0007	0.0002	0.0006
	8	0.00045	0.00018	0.00043
	11	0.0007	0.0002	0.0013
	12	0.00038	0.00021	0.00028
	13	0.00045	0.00022	0.00039
	27	0.00046	0.00014	0.00016
	28	0.00042	0.00014	0.00016
	31	0.0007	0.0003	0.0003
	39	0.0006	0.0005	0.0004
	35	0.0005	0.0004	0.0003
	38	0.0005	0.0003	0.0003
	61	0.00042	0.00014	0.00017
	62	0.0006	0.0006	0.0004
	65	0.0006	0.0002	0.0002
	66	0.0008	0.0007	0.0005
	67	0.0006	0.0003	0.0002
	68	0.0006	0.0003	0.0003
AO Psc	42	0.0006	0.0002	0.0006
	70	0.00028	0.00012	0.00016
AH Men	1	0.0009	0.0003	0.0003
	4	0.0011	0.0003	0.0003
	11	0.0007	0.0001	0.0002

	12	0.0008	0.0002	0.0002
	13	0.001	0.0004	0.0004
	27	0.0009	0.0002	0.0003
	31	0.0008	0.0003	0.0003
	38	0.0008	0.0002	0.0002
	39	0.0007	0.0001	0.0002
AB Dra	18	0.00041	0.00016	0.00015
	19	0.00047	0.00013	0.00016
	20	0.0008	0.0004	0.0006
	23	0.00041	0.0002	0.0004
	24	0.00046	0.00012	0.00014
	26	0.0005	0.0002	0.0003
	40	0.00039	9e-05	0.0001
	47	0.00032	8e-05	9e-05
	60	0.00021	6e-05	7e-05
	58	0.00039	0.0001	0.00012
	57	0.0005	0.0001	0.0002
	54	0.0005	0.0002	0.0003
	53	0.00039	0.00012	0.00014
	52	0.0006	0.0002	0.0003
	50	0.0008	0.0004	0.0007
	73	0.001	0.0005	0.0019
	74	0.00044	0.00018	0.00026
	77	0.00042	0.00013	0.00017
	78	0.0007	0.0004	0.0003
	79	0.00047	0.00013	0.00022
1813+6122	14	0.00033	9e-05	0.00016
	15	0.00039	0.0001	0.00014
	16	0.00035	0.00011	0.00017
	17	0.00046	0.00016	0.00029
	18	0.001	0.0002	0.0003
	19	0.0009	0.0003	0.0004

	26	0.00027	7e-05	0.00042
	25	0.0007	0.0002	0.0018
	24	0.00017	5e-05	9e-05
	22	0.00038	0.00014	0.00026
	21	0.0009	0.0003	0.0004
	23	0.0006	0.0005	0.0014
	41	0.0008	0.0003	0.0005
	47	0.0007	0.0003	0.0003
	56	0.00048	0.00011	0.00014
	60	0.00019	5e-05	7e-05
	59	0.001	0.0005	0.0009
	58	0.0007	0.0002	0.0003
	57	0.00047	0.0001	0.00011
	55	0.0003	8e-05	0.0001
	54	0.00048	0.00019	0.00032
	53	0.0005	0.0002	0.0003
	52	0.0004	0.00013	0.00022
	51	0.00021	5e-05	7e-05
	49	0.0008	0.0001	0.0012
	48	0.0013	0.0007	0.0018
	73	0.00035	0.00012	0.00018
	77	0.00048	0.00019	0.00036
	76	0.00037	0.00013	0.00021
	75	0.00028	8e-05	0.00012
0506+7725	19	0.0011	0.0002	0.0002
	20	0.0013	0.0003	0.0003
	25	0.001	0.0002	0.0002
	26	0.0013	0.0003	0.0003
	52	0.0006	0.0002	0.0002
	53	0.0007	0.0003	0.0003
	59	0.0008	0.0002	0.0002
	60	0.0006	0.0001	0.0002

	73	0.001	0.0002	0.0002
EI UMa	20	0.00015	0.00011	0.00012
	47	0.0001	7e-05	7e-05
J1509-6649	12	0.00025	0.00013	0.00024
	38	0.0006	0.0003	0.0008
	39	0.0011	0.0002	0.001
	65	0.00032	0.00012	0.00018
V709 Cas	17	0.00039	0.00011	0.00015
	18	0.00037	0.00014	0.00015
	24	0.00046	0.00017	0.00024
	57	0.0008	0.0002	0.0002
	58	0.0008	0.0002	0.0002
	78	0.0008	0.0002	0.0002
RX J2133.7+5107	15	0.0003	0.00015	0.00026
	16	0.00042	0.00021	0.00052
	56	0.0005	0.0003	0.0006
	57	0.00039	0.00015	0.00028
	76	0.00032	9e-05	0.00012
	77	0.0005	0.0002	0.0004
VY Scl	29	0.0009	0.0002	0.0002
	69	0.00028	5e-05	0.00046
MV Lyr	14	0.0008	0.0002	0.0001
	26	0.0009	0.0003	0.0003
	40	0.0011	0.0003	0.0003
	41	0.001	0.0003	0.0003
	53	0.001	0.0004	0.0003
	54	0.001	0.0003	0.0003
	55	0.0011	0.0003	0.0003
	80	0.0011	0.0003	0.0003
	81	0.0011	0.0003	0.0002
	82	0.0011	0.0002	0.0002
Z Cam	26	0.00034	0.00031	0.00022

	40	0.00035	0.00038	0.00023
	47	0.00048	0.0001	0.0005
	53	0.00034	0.00017	0.00012
	60	0.0005	0.0001	0.0006
	73	0.00049	8e-05	0.00036
WW Cet	29	0.0006	0.0001	0.0002
	70	0.0013	0.0015	0.0012
VZ Sex	45	0.0006	0.0003	0.0004
	46	0.00012	3e-05	4e-05
	62	0.0005	0.00013	0.00013
	72	0.0005	0.0002	0.0004
VZ Pyx	35	0.00037	9e-05	0.00013
	61	0.00034	9e-05	0.00016
	62	0.00037	0.0001	0.00013
VW Vul	41	0.00028	0.00012	0.00017
VW Hyi	1	0.00026	0.00017	0.00044
	2	0.00045	0.00024	0.0004
	3	0.00038	0.0002	0.00029
	4	0.0006	0.0005	0.0012
	5	0.0019	0.0007	0.0015
	6	0.0019	0.0001	0.0019
	7	6e-05	5e-05	0.00021
	8	0.00034	0.00015	0.0002
	9	0.0007	0.0004	0.0006
	10	0.0011	0.0005	0.0011
	11	0.0011	0.001	0.0008
	12	0.00033	0.00015	0.00017
	13	0.00044	0.00044	0.00038
	33	0.00041	0.00028	0.00025
	31	0.0012	0.0012	0.0012
	32	0.0006	0.0004	0.0013
	29	0.0015	0.0008	0.0014

	27	0.0018	0.0008	0.003
	30	0.0021	0.0021	0.0014
	34	0.0006	0.0003	0.0011
	35	0.0012	0.0012	0.0026
	36	0.0015	0.0013	0.0011
	37	0.0008	0.0003	0.0005
	39	0.00031	0.00017	0.00025
	69	0.00032	0.00032	0.00105
	67	0.00029	9e-05	0.00011
	66	0.00049	0.00022	0.00028
	65	0.00029	0.0001	0.00011
	62	0.0012	0.0002	0.0022
	63	0.0007	0.0003	0.0004
	61	0.00015	0.00011	0.00018
	64	0.00037	0.00012	0.00014
VAR Ret 2005	29	0.00045	0.00016	0.00025
	30	0.0006	0.0002	0.0003
	31	0.0009	0.0005	0.001
	32	0.0005	0.0002	0.0003
	35	0.00037	0.00015	0.00023
	38	0.00049	0.0002	0.00035
	62	0.00028	8e-05	0.00012
	65	0.00022	6e-05	0.0001
	68	0.00018	6e-05	7e-05
	69	0.0012	0.0005	0.0012
V1147 Cen	37	0.0005	0.0002	0.0002
	64	0.00028	7e-05	9e-05
UY Pup	34	0.00044	0.00028	0.00071
	61	0.00022	0.0001	0.00011
TW Vir	46	0.0009	0.0008	0.0006
	72	0.00049	0.00013	0.00013
SS Cyg	16	0.0005	0.0002	0.0002

	56	0.0004	7e-05	7e-05
	76	0.00032	0.00011	9e-05
MASTER OT J142023.5-4	38	7e-05	7e-05	7e-05
	65	0.00044	0.00012	0.00079
LX And	18	0.0005	0.0002	0.0003
	58	0.00044	0.00019	0.0002
HL CMa	33	0.00048	0.00027	0.00033
DT Oct	27	4.6e-05	2e-05	1.9e-05
	39	0.0006	0.0002	0.0002
	66	0.0006	0.0002	0.0003
	67	0.00043	0.00015	0.00021
CK Eri	29	0.00045	0.00013	0.0002
	30	0.0005	0.0002	0.0004
BY Cam	19	0.00025	9e-05	0.0003
	59	0.001	0.0003	0.001
BV Cen	64	0.00038	0.00017	0.00052
	65	0.00034	0.00018	0.00037
ASASSN-16hl	39	0.00022	9e-05	0.00036
	65	0.00039	0.00021	0.00027
	66	0.00044	0.00018	0.00034
AQ Eri	32	0.00027	0.00013	0.00012
AM Cas	18	0.001	0.0003	0.0005
	19	0.0006	0.0002	0.0004
	52	0.00028	8e-05	0.00012
	58	0.00033	0.00012	0.00017
	59	0.00018	6e-05	7e-05
V2069 Cyg	15	7e-06	7e-06	1.7e-05
	16	0.00025	5e-05	0.00029
	55	0.00012	4e-05	9e-05
	56	0.00025	0.0002	0.0002
	76	0.00023	6e-05	0.0002
GK Per	18	0.0011	0.0003	0.0004

	58	0.0011	0.0008	0.0008

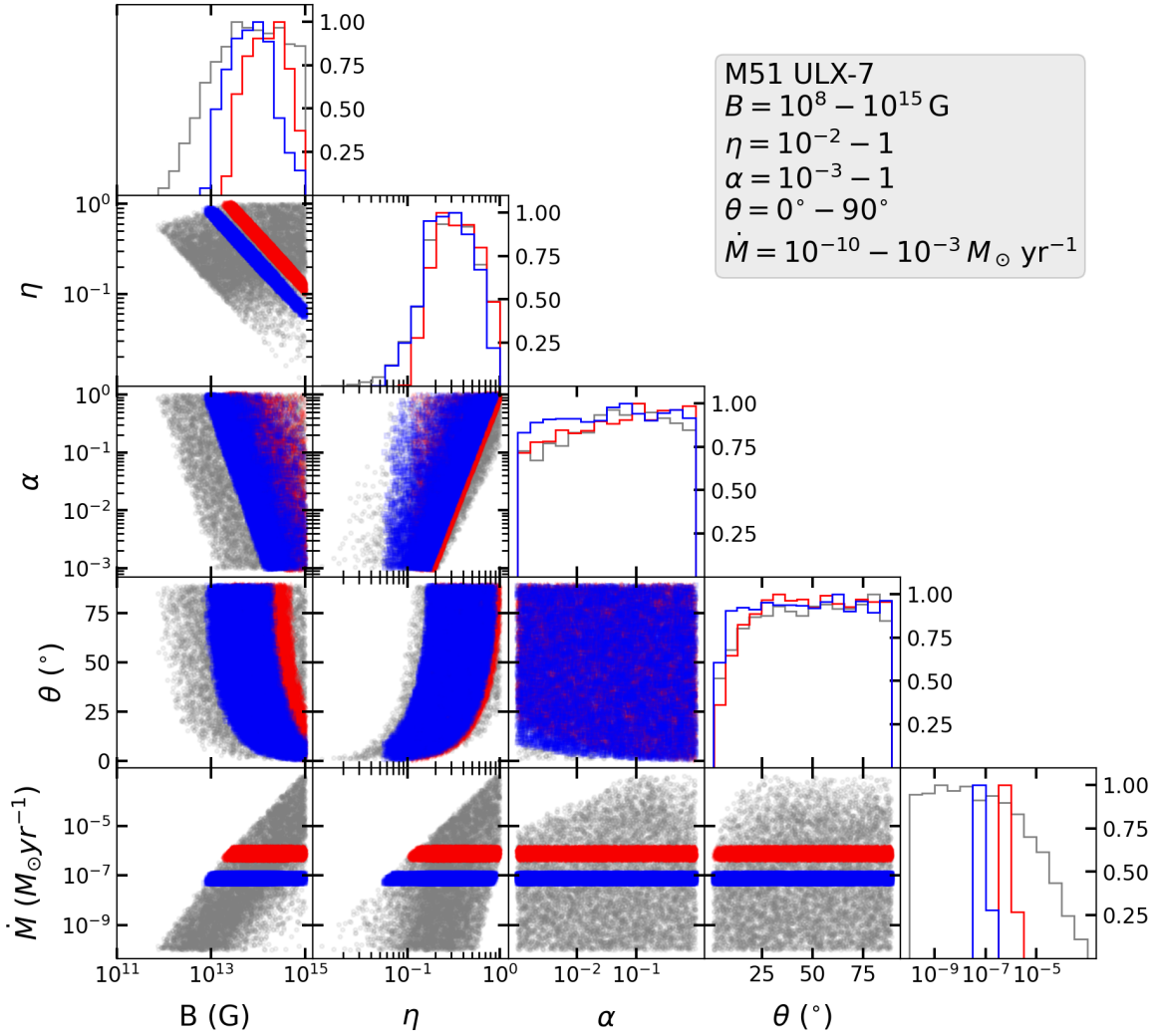

Figure A.6: Parameter space of the MDP model for M51 ULX-7 with all parameter combinations (in grey circles) producing QPO frequency and spin within the observed errors as noted in Table 5.2. All the solutions which also reproduce accretion rate within the range in Table 5.2 are given in red diamonds for no beaming (b = 1) and in blue squares for moderate beaming of b = 0.1. Distributions of all parameters are provided, with all being scaled to unity. The explored parameter ranges are noted as also shown in Table 5.1.

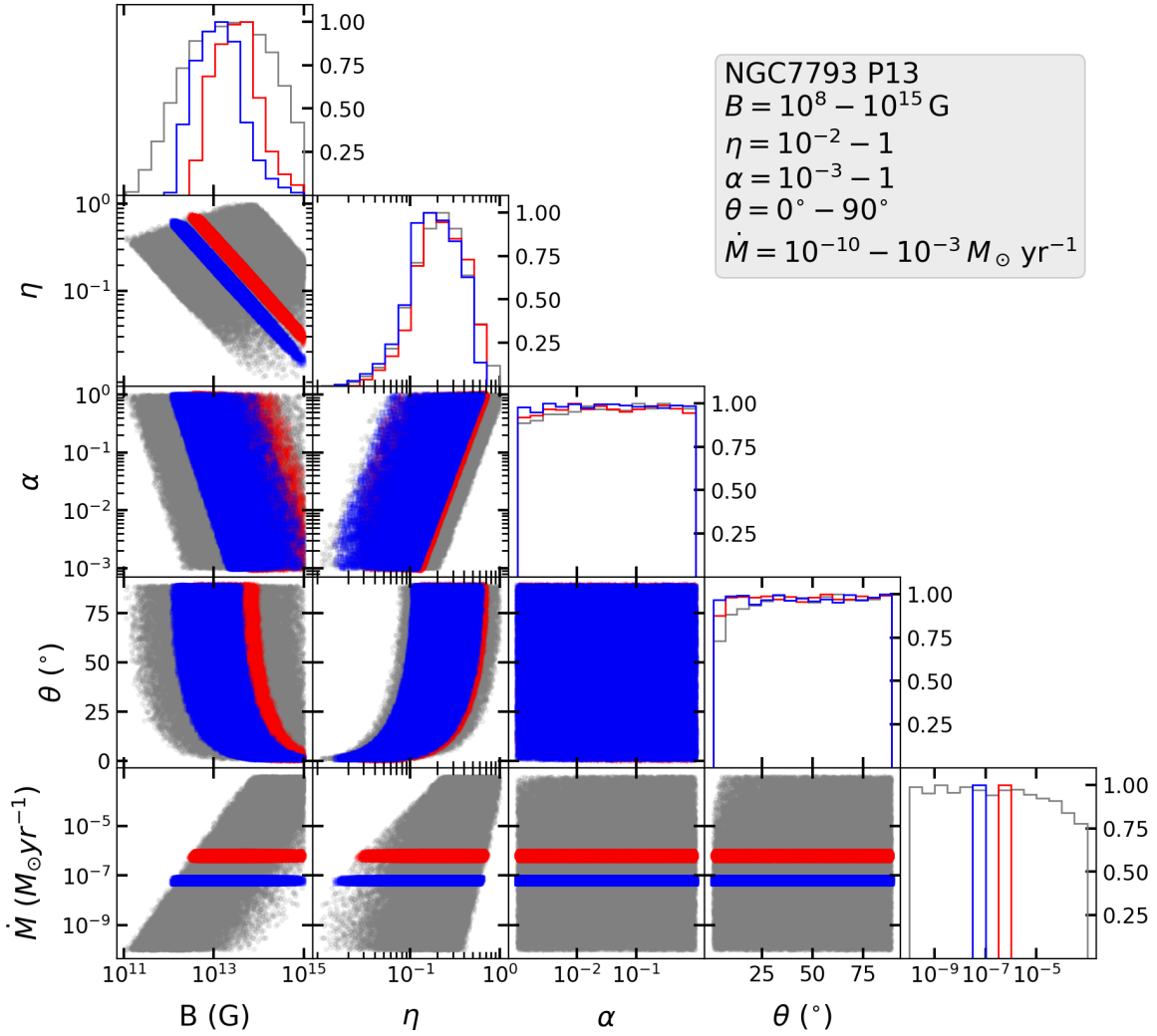

Figure A.7: Parameter space of the MDP model for NGC 7793 P13 with all parameter combinations (in grey circles) producing QPO frequency and spin within the observed errors as noted in Table 5.2. All the solutions which also reproduce accretion rate within the range in Table 5.2 are given in red diamonds for no beaming (b = 1) and in blue squares for moderate beaming of b = 0.1. Distributions of all parameters are provided, with all being scaled to unity. The explored parameter ranges are noted as also shown in Table 5.1.

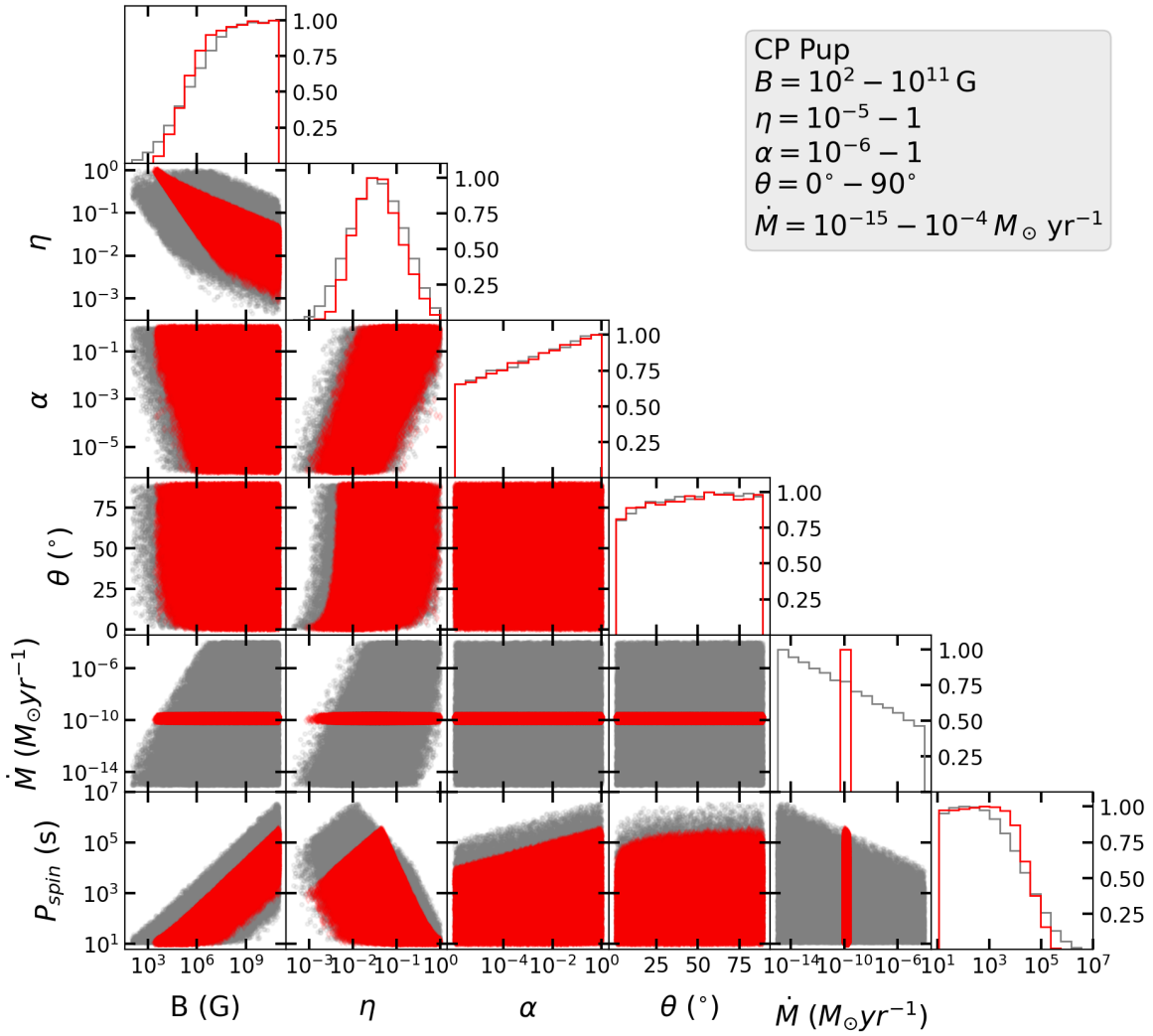

Figure A.8: Parameter space of the MDP model with all parameter combinations (in grey circles) producing QPO frequency and spin within the observed errors as noted in Table 4.2 and 5.4. All the solutions which also reproduce accretion rate within the range given in Table 5.4 are given in red diamonds. Distributions of all parameters are provided, with all being scaled to unity. The explored parameter ranges are noted as also shown in Table 5.3.

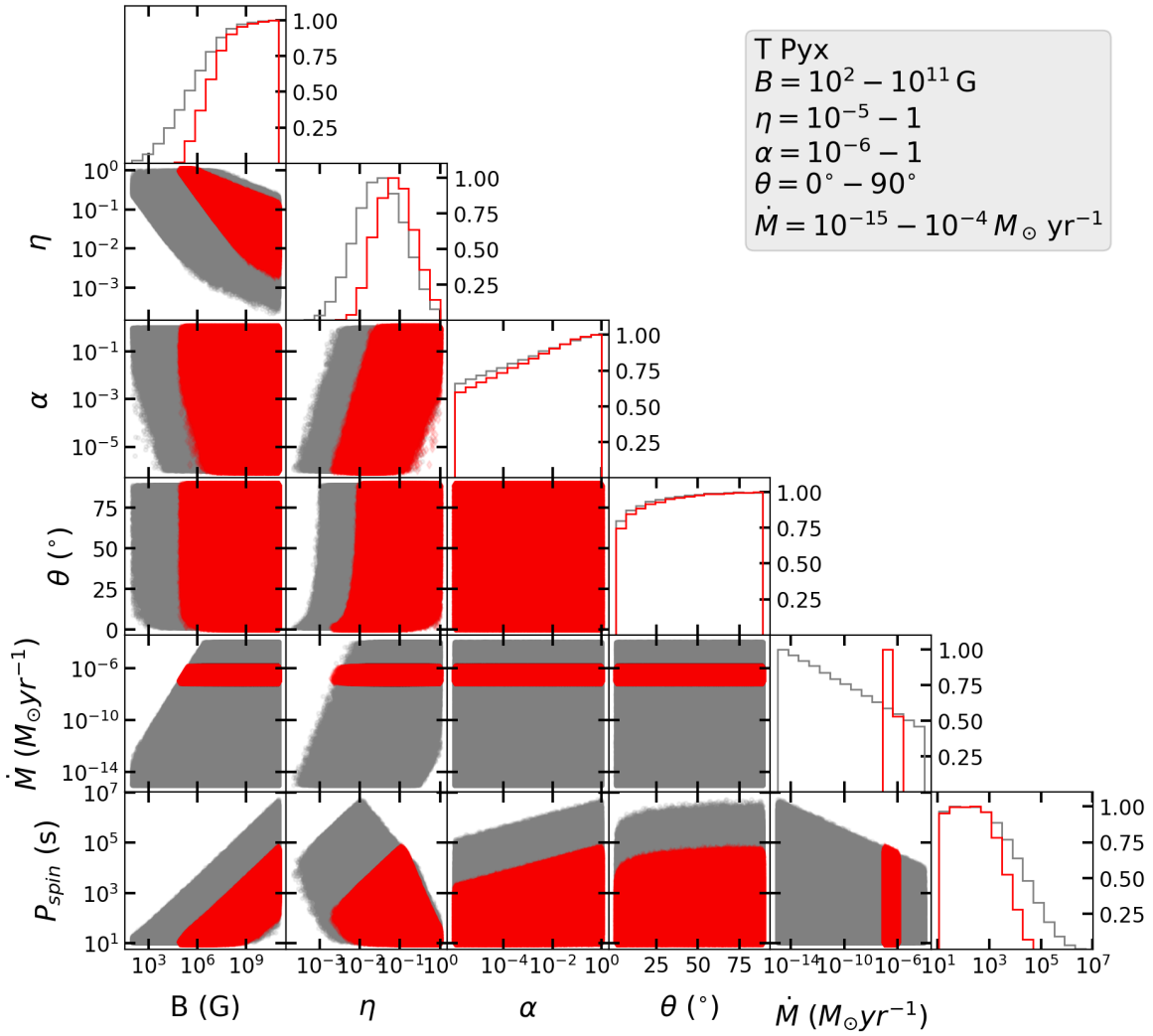

Figure A.9: Parameter space of the MDP model with all parameter combinations (in grey circles) producing QPO frequency and spin within the observed errors as noted in Table 4.2 and 5.4. All the solutions which also reproduce accretion rate within the range given in Table 5.4 are given in red diamonds. Distributions of all parameters are provided, with all being scaled to unity. The explored parameter ranges are noted as also shown in Table 5.3.

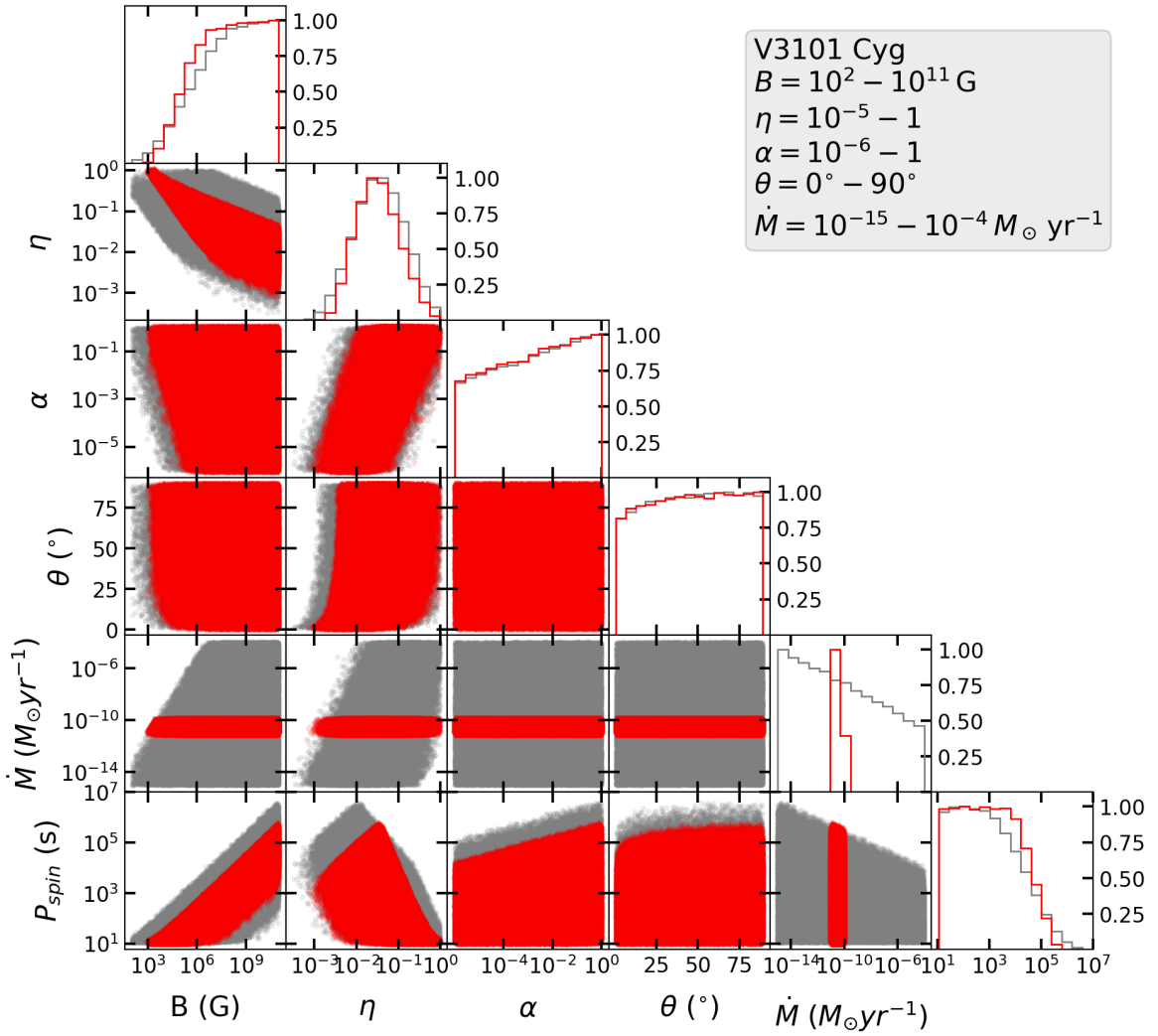

Figure A.10: Parameter space of the MDP model with all parameter combinations (in grey circles) producing QPO frequency and spin within the observed errors as noted in Table 4.2 and 5.4. All the solutions which also reproduce accretion rate within the range given in Table 5.4 are given in red diamonds. Distributions of all parameters are provided, with all being scaled to unity. The explored parameter ranges are noted as also shown in Table 5.3.

Bibliography

Althaus L. G., Córsico A. H., Isern J., García-Berro E., 2010, A&A Rev., 18, 471

Aly J. J., Kuijpers J., 1990, A&A, 227, 473

Amaro-Seoane P., et al., 2017, arXiv e-prints, p. arXiv:1702.00786

Andronov N., Pinsonneault M., Sills A., 2003, ApJ, 582, 358

Aranzana E., Scaringi S., Körding E., Dhillon V. S., Coppejans D. L., 2018, MNRAS, 481, 2140

Araujo-Betancor S., et al., 2005, A&A, 430, 629

Arévalo P., Uttley P., 2006a, MNRAS, 367, 801

Arévalo P., Uttley P., 2006b, MNRAS, 367, 801

Arnaud K. A., 1996, in Jacoby G. H., Barnes J., eds, Astronomical Society of the Pacific Conference Series Vol. 101, Astronomical Data Analysis Software and Systems V. p. 17

Aschenbach B., 2004, A&A, 425, 1075

Atapin K., Fabrika S., Caballero-García M. D., 2019, MNRAS, 486, 2766

Bachetti M., et al., 2014, Nature, 514, 202

Bachetti M., et al., 2020, ApJ, 891, 44

Bachetti M., et al., 2022, ApJ, 937, 125

Bagnoli T., in't Zand J. J. M., D'Angelo C. R., Galloway D. K., 2015, MNRAS, 449, 268

Bahramian A., Degenaar N., 2023, in , Handbook of X-ray and Gamma-ray Astrophysics. p. 120, doi:10.1007/978-981-16-4544-0_94-1

Balman 2019, Astronomische Nachrichten, 340, 296

Balman Š., Revnivtsev M., 2012, A&A, 546, 1

Balman S., Orio M., Ogelman H., 1995, ApJ, 449, 1993

Bardeen J. M., Petterson J. A., 1975, ApJ, 195, L65

Barker J., Kolb U., 2003, MNRAS, 340, 623

Belfiore A., et al., 2020, Nature Astronomy, 4, 147

Belloni T. M., Motta S. E., 2016, in Bambi C., ed., Astrophysics and Space Science Library Vol. 440, Astrophysics of Black Holes: From Fundamental Aspects to Latest Developments. p. 61 (arXiv:1603.07872), doi:10.1007/978-3-662-52859-4_2

Belloni T., Psaltis D., van der Klis M., 2002, ApJ, 572, 392

Belloni D., Schreiber M. R., Zorotovic M., Iłkiewicz K., Hurley J. R., Giersz M., Lagos F., 2018, MNRAS, 478, 5626

Bian W.-H., Zhao Y.-H., 2003, PASJ, 55, 599

Bianchini A., Friedjung M., Sabbadin F., 1985, Information Bulletin on Variable Stars, 2650

Bianchini A., Saygac T., Orio M., Della Valle M., Williams R., 2012, Astronomy & Astrophysics, 539, 1

Bloemen S., Marsh T. R., Steeghs D., Østensen R. H., 2010, MNRAS, 407, 1903

Bode M. F., Evans A., 2008, Classical Novae, 2nd edn. Cambridge University Press

Boirin L., Keek L., Méndez M., Cumming A., in't Zand J. J. M., Cottam J., Paerels F., Lewin W. H. G., 2007, A&A, 465, 559

Bond I., Freeth R. V., Marino B. F., Walker W. S. G., 1987, Information Bulletin on Variable Stars, 3037, 1

Bondi H., 1952, MNRAS, 112, 195

Brightman M., et al., 2020, ApJ, 895, 127

Brightman M., et al., 2022, ApJ, 925, 18

Bruch A., 2022, MNRAS, 514, 4718

Bruch A., 2023, MNRAS, 519, 352

Buckley D. A. H., Sekiguchi K., Motch C., O'Donoghue D., Chen A.-L., Schwarzenberg-Czerny A., Pietsch W., Harrop-Allin M. K., 1995, MNRAS, 275, 1028

Buisson D. J., et al., 2019, MNRAS, 490, 1350

Burdge K. B., et al., 2020, ApJ, 905, 32

Burdge K. B., et al., 2022, Nature, 610, 467

Campana S., Stella L., Mereghetti S., de Martino D., 2018, A&A, 610, A46

Cannizzo J. K., Nelemans G., 2015, ApJ, 803, 19

Cardelli J. A., Clayton G. C., Mathis J. S., 1989, ApJ, 345, 245

Carpano S., Haberl F., Maitra C., Vasilopoulos G., 2018, MNRAS, 476, L45

Casella P., Belloni T., Stella L., 2005a, ApJ, 629, 403

Casella P., Belloni T., Stella L., 2005b, ApJ, 629, 403

Casella P., Ponti G., Patruno A., Belloni T., Miniutti G., Zampieri L., 2008, MNRAS, 387, 1707

Castro Segura N., et al., 2021, MNRAS, 501, 1951

Castro Segura N., et al., 2022, Nature, 603, 52

Castro A., et al., 2019, Rev. Mexicana Astron. Astrofis., 55, 363

Castro A., et al., 2024, New A, 112, 102262

Charbonneau P., MacGregor K. B., 1997, ApJ, 486, 502

Chashkina A., Abolmasov P., Poutanen J., 2017, MNRAS, 470, 2799

Chashkina A., Lipunova G., Abolmasov P., Poutanen J., 2019, A&A, 626, A18

Chomiuk L., Metzger B. D., Shen K. J., 2021, ARA&A, 59, 391

Chote P., et al., 2021, MNRAS, 502, 581

Churazov E., Gilfanov M., Revnivtsev M., 2001, MNRAS, 321, 759

Cohen J. G., Rosenthal A. J., 1983, ApJ, 268, 689

Colbert E. J. M., Mushotzky R. F., 1999, ApJ, 519, 89

Coleman M. S. B., Blaes O., Hirose S., Hauschildt P. H., 2018, ApJ, 857, 52

Coriat M., Fender R. P., Dubus G., 2012, MNRAS, 424, 1991

Cornelisse R., Heise J., Kuulkers E., Verbunt F., in't Zand J. J. M., 2000, A&A, 357, L21

Covington A. E., et al., 2022, ApJ, 928, 164

Crawford T., Boyd D., Gualdoni C., Gomez T., MacDonald W. I., Oksanen A., 2008, JAAVSO, 36, 60

Cumming A., Bildsten L., 2001, ApJ, 559, L127

Cumming A., Macbeth J., in 't Zand J. J. M., Page D., 2006, ApJ, 646, 429

Darnley M. J., et al., 2006, MNRAS, 369, 257

Das S., Nandi A., Agrawal V. K., Dihingia I. K., Majumder S., 2021, MNRAS, 507, 2777

De Marco B., Ponti G., Cappi M., Dadina M., Uttley P., Cackett E. M., Fabian A. C., Miniutti G., 2013, MNRAS, 431, 2441

Della Valle M., Livio M., 1998, ApJ, 506, 818

Diaz M. P., Steiner J. E., 1991, PASP, 103, 964

Dobrotka A., Ness J. U., Mineshige S., Nucita A. A., 2017, MNRAS, 468, 1183

Dobrotka A., Negoro H., Konopka P., 2020, A&A, 641, A55

Done C., Magdziarz P., 1998, MNRAS, 298, 737

Done C., Magdziarz P., 1999, Nuclear Physics B Proceedings Supplements, 69, 376

Done C., Gierliński M., Kubota A., 2007, A&A Rev., 15, 1

Dubus G., Babusiaux C., 2024, A&A, 683, A247

Dubus G., Otulakowska-Hypka M., Lasota J. P., 2018, A&A, 617, 1

Duchêne G., Kraus A., 2013, ARA&A, 51, 269

Duerbeck H. W., Seitter W. C., Duemmler R., 1987, MNRAS, 229, 653

Duffy C., et al., 2022, MNRAS, 510, 1002

Dunn R. J. H., Fender R. P., Körding E. G., Belloni T., Cabanac C., 2010, MNRAS, 403, 61

Earnshaw H. M., et al., 2016, MNRAS, 456, 3840

Eggleton P. P., 1983, ApJ, 268, 368

El Mellah I., Sundqvist J. O., Keppens R., 2019, A&A, 622, L3

Event Horizon Telescope Collaboration et al., 2019, ApJ, 875, L1

Event Horizon Telescope Collaboration et al., 2022, ApJ, 930, L12

Fabbiano G., 1989, ARA&A, 27, 87

Fabian A. C., et al., 2009, Nature, 459, 540

Fabrika S. N., Atapin K. E., Vinokurov A. S., Sholukhova O. N., 2021, Astrophysical Bulletin, 76, 6

Fabry M., Marchant P., Langer N., Sana H., 2023, A&A, 672, A175

Faulkner J., Flannery B. P., Warner B., 1972, ApJ, 175, L79

Fausnaugh M., Huang X., Glidden A., Guerrero N., TESS Science Office 2018, in American Astronomical Society Meeting Abstracts #231. p. 439.09

Fender R., Gallo E., 2014, Space Sci. Rev., 183, 323

Fender R. P., Homan J., Belloni T. M., 2009, MNRAS, 396, 1370

Feng H., Rao F., Kaaret P., 2010, ApJ, 710, L137

Ferrario L., Wickramasinghe D. T., 1999, MNRAS, 309, 517

Fitzpatrick E. L., 1999, PASP, 111, 63

Fitzpatrick M., Placco V., Bolton A., Merino B., Ridgway S., Stanghellini L., 2024, arXiv e-prints, p. arXiv:2401.01982

Fontaine G., et al., 2011, ApJ, 726

Fragile P. C., Mathews G. J., Wilson J. R., 2001, ApJ, 553, 955

Frank J., King A., Raine D., 2002a, Accretion Power in Astrophysics. 3rd edition, Cambridge University Press, doi:10.1017/cbo9781139164245.004

Frank J., King A., Raine D. J., 2002b, Accretion Power in Astrophysics: Third Edition

Fryer C. L., Kalogera V., 2001, ApJ, 554, 548

Fürst F., et al., 2016, ApJ, 831, L14

Fürst F., et al., 2018, A&A, 616, A186

Fürst F., et al., 2021, A&A, 651, A75

Fürst F., Walton D. J., Bachetti M., Earnshaw H., Brightman M., 2025, Astronomische Nachrichten, 346, e20240106

Gaia Collaboration 2020, VizieR Online Data Catalog: Gaia EDR3 (Gaia Collaboration, 2020), VizieR On-line Data Catalog: I/350. Originally published in: 2021A&A...649A...1G; doi:10.5270/esa-1ug, doi:10.26093/cds/vizier.1350

Gaia Collaboration et al., 2016, A&A, 595, A1

Gaia Collaboration et al., 2023, A&A, 674, A1

Gallagher J. S., Starrfield S., 1978, ARA&A, 16, 171

Gandhi P., 2009, ApJ, 697

Gänsicke B. T., et al., 2009, MNRAS, 397, 2170

Ghosh P., Lamb F. K., 1979a, ApJ, 234, 296

Ghosh P., Lamb F. K., 1979b, ApJ, 234, 296

Gierliński M., Done C., 2004, MNRAS, 347, 885

Gladstone J. C., Roberts T. P., Done C., 2009, MNRAS, 397, 1836

Gleissner T., Wilms J., Pottschmidt K., Uttley P., Nowak M. A., Staubert R., 2004, A&A, 414, 1091

Godon P., Sion E. M., Williams R. E., Starrfield S., 2018, ApJ, 862, 89

Goliasch J., Nelson L., 2015, ApJ, 809, 80

Green M. J., et al., 2024, MNRAS, 527, 3445

Grindlay J., Gursky H., Schnopper H., Parsignault D. R., Heise J., Brinkman A. C., Schrijver J., 1976, ApJ, 205, L127

Groot P. J., 2001, ApJ, 551, L89

Groot P. J., et al., 2024, PASP, 136, 115003

Gúrpide A., Castro Segura N., 2024, MNRAS, 532, 1459

Gúrpide A., Godet O., Koliopanos F., Webb N., Olive J. F., 2021, A&A, 649, A104

Guver T., Ozel F., 2009, MNRAS, 400, 2050

Hamada T., Salpeter E. E., 1961, ApJ, 134, 683

Hameury J. M., 2020, Advances in Space Research, 66, 1004

Hameury J. M., Lasota J. P., 2002, A&A, 394, 231

Hameury J. M., Lasota J. P., 2017, A&A, 602, A102

Hameury J. M., Lasota J. P., 2021, A&A, 650, A114

Hameury J. M., Lasota J. P., Shaw A. W., 2022, A&A, 664, A7

Harrison C. M., Ramos Almeida C., 2024, Galaxies, 12, 17

Harrison F. A., et al., 2013, ApJ, 770, 103

Hawley J. F., Balbus S. A., 2002, ApJ, 573, 738

Heil L. M., Vaughan S., 2010, MNRAS, 405, L86

Heinze A. N., et al., 2018, AJ, 156, 241

Hellier C., Mason K. O., Smale A. P., Corbet R. H. D., O'Donoghue D., Barrett P. E., Warner B., 1989, MNRAS, 238, 1107

Hellier C., Kemp J., Naylor T., Bateson F. M., Jones A., Overbeek D., Stubbings R., Mukai K., 2000, MNRAS, 313, 703

Hermes J. J., et al., 2014, ApJ, 789

Hillman Y., Shara M. M., Prialnik D., Kovetz A., 2020, Nature Astronomy, 4, 886

Hilton E. J., Szkody P., Mukadam A., Mukai K., Hellier C., van Zyl L., Homer L., 2007, AJ, 134, 1503

Hoard D. W., Linnell A. P., Szkody P., Fried R. E., Sion E. M., Hubeny I., Wolfe M. A., 2004, ApJ, 604, 346

Homan J., 2001, PhD thesis, University of Amsterdam, Netherlands

Honeycutt R. K., Kafka S., 2004, AJ, 128, 1279

Howell S. B., Szkody P., Cannizzo J. K., 1995, ApJ, 439, 337

Howell S. B., Nelson L. A., Rappaport S., 2001, ApJ, 550, 897

Hu C.-P., Ueda Y., Enoto T., 2021, ApJ, 909, 5

Iben Jr. I., Tutukov A. V., 1987, ApJ, 313, 727

Iłkiewicz K., Scaringi S., Veresvarska M., De Martino D., Littlefield C., Knigge C., Paice J. A., Sahu A., 2024, ApJ, 962, L34

Imbrogno M., et al., 2024, A&A, 689, A284

Indebetouw R., et al., 2005, ApJ, 619, 931

Ingram A., Done C., 2011a, MNRAS, 415, 2323

Ingram A., Done C., 2011b, MNRAS, 415, 2323

Ingram A., Done C., 2012, MNRAS, 419, 2369

Ingram A. R., Motta S. E., 2019, New A Rev., 85, 101524

Ingram A., van der Klis M., 2013, MNRAS, 434, 1476

Ingram A., Done C., Fragile P. C., 2009, MNRAS, 397, L101

Irving Z. A., Altamirano D., Scaringi S., Veresvarska M., Knigge C., Castro Segura N., De Martino D., Iłkiewicz K., 2024, MNRAS, 530, 3974

Islam N., Mukai K., 2021, ApJ, 919, 90

Israel G. L., et al., 2017a, Science, 355, 817

Israel G. L., et al., 2017b, MNRAS, 466, L48

Ivanova N., Taam R. E., 2003, ApJ, 599, 516

Ivezić Ž., et al., 2019, ApJ, 873, 111

Jansen F., et al., 2001, A&A, 365, L1

Jenkins J. M., 2017, KEPLER DATA PROCESSING HANDBOOK: KSCI-19081-002

Jones D. I., Andersson N., 2001, MNRAS, 324, 811

José J., Shore S. N., Casanova J., 2020, A&A, 634, A5

Kaaret P., Ward M. J., Zezas A., 2004, MNRAS, 351, L83

Kaaret P., Feng H., Roberts T. P., 2017, ARA&A, 55, 303

Kato T., 2015, PASJ, 67, 108

Kawaler S. D., 1988, ApJ, 333, 236

Kawamura T., Axelsson M., Done C., Takahashi T., 2022, MNRAS, 511, 536

Kimura M., Osaki Y., Kato T., Mineshige S., 2020, PASJ, 72, 22

King A., Lasota J.-P., 2020, MNRAS, 494, 3611

King A., Lasota J.-P., 2021, arXiv e-prints, p. arXiv:2112.03779

King A. R., Wynn G. A., 1999, MNRAS, 310, 203

King A. R., Davies M. B., Ward M. J., Fabbiano G., Elvis M., 2001, ApJ, 552, L109

King A. R., Lubow S. H., Ogilvie G. I., Pringle J. E., 2005, MNRAS, 363, 49

King A. R., Pringle J. E., Livio M., 2007, MNRAS, 376, 1740

King A., Lasota J.-P., Kluźniak W., 2017, MNRAS, 468, L59

King A., Lasota J.-P., Middleton M., 2023, New A Rev., 96, 101672

Knigge C., Baraffe I., Patterson J., 2011, ApJ, Supplement Series, 194

Kochanek C. S., et al., 2017, PASP, 129, 104502

Kolb U., 1993, A&A, 271, 149

Kolb U., Baraffe I., 1999a, MNRAS, 309, 1034

Kolb U., Baraffe I., 1999b, MNRAS, 309, 1034

Kong A. K. H., Hu C.-P., Lin L. C.-C., Li K. L., Jin R., Liu C. Y., Yen D. C.-C., 2016, MNRAS, 461, 4395

Körding E. G., Migliari S., Fender R., Belloni T., Knigge C., McHardy I., 2007, MNRAS, 380, 301

Kotko I., Lasota J. P., 2012, A&A, 545, 1

Kouveliotou C., van Paradijs J., Fishman G. J., Briggs M. S., Kommers J., Harmon B. A., Meegan C. A., Lewin W. H. G., 1996, Nature, 379, 799

Kovetz A., Prialnik D., Shara M. M., 1988, ApJ, 325, 828

Kramer M., Schneider F. R. N., Ohlmann S. T., Geier S., Schaffenroth V., Pakmor R., Röpke F. K., 2020, A&A, 642, A97

Krawczynski H., et al., 2022, Science, 378, 650

Kupfer T., et al., 2015, MNRAS, 453, 483

Kupfer T., et al., 2018, MNRAS, 480, 302

Kupfer T., et al., 2024, ApJ, 963, 100

Lai D., 1999, ApJ, 524, 1030

Lai D., 2003, ApJ, 591, L119

Laor A., Netzer H., 1989, MNRAS, 238, 897

Lasota J.-P., 2001, New A Rev., 45, 449

Lasota J.-P., King A., 2023, MNRAS, 526, 2506

Lewin W. H. G., van Paradijs J., Taam R. E., 1993, Space Sci. Rev., 62, 223

Lewin W. H. G., van Paradijs J., van den Heuvel E. P. J., eds, 1995, X-ray binaries

Lightkurve Collaboration et al., 2018, Lightkurve: Kepler and TESS time series analysis in Python, Astrophysics Source Code Library (ascl:1812.013)

Lipunova G. V., 1999, Astronomy Letters, 25, 508

Littlefair S. P., Dhillon V. S., Marsh T. R., Gänsicke B. T., Southworth J., Baraffe I., Watson C. A., Copperwheat C., 2008, MNRAS, 388, 1582

Littlefield C., Garnavich P., Mukai K., Mason P. A., Szkody P., Kennedy M., Myers G., Schwarz R., 2019, ApJ, 881, 141

Littlefield C., Scaringi S., Garnavich P., Szkody P., Kennedy M. R., Iłkiewicz K., Mason P. A., 2021, AJ, 162, 49

Littlefield C., Lasota J.-P., Hameury J.-M., Scaringi S., Garnavich P., Szkody P., Kennedy M., Leichty M., 2022, ApJ, 924, L8

Littlefield C., et al., 2023, AJ, 165, 43

Liu J., 2024, ApJ, 961, 196

Livio M., 1992, ApJ, 393, 516

Lomb N. R., 1976, Ap&SS, 39, 447

Lopes de Oliveira R., Mukai K., 2019, ApJ, 880, 128

López Coto R., 2017, Introduction to Cataclysmic Variable Stars. Springer International Publishing, Cham, pp 167–172, doi:10.1007/978-3-319-44751-3_8, https://doi.org/10.1007/978-3-319-44751-3_8

Lubow S. H., 1991, ApJ, 381, 259

Luyten W., Hughes H., 1965a, Pub. Univ. Minnesota, 36

Luyten W., Hughes H., 1965b, Astrophys. J.„ 142, 1041

Lyubarskii Y. E., 1997, MNRAS, 292, 679

MacGregor K. B., Charbonneau P., 1997, ApJ, 486, 484

Magdziarz P., Zdziarski A. A., 1995, MNRAS, 273, 837

Majumder S., Das S., Agrawal V. K., Nandi A., 2023, MNRAS, 526, 2086

Marelli M., De Martino D., Mereghetti S., De Luca A., Salvaterra R., Sidoli L., Israel G., Rodriguez G., 2018, ApJ, 866, 125

Marsh T. R., 2011, Classical and Quantum Gravity, 28

Mason E., et al., 2013, MNRAS, 436, 212

Mason P. A., et al., 2022, ApJ, 938, 142

Mazeh T., Perets H. B., McQuillan A., Goldstein E. S., 2015, ApJ, 801

McAllister M., et al., 2019, MNRAS, 486, 5535

McHardy I. M., Papadakis I. E., Uttley P., Page M. J., Mason K. O., 2004, MNRAS, 348, 783

McHardy I. M., Koerding E., Knigge C., Uttley P., Fender R. P., 2006, Nature, 444, 730

McHardy I. M., et al., 2023, MNRAS, 519, 3366

Mestel L., Spruit H. C., 1987, MNRAS, 226, 57

Middleton M. J., Roberts T. P., Done C., Jackson F. E., 2011, MNRAS, 411, 644

Middleton M. J., Walton D. J., Fabian A., Roberts T. P., Heil L., Pinto C., Anderson G., Sutton A., 2015, MNRAS, 454, 3134

Middleton M. J., et al., 2018, MNRAS, 475, 154

Middleton M. J., Fragile P. C., Ingram A., Roberts T. P., 2019, MNRAS, 489, 282

Middleton M., Gúrpide A., Walton D. J., 2023, MNRAS, 519, 2224

Miller-Jones J. C. A., et al., 2012, MNRAS, 421, 468

Miller J. M., Homan J., Miniutti G., 2006, ApJ, 652, L113

Miyamoto S., Kimura K., Kitamoto S., Dotani T., Ebisawa K., 1991, ApJ, 383, 784

Mönkkönen J., Tsygankov S. S., Mushtukov A. A., Doroshenko V., Suleimanov V. F., Poutanen J., 2022, MNRAS, 515, 571

Motch C., Pakull M. W., Grisé F., Soria R., 2011, Astronomische Nachrichten, 332, 367

Motch C., Pakull M. W., Soria R., Grisé F., Pietrzyński G., 2014, Nature, 514, 198

Motta S., Belloni T., Homan J., 2009, MNRAS, 400, 1603

Motta S. E., et al., 2020, ApJ, 898, 174

Mukadam A. S., et al., 2013, AJ, 146, 54

Munari U., 2019, arXiv e-prints, p. arXiv:1909.01389

Mushotzky R. F., Szymkowiak A. E., 1988, in Fabian A. C., ed., NATO Advanced Study Institute (ASI) Series C Vol. 229, Cooling Flows in Clusters and Galaxies. p. 53, doi:10.1007/978-94-009-2953-1_6

Mushtukov A. A., Ingram A., Suleimanov V. F., DiLullo N., Middleton M., Tsygankov S. S., van der Klis M., Portegies Zwart S., 2024, MNRAS, 530, 730

Narayan R., Yi I., 1994, ApJ, 428, L13

Narayan R., Yi I., 1995a, ApJ, 444, 231

Narayan R., Yi I., 1995b, ApJ, 452, 710

Narayan R., Piran T., Kumar P., 2001, ApJ, 557, 949

Nauenberg M., 1972a, ApJ, 175, 417

Nauenberg M., 1972b, ApJ, 175, 417

Neilsen J., Lee J. C., 2009, Nature, 458, 481

Netzer H., 2015, ARA&A, 53, 365

Nixon C. J., Pringle J. E., 2019, A&A, 628, A121

Norton A. J., Watson M. G., King A. R., Lehto H. J., McHardy I. M., 1992, MNRAS, 254, 705

Nucita A. A., Conversi L., Licchelli D., 2019, MNRAS, 484, 3119

O'Donoghue D., Warner B., Wargau W., Grauer A. D., 1989, MNRAS, 240, 41

Oppenheim A. V., Schafer R. W., 1975, Digital signal processing

Orio M., Mukai K., Bianchini A., de Martino D., Howell S., 2009, ApJ, 690, 1753

Osaki Y., 1974, PASJ, 26, 429

Osaki Y., 1996, PASP, 108, 39

Paczyński B., 1967, Acta Astron., 17, 287

Paczynski B., Abramowicz M. A., 1982, ApJ, 253, 897

Paice J. A., Misra R., Gandhi P., 2024a, RAS Techniques and Instruments, 3, 453

Paice J. A., et al., 2024b, MNRAS, 531, L82

Pala A. F., et al., 2020, MNRAS, 494, 3799

Pala A. F., et al., 2022, MNRAS, 510, 6110

Pasham D. R., Cenko S. B., Zoghbi A., Mushotzky R. F., Miller J., Tombesi F., 2015, ApJ, 811, L11

Passy J.-C., et al., 2012, ApJ, 744, 52

Patterson J., 1980, ApJ, 241, 235

Patterson J., 1998, PASP, 110, 1132

Patterson J., Warner B., 1998, PASP, 110, 1026

Patterson J., Robinson E. L., Nather R. E., 1977, ApJ, 214, 144

Patterson J., Halpern J., Shambrook A., 1993, ApJ, 419, 803

Patterson J., Richman H., Kemp J., Mukai K., 1998, PASP, 110, 403

Patterson J., et al., 2004, PASP, 116, 516

Patterson J., et al., 2005, PASP, 117, 1204

Patterson J., et al., 2013, MNRAS, 434, 1902

Patterson J., et al., 2020, ApJ, 897, 70

Payne-Gaposchkin C., 1964, New York: Dover Publication

Payne-Gaposchkin C., Gaposchkin S., 1938, Variable stars. Vol. 5

Penna R. F., Sadowski A., Kulkarni A. K., Narayan R., 2013, MNRAS, 428, 2255

Pfeiffer H. P., Lai D., 2004, ApJ, 604, 766

Pinto C., Kosec P., 2023, Astronomische Nachrichten, 344, e20220134

Pinto C., Walton D. J., 2023, arXiv e-prints, p. arXiv:2302.00006

Pinto C., Middleton M. J., Fabian A. C., 2016, Nature, 533, 64

Plavec M., Kratochvil P., 1964, Bulletin of the Astronomical Institutes of Czechoslovakia, 15, 165

Plotkin R. M., Gallo E., Miller B. P., Baldassare V. F., Treu T., Woo J.-H., 2014, ApJ, 780, 6

Podsiadlowski P., Han Z., Rappaport S., 2003, MNRAS, 340, 1214

Poutanen J., Lipunova G., Fabrika S., Butkevich A. G., Abolmasov P., 2007, MNRAS, 377, 1187

Prialnik D., Kovetz A., 1995, ApJ, 445, 789

Prialnik D., Shara M. M., 1986, ApJ, 311, 172

Pringle J. E., 1996, MNRAS, 281, 357

Psaltis D., Norman C., 2000, arXiv e-prints, pp astro–ph/0001391

Ramírez S. H., Segura Montero O., Michel R., Echevarría J., 2022a, Rev. Mexicana Astron. Astrofis., 58, 47

Ramírez S. H., Segura Montero O., Michel R., Echevarría J., 2022b, Rev. Mexicana Astron. Astrofis., 58, 47

Ramsay G., et al., 2018, A&A, 620

Rapisarda S., Ingram A., Van Der Klis M., 2017, MNRAS, 469, 2011

Rappaport S., Joss P. C., Webbink R. F., 1982, ApJ, 254, 616

Rappaport S., Verbunt F., Joss P. C., 1983, ApJ, 275, 713

Rauer H., Heras A. M., 2018, in Deeg H. J., Belmonte J. A., eds, , Handbook of Exoplanets. p. 86, doi:10.1007/978-3-319-55333-7_86

Reig P., Belloni T., van der Klis M., Méndez M., Kylafis N. D., Ford E. C., 2000, ApJ, 541, 883

Reinhold T., Reiners A., Basri G., 2014, Rotation & differential rotation of the active Kepler stars, doi:10.1017/S1743921314002117

Remillard R. A., McClintock J. E., 2006, ARA&A, 44, 49

Revnivtsev M., Potter S., Kniazev A., Burenin R., Buckley D. A., Churazov E., 2011, MNRAS, 411, 1317

Ricker P. M., Taam R. E., 2012, ApJ, 746, 74

Ricker G. R., et al., 2015, Journal of Astronomical Telescopes, Instruments, and Systems, 1, 014003

Ritter H., Kolb U., 2003, A&A, 404, 301

Rivera Sandoval L. E., Maccarone T. J., Cavecchi Y., Britt C., Zurek D., 2021, MNRAS, 505, 215

Rodriguez A. C., 2024, PASP, 136, 054201

Rodríguez Castillo G. A., et al., 2020, ApJ, 895, 60

Rodríguez-Gil P., Gänsicke B. T., Araujo-Betancor S., Casares J., 2004, MNRAS, 349, 367

Röpke F. K., De Marco O., 2023, Living Reviews in Computational Astrophysics, 9, 2

Rosen S. R., Mason K. O., Cordova F. A., 1988, MNRAS, 231, 549

Rosino L., Romano G., Marziani P., 1993, PASP, 105, 51

Ruiz-Carmona R., Khangale Z. N., Woudt P. A., Groot P. J., 2020, MNRAS, 491, 344

Sand C., Ohlmann S. T., Schneider F. R. N., Pakmor R., Röpke F. K., 2020, A&A, 644, A60

Sathyaprakash R., et al., 2019, MNRAS, 488, L35

Savonije G. J., de Kool M., van den Heuvel E. P. J., 1986, A&A, 155, 51

Scargle J. D., 1998, ApJ, 504, 405

Scaringi S., 2014, MNRAS, 438, 1233

Scaringi S., Körding E., Uttley P., Knigge C., Groot P. J., Still M., 2012a, MNRAS, 421, 2854

Scaringi S., Körding E., Uttley P., Groot P. J., Knigge C., Still M., Jonker P., 2012b, MNRAS, 427, 3396

Scaringi S., Körding E., Groot P. J., Uttley P., Marsh T., Knigge C., Maccarone T., Dhillon V. S., 2013, MNRAS, 431, 2535

Scaringi S., et al., 2015, Science Advances, 1

Scaringi S., MacCarone T. J., D'Angelo C., Knigge C., Groot P. J., 2017a, Nature, 552, 210

Scaringi S., Maccarone T. J., D'Angelo C., Knigge C., Groot P. J., 2017b, Nature, 552, 210

Scaringi S., et al., 2022a, Nature Astronomy, 6, 98

Scaringi S., et al., 2022b, Nature Astronomy, 6, 98

Scaringi S., Groot P. J., Knigge C., Lasota J. P., de Martino D., Cavecchi Y., Buckley D. A. H., Camisassa M. E., 2022c, MNRAS, 514, L11

Scaringi S., et al., 2022d, Nature, 604, 447

Scaringi S., Breivik K., Littenberg T. B., Knigge C., Groot P. J., Veresvarska M., 2023, MNRAS, 525, L50

Schaefer B. E., Collazzi A. C., 2010, AJ, 139, 1831

Schaefer B. E., Pagnotta A., Zoppelt S., 2022, MNRAS, 512, 1924

Schreiber M. R., Belloni D., van Roestel J., 2023, A&A, 679, L8

Segura Montero O., Ramírez S. H., Echevarría J., 2020, MNRAS, 494, 4110

Selvelli P., Gilmozzi R., 2019, A&A, 622, A186

Shafter A. W., 2017, ApJ, 834, 196

Shakura N. I., Sunyaev R. A., 1973, A&A, 55, 155

Shappee B. J., et al., 2014, ApJ, 788, 1

Shara M. M., Livio M., Moffat A. F. J., Orio M., 1986, ApJ, 311, 163

Shara M. M., Prialnik D., Hillman Y., Kovetz A., 2018, ApJ, 860, 110

Shingles L., et al., 2021, Transient Name Server AstroNote, 7, 1

Shirakawa A., Lai D., 2002a, ApJ, 564, 361

Shirakawa A., Lai D., 2002b, ApJ, 564, 361

Shirakawa A., Lai D., 2002c, ApJ, 565, 1134

Singh K. P., White N. E., Drake S. A., 1996, ApJ, 456, 766

Smak J., 1971, Acta Astron., 21, 15

Smak J., 1993, Acta Astron., 43, 101

Smak J., 2009, Acta Astron., 59, 121

Smith K. L., Mushotzky R. F., Boyd P. T., Wagoner R. V., 2018, ApJ, 860, L10

Smith K. W., et al., 2020, PASP, 132, 085002

Solanki S., Kupfer T., Blaes O., Breedt E., Scaringi S., 2021, MNRAS, 500, 1222

Soleri P., Belloni T., Casella P., 2008, MNRAS, 383, 1089

Solheim J.-E. S. E., 2010, PASP, 122, 1133

Spruit H. C., Ritter H., 1983, A&A, 124, 267

Spruit H. C., Taam R. E., 1993, ApJ, 402, 593

Starrfield S., Truran J. W., Sparks W. M., Kutter G. S., 1972, ApJ, 176, 169

Steeghs D., Harlaftis E. T., Horne K., 1997, MNRAS, 290, L28

Stella L., Vietri M., 1998, ApJ, 492, L59

Stella L., Vietri M., Morsink S. M., 1999, ApJ, 524, L63

Stepanyan D. A., 1982, Peremennye Zvezdy, 21, 691

Still Martin B. T., 2012, Astrophysics Source Code Library, record ascl:1208.004

Stoughton C., et al., 2002, SLOAN DIGITAL SKY SURVEY : EARLY DATA RELEASE Istva The Sloan Digital Sky Survey (SDSS) is an imaging and spectroscopic survey that will eventually cover approximately one-quarter of the celestial sphere and collect spectra of % 10 6 galaxies , 100 , 00

Stroeer A., Vecchio A., 2006, Classical and Quantum Gravity, 23, S809

Strohmayer T., Bildsten L., 2003, arXiv e-prints, pp astro–ph/0301544

Strohmayer T. E., Brown E. F., 2002, ApJ, 566, 1045

Strohmayer T. E., Mushotzky R. F., 2009, ApJ, 703, 1386

Strohmayer T. E., Mushotzky R. F., Winter L., Soria R., Uttley P., Cropper M., 2007, ApJ, 660, 580

Suleimanov V. F., Doroshenko V., Werner K., 2019, MNRAS, 482, 3622

Sutton A. D., Roberts T. P., Middleton M. J., 2013, MNRAS, 435, 1758

Szkody P., Mateo M., 1984, ApJ, 280, 729

Szkody P., Wade R. A., 1981, ApJ, 251, 201

Szkody P., et al., 2012, ApJ, 753, 158

Tauris T. M., van den Heuvel E. P. J., 2006, in Lewin W. H. G., van der Klis M., eds, , Vol. 39, Compact stellar X-ray sources. pp 623–665, doi:10.48550/arXiv.astro-ph/0303456

Thorstensen J. R., Patterson J., Kemp J., Vennes S., 2002, PASP, 114, 1108

Timmer J., König M., 1995, Astronomy & Astrophysics, 300, 707

Tonry J. L., et al., 2018, PASP, 130, 064505

Townsley D. M., Bildsten L., 2004, ApJ, 600, 390

Townsley D. M., Arras P., Bildsten L., 2016, arXiv e-prints, p. arXiv:1601.02046

Tsugawa M., Osaki Y., 1997, PASJ, 49, 75

Tutukov A. V., Fedorova A. V., Ergma E. V., Yungelson L. R., 1985, Soviet Astronomy Letters, 11, 52

Urquhart R. T., et al., 2022, MNRAS, 511, 4528

Uttley P., McHardy I. M., 2001, MNRAS, 323, 1

Uttley P., McHardy I. M., Vaughan S., 2005, MNRAS, 359, 345

Uttley P., Wilkinson T., Cassatella P., Wilms J., Pottschmidt K., Hanke M., Böck M., 2011, MNRAS, 414, L60

Van Cleve J. E., Caldwell D. A., 2016, Kepler Instrument Handbook, Kepler Science Document KSCI-19033-002, id.1. Edited by Michael R. Haas and Steve B. Howell

Van Cleve J. E., et al., 2016, Kepler Data Characteristics Handbook, Kepler Science Document KSCI-19040-005, id. 2. Edited by Doug Caldwell, Jon M. Jenkins, Michael R. Haas and Natalie Batalha

Van de Sande M., Scaringi S., Knigge C., 2015, MNRAS, 448, 2430

VanderPlas J. T., 2018, ApJSupplement Series, 236, 16

Vasilopoulos G., Lander S. K., Koliopanos F., Bailyn C. D., 2020, MNRAS, 491, 4949

Vasilopoulos G., Koliopanos F., Haberl F., Treiber H., Brightman M., Earnshaw H. P., Gúrpide A., 2021, ApJ, 909, 50

Vaughan B. A., Nowak M. A., 1997, ApJ, 474, L43

Verbunt F., Zwaan C., 1981, A&A, 100, L7

Veresvarska M., Scaringi S., 2023, MNRAS, 518, 5576

Veresvarska M., Scaringi S., Hagen S., De Martino D., Done C., Ilkiewicz K., Knigge C., Littlefield C., 2024a, MNRAS, 529, 664

Veresvarska M., et al., 2024b, MNRAS, 534, 3087

Veresvarska M., et al., 2025b, MNRAS,

Veresvarska M., et al., 2025a, MNRAS,

Walton D. J., et al., 2016, ApJ, 827, L13

Wang Y. M., 1987, A&A, 183, 257

Warner B., 1985, MNRAS, 217, 1P

Warner B., 1986, Monthly Notes of the Astronomical Society of South Africa, 45, 117

Warner B., 1995, Ap&SS, 225, 249

Warner B., 2003, Cataclysmic Variable Stars, doi:10.1017/CBO9780511586491

Warner B., 2004, PASP, 116, 115

Warner B., Robinson E. L., 1972, Nature Physical Science, 239, 2

Warner B., Woudt P. A., 2002, MNRAS, 335, 84

Warner B., van Zyl L., 1998, in Deubner F.-L., Christensen-Dalsgaard J., Kurtz D., eds, Vol. 185, New Eyes to See Inside the Sun and Stars. p. 321

Warner B., Woudt P. A., Pretorius M. L., 2003, MNRAS, 344, 1193

Webbink R. F., 1976, ApJ, 209, 829

Webster B. L., Murdin P., 1972, Nature, 235, 37

Weisskopf M. C., Tananbaum H. D., Van Speybroeck L. P., O'Dell S. L., 2000, in Truemper J. E., Aschenbach B., eds, Society of Photo-Optical Instrumentation Engineers (SPIE) Conference Series Vol. 4012, X-Ray Optics, Instruments, and Missions III. pp 2–16 (arXiv:astro-ph/0004127), doi:10.1117/12.391545

White James C. I., Honeycutt R. K., Horne K., 1993, ApJ, 412, 278

Wijnands R., van der Klis M., 1999, ApJ, 514, 939

Wood M. A., Thomas D. M., Simpson J. C., 2009, MNRAS, 398, 2110

Woudt P. A., Warner B., Pretorius M. L., Dale D., 2005, in Hameury J. M., Lasota J. P., eds, Astronomical Society of the Pacific Conference Series Vol. 330, The Astrophysics of Cataclysmic Variables and Related Objects. p. 325

Wu K., Cropper M., Ramsay G., Saxton C., Bridge C., 2003, Chinese Journal of Astronomy and Astrophysics Supplement, 3, 235

Yanny B., et al., 2009, AJ, 137, 4377

Yaron O., Prialnik D., Shara M. M., Kovetz A., 2005, ApJ, 623, 398

Yuan F., Narayan R., 2014, ARA&A, 52, 529

Zampieri L., Roberts T. P., 2009, MNRAS, 400, 677

Zorotovic M., Schreiber M. R., Gänsicke B. T., 2011, A&A, 536, A42

de Marco B., Ponti G., Uttley P., Cappi M., Dadina M., Fabian A. C., Miniutti G., 2011, MNRAS, 417, L98

in't Zand J. J. M., Cornelisse R., Méndez M., 2005, A&A, 440, 287

in't Zand J. J. M., Galloway D. K., Ballantyne D. R., 2011, A&A, 525, A111

van der Klis M., 1988, NATO Advanced Study Institutes Series. Series C, Mathematical and Physical Sciences Link, pp 27–70

van der Klis M., 1989, ARA&A, 27, 517

van der Klis M., 2006, Rapid X-ray variability. NATO Advanced Study Institutes Series. Series C, Mathematical and Physical Sciences, doi:https://doi.org/10.1017/CBO9780511536281.003